FACHBEREICH C - FACHGRUPPE PHYSIK
BERGISCHE UNIVERSITÄT
WUPPERTAL

Prospects of a cross section ratio measurement of W and Z events as a function of the jet multiplicity with early ATLAS data

Dissertation
von
Marisa Sandhoff

Februar 2010

Die Dissertation kann wie folgt zitiert werden:

urn:nbn:de:hbz:468-20100341
[http://nbn-resolving.de/urn/resolver.pl?urn=urn%3Anbn%3Ade%3Ahbz%3A468-20100341]

Contents

Introduction

Particle physics tries to "perceive whatever holds the world together in its inmost folds" [1]. The aim is the investigation of the fundamental particles and their interactions. In order to be able to explore the tiny inner structures of matter, microscopes have to be constructed, which provide the appropriate resolution power. Via the uncertainty principle small distances correspond to high energies. The energies, which are necessary to resolve the fundamental particles and their interactions, are comparable to the energies, which were relevant shortly after the beginning of the universe, the Big Bang.

Today these energies are provided by particle accelerators, by accelerating and colliding electrons or protons. Until now a large variety of colliding experiments has been performed, leading to a deeper and deeper understanding. To expand this knowledge, consistently new experiments with higher energies are needed and were constructed.

The Large Hadron Collider (LHC), located at the "European Organization for Nuclear Research" (CERN)[1] near Geneva, Switzerland, has recently been put into operation. By accelerating and colliding protons of a centre-of-mass energy of up to 14 TeV it will provide the opportunity to investigate physics processes unreachable so far. One of the collision experiments situated at the LHC is the ATLAS detector. At the center of ATLAS a large variety of physics processes takes place with a frequency of 40 MHz. Among these interactions the Higgs boson and perhaps evidences for New Physics hopefully will be found. Also further measurements of Standard Model processes, like top quark production, will be possible.

A major difficulty is to filter these events from the other much more frequent Standard Model processes. A decisive role is played by the production of W and Z bosons in association with jets. They will be produced in a huge amount by Standard Model processes at the LHC. However, almost all expected New Physics and other Standard Model processes, like top quark production, also include the production and decay of a W or Z boson and the production of jets. Therefore, a precise knowledge of W and Z production is crucial.

However, due to the complexity of W and Z events, which are accompanied by more than two jets, the cross sections can so far not be calculated precisely. The only possibility is to measure these events.

When decaying into two charged leptons, the Z boson is easy to investigate, because of its clear signature of decay particles. The W boson is much more difficult to detect. It decays into a charged lepton and a neutrino, whereas the neutrino can only be mea-

[1] "Conseil Européen pour la Recherche Nucléaire"

sured indirectly. Furthermore, the W boson is background to many other processes like for example top quark production. Hence, if W production is background to top quark production, top quark production is also background to W production. W events and top events are difficult to keep apart.
The general structure of W+jets and Z+jets events is very similar. Therefore, the idea of this analysis is to use Z events as tool to investigate W events. If the cross section ratio W+$n$jets/Z+$n$jets is measured, Z+$n$jet events can be used to estimate the cross section of W+$n$jet events. This approach will clearly improve the investigation of W background of top quarks and finding possible New Physics processes.
Due to their similarity another advantage is that in the cross section ratio of W+jets and Z+jets events many uncertainties - especially the uncertainties expected to be relevant at the beginning of ATLAS data acquisition - cancel out. This cross section ratio measurement is a very robust analysis, which can be done with the first data. It will provide indications of New Physics by itself, in case it clearly deviates from the Standard Model prediction. Furthermore, the ratio will make important contributions in tuning and testing generator predictions to describe LHC data. Until now no data are available at that energy, herefore mostly LEP data are still used.
This analysis concentrates on the investigation of W+jets and Z+jets events. The event structures are compared in order to confirm the expected similarities. Then the measurement of the cross section ratio of W+jets/Z+jets as a function of the jet multiplicity is prepared. Here the focus is put on the development of an analysis, which can be performed with early data. Afterwards a method is presented, to correct the measured ratio for detector effects in order to be able to compare theoretical predictions directly to the results.

Chapter 1

The physical context of the analyses

In this chapter the general concepts of elementary particle physics are summarized. Here only a brief compendium of elementary particle physics based on [2, 3] is presented. A more detailed description can be found in the cited publications.

1.1 The Standard Model of particle physics

The fundamental particles and their interactions are described by the Standard Model of elementary particle physics.
All known matter consists of two types of fundamental particles: quarks and leptons, in common representing the fermions. Fermions carry a half-integral spin and obey the Fermi-Dirac statistics. Both quarks and leptons are grouped into three families, each consisting of four particles, resulting in six quarks (u (up), d (down), c (charm), s (strange), t (top), b (bottom)) and six leptons (e, ν_e, μ, ν_μ, τ, ν_τ). For each particle an anti particle with the same mass, but opposite charge exists. The fermions and their properties are summarized in table 1.1.

		1st generation		2nd generation		3rd generation	
lep–tons	name	e	ν_e	μ	ν_μ	τ	ν_τ
	charge [e]	-1	0	-1	0	-1	0
	mass [MeV]	0.511	$< 3{\cdot}10^{-6}$	105.658	< 0.19	1776.84	< 18.2
quarks	name	**d**own	**u**p	**s**trange	**c**harm	**b**ottom	**t**op
	charge [e]	$-1/3$	$2/3$	$-1/3$	$2/3$	$-1/3$	$2/3$
	mass [MeV]	3.5-6	1.5-3.3	104^{+26}_{-34}	1270^{+70}_{-110}	4200^{+170}_{-70}	$(171.2\pm2.1)\cdot10^3$

Table 1.1: The fundamental fermions of the standard model [4].

Fermions interact by four fundamental interactions: the strong force, the electromagnetic force, the weak force and the gravitation. The gravitation could not be included into the Standard Model until now. However, as its strength is about 43 orders of magnitude weaker than the strong interaction, it can be neglected in high energy

physics. Interactions of particles take place by the exchange of particles, named exchange bosons. Bosons carry an integral spin and obey the Bose-Einstein statistics. The mediators of the strong force are eight gluons, of the electromagnetic force the photon and of the weak force the $W^{\pm}$ and Z bosons. Which particles participate in which interaction and their quantum numbers are listed in table 1.2.
The Standard Model is a quantum gauge theory, based on the $SU(3) \times SU(2) \times U(1)$ symmetry, where $SU(3)$ is the symmetry group of the strong interaction, $SU(2)$ of the weak interaction and $U(1)$ of the electromagnetic interaction. Gauge invariance under transformation inside a symmetry group ensures that the calculated variables are finite. The number of gauge bosons of each fundamental interaction is a direct result of requiring local gauge invariance in the dedicated symmetry group.

	generation 1.	2.	3.	**interaction**	**Y**	**I**	**I_3**	**Q**
leptons	$\begin{pmatrix}\nu_e\\ e\end{pmatrix}_L$	$\begin{pmatrix}\nu_\mu\\ \mu\end{pmatrix}_L$	$\begin{pmatrix}\nu_\tau\\ \tau\end{pmatrix}_L$	weak	-1	1/2	1/2	0
				electromagnetic, weak			-1/2	-1
	e_R	μ_R	τ_R	electromagnetic, (weak)	-2	0	0	-1
quarks	$\begin{pmatrix}u_i\\ d'_i\end{pmatrix}_L$	$\begin{pmatrix}c_i\\ s'_i\end{pmatrix}_L$	$\begin{pmatrix}t_i\\ b'_i\end{pmatrix}_L$	strong, weak, electromagn.	1/3	1/2	1/2	2/3
							-1/2	-1/3
	$u_{i,R}$	$c_{i,R}$	$t_{i,R}$		4/3	0	0	2/3
	$d_{i,R}$	$s_{i,R}$	$b_{i,R}$		-2/3	0	0	-1/3

Table 1.2: The fundamental fermions, their interactions and their quantum numbers hypercharge Y, weak isospin I, the third component I_3 and the charge $Q=I_3+Y/2$ [5].

1.1.1 The strong interaction

The gauge theory of the strong interaction is called Quantum Chromodynamics (QCD), based on the $SU(3)_{\text{colour}}$ symmetry group [6]. Local gauge invariance in this symmetry group leads to the presence of eight massless gauge bosons, called gluons.
The name "chromo" already implies colour playing an important role in the QCD. Colour is the "charge" of the strong interaction. Colour charge as additional quantum number had to be introduced to avoid spin statistics problems with baryons (particles consisting of quarks are called baryons). The Δ^{++} resonance consists of three up quarks with parallel spin. Without additional quantum number the Pauli principle, which postulates that each quantum state can only be occupied by one fermion, would be violated. Three colours differentiating the states solve the problem.
Quarks carry one of the three existing colours named red, green and blue; gluons carry one colour and one (different) anti colour. The colour charge neutralizes if three quarks of different colours (red, green and blue) are bound or two quarks with colour and the same anti colour. So, for example, the Δ^{++} resonance or the proton (consisting of two up quarks and one down quark) are colour neutral like all macroscopic objects. Hence,

it has to be explained, why on the one hand sometimes quarks can be considered as free particles, like for example the top quark subsequent to a proton - (anti-) proton collision or quarks observed in deep inelastic scattering inside a hadron, and on the other hand no macroscopic colour charged objects can be observed.
This leads to the model of "asymptotic freedom". At small distances or large momentum transfers (Heisenberg's uncertainty relation: $\Delta p \cdot \Delta x \geq h$) the forces between the quarks are small. So the top quark, which is produced at high momentum, can be handled as free quark. Also quarks inside a hadron appear free if probed at high momentum transfer. With increasing distances or small momentum transfers the field energy between the quarks increases and prevents quarks from being free particles. The described asymptotic freedom suggests the "confinement" of the QCD, which prohibits the generation of free quarks and macroscopic colour charged objects.
The Lagrangian of the QCD has to explain the aspect of confinement. It is given by [3]:

$$\mathcal{L} = \underbrace{\bar{\psi}(i\gamma^\mu \partial_\mu - m)\psi}_{\text{free fermion}} - \underbrace{g(\bar{\psi}\gamma^\mu T_a \psi) \cdot G^a_\mu}_{\text{interaction}} - \underbrace{\frac{1}{4} G^a_{\mu\nu} G^{\mu\nu}_a}_{\text{gauge boson}} \tag{1.1}$$

with the gauge invariant field strength tensor

$$G^a_{\mu\nu} = \partial_\mu G^a_\nu - \partial_\nu G^a_\mu - g f_{abc} G^b_\mu G^c_\nu. \tag{1.2}$$

and

$$\begin{aligned}
\psi &= \text{the quark fields} \\
G^a_\mu &= \text{the eight (a=1,...,8) vector gluon fields} \\
\gamma^\mu &= \text{the Dirac matrices} \\
T_a &= \text{the 8 Gell-Mann matrices, the generators of SU(3)} \\
m &= \text{the quark mass} \\
g &= \text{the coupling constant} \\
f_{abc} &= \text{the structure constants of the group}
\end{aligned}$$

In addition to the propagation term, which is quadratic in G, the gauge boson contribution includes third and forth order terms in G, establishing the fundamental vertices of the QCD, which are presented in figure 1.1.
The feature of QCD is that the gauge bosons, the gluons, carry colour charge themselves. Hence, they interact with each other and let the force remain constant with increasing distance. Then the field energy between the two quarks becomes so strong that new quark-antiquark pairs are generated, which enclose the quarks and confine the colour.
However, the QCD Lagrangian does not include a scale. The asymptotic behaviour of the strong force cannot be explained at this point. The aspect of the "running" coupling

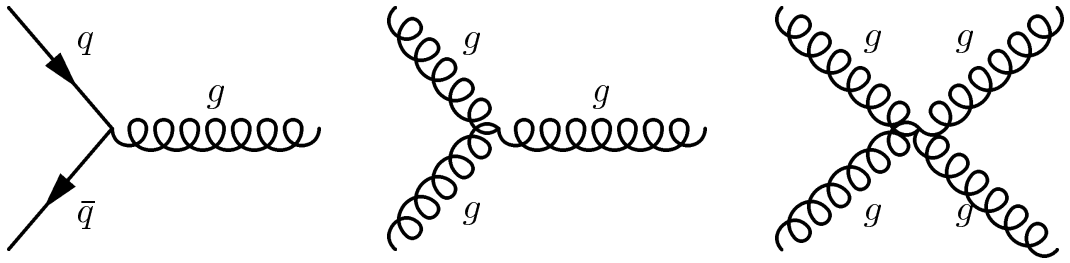

Figure 1.1: The fundamental vertices of Quantum Chromodynamics.

constant of the QCD, α_s, results from the the renormalization group equation. The value for α_s is given by [3]:

$$\alpha_s(Q^2) = \frac{12\pi}{(33 - 2n_f) ln(\frac{Q^2}{\Lambda^2})} = \beta_0 \cdot \frac{4\pi}{ln(\frac{Q^2}{\Lambda^2})} \tag{1.3}$$

with n_f being the number of involved quark flavours. Λ is the integration constant and a fundamental parameter of the QCD, $\Lambda \sim$ 0.1-0.5 GeV [3]. For $Q^2 \approx \Lambda^2$, α_s diverges. β_0 is the leading parameter of the beta-function and was first computed pertubatively by Wilczek, Gross and Politzer (Nobel Prize in physics 2004). Hence, as long as the number of involved flavours is smaller than 33/2, with increasing Q^2 (= momentum transfer) α_s decreases.

The production of jets

Typically hadron-hadron collisions produce outgoing partons. These partons can be for example gluons from initial or final state radiation or particles decaying into a $q\bar{q}$ pair (for example $W \rightarrow q\bar{q}'$). With increasing distance from the next colour charged particle, the field energy of the strong force increases and new quark-antiquark pairs are generated. This process repeats as long as the energy of the emerging partons is high enough to produce $q\bar{q}$ pairs. Initially, at still high Q^2, the state can be considered as multi parton state. With decreasing Q^2 this state cannot be longer referred to as multi parton state, but as multi hadron state. The generated partons form to hadrons, which then eventually decay into stable particles. This process is called fragmentation and leads to a bundle of particles, called jets, moving in the direction of the initial parton.

1.1.2 The electroweak interaction

The electromagnetic and the weak interaction are successfully combined into one theory, called electroweak interaction. The founders of the electroweak model are Glashow, Weinberg and Salam [7–10]. They were rewarded with the the Nobel Prize in physics in 1979.

Before describing the electroweak model, first its ingredients, the electromagnetic and the weak interaction, are introduced.

The electromagnetic interaction

The electromagnetic interaction is based on the $U(1)$ symmetry group and is described by a gauge theory called Quantum Electrodynamics (QED). QED was the first gauge theory of an interaction [11]. The gauge boson of the QED is the massless photon, γ, which couples to all particles which carry electrical charge. The photon itself carries no electrical charge, hence photons do not interact with each other. The coupling constant of the QED is called α_{QED}. For α_{QED} also a renormalization group equation applies and α_{QED} is described similar to 1.3. At $Q^2 = 0$ α_{QED} is of the order of $\frac{1}{137}$ and $\frac{1}{128}$ for energies at $Q^2 = m_W$ [4]. α_{QED} increases only slowly with increasing energy.

The weak interaction

The gauge bosons of the weak interaction are the $W^{\pm}$ and the Z^0 bosons. In contrast to the gauge bosons of the strong and the electromagnetic interactions, the $W^{\pm}$ and the Z^0 bosons are massive. The weak interaction is the only interaction, which can change the flavour of a fermion. The weak interaction violates parity, because the charged-current weak interaction only couples to left-handed fermions.
The first indication of the Z^0 boson was found at the Gargamelle bubble chamber experiment at CERN [12] and published in 1973. Electrons were observed to start moving suddenly. This was interpreted as an interaction with neutrinos by exchanging a Z^0. The bosons were directly observed in 1983 by the experiments UA1 and UA2 at the Super Proton Synchrotron (SPS) at CERN (a review can be found in [13]). First, in January, the $W^{\pm}$ was detected, followed by the Z^0 in May.

The electroweak model

Two fermion fields are introduced:

$$\psi_L = \frac{1}{2}(1-\gamma_5)\psi \tag{1.4}$$

$$\psi_R = \frac{1}{2}(1+\gamma_5)\psi \tag{1.5}$$

ψ_R describes right-handed fermions and ψ_L left-handed. The left-handed structure of the charged-current weak interactions is generated by applying the $SU(2)_L$ gauge symmetry only to left-handed fermion fields. The conserved quantum number of the $SU(2)_L$ gauge symmetry is the weak isospin I.
In addition to the $SU(2)_L$ the independent gauge symmetry $U(1)_Y$ is introduced, here the conserved quantum number is the weak hypercharge Y, defined by

$$Y = 2(Q - I_3) \tag{1.6}$$

where Q is the electrical charge. The electrical charge combines the quantum numbers of the electromagnetic and the weak interaction. ψ_R only transforms under the $U(1)_Y$ symmetry, ψ_L transforms under the $U(1)_Y$ and $SU(2)_L$ symmetry. The massless gauge fields in this model are an isospin triplet W^i_μ, i=1,2,3 for $SU(2)_L$ and and a singlet B_μ for $U(1)_Y$. The coupling constant of $SU(2)_L$ is g, of $U(1)_Y$ g'. $W^\pm$ are given by:

$$W^\pm = \sqrt{\frac{1}{2}}(W^1_\mu \mp i \cdot W^2_\mu) \tag{1.7}$$

To unify the electromagnetic and the weak interaction, W_3 and B have to be linear combinations of A (A is the massless electromagnetic field) and another neutral field Z of $SU(2)$:

$$\begin{pmatrix} W_3 \\ B \end{pmatrix} = \begin{pmatrix} \cos\Theta_W & \sin\Theta_W \\ -\sin\Theta_W & \cos\Theta_W \end{pmatrix} \cdot \begin{pmatrix} Z \\ A \end{pmatrix}. \tag{1.8}$$

Θ_W is the electroweak mixing angle, called Weinberg angle. This mixing explains the differences in the coupling of the Z to charged leptons and neutrinos and the coupling of the Z to right-handed particles. For the coupling constants one obtains:

$$g = \frac{e}{\sin\Theta_W} \tag{1.9}$$

$$g' = \frac{e}{\cos\Theta_W} \tag{1.10}$$

$$g_Z = \frac{e}{\cos\Theta_W \cdot \sin\Theta_W} \tag{1.11}$$

The weak interaction and the electromagnetic interaction are unified. Θ_W is the parameter of the model.
Until now the $W^\pm$ bosons and the Z boson are massless like the fermions. This is in contrast to observations. The masses have to be generated, but the theory has to remain re-normalizable, meaning that local gauge invariance has to remain conserved.
The principle of spontaneous symmetry breaking was introduced to solve this problem. Spontaneous symmetry breaking occurs if the basic equations of a system show a symmetry, which is not reflected by the basic state. A possibility to give mass to the $W^\pm$ and Z^0 bosons, while keeping the γ massless, has been discussed by Weinberg and Salam [8], based on ideas of Higgs [14]. Detailed descriptions of the Higgs Mechanism (and the electroweak theory) can be found additionally in for example in [3,11]. In this Higgs Mechanism a complex scalar isospin doublet is introduced [3]

$$\Phi(x) = \begin{pmatrix} \Phi^+(x) \\ \Phi^0(x) \end{pmatrix} = \begin{pmatrix} (\Phi_1 + i\Phi_2)/\sqrt{2} \\ (\Phi_3 + i\Phi_4)/\sqrt{2} \end{pmatrix} \tag{1.12}$$

A scalar potential V, called Higgs potential, is added to the Lagrangian. V is given by

$$V(\Phi) = \mu^2\Phi^*\Phi + \lambda(\Phi^*\Phi)^2 \tag{1.13}$$

with $\mu^2 < 0$ and $\lambda > 0$. The vacuum expectation value is chosen to be

$$\Phi_0 \equiv \sqrt{\frac{1}{2}}\begin{pmatrix}0\\ \nu\end{pmatrix}, \tag{1.14}$$

breaking the symmetry of the ground state, with ν being the vacuum expectation value of the Higgs field. The masses of the gauge boson are then acquired by their dynamical coupling to the Higgs field Φ:

$$m_W = \frac{1}{2}g\nu \tag{1.15}$$
$$m_Z = \frac{1}{2}g_Z\nu = m_W/\cos\Theta_W \tag{1.16}$$
$$m_\gamma = 0 \tag{1.17}$$

The measured masses of $W^{\pm}$ and Z^0 are [4]:

$$m_{W^\pm} = 80.398 \pm 0.025\,\text{GeV}$$
$$m_{Z^0} = 91.1876 \pm 0.0021\,\text{GeV}$$

From the measured value of m_W and m_Z, ν = 246 GeV [11] and $\sin^2\Theta_W$=0.23 [3].
A by-product of the described mechanism is a new massive scalar boson, called Higgs boson. m_{Higgs} is a free parameter of the Standard Model. Todate the Higgs boson could not be observed.
Spontaneous symmetry breaking also generates the masses of the fermions. These masses are generated by the Yukawa coupling of the fermion fields to the Higgs field Φ. For each fermion mass a Yukawa coupling parameter is obtained. The masses of the fermions are not predicted by the model, but have to be measured.
The mass eigenstates of the quarks (d',s',b') are not identical to the weak states (d,s,b). The relation is described by a mixing matrix defined by

$$\begin{pmatrix} d' \\ s' \\ b' \end{pmatrix} = \begin{pmatrix} V_{ud} & V_{us} & V_{ub} \\ V_{cd} & V_{cs} & V_{cb} \\ V_{td} & V_{ts} & V_{tb} \end{pmatrix} \cdot \begin{pmatrix} d \\ s \\ b \end{pmatrix}. \tag{1.18}$$

The matrix is a complex, unitary matrix and is called Cabibbo-Kobayashi-Maskawa (CKM) matrix. If the mass eigenstates would be identical to the electroweak eigenstates, all off-diagonal elements of the matrix would be zero. The off-diagonal elements explain the possible transitions from one quark family to another quark family by the weak interaction. The probability for a quark of flavour i to be transited to a quark of flavour j by exchange of a W boson is proportional to $|V_{ij}|^2$.

1.2 The top quark

The top quark was discovered in 1995 at the TEVATRON collider of the "Fermi National Accelerator Laboratory" near Chicago, USA [15, 16]. Its existence as the weak isospin partner of the bottom quark had been predicted since the discovery of the bottom quark in 1977. With its mass of about 170 GeV the top quark, an elementary particle with no extension, is almost as heavy as a gold atom. Because the top mass is near the electroweak scale, the top quark plays an important role in the Standard Model. For example the still unobserved Higgs boson couples to mass, and due to the high top mass its coupling to the top quark is stronger than to other fermions. So a discovery of the Higgs boson near the top quark has high probability. The top quark plays also a key role in searches for new physics. On the one hand the top quark will be background to these processes and a good knowledge of its properties will improve the searches. On the other hand the top quark will not only be background, but also the key in searches for new physics. For example the top quark is decay product of many new physics processes, like the top resonance Z' [17, 18].

1.2.1 top quark pair production

At hadron-hadron colliders top quark pairs are produced via the strong interaction. The $t\bar{t}$ cross section at leading order is given by

$$\sigma(AB \to t\bar{t}) = \sum_{i,j=q,\bar{q},g} \int dx_i dx_j f_{i(A)}(x_i, \mu_F^2) f_{j(B)}(x_j, \mu_F^2) \hat{\sigma_{ij}}(ij \to t\bar{t}; \hat{s}, \mu_R^2) \qquad (1.19)$$

with

- A and B: initial state hadrons; proton and proton for LHC, proton and antiproton for TEVATRON
- $f_{i(A)}(x_i, \mu^2)$: The parton distribution function (PDF); the PDF describes the probability density to find a parton of flavour i inside the hadron A carrying the momentum fraction x
- i,j run over all partons
- $\hat{s}$: the squared centre-of-mass energy of the colliding partons: $\hat{s} = (p_i + p_j)^2 = (x_i p_A + x_j p_B)^2$
- μ_F: the factorization scale; μ_R: the renormalization scale, typically $\mu_F = \mu_R = \mu = m_t$

In leading order top quark pairs can be produced by quark-antiquark annihilation and by gluon fusion. At the TEVATRON, a proton-antiproton collider, 90% of the top quarks are produced via $q\bar{q}$ annihilation. The LHC, a proton-proton collider, will produce most top quark pairs via gluon fusion. The explanation for this behaviour can be found mostly in the different centre-of-mass energies, in the PDFs for protons (and

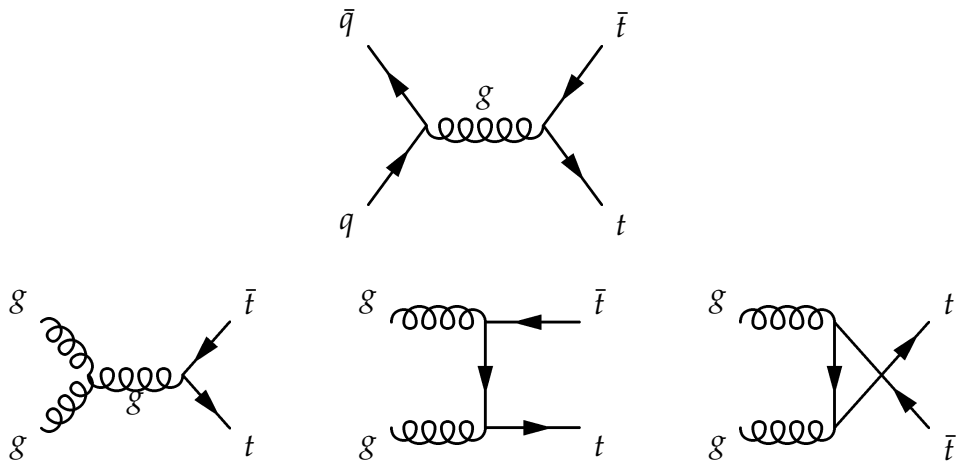

Figure 1.2: Born level Feynman diagrams contributing to top quark pair production [19].

antiprotons) and in the coupling of quark-antiquark and gluon-gluon. The Feynman diagrams for the leading order processes are presented in figure 1.2.
The $t\bar{t}$ cross section at the TEVATRON is calculated to be [20]:

$6.90^{+0.46}_{-0.64}$ pb at 1.96 TeV

The $t\bar{t}$ cross section at LHC is predicted to be [20]:

374^{+18}_{-33} pb at 10 TeV

827^{+27}_{-63} pb at 14 TeV

For a centre-of-mass energy of 7 TeV, which will be achieved in the early days of the LHC, the $t\bar{t}$ cross section will be a factor of about two lower than for 10 TeV.

1.2.2 top quark pair decay

The top quark decays with a probability of almost 100% into its weak isospin partner, the b quark, and a $W^{\pm}$ boson. The top quark decay width is given by [21–23]:

$$\Gamma_t = \frac{G_F m_t^3}{8\pi\sqrt{2}} |V_{tb}|^2 (1-y)^2 (1+2y) \left[1 - \frac{2\alpha_s}{3\pi} f(y)\right] \tag{1.20}$$

with

$$y = \left(\frac{M_W}{m_t}\right)^2 \tag{1.21}$$

$$f(y) = \frac{2\pi^2}{3} - 2.5 - 3y + 4.5y^2 - 3y^2 \ln y \tag{1.22}$$

The current world average value for the top mass is $m_t = 173.1 \pm 1.3$GeV [24]. For this mass a decay width of $\Gamma_t = 1.34$ GeV is obtained.

The high mass of the top quark results in a very short lifetime τ_t

$$\tau_t = \frac{1}{\Gamma_t} \approx 5 \cdot 10^{-25} s \tag{1.23}$$

Hadronization takes place at a time span of about 10^{-24} s, which corresponds to a mass of about 500 MeV. This means that the top quark decays before hadronization occurs. So there are no top hadrons. Investigating top quarks is the physics of an almost free quark.
As the top quark decays into a b quark and a $W^{\pm}$ boson with a probability of almost 100%, the top quark pair decay is classified by the decay channels of the W boson. The W boson decays into a $q\bar{q}$ or into a $l\nu$ pair, resulting in three possible decay channels for a $t\bar{t}$ pair:

- full hadronic (all-jets) (46.2%)
  $t\bar{t} \rightarrow W^+bW^-\bar{b} \rightarrow q\bar{q}'bq''\bar{q}'''\bar{b}$
- semi-leptonic (single lepton, lepton+jets) (43.5%)
  $t\bar{t} \rightarrow W^+bW^-\bar{b} \rightarrow q\bar{q}'bl\bar{\nu}_l\bar{b} + \bar{l}\nu_l bq\bar{q}'\bar{b}$
- full leptonic (dilepton) (10.3%)
  $t\bar{t} \rightarrow W^+bW^-\bar{b} \rightarrow \bar{l}\nu_l bl'\bar{\nu}_{l'}\bar{b}$

1.2.3 top quark mass

The top quark mass is an important free parameter of the Standard Model, which heavily impacts the possible Higgs mass range by radiative corrections. The so called "blue band plot" limits the Higgs mass by taking into account many Standard Model electroweak parameters, among others the top quark mass. The current blue band plot is presented in figure 1.3.
The current world average value for the top mass is [24]

$$m_t = 173.1 \pm 1.3\,\text{GeV}$$

1.2.4 single top quark production

In addition to the top quark pair production via the strong interaction, a production of single top quarks via the electroweak interaction is possible. The leading order Feynman diagrams are presented in figure 1.4. Recently single top quark production could be observed for the first time by the experiments DØ and CDF [26]. The cross section is measured to be $\sigma = 2.46^{+0.58}_{-0.47}$ pb.

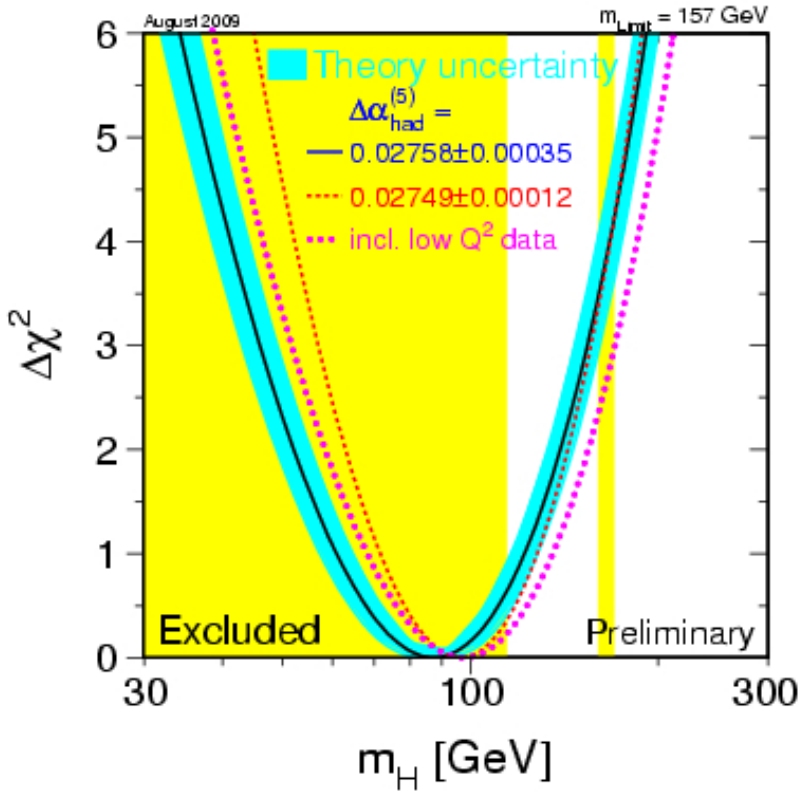

Figure 1.3: Blue band plot, the indirect determination of the Higgs mass from precision electroweak data. The figure shows the $\Delta\chi^2$ curve derived from high-Q^2 precision electroweak measurements, performed at LEP and by SLD, CDF, and D0, as a function of the Higgs-boson mass, assuming the Standard Model to be the correct theory of nature. The preferred value for its mass, corresponding to the minimum of the curve, is at 87 GeV, with an experimental uncertainty of +35 and -26 GeV (at 68 percent confidence level derived from $\Delta\chi^2 = 1$ for the black line, thus not taking the theoretical uncertainty shown as the blue band into account) [25].

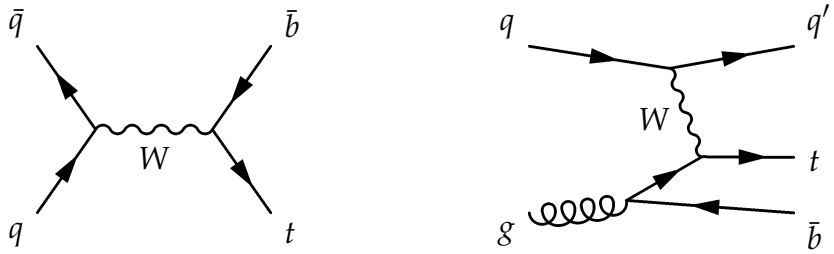

Figure 1.4: Leading order Feynman diagrams contributing to single top quark production. According to the structure of the diagrams the left process is called *s*-channel and the right *t*-channel production [19].

1.3 Experimental particle physics

The Standard Model of particle physics is a mathematical model with the aim to describe and explain fundamental interactions. There are many free parameters, for example the masses of the particles, which are not predicted by the theory. Measurements are necessary to verify the predictions of the Standard Model and to determine the free parameters.
The difficult task is to construct an experimental apparatus, which provides a resolution power high enough to perform these measurements. Here the choice falls on particle accelerators and colliders. The centre-of-mass energy of the collision is connected via the de-Broglie wavelength to the resolution power. Until now no prediction of the Standard Model was disproved.

Chapter 2

The LHC particle accelerator and the ATLAS detector

The Large Hadron Collider (LHC) is a circular particle accelerator measuring a length of 26.7 km. It is located at the "European Organization for Nuclear Research" CERN ("Conseil Européen pour la Recherche Nucléaire") near Geneva, Switzerland. The LHC was built inside the former LEP ("Large Electron Positron Collider") tunnel about 100 m beneath the surface.
The LHC will mostly be used as a proton-proton collider colliding protons with a centre-of-mass energy of 14 TeV[1] (7 TeV per proton), but the LHC is able to work as lead ion collider of an energy of 5.6 TeV (2.8 TeV per nucleon), too. A general introduction into CERN and the LHC can be found in [27], a very detailed overview in [28].

There are six experiments acquiring collision data provided by the LHC: CMS [29], ALICE [30], LHC-B [31], LHCf [32], TOTEM [33] and ATLAS [34]. An overview of the LHC and the experiments can be seen in figure 2.1 (LHCf and TOTEM not shown).
The analyses presented in chapters 7 and 8 take place within the ATLAS experiment.

2.1 Particle accelerators and collision experiments

Particle accelerators can be classified into two types: Linear and circular accelerators.

In linear accelerators particles are accelerated via different accelerator steps, which are arranged consecutively one after the other in space. As particles pass each acceleration unit only once, linear accelerators need passages of several kilometers of length. After acceleration the particles have only one chance to collide. The advantage of linear colliders is that particles do not radiate synchrotron radiation like in circular accelerators. Hence, linear accelerators are well adapted for accelerating electrons and positrons.

[1] The design energy of the LHC is 14 TeV. However, restrictions of the dipole magnets will limit its first operation phase to 10 TeV or rather 7 TeV.

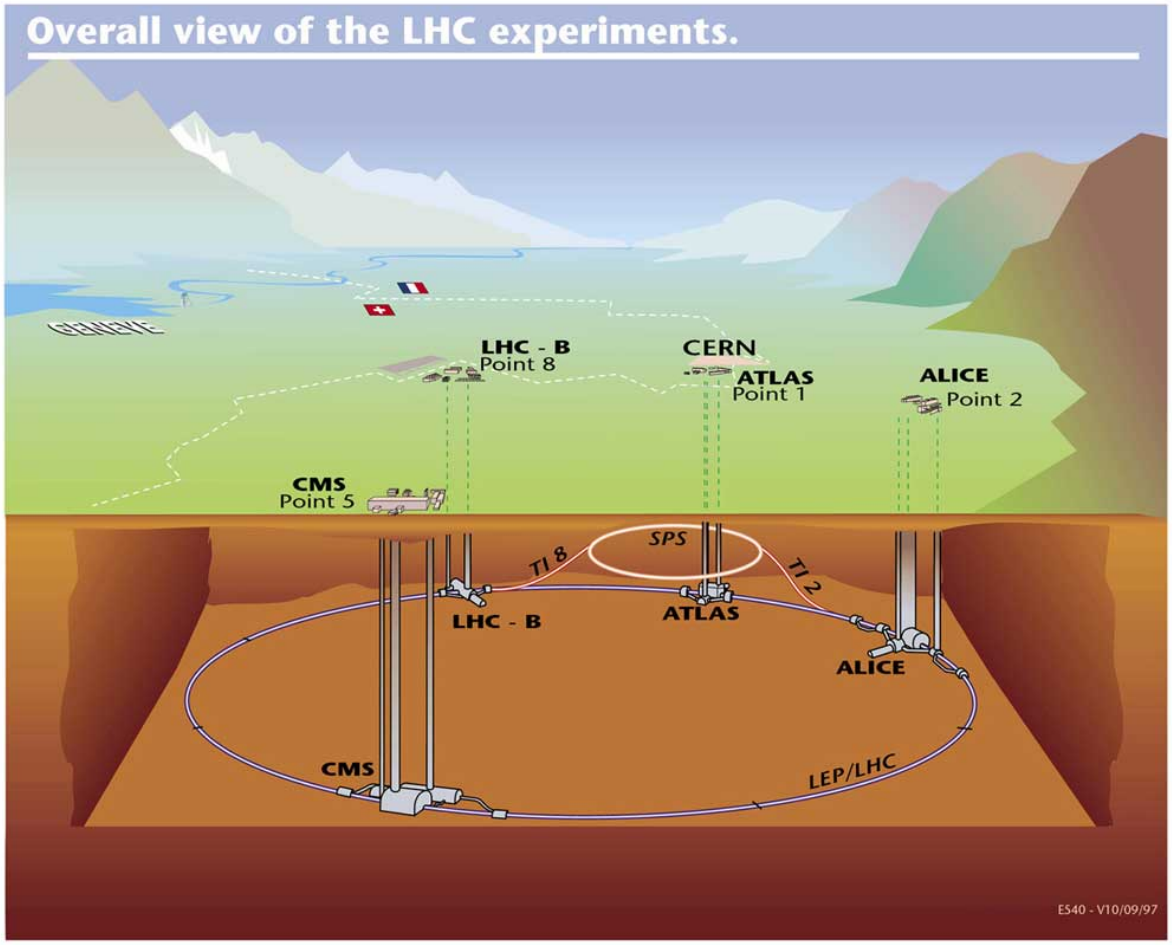

Figure 2.1: The LHC and its experiments [34].

In circular accelerators particles cycle on a stable orbit inside the collider. At each cycle they pass the acceleration unit. This results in a very long distance, during which the particles are accelerated. After acceleration the particles remain in the accelerator and are brought to collision at each cycle. Due to energy losses caused by synchrotron radiation, centre-of-mass energies of electrons and positrons gained by circular accelerators are limited. As synchrotron radiation is proportional to $\frac{1}{m^4}$ [35], for higher energies particles of higher masses, like protons, have to be chosen. The energy loss due to synchrotron radiation of protons with respect to electrons is a factor of $(\frac{m_e}{m_p})^4$ smaller.

Electron-positron collisions are a clean environment for analysis. The electron and the positron annihilate, so the rest frame of the collision is identical with the laboratory system (if both beams have the same energy). There are no beam remnants left to initiate a secondary event, which would interfere with the primary event.

In contrast to electrons protons are no elementary particles, but consist of partons, namely quarks and gluons. Hence, in a proton-(anti)proton collision the protons do not collide on the whole, but their partons. As each parton carries only the fraction x of the proton momentum, the centre-of-mass energy of the collision is smaller than two times the proton energy. The momentum fraction x of partons is described by Parton Distribution Functions (PDFs). So it is unknown after the collision, how much momentum was transferred and which partons interacted. Normally the rest frame of the collision is not identical with the laboratory system, because the probability that two partons with the same x collide is near to zero. Also, the remnants of the protons can lead to additional interactions, which interfere with the primary event.

2.2 Short overview of recent experiments in high energy physics

The forerunner of the LHC, the "Large Electron Positron Collider" (LEP), was a circular electron-positron collider. It operated from 1989 to 2000 and reached centre-of-mass energies of up to 209 GeV. Its four experiments OPAL, Delphi, L3 and ALEPH performed many precision measurements during this time. The W mass for example was measured with an accuracy of 0.04% [36] and the Z mass with an accuracy of 0.002% [37]. At its maximum centre-of-mass energy the energy loss to synchrotron radiation was around 3 GeV per revolution [38]. So higher energies could not be reached with LEP.
There are plans to build an electron-positron linear accelerator with centre-of-mass energies of 500 - 1000 GeV. This "International Linear Collider" (ILC) will have a length of about 31 km. However, until now neither a location nor a start of construction day are determined.

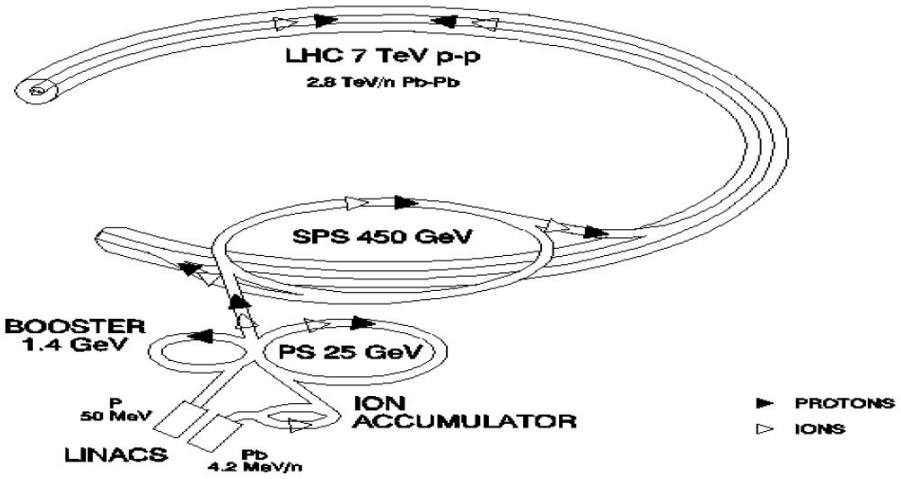

Figure 2.2: The LHC injection chain [28].

So the other possibility to achieve higher collision energies was realized. The TEVATRON accelerator at the "Fermi National Accelerator Laboratory" near Chicago with its experiments D0 and CDF is a circular proton-antiproton collider of a centre-of-mass energy of 1.96 TeV. Here the top quark was discovered in the year 1995 [15, 16].
At the moment the TEVATRON reaches the highest proton energies and is the only accelerator, where top pairs can be produced. Once the LHC starts operations[2] it will inherit the status of the most powerful particle accelerator.

2.3 Large Hadron Collider (LHC)

The acceleration of protons in the LHC from 0 to 7 TeV is performed in several steps, which are illustrated in figure 2.2. At the beginning protons are obtained by removing the electrons from hydrogen atoms.
These protons are accelerated by a linear accelerator ("LINACS") to an energy of 50 MeV. Acceleration to higher proton energies is then achieved by a chain of circular accelerators. The PS Booster ("BOOSTER") increases the proton energy to 1.4 GeV, the Proton Synchrotron ("PS") to 25 GeV and finally the Super Proton Synchrotron ("SPS") to 450 GeV. At this stage the protons are injected (one part circling clock wise, the other circling counter clock wise) into the LHC, where the final acceleration to 7 TeV is done. The proton beam has to be kept focused and on a stable, nearly circular orbit. For this a total number of 9593 magnets including 1232 dipoles and 392 quadrupoles are installed inside the LHC. The magnetic field keeping the particles on the path is proportional to the centre-of-mass energy. For the energies at the LHC a magnetic dipole field of 8.33 Tesla is necessary - corresponding to 11850 A. Hence, superconducting magnets

[2] In March 2010 the LHC started operating at a centre-of-mass energy of 7 TeV.

are needed. The quadrupoles and additional magnets of higher orders focus the beam to provide a high probability for collisions at the four interaction points.
The protons do not circle equally distributed inside the LHC. They are organized in 2808 packets (called "bunches") of 1.1*10^{11} protons each. The gaps between the bunches are 7 m long corresponding to time intervals between the bunches of 25 ns. This corresponds to a collision frequency of 40MHz. The bunch structure of the beam is a consequence of the acceleration by radio frequency. A particle can only be accelerated if it passes through the cavities in a well defined moment of the radio frequency cycle. If a particle passes the cavity too early or too late, it is slowed down or accelerated more than particles passing in the correct moment of the radio frequency cycle. Hence, bunches of protons are formed.
The two opposite circling proton beams are brought to collision at the four interaction points, where the experiments CMS, ALICE, LHCb and ATLAS are situated (see figure 2.1).
Before the proton beams are crossed, they are focused as much as possible to increase the probability for protons to collide. A measure for the probability of collisions is given by the luminosity L, which is defined as

$$\mathcal{L} = \frac{n_1 n_2 f}{A}$$

with

n_1 = number of protons in bunch 1
n_2 = number of protons in bunch 2
f = frequency of collisions
A = cross sectional area of the beam

It is differentiated between instantaneous and integrated luminosity. The relation is

$$\mathcal{L}_{int} = \int_{t=t_1}^{t=t_2} \mathcal{L}_{inst}(t)\mathrm{d}t. \tag{2.1}$$

The number N of events of a given process with cross section σ then yields to

$$N = \sigma * \mathcal{L}_{int}$$

At start up the instantaneous luminosity of the LHC will be $10^{33}\frac{1}{cm^2 s}$. It is planned to increase the luminosity to $2.3 * 10^{34}\frac{1}{cm^2 s}$ later on.
Inside each experiment there will be proton-proton collisions with a frequency of 40MHz. With each collision the instantaneous luminosity decreases. After about 10 hours the luminosity will be sunken to a level with small probability of collisions. Then the remaining beam is extracted from the LHC and a new acceleration cycle is started.

2.4 ATLAS Experiment

The ATLAS detector is a multipurpose detector and the largest of the four detectors at the LHC. It measures 44 m in length, has a diameter of 25 m and its weight is about 7000 tons. The ATLAS detector is built to measure the momentum, energy and type of particles originating from a proton-proton collision. It is arranged symmetrically with respect to the interaction point.
Table 2.1 summarizes the performance goals, defined by the physics processes, which will be studied with the ATLAS detector. In Figure 2.3 a general overview of the detector is given. From inside to outside it can be divided into three parts: The Inner Detector, the calorimeters and the Muon System.

Detector component	**Required resolution**	η **coverage**	
		Measurement	Trigger
Tracking	σ_T/p_T= 0.05% $p_T \oplus$ 1%	$\pm$2.5	
EM calorimetry	σ_E/E= 10%/$\sqrt{E} \oplus$ 0.7%	$\pm$ 3.2	$\pm$2.5
Hadronic calorimetry (jets)			
barrel and end-cap	σ_E/E= 50%/$\sqrt{E} \oplus$ 3%	$\pm$3.2	
forward	σ_E/E= 100%/$\sqrt{E} \oplus$ 10%	3.1 $<$ $\lvert\eta\rvert$ $<$ 4.9	
Muon spectrometer	σ_T/p_T= 10% at p_T=1 TeV	$\pm$2.7	$\pm$2.4

Table 2.1: General performance goals of the ATLAS detector. Units for E and p_T are in GeV [39].

The coordinate system of the ATLAS detector is defined as described below. The x-axis points to the center of the LHC, the y-axis to the surface and the z-axis is parallel to the beam. The point (0,0,0) is identical with the nominal interaction point. Instead of the Cartesian coordinates (x,y,z) usually polar coordinates (r,Φ) are used:

$$\begin{aligned} r &= \sqrt{x^2+y^2} \\ \Phi &= \tan(\frac{y}{x}) \end{aligned}$$

The polar angle Θ is defined with respect to the positive z-axis. Commonly used at hadron accelerators is the pseudorapidity η

$$\eta = -\ln \tan(\frac{\Theta}{2})$$

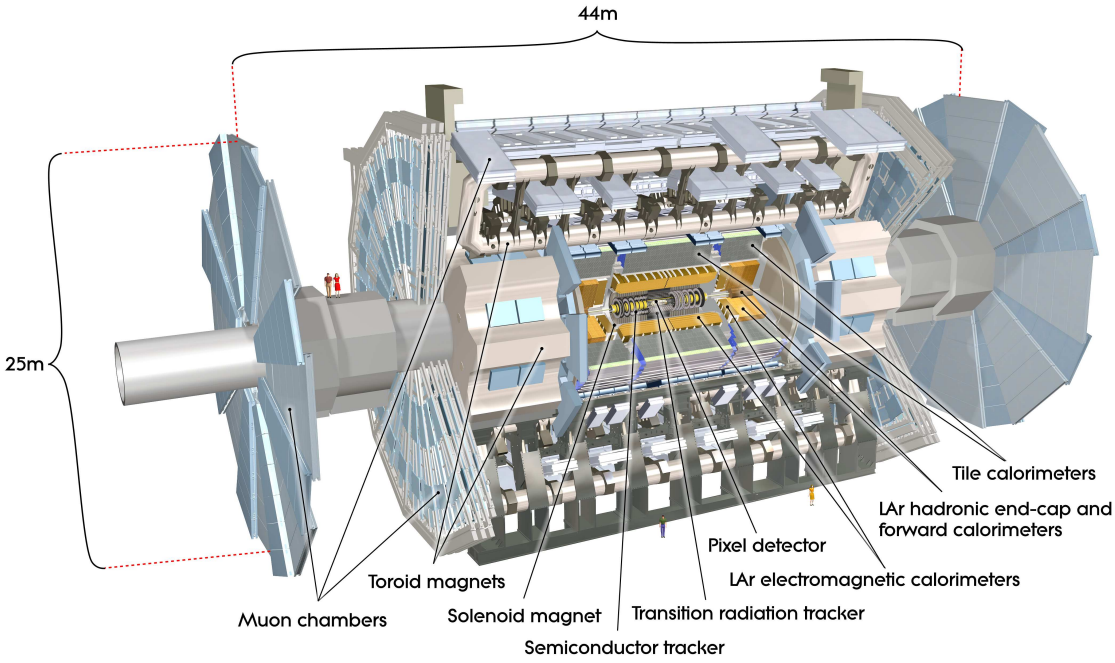

Figure 2.3: The ATLAS detector [39].

The advantage of the pseudorapidity η is that a Lorentz transformation leads only to a shift in η. However, η is an approximation of the rapidity y (defined as $y = \frac{1}{2} \ln \left(\frac{E+p_L}{E-p_L} \right)$), valid only for massless particles.

In the following the different components of the ATLAS detector are described. A very precise description of the ATLAS detector can be found in [39]. Here only a short summary of the most important properties of the detector components is presented.

2.4.1 Inner Detector

The information collected in the Inner Detector is used to reconstruct the tracks of charged particles. The whole Inner Detector is located inside a solenoid of 5.3 m length and a diameter of 2.5 m, providing a 2 Tesla magnetic field. By this magnetic field the trajectories of the particles are forced to a curve, which allows the determination of the particles´ charge and momentum.
The buildup of the Inner Detector is illustrated in Figure 2.4. From inside to outside, the Inner Detector consists of three sub-detectors: The silicon pixel detector closest to the interaction point with its innermost layer at a radius of only 5 cm, surrounded by the silicon strip detector (SCT, "Semiconductor Tracker") and last the "Transition Radiation Tracker" (TRT), composed of straw tube drift chambers. All three sub-detectors are divided into a barrel region and two end-cap regions. The dimensions of the sub-detectors are summarized in table 2.2.
The pixel detector consists of pixel sensors sizing R - $\Phi \times$ z = 50 x 400 μm^2. In the barrel

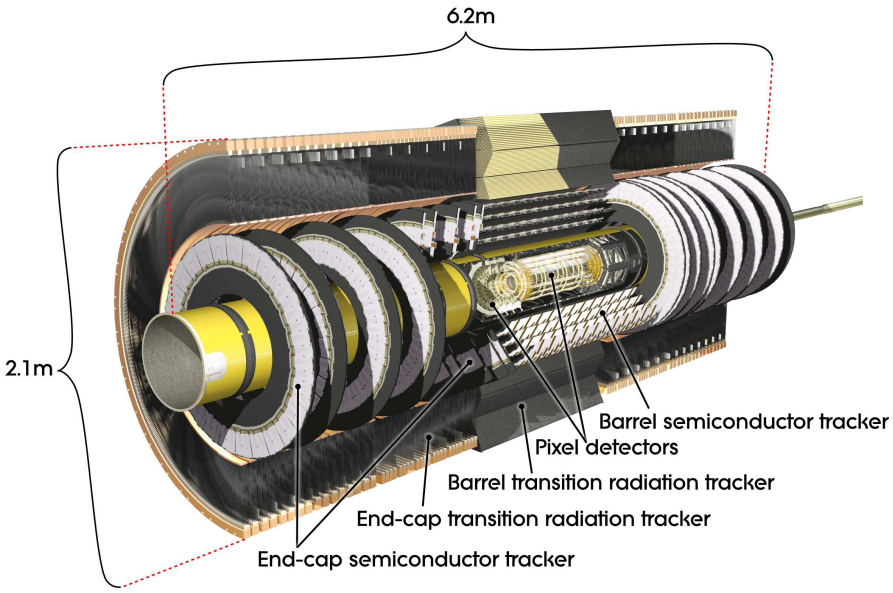

Figure 2.4: Overview of the ATLAS inner detector [39].

region these are located on concentric cylinders and in the end-cap region on perpendicular disks. Due to the fine segmentation in the barrel (end-cap) region an accuracy of 10μm (10 μm) in R - Φ and 115 μm in z (R) is achieved. To avoid gaps between the pixel sensors, both in R - Φ and in z overlapping layers are installed.

Similar to the pixel detector, the SCT consists of cylinders in the barrel region and disks in the end-cap region. In the barrel region the micro strips run parallel to the beam axis with a strip pitch of 80 μm. To allow also a measurement in z direction, the four barrel layers are build as stereo layers, with one strip layer running exactly parallel to the beam axis and the other layer at an angle of 40 mrad. The accuracies in the barrel are 17 μm in R - Φ and 580 μm in z. In the end-caps the micro strips run radially and on each disks the strip layers are arranged as stereo layers, too, with a stereo angle of 40 mrad. The strip pitch is also approximately 80 μm. In the disks the accuracies are 17 μm in R - Φ and 580 μm in R.

The TRT only provides R -Φ information of tracks with a coverage of up to $|\eta| = 2.0$. In the barrel region the straws run parallel to the beam axis and are 1.44 m long, divided in two halves at $\eta = 0$. In the end-cap region the straws are 37 cm long and run radially in wheels. Each straw has a diameter of 0.4 cm achieving an accuracy of 130 μm.

A particle emerging from the interaction point leaves a number of hits passing through the Inner Detector. Inside a pseudorapidity region of $|\eta| < 2.5$ 3 hits in the pixel detector, 8 hits in the SCT (corresponding to 4 space points) and about 36 hits in the TRT are obtained, which allow the reconstruction of the particle´s track. Although from its dimensions the Inner Detector is the smallest sub-detector of ATLAS, with approximately 80 million readout channels of the pixel detector, 6 million readout channels in the SCT and 400 thousand in the TRT it is the most data intensive part of the whole detector.

Item	Radial extension (mm)	Length (mm)
Overall ID envelope	$0 < R < 1150$	$0 < \|z\| < 3512$
Beam-pipe	$29 < R < 36$	
Pixel overall envelope	$45.5 < R < 242$	$0 < \|z\| < 3092$
3 cylindrical layers (barrel)	$50.5 < R < 122.5$	$0 < \|z\| < 400.5$
2 x 3 disks (end-cap)	$88.8 < R < 149.6$	$495 < \|z\| < 650$
SCT overall envelope		
barrel	$255 < R < 549$	$0 < \|z\| < 805$
end-cap	$251 < R < 610$	$810 < \|z\| < 2797$
4 cylindrical layers (barrel)	$299 < R < 514$	$0 < \|z\| < 749$
2 x 9 disks (end-cap)	$275 < R < 560$	$839 < \|z\| < 2735$
TRT overall envelope		
barrel	$554 < R < 1082$	$0 < \|z\| < 780$
end-cap	$617 < R < 1106$	$827 < \|z\| < 2744$
73 straw planes (barrel)	$563 < R < 1066$	$0 < \|z\| < 712$
160 straw planes (end-cap)	$644 < R < 1004$	$848 < \|z\| < 2710$

Table 2.2: Main parameters of the Inner Detector [39].

2.4.2 Calorimeter System

In the ATLAS calorimeter system the energies of particles emerging proton-proton collisions are measured. To determine the energies precisely the electromagnetic and hadronic showers have to be contained completely inside the calorimeter. Also, a leakage of electrons, photons and hadrons into the muon system would lead to noise there. To achieve spatial resolution of the deposited energy the whole calorimeter system is segmented into cells. Many physics processes to be studied at ATLAS contain neutrinos in the final state. Neutrinos are uncharged and take only part in the weak interaction. So with high probability they will not interact with the detector material and are thus invisible. They have to be detected indirectly by the missing transverse energy they carried away. To calculate the missing transverse energy (E_T^{miss}) via the E_T imbalance, a good coverage in η is needed.

Describing the energy resolution of a calorimeter two contributions have to be taken into account: The stochastic and the intrinsic part. The intrinsic contribution is caused by electronic noise and is independent of the particles´ energy. The stochastic contribution describes fluctuations in the energy deposition and hence in the number of particles produced in the shower. It decreases with increasing particle energy (= increasing number of produced particles), described by resolution (in %)/$\sqrt{E}$.

The calorimeter system is divided into an electromagnetic and a hadronic calorimeter. Both are subdivided into a barrel and two end-cap regions. A cut-away view of the calorimeter system can be seen in figure 2.5.

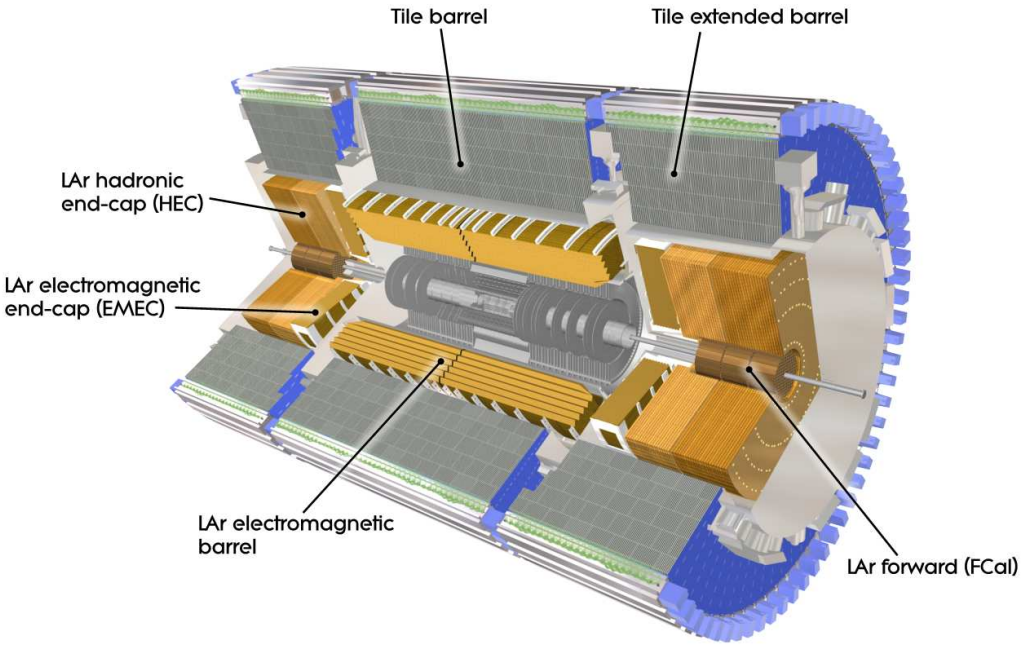

Figure 2.5: Overview of the ATLAS calorimeter system [39].

Electromagnetic Calorimeter

The electromagnetic calorimeter measures the energies of electrons and photons. It is a sampling calorimeter using lead as absorber and liquid argon (LAr) as active material. A sampling calorimeter separates the particle absorption and the signal readout. In the central region ($0 < |\eta| < 2.5$), which provides full tracking coverage, there are radially 3 active layers and 2 active layers in the higher pseudorapidity regions ($2.5 < |\eta| < 3.2$). To ensure full covarage in Φ the alternating lead/LAr structure is built in accordion shape. As electrons and photons already crossed an amount of material before reaching the calorimeter (for example the central solenoid accounts for 2.3 radiation lengths), presamplers, consisting of a layer of argon, are installed in the pseudorapidity region $|\eta| < 1.8$ in front of the electromagnetic calorimeter. Their task is to measure the lost energy, which does not reach the calorimeter. Table 2.3 summarizes the main parameters of the electromagnetic calorimeter, like the granularity as a function of the pseudorapidity region and depth. In radiation length X_0, the thickness of the electromagnetic calorimeter is $> 22\ X_0$ in the barrel and $> 24\ X_0$ in the end-cap region. This limits the electromagnetic leakage into the hadronic calorimeter and leads to a precise energy measurement. The resolution of the electromagnetic calorimeter is expected to be $\sigma_E/E = 10\%/\sqrt{E} \oplus 0.7\%$.

	Barrel		End-cap	
EM calorimeter				
Number of layers and η coverage				
Presampler	1	$\|\eta\| < 1.52$	1	$1.5 < \|\eta\| < 1.8$
Calorimeter	3	$\|\eta\| < 1.35$	2	$1.375 < \|\eta\| < 1.5$
	2	$1.35 < \|\eta\| < 1.475$	3	$1.5 < \|\eta\| < 2.5$
			2	$2.5 < \|\eta\| < 3.2$
Granularity $\Delta\eta \times \Delta\Phi$ versus η				
Presampler	0.025×0.1	$\|\eta\| < 1.52$	0.025×0.1	$1.5 < \|\eta\| < 1.8$
Calorimeter	$0.025/8 \times 0.1$	$\|\eta\| < 1.40$	0.050×0.1	$1.375 < \|\eta\| < 1.425$
1st layer	0.025×0.025	$1.40 < \|\eta\| < 1.475$	0.025×0.1	$1.425 < \|\eta\| < 1.5$
			$0.025/8 \times 0.1$	$1.5 < \|\eta\| < 1.8$
			$0.025/6 \times 0.1$	$1.8 < \|\eta\| < 2.0$
			$0.025/4 \times 0.1$	$2.0 < \|\eta\| < 2.4$
			0.025×0.1	$2.4 < \|\eta\| < 2.5$
			0.1×0.1	$2.5 < \|\eta\| < 3.2$
Calorimeter	0.025×0.025	$\|\eta\| < 1.40$	0.050×0.025	$1.375 < \|\eta\| < 1.425$
2n layer	0.075×0.025	$1.40 < \|\eta\| < 1.475$	0.025×0.025	$1.425 < \|\eta\| < 2.5$
			0.1×0.1	$2.5 < \|\eta\| < 3.2$
Calorimeter	0.050×0.025	$\|\eta\| < 1.35$	0.050×0.025	$1.5 < \|\eta\| < 2.5$
3rd layer				
Number of readout channels				
Presampler	7808		1536 (both sides)	
Calorimeter	101760		62208 (both sides)	

Table 2.3: Main parameters of the electromagnetic calorimeter [39].

Hadronic Calorimeter

Behind the electromagnetic calorimeter the hadronic calorimeter is placed. It consists of a barrel ($|\eta| < 1.0$), an extended barrel ($0.8 < |\eta| < 1.7$), two end-cap ($1.5 < |\eta| < 3.2$) and two forward calorimeters ($3.1 < |\eta| < 4.9$). To reach overall coverage, the different components are situated overlapping in η. The main parameters of the hadronic calorimeter are summarized in table 2.4. All constituents of the hadronic calorimeter are sampling calorimeters.

In the barrel and extended barrel, the hadronic calorimeter uses iron plates as absorber and scintillating tiles as active material. In depth, both barrel and extended barrel are divided into three layers with 1.5, 4.1 and 1.8 interaction lengths (λ) per layer for the barrel and 1.5, 2.6 and 3.3 λ for the extended barrel. This leads to a total thickness of 9.7 λ at $\eta = 0$, which provides good resolution for high energy jets. Azimuthally the tile calorimeter is segmented into 64 modules. In the end-cap part copper is used as absorber and liquid-argon as active material. The end-cap calorimeter consists of two wheels per end-cap, each divided into two segments in depth and built of 32 wedge-shaped modules.

The forward calorimeter, covering the high pseudorapidity regions $3.1 < |\eta| < 4.9$, is important for E_T^{miss} determination. It measures both electromagnetic and hadronic

showers. The first layer of absorber material consists of copper, optimised for electromagnetic shower measurements, the second and third layer consists of tungsten, good for hadronic shower determination. As active material liquid-argon is used. In total the forward calorimeter provides 10 λ, limiting loss of electromagnetic and hadronic energy into the Muon System.
For the expected energy resolution of the hadronic calorimeter see table 2.1.

	Barrel	End-cap	
LAr hadronic end-cap			
$\|\eta\|$ coverage		$1.5 < \|\eta\| < 3.2$	
Number of layers		4	
Granularity $\Delta\eta \times \Delta\Phi$		0.1×0.1	$1.5 < \|\eta\| < 2.5$
		0.2×0.2	$2.5 < \|\eta\| < 3.2$
Readout channels		5632 (both sides)	
LAr forward calorimeter			
$\|\eta\|$ coverage		$3.1 < \|\eta\| < 4.9$	
Number of layers		3	
Granularity $\Delta x \times \Delta y$ (cm)		FCal1: 3.0×2.6	$3.15 < \|\eta\| < 4.30$
		FCal1:	$3.10 < \|\eta\| < 3.15$,
		$\sim$ four times finer	$4.30 < \|\eta\| < 4.83$
		FCal2: 3.3×4.2	$3.24 < \|\eta\| < 4.50$
		FCal2:	$3.20 < \|\eta\| < 3.24$,
		$\sim$ four times finer	$4.50 < \|\eta\| < 4.81$
		FCal3: 5.4×4.7	$3.32 < \|\eta\| < 4.60$
		FCal3:	$3.29 < \|\eta\| < 3.32$,
		$\sim$ four times finer	$4.60 < \|\eta\| < 4.75$
Readout channels		3524 (both sides)	
Scintillator tile calorimeter			
	Barrel	Extended barrel	
η coverage	$\|\eta\| < 1.0$	$0.8 < \|\eta\| < 1.7$	
Number of layers	3	3	
Granularity $\Delta\eta \times \Delta\Phi$	0.1×0.1	0.1×0.1	
Last layer	0.2×0.1	0.2×0.1	
Readout channels	5760	4092 (both sides)	

Table 2.4: Main parameters of the hadronic calorimeter [39].

2.4.3 Muon System

The outermost part of the ATLAS detector is formed by the Muon Spectrometer. All charged particles, which are not stopped by the electromagnetic and hadronic calorimeters and reach the Muon System, are assumed to be muons. So a good containment of electromagnetic and hadronic showers in the calorimeters limits the noise and misidentification of particles as muons. The Muon System has to fulfill two performance goals: present a stand-alone tracking detector on the one hand and provide

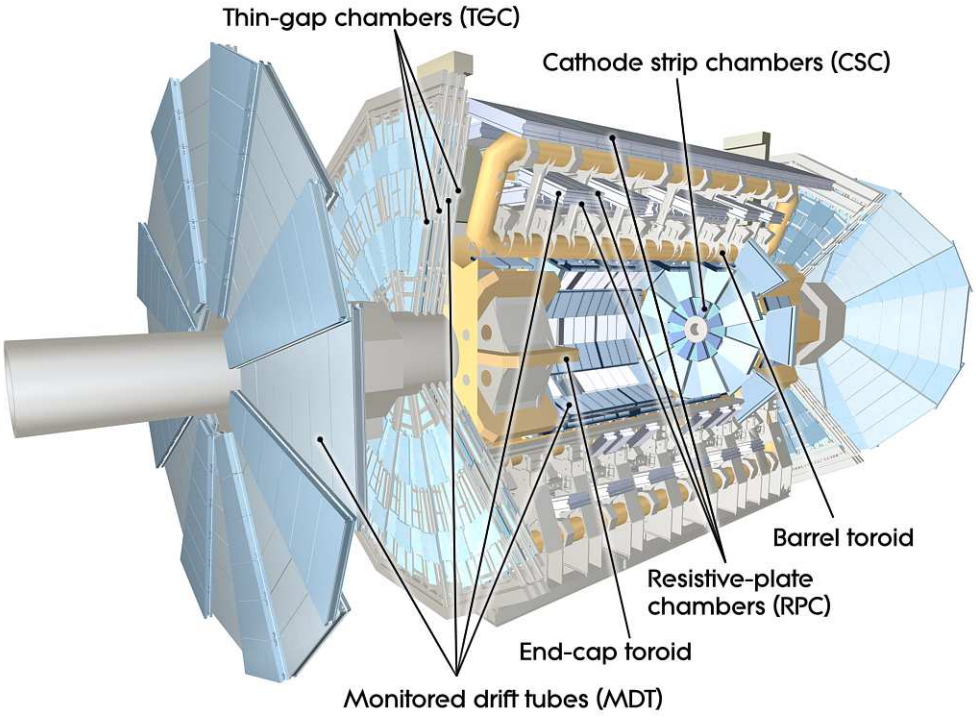

Figure 2.6: Overview of the ATLAS muon system [39].

a trigger on muon tracks on the other hand. Considering these standards the Muon System is built of different types of drift chambers, which can be split into two main classes: High resolution drift chambers for precision tracking and fast chambers for triggering. The particles´ momentum and charge is determined by the deflection of the particles trajectories in a magnetic field provided by a toroidal magnet system surrounding the drift chambers. The Muon System covers the range $|\eta| < 2.7$ for tracking and $|\eta| < 2.4$ for triggering. Figure 2.6 shows a cut-away view.
The magnetic field of the Muon System is provided by a large barrel and two end-cap toroids. The two end-cap toroids are situated inside the barrel toroid subsequent to the central solenoid. Each of the three toroids consists of 8 coils, which are installed radially around and symmetrically to the beam axis. To avoid gaps the end-cap toroids are rotated by 22.5° with respect to the barrel toroid. The barrel toroid provides a magnetic field with a bending power of 1.5 to 5.5 Tm inside $0 < |\eta| < 1.4$ and the end-cap toroids of 1 to 7.5 Tm for $1.6 < |\eta| < 2.7$. The bending power is lower in the region with overlapping fields of barrel and end-cap toroids ($1.4 < |\eta| < 1.6$). For magnetic fields of this strength superconducting magnets have to be used. The magnets of the Muon System are the most eye catching part of the ATLAS detector. The 8 barrel toroids have a length of about 25 m, a radial width of about 5 m and the tube diameter is about 1 m.
In the barrel region the drift chambers for precision tracking are situated on three concentric cylinders with the eight coils of barrel toroids around them. In the end-cap region the drift chambers are assembled to four large wheels per end-cap. The end-cap

toroids are placed in between these wheels. For precision tracking Monitored Drift Tube chambers (MDT´s) are used, covering the pseudorapidity region of $|\eta| < 2.7$ for the two outer layers and $|\eta| < 2.0$ for the inner layer. For the pseudorapidity region of $2.0 < |\eta| < 2.7$ of the inner layer Cathode-Strip Chambers (CSC) are used. These have a finer granularity and are faster than MDTs. This is an advantage with regard to the increasing number of tracks with higher pseudorapidity.
To be able to provide trigger information, fast chambers have been installed in addition to the precision tracking chambers. In the barrel region ($|\eta| < 1.05$) Resistive Plate Chambers (RPC) are used, in the end-cap region ($1.05 < |\eta| < 2.4$) Thin Gap Chambers (TGC). Table 2.5 summarizes the main parameters of the employed drift chambers, and table 2.6 lists the resolutions and hit multiplicities per track available for track reconstruction.

Monitored drift tubes	**MDT**
Coverage	$\|\eta\| < 2.7$ (innermost layer: $\|\eta\| < 2.0$)
Number of chambers	1088 (1150)
Number of channels	339000 (354000)
Function	Precision tracking
Cathode strip chambers	**CSC**
Coverage	$2.0 < \|\eta\| < 2.7$
Number of chambers	32
Number of channels	31000
Function	Precision tracking
Resistive plate chambers	**RPC**
Coverage	$\|\eta\| < 1.05$
Number of chambers	544 (606)
Number of channels	359000 (373000)
Function	Triggering, second coordinate
Thin gap chambers	**TGC**
Coverage	$1.05 < \|\eta\| < 2.7$ (2.4 for triggering)
Number of chambers	3588
Number of channels	318000
Function	Triggering, second coordinate

Table 2.5: Main parameters of the muon spectrometer. Numbers in brackets for the MDT´s and the RPC´s refer to the final configuration of the detector in 2009 [39].

2.4.4 Trigger

Inside the ATLAS detector collisions will take place with a rate of 40 MHz. Recording event data with this frequency exceeds today´s technical possibilities. As the total cross section of the LHC is several magnitudes higher than the cross sections of the interesting physics processes (for example W, Z and top-quark production, see Figure 2.7), the challenge is to reduce the event rate by picking up only these events. This task is done by the ATLAS Trigger chain.

		Chamber resolution			Measurements/track	
Type	**Function**	**z/R**	**Φ**	**time**	**barrel**	**end-cap**
MDT	tracking	32 μm	-	750 ns	20	20
CSC	tracking	40 μm	5 mm	7 ns	-	4
RPG	trigger	10 mm	10 mm	1.5 ns	6	-
TGC	trigger	2-6 mm	3-7 mm	4 ns	-	9

Table 2.6: Parameters of the four types of drift chambers of the Muon System [39, 40]. The quoted spatial resolution does not include chamber-alignment uncertainties. Column 5 lists the intrinsic time resolution of each chamber type, to which contributions from signal-propagation and electronics contributions need to be added.

The trigger system consists of three levels: The Level-1 trigger (L1), the Level-2 trigger (L2) and the event filter (EF). The L2 trigger and the event filter form the high level trigger (HLT). The L1 trigger reduces the event rate from 40 MHz to 75 kHz, the L2 trigger to 3.5 kHz and the EF to 200 Hz. This gives a time of 2.5 μs for event procession for the L1, 40 ms for the L2 and about 4 s for the EF. From one trigger level to the next one, the decisions are refined and additional cuts are applied.

The L1 trigger only uses reduced-granularity information from a subset of the detector components. In this first trigger step, signatures from high-p_T muons, electrons/photons, jets, hadronic decaying τ-leptons, large missing E_T and large total E_T are searched. Around detected interesting objects Regions-of-Interests (ROI´s), containing information on η, Φ, energy and type of signature, are defined. These are handed to the L2 trigger. The L2 trigger concentrates on the previously built ROI´s, but uses the full granularity and precision provided by the detector components. As last step the EF performs its decision on already fully reconstructed events.

2.4.5 Luminosity

To measure the luminosity delivered to ATLAS three dedicated detectors are installed. At a distance of 17 m to the interaction point at both sides of ATLAS the LUCID detectors ("LUminosity measurement using Cerenkov Integrating Detector") are located. LUCID will measure inelastic p-p scatterings in the forward direction and so act as an online monitor of the instantanous luminosity and the beam conditions determining relative differences of the luminosity. In the start-up phase of the LHC, LUCID will be able to measure the luminosity with an uncertainty of about 20-30%. A more precise determination of the luminosity will be possible with the ALFA ("Absolute Luminosity For ATLAS") detectors at $\pm$ 240 m from the interaction point. The ALFA detectors consist of scintillating-fibre trackers inside Roman pots and will measure elastically scattered protons at very small angles. ATLAS aimes for a determination of the luminosity with an uncertainty of less than 5%. In between LUCID and ALFA, at $\pm$ 140 m the ZDC ("Zero-Degree Calorimeter") are located. The primary purpose of these detectors is to detect forward neutrinos in heavy-ion collisions.

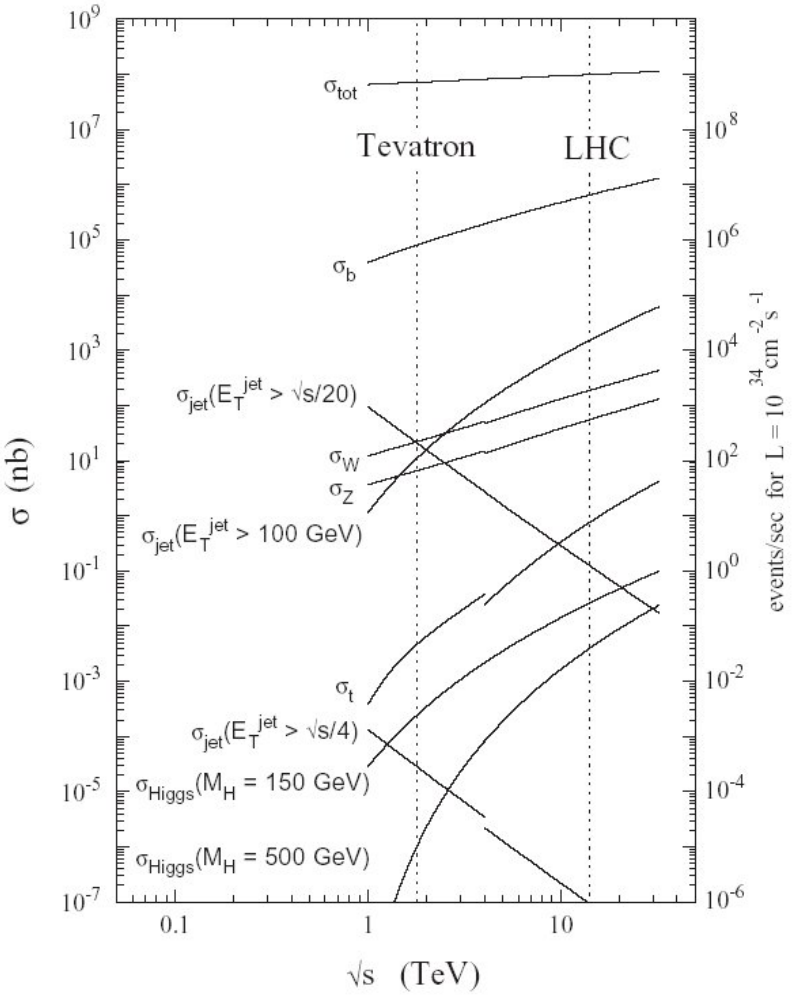

Figure 2.7: Cross sections for selected processes at LHC as a function of the center of mass energy [42].

2.4.6 Data processing

ATLAS will deliver about 2 PB of data per year of operation. These have to be processed and stored. In addition to this, simulated data for physics analysis is needed, summing up to 15 PB per year. Here a concept had to be developed to be able to provide appropriate computing power and storage, which is called the "ATLAS Computing Model" [41]. In this model participating institutes are classified hierarchically into so called Tier-0 to Tier-3 centers, connected by the LHC Computing Grid, with CERN being the Tier-0 at the one hand and a participating institue being a Tier-3 on the other. In between, national (Tier-1) and regional (Tier-2) computing centers have been established. Each Tier has its specific well defined tasks, splitting the work. By this structure data processing and storage is guaranteed and each ATLAS user should have access to the stored data and computing resources.

Chapter 3

Object identification and reconstruction

At the center of the ATLAS detector proton-proton collisions take place, initiating a large variety of physic processes, which produce particles of different types: electrons, muons, quarks etc. These emerge from the interaction point and pass through the different components of the detector. The particles leave traces in form of electrical charges, which are collected, digitized and read out by the detector. However, physics analyses needs the initial physical objects. Hence, the task is to deduce the initial physical objects from the signals left in the components of the detector.
Figure 3.1 shows an example of particle tracks of different types passing through or being stopped by the ATLAS detector. The pattern of the tracks, together with additional information from the detector, such as patterns of energy deposition, form the "signature" of a particle. As different particles exhibit different signatures, it is possible to identify particles with a low degree of ambiguity.
The information provided by the different components of the detector is used to reconstruct each particle from the interaction point on its way through the detector. From the combined information of the signals the reconstruction algorithm is able to identify the type of a particle and to reconstruct its energy, momentum, charge and direction of flight.
A very detailed description of the identification and reconstruction of physical objects in the ATLAS detector is given in [39]. Here a short summary is presented with special emphasis on electrons, jets and neutrinos. These object are of special interest for the analyses described in chapters 4, 6, 7 and 8.

3.1 Tracks

The Inner Detector reconstructs the tracks of charged particles. From the track the momentum, charge and production vertex of each particle can be identified.
Charged particles passing through the Inner Detector generate signals, called hits, in the different layers of the pixel detector, SCT and TRT. Due to the fine segmentation of the Inner Detector, these hits - associated with several quantitative information - yield space points with high accuracy. Tracks are reconstructed by recombining these space points with particle trajectories. From the tracks also the primary vertex (the point of the proton-proton collision) of the interaction and secondary vertices (particles from

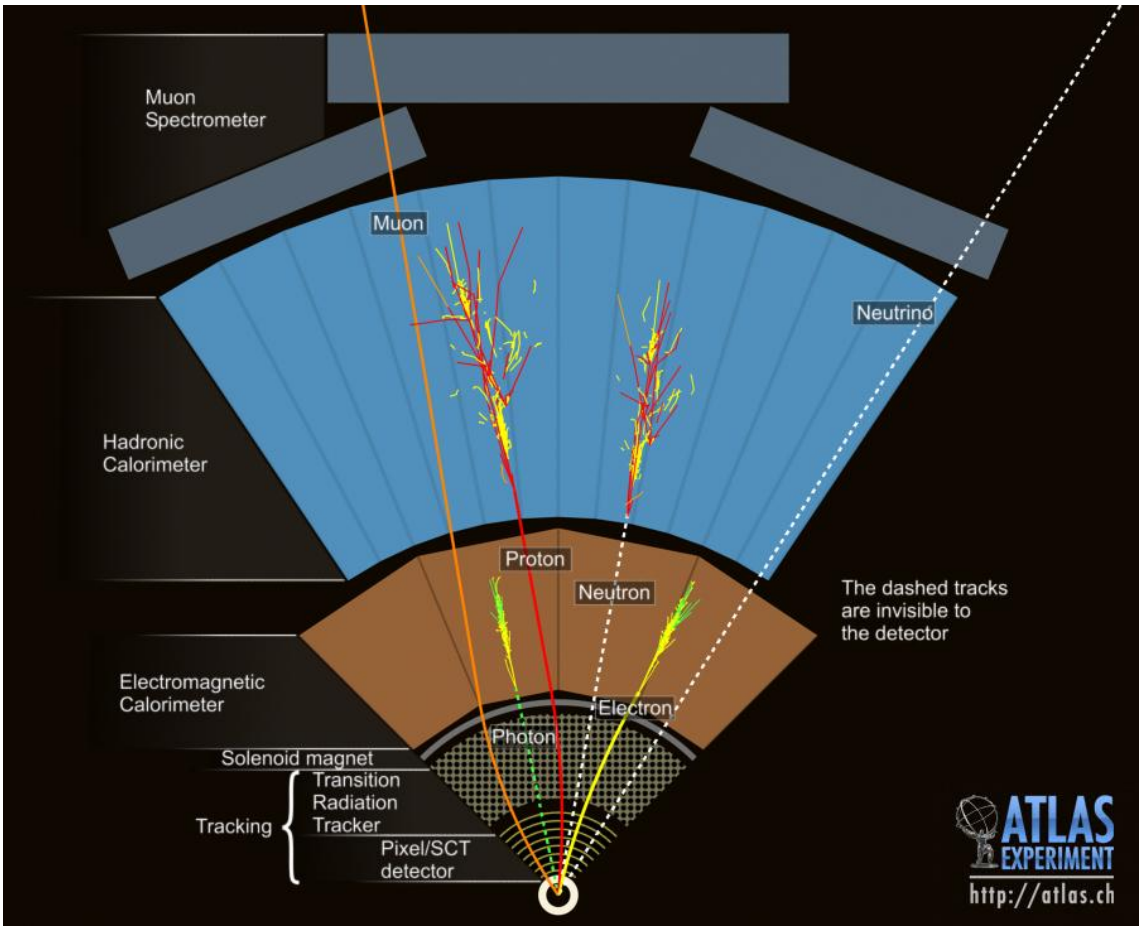

Figure 3.1: This figure shows the trajectories and energy depositions of different particle types in the ATLAS detector [34].

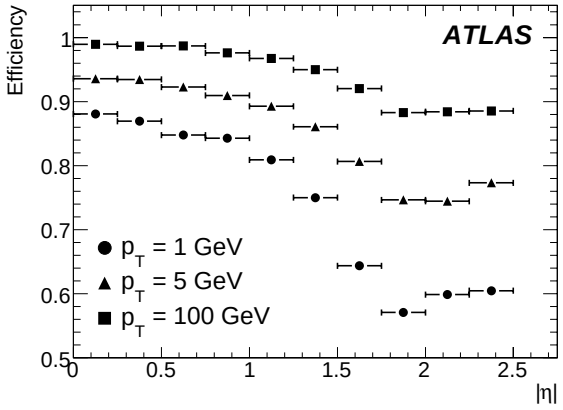

Figure 3.2: Track reconstruction efficiencies as a function of $|\eta|$ for electrons with p_T = 1, 5 and 100 GeV [44].

the primary vertex, which decay inside the Inner Detector, produce a secondary vertex displaced from the primary vertex) can be identified. A detailed description of the working principle of the tracking algorithms can be found in [43].
The track reconstruction efficiencies of electrons of different transverse momenta are presented in figure 3.2. The efficiency decreases with higher pseudorapidity $|\eta|$, because the amount of material to pass through increases. The probability of a particle to radiate bremsstrahlung photons increases proportionally to the detector material the particle passes through. The reconstruction of electrons relies on tracking in combination with calorimeter information (see section 3.2), hence the electron reconstruction efficiency suffers from the decreasing tracking efficiency with increasing $|\eta|$.

3.2 Electrons and photons

An electron is a charged particle, which leaves a track inside the Inner Detector and deposits most of its energy in the electromagnetic calorimeter. If an electron is accelerated, for example by interacting with matter, it radiates photons via bremsstrahlung. These photons convert to electron-positron pairs, which again radiate photons, producing an electromagnetic shower.
By the same procedure photons initiate electromagnetic showers. Here the first step is the production of an electron-positron pair. So the showers of electrons and photon are very similar. Because photons carry no charge, they do not leave a track in the Inner Detector. Hence, electrons and photons can be differentiated.
But there are objects, which show a similar signature in the detector and can be misidentified as electrons or photons. These are mostly hadrons, like pions or protons, and complete jets. Hadronic showers always include an electromagnetic shower fraction and thus can be identified as electromagnetic object. To discriminate electrons and photons from these objects, the properties of the particles and the differences of the signatures in the detector are compared.

- Electrons and photons produce narrow showers well contained in the electromagnetic calorimeter with a core of high activity surrounded by a small halo of low activity (an electromagnetic shower inside an electromagnetic calorimeter is illustrated in figure 3.3). Jets normally consist of more than one particle (in general there is more than one track matched to jet clusters) and thus produce broader showers extending into the hadronic calorimeter.

- Hadrons, like protons and neutrons, only deposit a small fraction of their energy inside the electromagnetic calorimeter. The main part of their energy is placed in the hadronic calorimeter. So a criterion for identifying electrons and photons is the amount of energy deposited in the hadronic calorimeter with respect to the electromagnetic calorimeter, called hadronic leakage, which is smaller for electrons and photons than for hadrons.

- Hadrons deposit only a small part of their energy in the electromagnetic calorimeter. So in general for true electrons the ratio E/p (=energy of the cluster/momentum of the tracks) is larger than for protons and neutrons.

- In addition to protons, neutrons and whole jets, pions are often misidentified as electrons. Pions decaying into two photons can be misidentified as isolated electrons or photons. To reject pions, the electromagnetic shower is investigated. If the shower consists of one maximum, it is probably caused by only one particle, hence an electron or a photon. If it consists of of two maxima close by, which are caused by two particles, it is probably caused by the two photons from a pion decay.

Most information concerning electrons and photons is found in the electromagnetic calorimeter. Hence, the reconstruction is initiated inside the second (middle) layer with towers of $E_T \geq 3$ GeV taken as seeds. Because electrons and photons produce narrow showers, a window of the size of only 5×5 calorimeter cells is placed around these seeds. Its location is varied to find the maximum of deposited energy contained in this window. A track reconstructed in the Inner Detector is then searched for, matching - if extrapolated to the electromagnetic calorimeter - the clusters with an accuracy of $\Delta\eta \times \Delta\Phi = 0.05 \times 0.10$.
If a matching track is found and this track does not belong to a converted photon ($\gamma \rightarrow e^+e^-$) , the seed is identified as an electron candidate, otherwise as a photon candidate. For electrons the energy is collected over an area of 3×7 cells, corresponding to 0.075×0.175 in $\Delta\eta \times \Delta\Phi$, for unconverted photons an area of 3×5 cells. Converted photons are handled like electrons. For the end-cap region an area of 5×5 cells has been chosen for both electrons and photons. The E/p ratio has to be smaller than 10.
At this point electron and photon candidates are found. Now the true electrons and photons have to be filtered from the candidate objects. Hence, additional criteria are required. These criteria are described in the following sections.

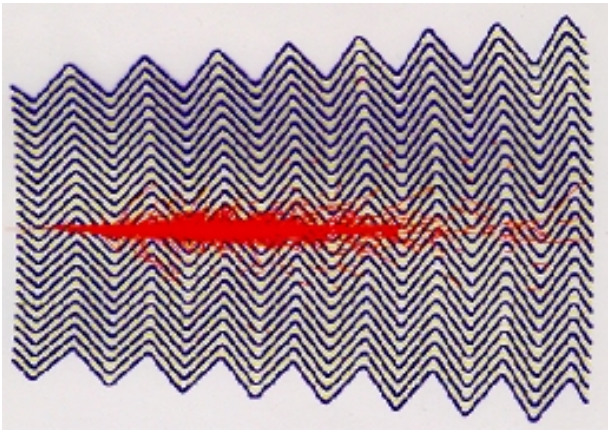

Figure 3.3: Shower inside an electromagnetic calorimeter caused by an electron or photon [46].

3.2.1 Electrons

True electrons can be filtered from the electron candidates by requiring particular properties of the track in the Inner Detector and of the shower in the electromagnetic calorimeter. In addition to the discrimination of electron candidates from hadrons and jets, electrons have to be discriminated from photons. Especially the discrimination of electrons from converted photons is difficult.
A very detailed description of the reconstruction of electrons can be found in [45] additionally to [39].
Three sets of cuts, which are sensitive to properties of track and shower and mostly are a function of $|\eta|$ and Φ, have been developed classifying isolated electrons in three groups of quality: "loose", "medium" and "tight". The quality of an electron defines the probability that the electron candidate has been initiated by a true electron.
The variables used for the classification of electron candidates are listed in table 3.1. Briefly summarized the quality criteria are:

- "loose" cuts
  - simple shower shape cuts using only information provided by the second layer of the electromagnetic calorimeter
  - cut on the amount of energy deposition in the first sampling layer of the hadronic calorimeter ("hadronic leakage")
  - loose matching constraints between the track in the Inner Detector and the electromagnetic cluster
- "medium" cuts
  - include "loose" cuts
  - shower-shape cuts using additionally the finer segmented first layer of the electromagnetic calorimeter

  - cuts on the quality of the matched track, using information provided by the Pixel Detector and SCT
  - additional strip-based (first layer of the electromagnetic calorimeter) cuts to reject $\pi^0 \rightarrow \gamma\gamma$ decays; $\pi^0 \rightarrow \gamma\gamma$ decays result in energy-deposits showing two maxima close by. In a region of $\Delta\eta \times \Delta\Phi = 0.125 \times 0.2$ surrounding the cell with the highest E_T a second maximum of energy deposition is searched for. Several variables have been developed to identify and reject two-maximum patterns resulting from π^0 decays.

- "tight" cuts
  - include "medium" cuts
  - tighter requirements on the matching between cluster and associated track
  - tighter cut on E/p ratio
  - require a hit in the vertexing-layer of the pixel detector (= innermost layer of the pixel detector at r = 5 cm) to reject electrons from photon conversions
  - include information provided by the TRT to reject background caused by hadrons
  - two subclasses: tight (isolated) and tight (TRT)
    * tight (isolated): cut on the isolation of the electron; the ratio of the transverse energy inside a cone of $\Delta R < 0.2$ around the seed tower divided by the energy of the whole cluster
    * tight (TRT): tighter requirements on TRT cuts

The expected reconstruction efficiency for isolated electrons and jet rejection is presented in table 3.2. The reconstruction efficiency and the jet rejection for "medium" electrons offer values adopted to select W+jets and Z+jets events. The jet rejection is high enough to reject W+jets events misidentified as Z+jets events (if a jet is misidentified as an electron).

3.2.2 Photons

All electromagnetic clusters not matched to a track or vetoed as electrons are considered as photon candidates. The identification of photon candidates as isolated photons is very similar to the electron identification. They have to be discriminated from electrons, pions and other neutral hadrons, like for example neutrons. Because photons are not needed for the analyses described in this thesis, only a very short summary is presented. A very detailed introduction into the reconstruction of photons can be found in [47] additionally to [39]. Several cuts have been defined, which are comparable to the "tight" cuts for isolated electrons. The cuts are mainly based on shower-shape variables. Information provided by the first layer of the electromagnetic calorimeter is used to reject $\pi^0 \rightarrow \gamma\gamma$ decays. The efficiency of photon reconstruction of one of the ATLAS benchmark processes, $H \rightarrow \gamma\gamma$ at m_H = 120 GeV, is about 84% at a jet rejection rate of about 5000.

Type	Description
loose cuts	
Acceptance of the detector	$\|\eta\| < 2.47$
Hadronic leakage	Ratio of E_T in the first sampling of the hadronic calorimeter to E_T of the EM cluster
Second layer of EM calorimeter	Ratio in η of cell energies in grid of 3×7 cells versus 7×7 cells
	Ratio in Φ of cell energies in grid of 3×3 cells versus 3×7 cells
	Lateral width of the shower
medium cuts (include loose cuts)	
First layer of EM calorimeter	Difference between energy associated with the second largest energy deposit and energy associated with the minimal value between the first and second maxima
	Second largest energy deposit normalised to the cluster energy
	Total shower width
	Shower width for three strips around maximum strip
	Fraction of energy outside core of three central strips but within seven strips
Track quality	Number of hits in pixel detector (≥ 1)
	Number of hits in the pixels and SCT (≥ 9)
	Transverse impact parameter (< 1 mm)
tight (isolated) cuts (include medium cuts)	
Isolation	Ratio of transverse energy in a cone $\Delta R < 0.2$ to the total cluster transverse energy
Vertexing-layer	Number of hits in the vertexing-layer (≥ 1)
Track matching	$\Delta\eta$ between cluster and track (< 0.005)
	$\Delta\Phi$ between cluster and track (< 0.002)
	Ratio of the cluster energy to the track momentum E/p
TRT	Cut on total number of hits in the TRT
	Cut on ratio of the number of high-threshold hits to the total number of hits in the TRT
tight (TRT) cuts (include tight (isolated) cuts except isolation)	
TRT	Same as TRT cuts above, but with tighter values corresponding to about 90% efficiency for isolated electrons

Table 3.1: Definition of variables used for "loose", "medium" and "tight" electron identification cuts. If depending on $|\eta|$ or Φ the exact cut values are not given [45].

Cuts	efficiency (%) for Z → ee	Jet rejection = $1/\epsilon_{jet}$
loose	87.96 ± 0.07	567 ± 1
medium	77.29 ± 0.06	2184 ± 13
tight (TRT)	61.66 ± 0.07	$(8.9 \pm 0.3)10^4$
tight (isolated)	64.22 ± 0.07	$(9.8 \pm 0.4)10^4$

Table 3.2: Expected efficiency of the reconstruction of isolated electrons ($E_{T,electron} > 17$ GeV) and rejection of jets [45]. The results are shown for simulated filtered di-jet and minimum-bias samples, corresponding respectively to E_T - thresholds of 17 GeV.

3.3 Jets

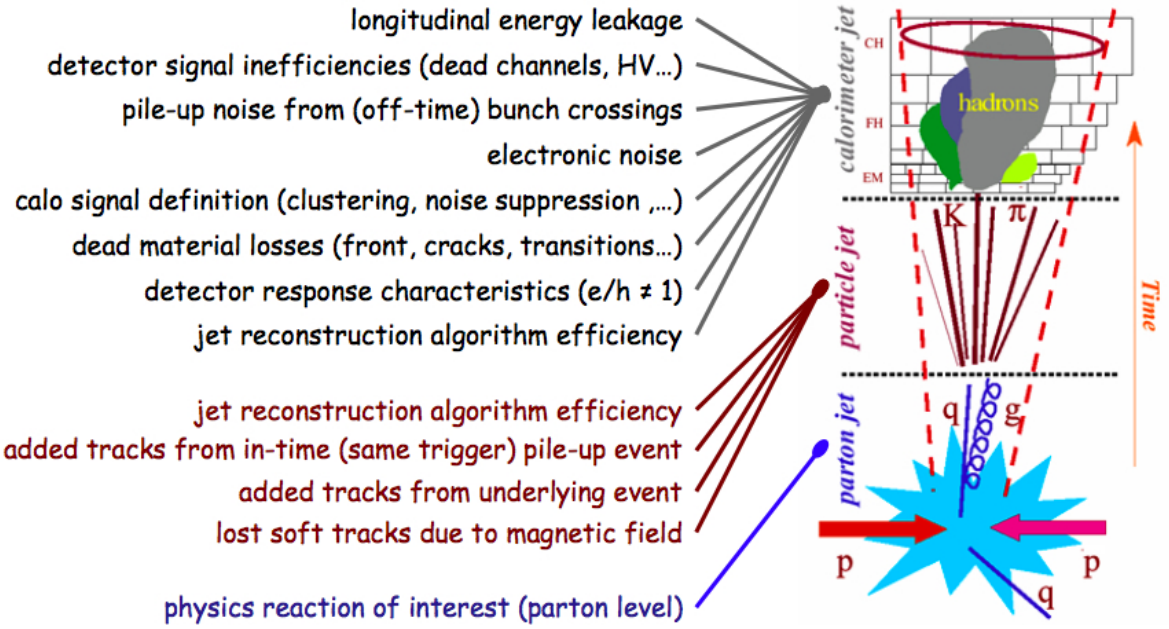

Figure 3.4: The stages from jet production to jet measurement in the calorimeter. Causes for mismeasurements are shown [48].

Many interesting physics processes include the production of jets (see section 1.1.1) in the final state. To some extent these jets are decay products of the hard interaction itself (for example $t\bar{t}$ decays). In hadron-hadron collisions jets typically arise from initial/final state radiation and/or the underlying event and contribute to the jet structure of the event.
Jets are initiated by outgoing partons. The fragmentation process results in a bundle of particles moving in the direction of the initial parton. These particles deposit their energy in the calorimeter system and are detected as signals in calorimeter cells. The task of jet building is to reconstruct the properties of the particle jet from the signals measured in the calorimeter cells. A reconstruction of the parton properties is not

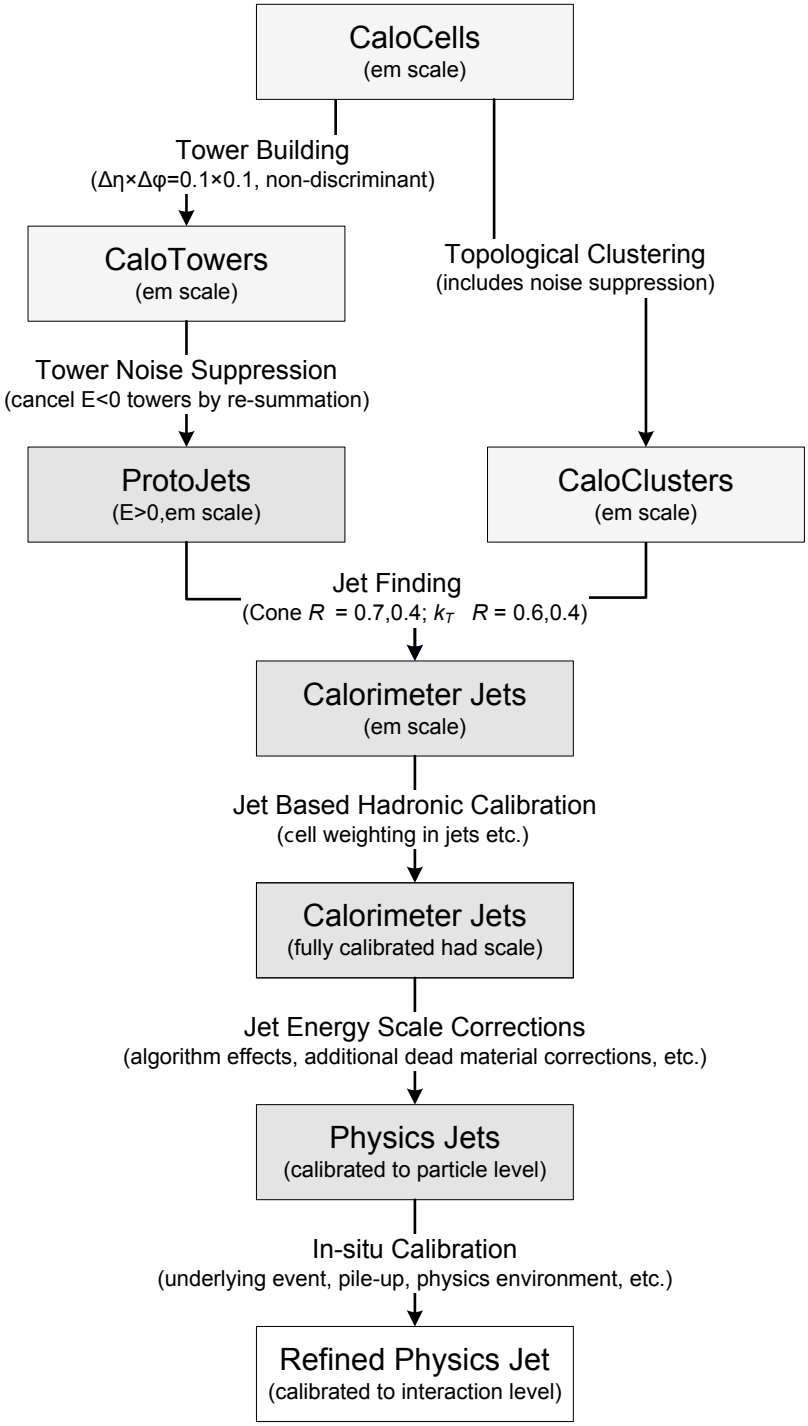

Figure 3.5: Jet reconstruction flow for calorimeter jets from towers or clusters in ATLAS [39].

possible, because the parton showers and the resulting hadron bundles are difficult to be identified with the initial parton. In addition to the uncertainties associated with each measurement of physical objects, for example noise and dead material, some jet specific uncertainties arise. These are visualized in figure 3.4.
Only the particles of the particle jets are detectable, the parton itself does not reach the detector. These particles are only a small part of all the particles generated in the event. Hence, it is difficult to identify which particles come from the initial parton. The particles have to be measured in the calorimeter, so particles of the rest of the event can distort the measurement. And it can happen that some low p_T particles from the parton do not reach the calorimeter. They may have been stopped by the magnetic field of the Inner Detector or by material in front of the calorimeter.
The hadrons contained in the particle jet produce hadronic showers in the hadronic calorimeter. Each hadronic shower consists of both electromagnetic and hadronic fractions. These fractions differ from jet to jet. The calorimeter typically responses differently to electromagnetic and hadronic particles. The actual electromagnetic fraction of a hadronic shower cannot be determined resulting in an uncertainty on the energy measurement. Furthermore the hadronic energy fraction of a hadronic shower consists of both visible and invisible energy depositions. The invisible energy depositions can be put down to for example nuclear break-ups. Hence, the hadron's measured energy differs clearly from the true hadron energy and has to be corrected for.

3.3.1 ATLAS jet clustering

The ATLAS jet reconstruction is divided into several steps in order to reconstruct the properties of the particle jet from the signals measured in the calorimeter cells. Figure 3.5 shows the different steps from calorimeter cells to physical jets, which reflect the properties of the initial parton at interaction level. The steps are described in the following sections.
The jet reconstruction in ATLAS is based on calorimeter information only. Here the particles of the particle jets deposit a large fraction of their energy. Normally particles scatter their energy into more than one calorimeter cell. Hence, the calorimeter cells have to be grouped together to represent the particle as one object and collect the whole particle energy. Two different approaches are used to recombine the calorimeter cells: building calorimeter towers and building topological calorimeter clusters. These objects are then used by the jet clustering algorithms as inputs to build jets.

Calorimeter towers

To build calorimeter towers all cell energies in a fixed grid of $\Delta\eta \times \Delta\Phi = 0.1 \times 0.1$ are summed up. Calorimeter towers are only two dimensional objects not using the longitudinal segmentation of the calorimeter system. This is illustrated in the left plot of figure 3.6. If a cell dominated by noise gives negative signals, it is recombined with positive signals from neighbouring towers until the sum of cell energies is positive, but no cell information is dropped. So no noise suppression is performed, but noise is added to the tower energy.

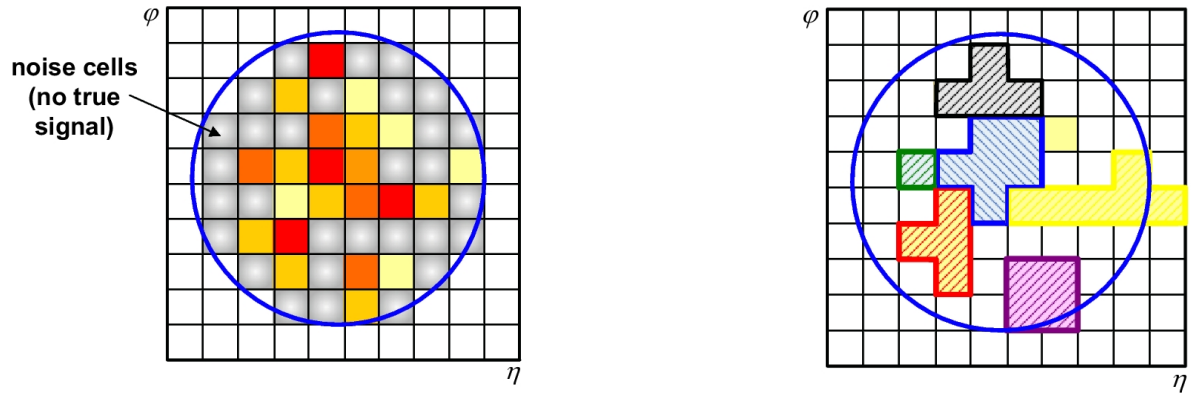

Figure 3.6: This graphic illustrates the building of calorimeter towers (left plot) and calorimeter clusters. Calorimeter towers include significantly more noise than calorimeter clusters [48].

Topological cell clusters

In contrast to calorimeter towers topological cell cluster are three dimensional objects with more flexibility in size and form. Reconstruction of topological clusters is seeded by cells with a significant amount of energy above noise level ($|E_{cell}| > 4\sigma_{cell}$; σ = typical amount of noise). Then all nearest neighbour cells are collected. If their signal is significantly over the threshold (typically $|E_{cell}| > 2\sigma_{cell}$), they are assumed as secondary seeds and their nearest neighbour cells are also collected. If more than one maximum is contained in the cell cluster, the cluster is split along the three dimensional minimum. The right plot of figure 3.6 shows the building of topological cell clusters. Here noise suppression is performed, as cells with no signal are likely not to be included in the cluster. So jets built of topological cell clusters contain less noise than jets built of calorimeter towers (this is discussed in [39]).

3.3.2 Jet reconstruction algorithms

Each particle of the particle jet causes signals in the calorimeter cells. The cells are put together as calorimeter towers or topological cell clusters to collect the energy deposited by a particle. To reconstruct the particle jet from the calorimeter objects, the objects have to be bundled. This is the task of jet clustering algorithms.
At the moment two jet algorithms are implemented in ATLAS [44]: the seeded Cone jet algorithm with $\Delta R = 0.4$ (used as jet finder in chapters 6, 7 and 8) and 0.7 and the k_T jet algorithm[1] with R=0.4 and 0.6 (R is sometimes referred to as D).
In general, jet algorithms form jets from all types of input objects, which can be presented by their four momentum. In ATLAS jets are built from particles, forming the particle jets (only available for simulated data, important for calibration, jet finding efficiency and performance studies), from calorimeter towers and topological cell clusters.

[1] the stand-alone C++ implementation as described in [49]

There are two important requirements on jet algorithms in order to obtain a stable jet configuration: the reconstructed jets have to be infrared and collinear safe.

- Infrared safeness of a jet:
  The addition of a soft parton to the jet does not affect the properties of the reconstructed jet.
- Collinear safeness of a jet:
  The splitting of a parton into two collinear partons of half the original energy does not affect the properties of the reconstructed jet.

Cone jet finder

The Cone jet algorithm is a geometrical algorithm, which clusters objects lying near to each other in the (η,Φ)-plane. As seeds objects with $p_T > 1$ GeV are defined. Around these seeds a cone of the chosen radius ΔR is drawn. The energy of all objects inside this region is summed up and the weighted center axis of E_T is calculated. Then a new cone is drawn around this new axis. The procedure is repeated until a stable jet axis has been found. The complete algorithm is repeated until all seeds are associated to a jet. Jets with $E_T < 7$ GeV are discarded. The four-momentum of the jet is constructed by applying full four-vector algebra (following section 3.2.3 in [50]). After jet clustering overlapping jets are possible. Hence, a split and merge routine splits or merges objects with an overlapping fraction of 50% [39].
The disadvantages of the Cone algorithm are:

- All energy depositions inside the ΔR region are summed up. This involves energy depositions caused by particles of the particle jet, but also possibly caused by particles from the underlying event for example.
- It can occur that some energy fractions of the particle jet lie outside the ΔR region and are discarded.
- The seeded Cone is not collinear and not infrared safe.

The advantage is that it is a fast and simple algorithm producing simple jet shapes. It is easy to reproduce, which calorimeter towers or topological clusters are contained in the jet. Hence, jet energy calibrations are easier to apply.

k_T jet finder

The k_T jet finder clusters objects, which are in p_T close to each other. This means in some sense that the splitting of objects that occurs during the fragmentation process is undone. Hence, the k_T algorithm runs the parton shower backwards. The procedure is as follows:

1. calculate distances
   - d_{ij} between all objects i and j
   - d_i between object i and beam
2. find the smallest of all d_{ij} and d_i
   - if $d_{ij} < d_i$: recombine i and j to one object
   - if $d_i < d_{ij}$: i is a jet; remove i from list of objects
3. start with step one until no objects remain

The k_T jet algorithm is varied by different definitions of d_{ij} and d_i. The definition used in ATLAS is [51]:

$$\begin{aligned} d_{ij} &= min(p_{T,i}^2, p_{T,j}^2) * R_{i,j}^2 / R^2 \text{ with} \\ R_{i,j}^2 &= (\Phi_i - \Phi_j)^2 + (\eta_i - \eta_j)^2 = \Delta R^2 \\ d_i &= p_{T,i}^2 \end{aligned}$$

R (D) is the parameter of the jet algorithm. At the moment the choices R = 0.4 and R = 0.6 are available in ATLAS.
Two objects are recombined by adding both four momenta:

$$p_{i,j}^{\mu} = p_i^{\mu} + p_j^{\mu}$$

Jets with $E_T < 7$ GeV are discarded.

The fast version of the k_T is used, which has been proposed by Cacciari and Salam [52]. The idea of the fast k_T is that objects with the minimum value for d_{ij} have to be close to each other in geometrical sense. So d_{ij} is not calculated of all object combinations, but only of nearest neighbours in the (η,Φ) plane. For more information on the performance of the fast k_T in ATLAS see [51].

3.3.3 Jet calibration

After clustering the obtained calorimeter jet objects do not reflect the properties of the initial particle jet. Inaccuracies like for example noise in the calorimeter and dead detector material, which are described in figure 3.4, bias the jet energy and jet position with respect to the initial particle jet. These uncertainties are completed by uncertainties associated with the hadronic showers themselves. A hadronic shower consists of both an electromagnetic fraction and a hadronic fraction. The hadronic fraction consists of both visible and invisible[2] parts. Typically the detector response differs for the

[2]invisible are for example nuclear excitations and nuclear breakups

electromagnetic and hadronic fraction. Hence, to reconstruct the jet energy, it has to be determined, which energy depositions in which cells are more hadron-like or more electromagnetic-like and the measured energy has to be corrected for the different responses. Then the measured energy is corrected for the invisible part of the hadronic fraction.
By applying jet calibration the measured jet energy is corrected for the mentioned effects. It is performed after the H1-style [53] by multiplying a weight factor to each calorimeter cell, which is contained in a jet, and re-summation of the weighted cell energies. The weight factor is obtained by comparing truth jets with calorimeter jets nearby (matched by the minimum ΔR) in simulated QCD di-jet events. The weights depend on the energy density in the calorimeter cells and their location in the calorimeter. The jet algorithm used to determine the cell weights is the Cone algorithm with ΔR=0.7 using calorimeter towers. This weighting procedure corrects the jet energy and jet axis for detector and shower effects to be consistent with truth particle jets after fragmentation.
Then each jet is corrected for jet algorithm effects and remaining mis-calibrations. This calibration is different for each jet algorithm in contrast to the cell weighting. This last calibration step is again based on the comparison of calorimeter jets and matched truth particle jets and relies on detector simulations.

3.3.4 b jet identification

The presence of b jets in some physics processes (for example $t\bar{t}$ events) provides the possibility to improve the filtering from the whole amount of physics processes taking place.
The long lifetime (order of pico seconds) of b quarks leads to a covered distance of several millimeters, before the b hadrons decay into lighter particles. This results in the production of a secondary vertex in addition to the primary vertex of the pp collision. These secondary vertices inside jets can be reconstructed. Particles coming from secondary vertices show different properties than particles coming from the primary or other secondary vertices. These facts are used to identify b jets and discriminate them from light jets. The procedure is called b-tagging. A detailed description of b-tagging algorithms and their performance can be found in [54] and [39].
In ATLAS jets are only built out of calorimeter information. So for the b-tagging procedure first particle tracks have to be matched to the jets by calculating the distance in ΔR between the track in the Inner Detector and the jet axis in the calorimeter. If $\Delta R < 0.4$ the track is assigned to the jet (for all jet clustering algorithms). This leads to a set of tracks assigned to each jet. Then dedicated vertexing algorithms use these tracks to search for secondary vertices inside the jet and the properties of the particle tracks are investigated. In the end for each jet a probability weight is calculated, if the jet is a b jet or not.

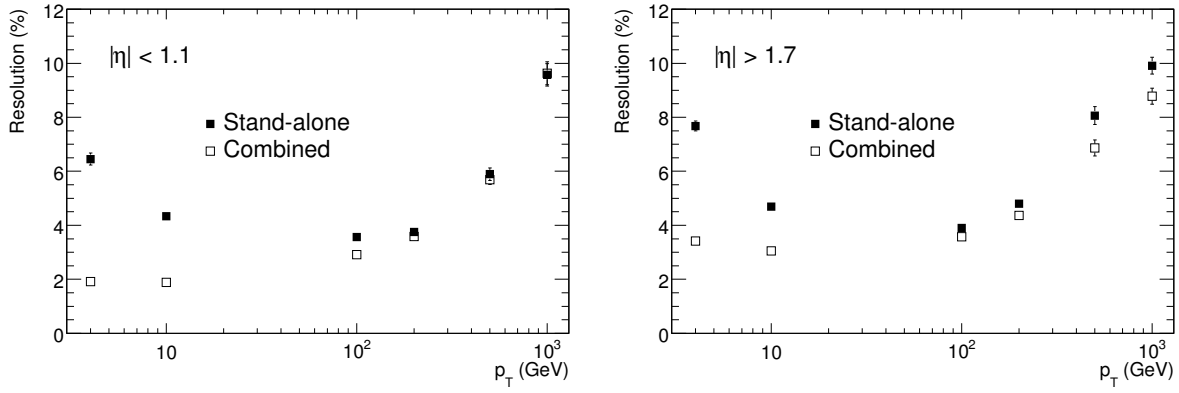

Figure 3.7: Expected stand-alone and combined fractional momentum resolution for single muons as a function of p_T for the barrel (left) and the end-cap (right) region [39].

3.4 Muons

The reconstruction and identification of muons is mainly performed inside the Muon System, which represents a stand-alone tracking detector. Improvement of the reconstruction efficiency and momentum resolution is achieved by taking information provided by the Inner Detector and the calorimeter system into account. The signature of a muon passing through the ATLAS detector consists of a track in the Inner Detector, a track in the Muon System and only a very small amount of energy deposited in the calorimeter system. Combining the tracks from the Inner Detector and the Muon System improves the momentum resolution for muons with $p_T < 100$ GeV, as can be seen in figure 3.7. The efficiency of the muon reconstruction for both stand-alone and combined muon algorithms is $> 90\%$ for muons with $p_T > 15$ GeV [39].

3.5 τ-leptons

With a mass of $m_\tau \approx 1.7\,\text{GeV}$ τ-leptons are the only leptons, which can decay into an electron ($\tau \rightarrow e\bar{\nu}_e\nu_\tau$) or muon ($\tau \rightarrow \mu\bar{\nu}_\mu\nu_\tau$) or into a quark-antiquark pair, forming jets with a low particle multiplicity.
Reconstructing hadronic τ-decays (τ jets) is a challenging task due to their pattern being similar to hadron jets. τ-decays are identified as narrow calorimeter clusters with a small number of tracks assigned. The sum of charges of these tracks has to be consistent with the charge of a τ-lepton. Here the correct charge measurement done by the inner detector becomes important. The matched tracks have to emerge one secondary vertex with most energy of the calorimeter cluster located inside a narrow cone around the leading track in p_T. Cuts on shower-shape variables are applied to reject background from hadron jets. Leptonic τ-decays are almost impossible to discriminate from direct electrons and muons. Hence, the reconstruction does not differ from the electron or muon identification and reconstruction. For the analysis presented in chapters 7 and 8, this means that the background to $W \rightarrow e\nu$ from $W \rightarrow \tau\nu$ with $\tau \rightarrow e\nu_\tau\bar{\nu}_e$ is an almost irreducible background.

3.6 Neutrinos (missing transverse energy)

Neutrinos interact with other particles only via the weak interaction. Hence, the probability for neutrinos to interact with the detector material is extremely low. They escape the ATLAS detector undetected and have to be identified indirectly.
A neutrino coming from a $W \rightarrow e\nu$ decay for example carries an energy of approximately $m_W/2$. Because the total transverse momentum (or energy) of an event has to be zero, the p_T carried away by the undetected neutrino misses in the total p_T balance and hence helps to measure the neutrino. The imbalance initiated by the neutrino is called missing transverse energy ($\not{E}_T$). For $\not{E}_T$ reconstruction a good azimuthal and η coverage of the calorimeters is crucial. If p_T is lost, $\not{E}_T$ cannot be found. A high spatial resolution of the calorimeter system leads to an exact determination of the flight direction of the neutrino.

Neutrinos are identified by the p_T imbalance they produce in the detector. Hence, the neutrino reconstruction is performed after the identification and reconstruction of all other objects. In principle, the $\not{E}_T$ is determined by calculating the vector sum of all calorimeter cell energies and the energies of reconstructed muons. The resulting $\vec{E}_T$ then should be identical to the $\vec{E}_T$ of the neutrino. However, in advance all calorimeter cells are calibrated globally for the electromagnetic scale (see section 3.3.3). Without cell calibration the calculated p_T of the neutrino would be biased by 10-30% to the true neutrino p_T. Muons are only taken into account if reconstructed by the stand-alone tracking algorithm of the Muon System with a track from the Inner Detector matched. At this level an accuracy of $\not{E}_T$ reconstruction of about 5% is achieved [39].
In the next step energy losses in the calorimeter are considered, which bias the $\not{E}_T$ determination. Energy is lost in the cryostats between the electromagnetic and hadronic barrel calorimeters. Hence, the $\not{E}_T$ vector is corrected for these losses.
To improve the $\not{E}_T$ resolution, now each high-p_T object is associated with its calorimeter cluster. The energy (vector) of the calorimeter cells is replaced by the energy (vector) of the associated object (taking into account also information provided by the Inner Detector and the Muon System). After reconstruction the $\vec{p}_T$ of the objects should be determined much more precisely than the pure calorimeter information. The order of the replacements are not taken randomly. The replacements start with the objects, which are detectable most precisely. It starts with electrons, then photons, hadronically decaying τ-leptons, b jets, light quark jets and muons.

The performance of $\not{E}_T$ reconstruction is shown in the figures 3.8 and 3.9. The performance is based on simulated data and evaluated by the comparison with the true $\not{E}_T$ before detector simulation. Figure 3.8 presents the linearity = $\frac{|E_T^{miss,true}|-|E_T^{miss}|}{|E_T^{miss,true}|}$ as a function of true $\not{E}_T$, which demonstrates a constant behaviour. Figure 3.9 shows the resolution in energy and in Φ for different physics processes. For $W \rightarrow e\nu$ decays high resolutions in E and Φ are achieved.

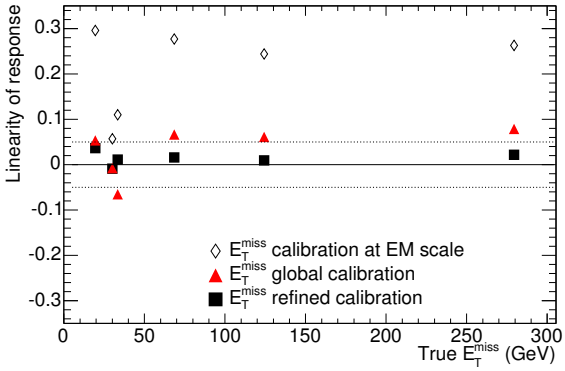

Figure 3.8: Linearity of response for reconstructed $\not{E}_T$ as a function of the average true $\not{E}_T$ for different physics processes covering a wide range of true $\not{E}_T$ and for different steps of reconstruction (see text). The points of average true $\not{E}_T$ at 35 GeV are from W $\rightarrow$ eν decays and those at 68 GeV from semi-leptonic $t\bar{t}$ decays [39].

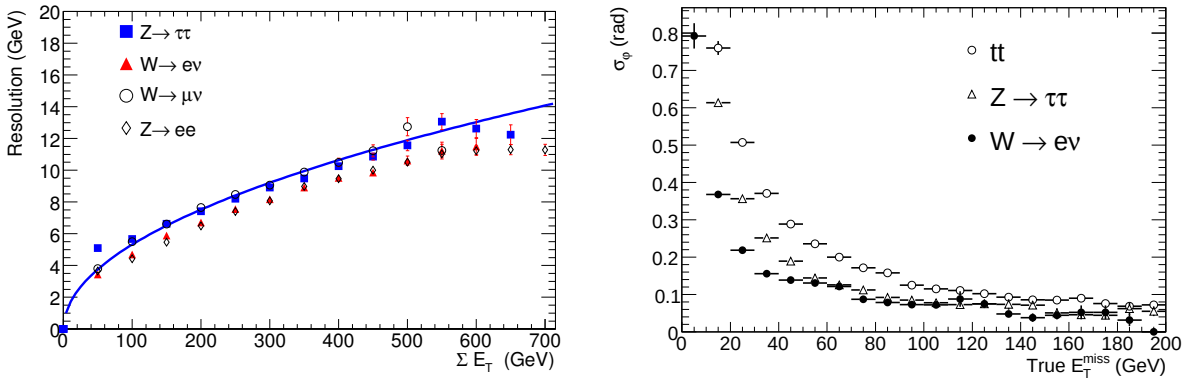

Figure 3.9: Left side: Resolution σ of the two components (x,y) of the $\not{E}_T$ vector after refined calibration as a function of the total sum of E_T of the event measured in the calorimeters for different physics processes. The curves correspond respectively to the best fit. Right side: Accuracy of the measurement of the azimuth of the $\not{E}_T$ vector as a function of the true $\not{E}_T$ for three different physics processes [39].

3.7 Data simulation

The previous sections describe how the fermions and bosons introduced in section 1.1 are identified and reconstructed in proton-proton collisions at the LHC using the ATLAS detector. The measured objects clearly differ from the initial particles. However, the aim of collision experiments is to compare theoretical calculations to the measured results, in order to test the theory. Theoretical calculations predict partonic cross sections and distributions. Hence, a method has to be found to let the theoretical predictions match to experimental data.
Hypothetical events are simulated according to the theoretical predictions of the frequency and signature of a process. The final state particles are then tracked through the detector, interactions with the detector material are simulated including the signals and particle responses. After this step the simulated events should look like data. These simulated events can also be used to plan analyses and to correct the influence of the detector.

3.7.1 Simulation of the events

Simulations generate hypothetical events according to theoretical predictions. These events show the predicted properties and can be compared to results of collision experiments. The simulation of events is adapted to the sequence of a hard scattering event. From stage to stage the energy of the generated particles decreases and different processes take place. These stages or phases are presented in figure 3.10 and are briefly summarized in the following:

1. hard process

   The production of high energy or heavy partons. Due to the high energy the production mechanism can be described by matrix elements, which are exact at some pertubative order. The decay of the generated high energetic particles (for example top quarks) can be described by exact matrix elements, too.

2. parton shower

   The generated strong interacting partons radiate gluon bremsstrahlung and loose energy, until the energy is too small to radiate further. This process is described by parton shower models, which are accurate at leading logarithmic order.

3. hadronization and decay

   The partons form hadrons. Due to the small energy of the partons this process can only be described by phenomenological models. These hadrons then decay eventually into long-lived particles, i.e. the lifetime long enough to allow the particles to reach the detector and be observed.

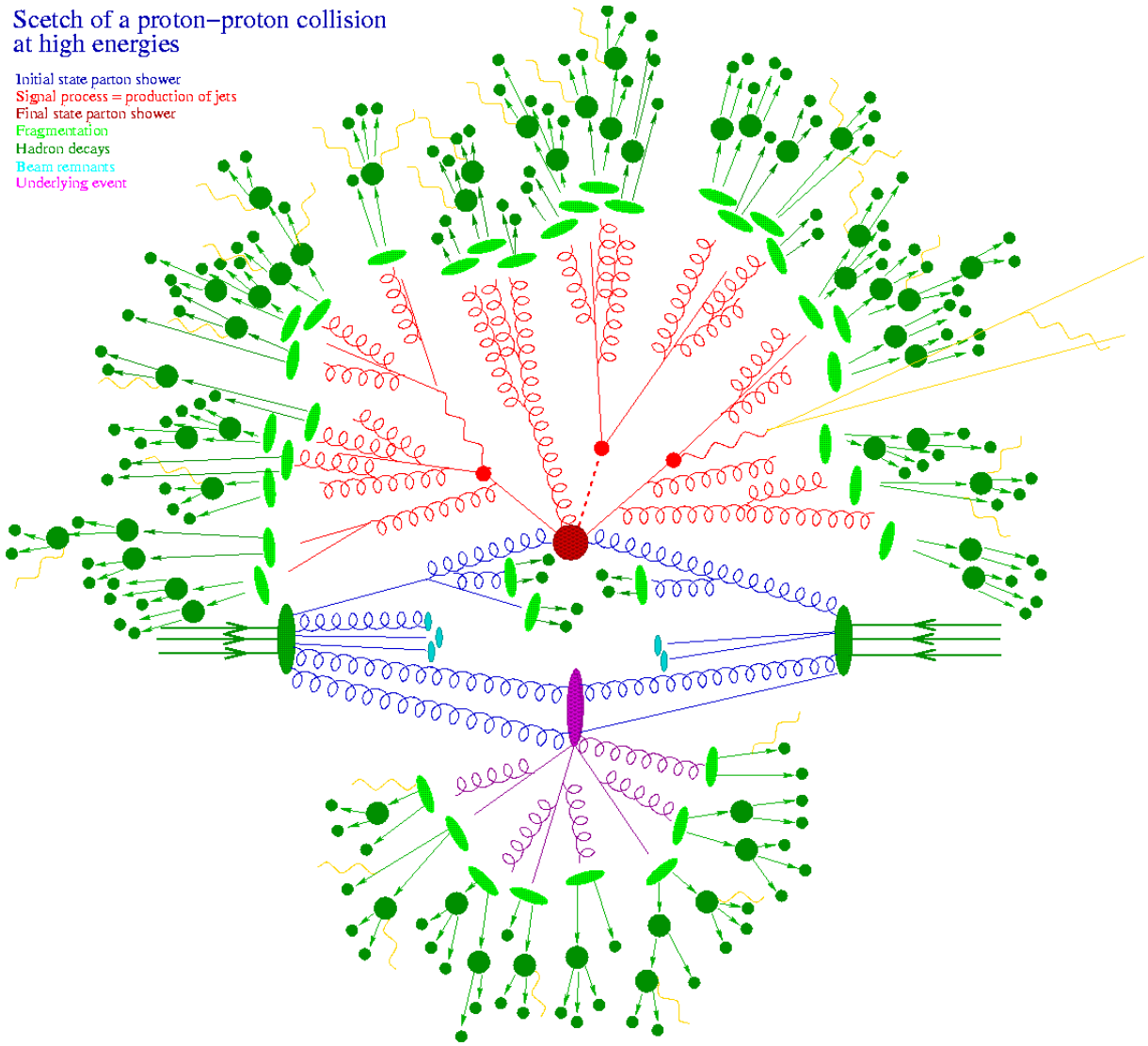

Figure 3.10: Pictorial representation of an event (here a $t\bar{t}H$ event, but the shown processes apply to all physics processes) as produced by an event generator. The hard interaction (big red blob) is followed by the decay of both top quarks and the Higgs boson (small red blobs). Additional hard QCD radiation is produced (red) and a secondary interaction takes place (purple blob) before the final-state partons hadronise (light green blobs) and hadrons decay (dark green blobs). Photon radiation occurs at any stage (yellow) [55].

A large variety of Monte Carlo event generators exists, which use the described factorisation scheme to simulate hypothetical events of different processes. The event generators differ in the methods and models they use to realize the above mentioned phases. An overview of available event generators is given in [56]. Due to the implementation of different methods, differences in the distributions of the hypothetical events occur.
Common event generators to simulate W+jets and Z+jets events are PYTHIA [57], ALPGEN [58] and SHERPA [55]. These were used in this thesis to simulate the signal events. Their predictions are compared.

3.7.2 Simulation of the detector

After simulation of an event a list of particles generated in the hard interaction exists. For each particle its properties, like type, mass and momentum vector, are specified. In the next step a simulation is performed, how the ATLAS detector would measure these particles.
For each generated particle the detector simulation includes:

- Where the particle passes through the detector and in which detector component which amount of energy is deposited.
- The energy depositions are converted into the expected detector signals (voltages, time-over-thresholds, etc.). For each particle of an event a set of detector signals is obtained. This set of signals does not differ from the signals obtained in data.
- The object identification and reconstruction procedure converts the signals in physical objects. This step is the same for simulated events and data.

If not mentioned differently, in this thesis the simulation of the detector is performed using the tool GEANT4 [59]. There exists a method to provide a fast simulation of the ATLAS detector called ATLFAST-II [60]. This fast simulation is based on simplified models of the detector and needs much less CPU-time compared to the full detector simulation. It is mentioned explicitly in this thesis if this fast simulation is used for a data set.
After applying the detector simulation to the generated events, simulated events and data show the same properties and can be directly compared.

Chapter 4

Comparison of the performance of jet algorithms for top quark analyses

Top quarks decay before hadronization can take place, hence all properties of the top quark can be directly deduced from its decay products. These are a b quark and either a charged lepton-neutrino or a quark-antiquark pair from the W decay. All quarks form particle jets as described in section 1.1.1. So the precision of top quark analysis is directly linked to the accuracy of the measured properties of the initial quarks.
The stable particles of the particle jets pass the detector and interact with the detector material. They deposit most of their energy in the calorimeter. From the obtained calorimeter signals the jet clustering algorithms reconstruct calorimeter jets. For the top quark analysis it is important that the calorimeter jets reflect the properties of the initial quarks. The stages between the quarks and the calorimeter jets and the associated arising uncertainties are summarized in figure 3.4.
In this chapter the performance of various jet clustering algorithms is compared. Several aspects are investigated, which are important for $t\bar{t}$ analyses :

- the precision of the energy measurement of the jet with respect to the quark
- the precision of the position measurement of the jet with respect to the quark

  Comparisons of jets and quarks are unscientific in some sense. This is a study based on simulated events. In case of a simulated $t\bar{t}$ event the event record explicitly contains and describes the decay of the top quark into a b quark and a W boson and the subsequent decay of the W boson into leptons or quarks. Hence, the quarks are clearly defined and it is possible to compare their properties to the properties of the jets.

- the b-tagging performance

Only the semi-leptonic $t\bar{t}$ decay channel[1] is taken into account. Hence, the performance of the jet algorithms has to be compared for both heavy (bottom) and light (up, down, charm, strange) flavour jets.

[1] including two b quarks and two light (up, down, charm, strange) quarks from the hadronic W decay

The current ATLAS standard jet algorithm is Cone $\Delta R = 0.4$ built of calorimeter towers. In the following a qualitative investigation is described. The aim is to state if this jet algorithm choice is advantageous or disadvantageous for $t\bar{t}$ analyses. The studies showed in this chapter are also published in [44].

4.1 ATLAS jet algorithms

The ATLAS reconstruction software offers two jet algorithms: the Cone ($\Delta R = 0.4$ and $\Delta R = 0.7$) and the k_T ($R = 0.4$ and $R = 0.6$)[2]. These jet algorithms are used to reconstruct both particle jets and calorimeter jets. Particle jets use the stable particles of the event as input objects (before interaction with the detector) and are only available in simulated events. Calorimeter jets are reconstructed from calorimeter information and are available for both data and simulated events. Here the Cone and the k_T algorithms offer calorimeter jets based on calorimeter towers and topological cell clusters (see 3.3.1).

4.2 Event selection

In this chapter the performance of different jet algorithms for $t\bar{t}$ analyses is investigated. For these studies only $t\bar{t}$ signal events, simulated with the ATLAS default Monte Carlo generator for $t\bar{t}$ analyses, MC@NLO [61] interfaced with the HERWIG [62] parton shower and including detector simulation with GEANT4 , are used.
At the LHC $t\bar{t}$ events are produced among a large variety of other processes (see figure 2.7). To investigate these $t\bar{t}$ events, an LHC event sample has to be enriched by $t\bar{t}$ events. Non $t\bar{t}$ events should be filtered. This procedure is known as $t\bar{t}$ event selection and the filter criteria are called cuts.
For these studies only $t\bar{t}$ signal events are used, so in principal no event selection is necessary. However in order to test the performance of different jet algorithms, only $t\bar{t}$ events are of interest, which pass the $t\bar{t}$ event selection cuts. Therefore a $t\bar{t}$ event selection is applied to the Monte Carlo signal events, too.
The filter cuts are adopted to the expected event signature of a semi-leptonic $t\bar{t}$ event, containing two b jets with a p_T of roughly $m_{top}/2$ and two light jets with very roughly $m_{top}/2 + m_W/2$ (possible p_T of top quark not considered). The same applies for the charged lepton and the neutrino from the leptonic W decay.
Particle jets ("truth jets") and calorimeter jets ("jets") are handled equally. They are defined by

- $p_T > 15\,\text{GeV}$, $|\eta| < 2.0$
- jet objects overlapping with electron/muon objects within $\Delta R < 0.4$ are removed

All events have to contain:

- exactly one isolated charged lepton (electron or muon), $p_T > 20\,\text{GeV}$, $|\eta| < 2.0$

[2]By the time of these studies, these algorithms were available in athena release 12.0.6.

- $\not{E}_T > 20\,\text{GeV}$
- ≥ 4 jets with $p_T > 20\,\text{GeV}$; ≥ 3 jets with $p_T > 40\,\text{GeV}$

After applying these event selection cuts, the Monte Carlo data set only contains those simulated $t\bar{t}$ signal events, whose properties are similar to selected $t\bar{t}$ events in data. Using these events the performance of different jet algorithms is investigated.

4.3 Matching of quark - particle jet - calorimeter jet

In this chapter the properties of quarks, truth jets and jets are compared to test the performance of various jet algorithms. The event record contains the quarks from the top decay, the truth jets and the reconstructed jets. These objects are physically related, but these relations cannot be stored. Hence in the event record quarks, truth jets and jets are independent and different objects. A method has to be found to assign truth jet and jet to their initial quark and to each other.
In this analysis only the four quarks from the top quark decay are investigated as their properties reflect those of the top quarks (apart from the neutrino and the charged lepton from the leptonic W decay). The procedure to compare the properties of truth jets and jets with quarks is unscientific as already mentioned in the introduction to this chapter, but in the event record the decay chain of the quarks is stored and clearly defined, hence comparisons are possible.
The chosen matching procedure follows the chronological evolution of a simulated event: truth jets are matched to quarks by calculating the ΔR(truth jet, quark) between each truth jet and each quark, giving for each truth jet a set of four ΔR values (= four quarks). Then for each truth jet the minimal value of $\Delta R = \Delta R_{min}$ is selected. If ΔR_{min} is smaller than 0.3 the truth jet is matched to the particular quark. By the same procedure jets are matched to truth jets and to quarks. This method induces ambiguities. It can for example happen that one quark is matched to two or more jets. This indicates basic physical effects like for example gluon radiations, but also inaccuracies and inefficiencies of the reconstruction software. Hence, these jets are not discarded but treated in the same way as uniquely matched jets.
After performing the matching procedure, each truth jet and each jet is assigned to its initial quark. From now on jets assigned to the b quarks are called b jets, jets assigned to the light quarks are called light jets. Jets, which are assigned to no quark, are considered as jets arising from initial or final state radiation. These jets are not considered in the following.

4.4 Jet energy

For top quark analysis it is important that the reconstructed calorimeter jet reflects the energy of its initial quark as accurately as possible. Hence, the energy resolution $((E_{quark}\text{-}E_{jet})/E_{quark})$ of the ATLAS jet algorithms is compared for both b jets and light jets.

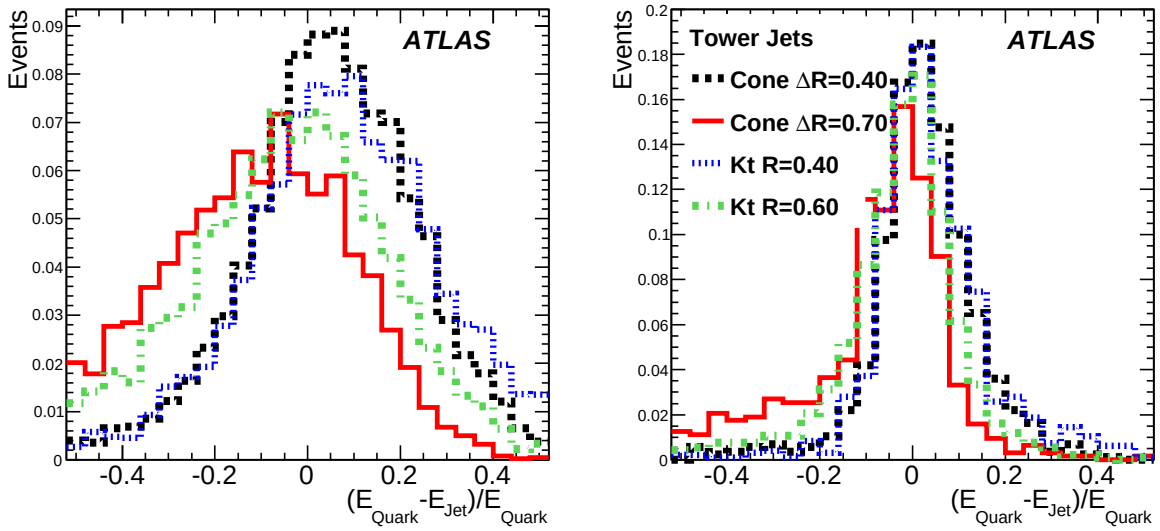

Figure 4.1: The energy resolution $(E_{quark}\text{-}E_{jet})/E_{quark}$ of calorimeter jets w.r.t.the quarks for light jets as a function of the quark energy. The left plot shows the energy resolution for quark energies between 15 and 50 GeV, the right plot for quark energies above 350 GeV.

Figure 4.1 presents this energy resolution of light jets. The energy resolution is shown for two different quark energy ranges (15 - 50 GeV and $>$ 350 GeV) and for different jet algorithms, using calorimeter towers as input objects. The figure reveals:

- The deviation of the jet energy from the quark energy depends on the quark energy. For $E_{quark} > 350$ GeV the width of the distribution is smaller than for $15\,\text{GeV} < E_{quark} < 50\,\text{GeV}$ and the maximum is closer to zero.
- Jets with a larger parameter value (Cone $\Delta R = 0.7$ and k_T R = 0.6) tend to overestimate the energy of the quark. This means that particles are clustered to the jet, which physically do not belong to the jet but to the underlying event or initial state radiation. Smaller jets tend to underestimate the quark energy. Particles physically belonging to the jet are not clustered to the reconstructed jet.
- The width of the distribution is smaller for the jet algorithms with a smaller opening angle, indicating a better energy resolution.

From figure 4.1 it becomes transparent that two aspects concerning the jet energy reconstruction have to be considered: The mean and the width of the distributions $((E_{quark}\text{-}E_{jet})/E_{quark})$.
Typically the energy measurement of a calorimeter jet scatters around the "true" value due to fluctuations in number of produced particles in the electromagnetic and hadronic showers and hence in the energy depositions. So the width of the distribution defines the statistical effect of the resolution. The mean of the distribution describes the

energy scale of a jet, which is a systematic effect. If the mean is unequal to zero the jet on average collects too much or too less energy. So for an ideal jet algorithm the width of the $((E_{quark}\text{-}E_{jet})/E_{quark})$ distribution is small and the mean of the distribution is equal to zero.
Hence in the following, the mean and the width of the $(E_{quark}\text{-}E_{jet})/E_{quark}$ distributions are further investigated.

4.4.1 Jet energy scale and resolution including effects due to fragmentation and measurement

The width and the mean of the $(E_{quark}\text{-}E_{jet})/E_{quark}$ distributions have to be determined to be able to make quantitative comparisons between the jet algorithms. For this the energy distributions are fitted with a Gaussian distribution. To make the fit stable, a first Gaussian is fitted between the mean of the histogram and $\pm$ two times the RMS (Root Mean Square). A second fit is then performed in the same way using the mean and the width of the first fit. The mean of the second Gaussian is then the 'mean' of the energy distribution and the 'sigma' the width. All fits converged; tails, which only contained a small fraction of events, were not considered in the fits.

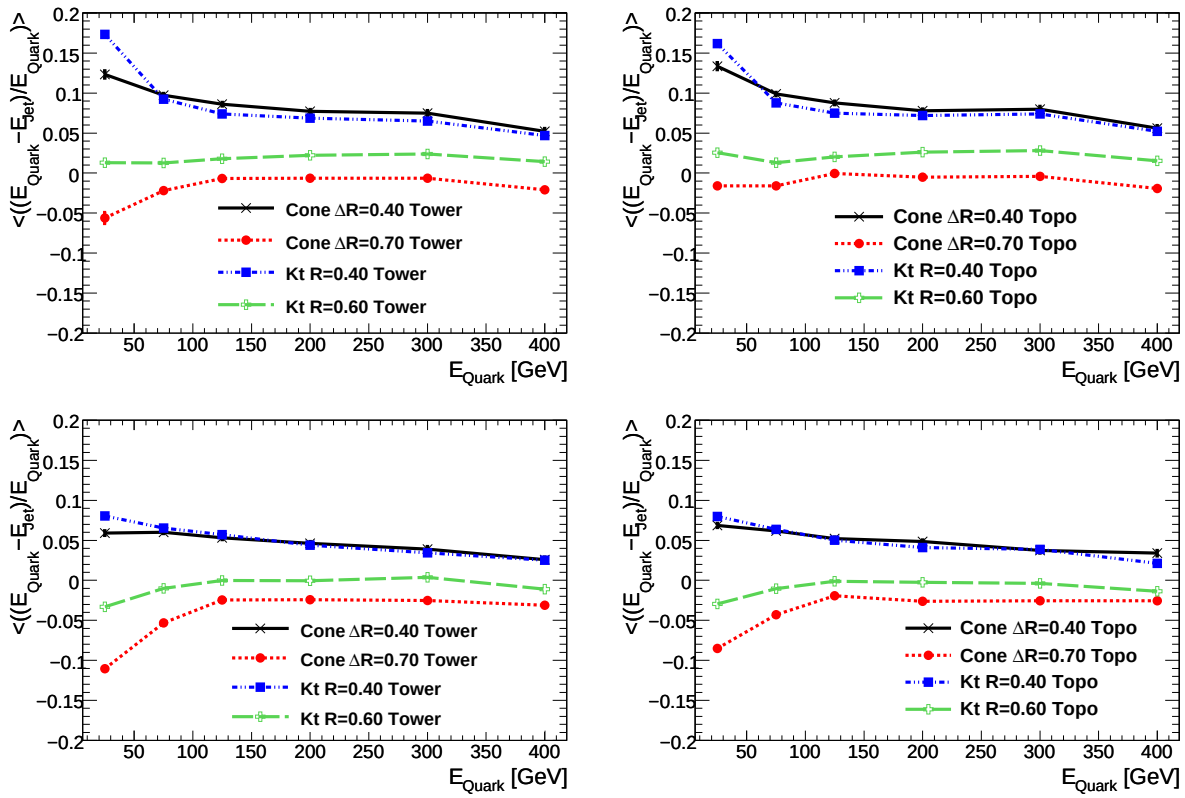

Figure 4.2: 'Mean' of $(E_{quark}\text{-}E_{jet})/E_{quark}$ for b jets (upper plots) and light jets (lower plots) comparing jets built of calorimeter towers and topological cell clusters.

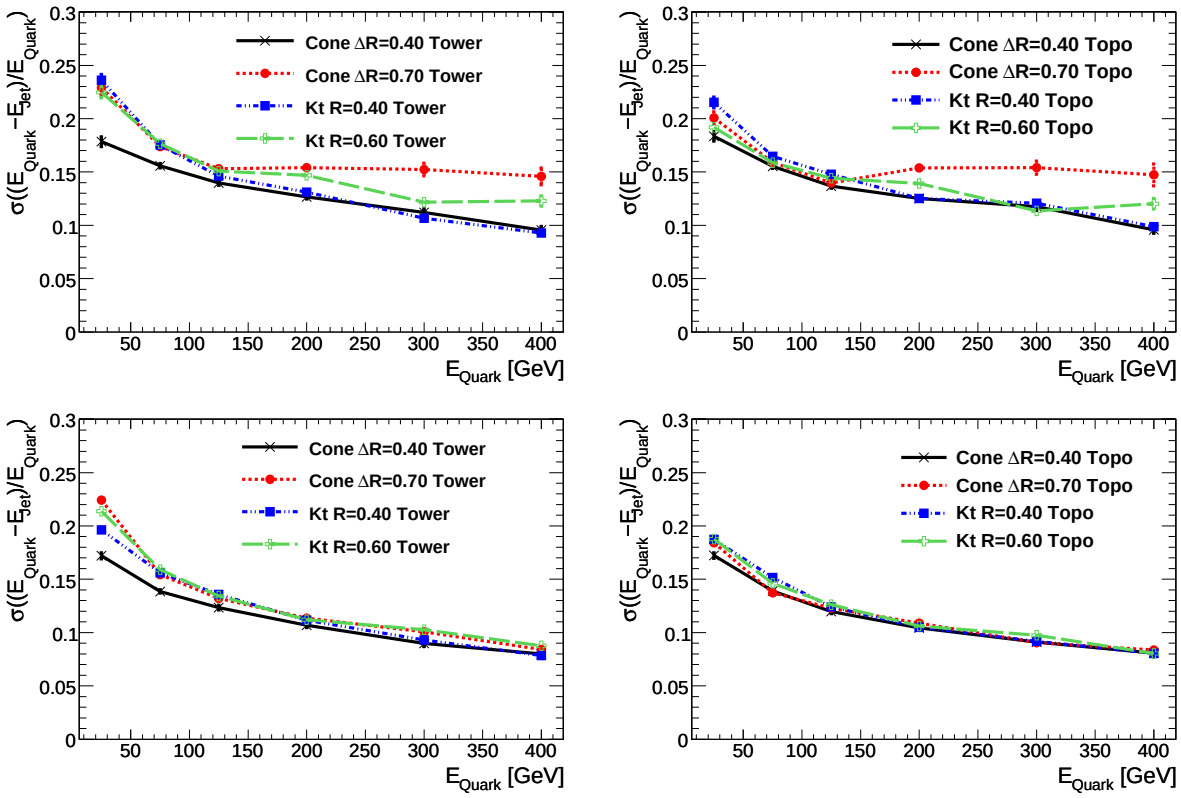

Figure 4.3: 'Sigma' of (E_{quark}-E_{jet})/E_{quark} for b jets (upper plots) and light jets (lower plots) comparing jets built of calorimeter towers and topological cell clusters.

Figure 4.2 presents the 'mean' values of (E_{quark}-E_{jet})/E_{quark} for various jet algorithms for b jets and light jets, comparing jets built of calorimeter towers and topological cell clusters. The smallest 'mean' value shows the k_T R = 0.6 for both b jets and light jets, built of calorimeter towers or topological clusters. For b jets also the Cone ΔR = 0.7 shows a good performance. For quark energies above 100 GeV jet algorithms with larger sizes reflect the quark energy most accurately. This means that the jets are big enough to collect the energies of all particles coming from the initial quarks.
Comparing the jet energy resolutions of the different jet algorithms - as presented in figure 4.3 - clearly the Cone ΔR = 0.4 reveals the best performance for b jets and light jets. It is expected that the jet energy resolution shows a $1/\sqrt{E}$ dependency. The accuracy of the energy determination in the calorimeter increases with increasing number of measured particles. The higher the energy of a jet is the more particles are produced in the electromagnetic hadronic shower and hence the precision of the energy determination increases. The statistical error of a number N is described by $\sqrt{N}$. This behaviour is confirmed by all jet algorithms except Cone ΔR = 0.7 and k_T R = 0.6.
For b jets the Cone and k_T with the larger value show a very surprising behaviour with low resolution for higher quark energies. The reason for this unphysical behaviour is so far not understood. For light jets the performance differences are smaller than for b jets.

4.4.2 Comparison of effects from fragmentation and measurement separately

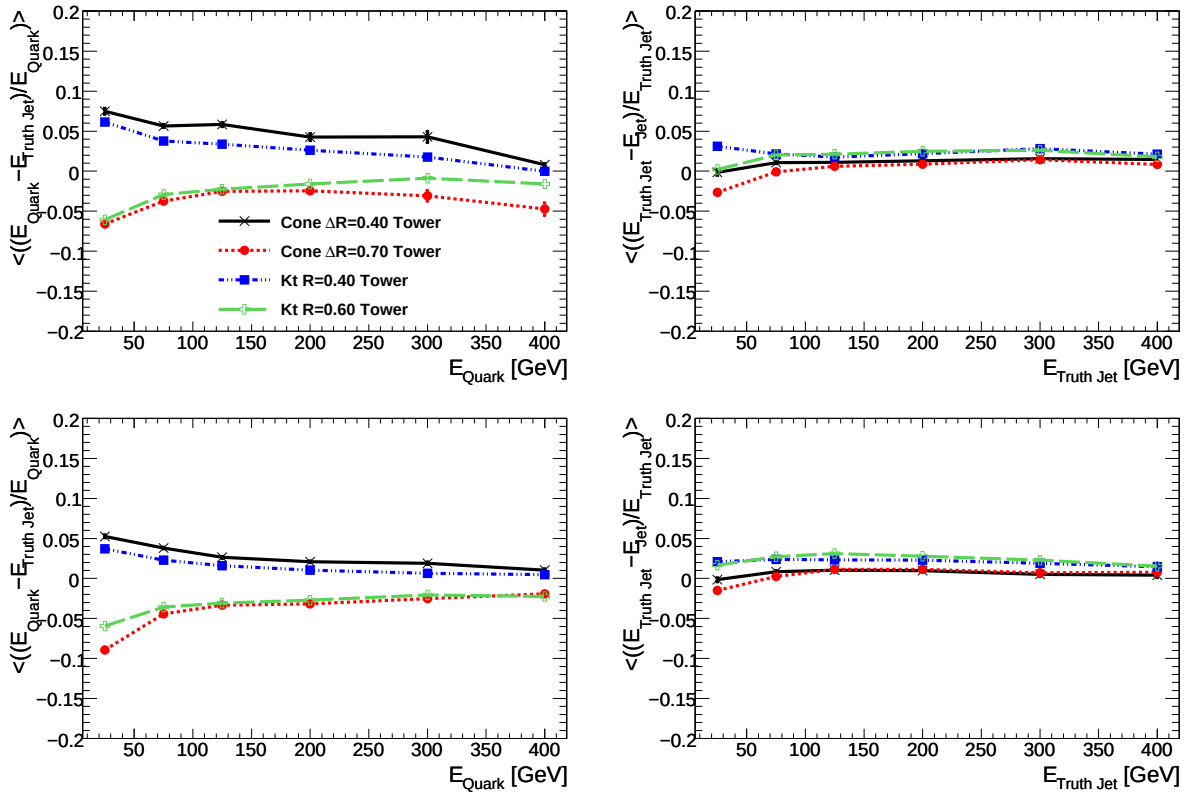

Figure 4.4: 'Mean' of (E_{quark}-$E_{truth\ jet}$)/E_{quark} and ($E_{truthjet}$-E_{jet})/$E_{truth\ jet}$ for b jets (upper plots) and light jets (lower plots) comparing jets built of calorimeter towers and topological cell clusters.

The transition from quark → truth jets includes, besides the jet clustering of the stable particles, all QCD effects like parton shower and fragmentation. To improve the energy resolution of E_{quark} to $E_{truth\ jet}$, only the jet clustering can be influenced, the QCD effects cannot be changed. The step truth jet → jet consists of the measurement of the jet constituents by the detector and the reconstruction. Here a precise calorimeter and efficient jet algorithms are useful.
The jet calibration in ATLAS (see section 3.3.3) is done for Cone ΔR = 0.7 jets, built of calorimeter towers, using QCD di-jet events. This calibration is equally applied to all jet algorithms. Especially for top quark analysis this procedure could be disadvantageous. The jets in QCD di-jet events are dominantly low p_T jets, which are typically very different to the high p_T jets from the quarks in top analysis. Furthermore, top analyses need the properties of the quarks rather than of the truth jets.
Figure 4.4 shows the 'mean' of the distributions (E_{quark}-$E_{truth\ jet}$)/E_{quark} and ($E_{truth\ jet}$-E_{jet})/$E_{truth\ jet}$. It is visible that the energies of truth jet and jet agree at an accuracy of $< 5\%$. So the calibration using QCD di-jet events seems to lead to an agreement of

jet and truth jet for jets from top quarks, too. The 'mean' of the step quark - truth jet shows deviations of up to 10%. Here the jets with larger jet sizes clearly collect too much energy, jets with smaller jet sizes too few energy. It is important to mention that the relation $\Delta(E_{quark},E_{truth\,jet}) \oplus \Delta(E_{truth\,jet},E_{jet}) = \Delta(E_{quark},E_{jet})$ is not valid as expected. In addition to the physical effects responsible for this behaviour (the difficulties of the reconstruction of the transition from quark to particle jet and calorimeter jet are already discussed in section 3.3) the jet multiplicity can change between the different stages with influence on the resolution. This aspect will be discussed in more detail in chapter 8.

4.5 Angular resolution

To be able to reconstruct the top quark from the measured jets, $\vec{p}_{quark}$ and $\vec{p}_{jet}$ have to agree to a certain degree.
Figure 4.5 shows the ΔR between quark and assigned jet for different jet algorithms and for two quark energy intervals. Because jets are assigned to a quark if $\Delta R(quark,jet) < 0.3$, the $\Delta R(quark,jet)$ cannot be larger than 0.3. As expected, the angular resolution clearly improves with increasing quark and hence jet energy and with smaller jet sizes.

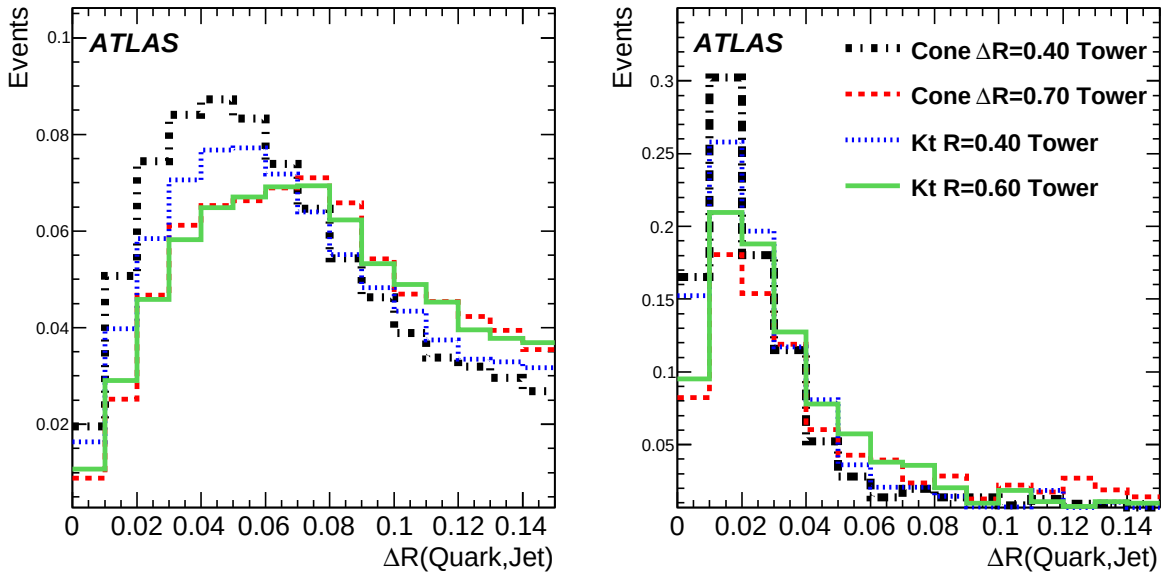

Figure 4.5: Angular resolution $\Delta R(quark,jet)$ for light jets for two different quark energy ranges. The left plot shows the energy resolution for quark energies between 15 and 50 GeV, the right plot for quark energies above 350 GeV.

Figure 4.6 presents the 'mean' of ΔR(quark,jet) for b jets and light jets as a function of the quark energy for different jet algorithms. Smaller jet sizes improve the angular resolution, because they disregard soft particles which are radiated at big angles and increase the uncertainty on the jet axis determination. For Cone ΔR = 0.7 big deviations can be attested. The most accurate angular resolution shows the Cone ΔR = 0.4 jet algorithm (both built of calorimeter tower and topological cell clusters) for both b jets and light jets.

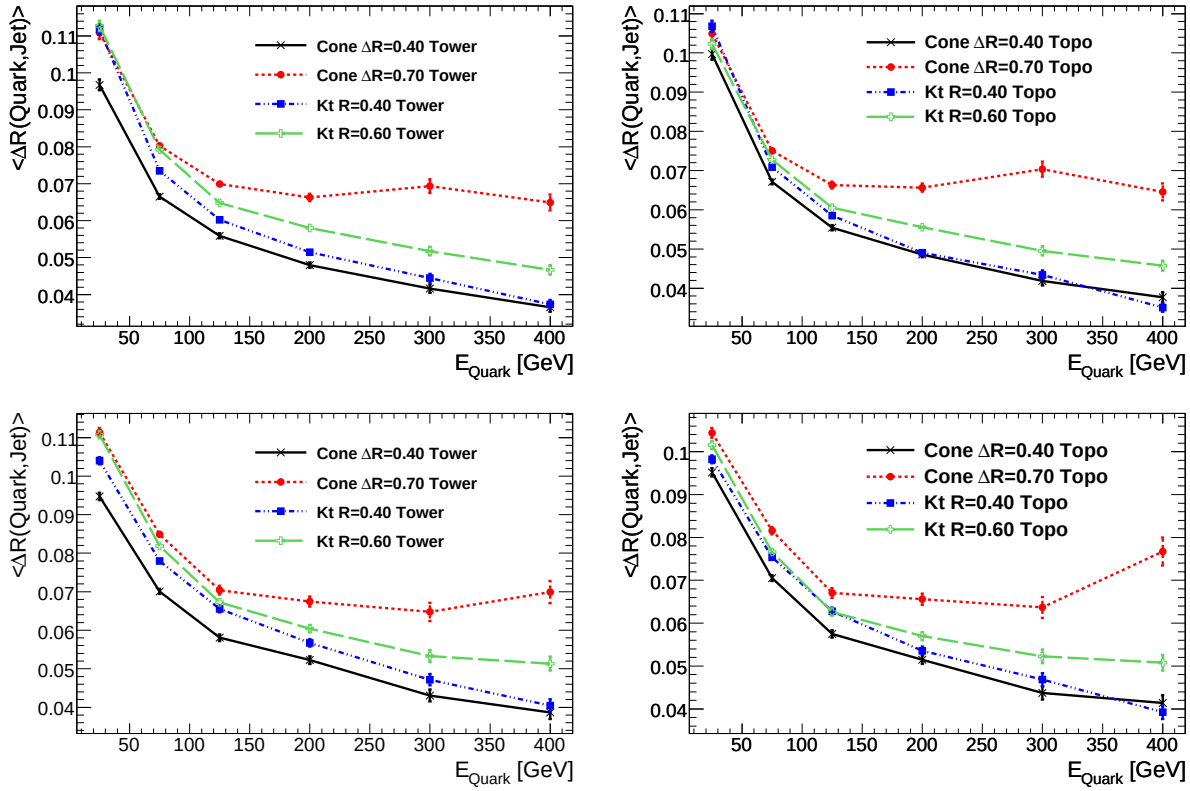

Figure 4.6: 'Mean' of ΔR(quark,jet) for b jets (upper plots) and light jets (lower plots) for different jet algorithms and jets built of calorimeter towers (left) and topological cell clusters (right).

4.6 Influence of pile up on energy resolution

In the previous sections the performance of jet algorithms was compared using only pure $t\bar{t}$ signal events. The ATLAS standard jet algorithm, Cone ΔR = 0.4 built of calorimeter towers, showed a reasonable performance. At an instantaneous luminosity of $10^{33}\,cm^{-2}s^{-1}$ soft interactions, so called pile-up events, are expected to appear in addition to the hard interaction producing a $t\bar{t}$ pair. These pile-up events mainly produce a uniform "noise" in the calorimeter, which is subtracted before jet clustering.

In this section the performance of the energy reconstruction of the Cone ΔR = 0.4 jet algorithm in the presence of pile-up events is investigated.

Figure 4.7 shows distributions for Cone ΔR = 0.4 built of calorimeter towers and topological cell clusters with and without pile-up. The presence of pile-up degrades the energy resolution. Both the 'mean' and the 'width' of the energy resolution attest a more stable behaviour using topological clusters as input objects. The 'mean' distributions show for both tower and topo jets an inaccurate pile-up subtraction. Too much energy is subtracted, leading to a larger deviation of E_{jet} from E_{quark}. Hence, the treatment of pile-up has to be improved and the use of topological cell clusters instead of calorimeter towers should be considered.

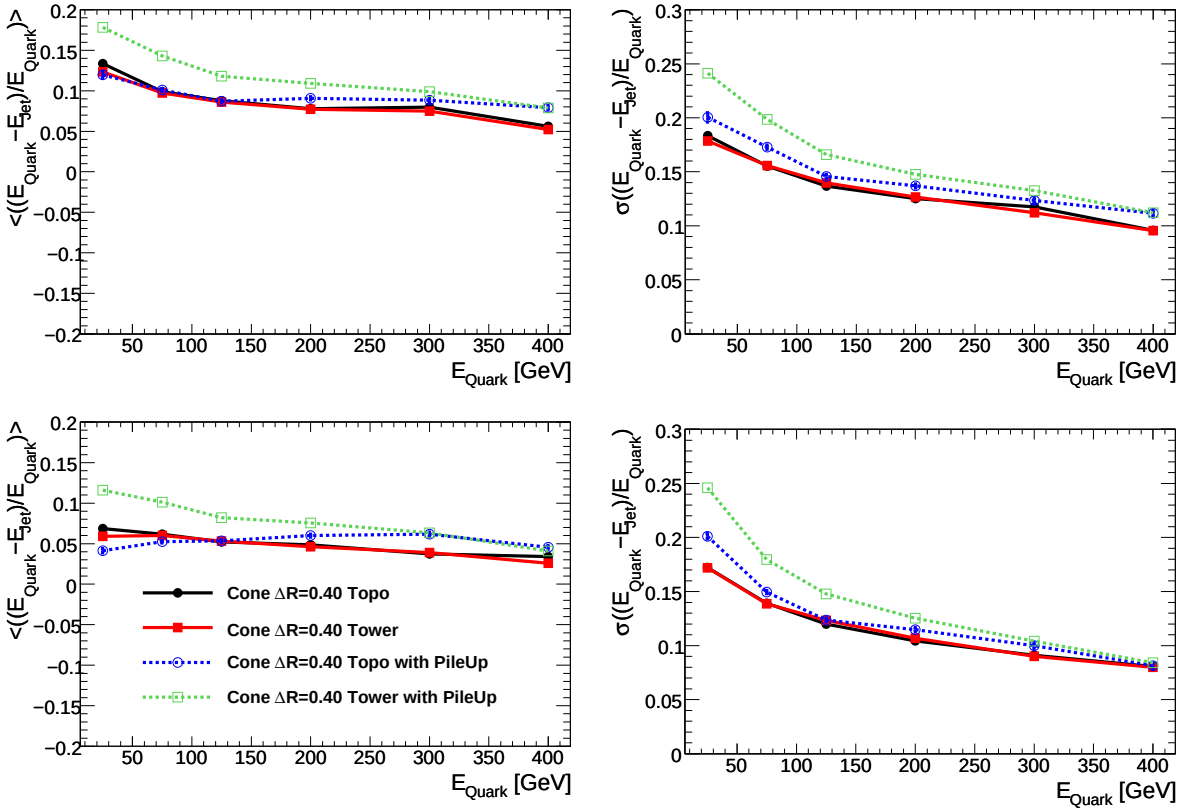

Figure 4.7: 'Mean' and 'sigma' of $(E_{quark}\text{-}E_{jet})/E_{quark}$ for b jets (upper plots) and light jets (lower plots) comparing for Cone ΔR = 0.4 the reconstruction accuracy for jets built of calorimeter towers and topological cell clusters in the presence of pile-up assuming an instantaneous luminosity of $10^{33}\,cm^{-2}s^{-1}$.

4.7 Influence of the choice of the jet algorithm on b-tagging

W+jets events are the main physical and irreducible background to top quark analysis, because all top quark events contain W bosons and jets in their final state. A possibility to separate $t\bar{t}$ events and W+jets events is based on the presence of two b jets in $t\bar{t}$ events, which can be additionally identified, called b-tagging.
B-tagging is possible, because the long lifetime of b quarks leads to a flight length distance of several millimeters, before the b hadrons decay to lighter particles. This results in a secondary vertex in addition to the primary vertex of the pp collision. Hence, the particles of a b jet show different properties compared to particles of light jets. B-tagging algorithms look at these properties of particles in a jet to calculate the probability weight, if the particular jet is more likely a b jet or a light jet. For this reference distributions are used.
B-tagging is based on the reconstruction of secondary vertices or likelihood/multivariate functions of impact parameters using the particle tracks matched to a jet. In ATLAS jets are only built out of calorimeter information. Particle tracks are matched to the resulting jet axis ($\vec{p}_{jet}$ of the jet) by calculating the ΔR(particle track, jet). If $\Delta R < 0.4$ the track is assigned to the jet. So the accuracy of the jet axis position is of importance for the b-tagging performance. A displaced jet axis leads to loss of tracks, which belong to the jet, or to misassignment of tracks not belonging to the jet.
So differences in the b-tagging performance for the different jet algorithms are possible. Especially the k_T with R = 0.6 and the Cone ΔR = 0.7 are expected to show a lower efficiency, because in section 4.5 the angular resolution for these jet algorithms was already found to be worse.

4.7.1 The standard ATLAS IP3D+SV1 algorithm

The b-tagging performance of the different jet algorithms is investigated using the ATLAS standard b-tagging algorithm. It is a combination of secondary vertex and impact parameter tagger, called "SV1+IP3D" [39]. Its performance is compared for the different jet algorithms. Important properties of a b-tagging algorithm are a high efficiency to recognize b-jets, whereas the efficiency of light jets to be tagged as b-jets has to be small. Figure 4.8 shows the b-tag efficiency versus the light jet rejection (= 1/(efficiency of light jets)).
For efficiencies of $< 65\%$ the best performances can be attested for the k_T algorithm with R = 0.4 using topological cell clusters as input, the second best performance shows the same jet algorithm, using calorimeter towers as input. The worst performance is achieved by the Cone ΔR = 0.7. The ATLAS default jet algorithm, Cone ΔR = 0.4, shows the best performance for high efficiency regions of $> 65\%$, for efficiencies $< 65\%$ its performance is between the k_T R = 0.4 and the Cone ΔR = 0.7. Hence, the ATLAS standard, the Cone ΔR = 0.4 (built of calorimeter towers), jet algorithm is a reasonable choice for b-tagging.

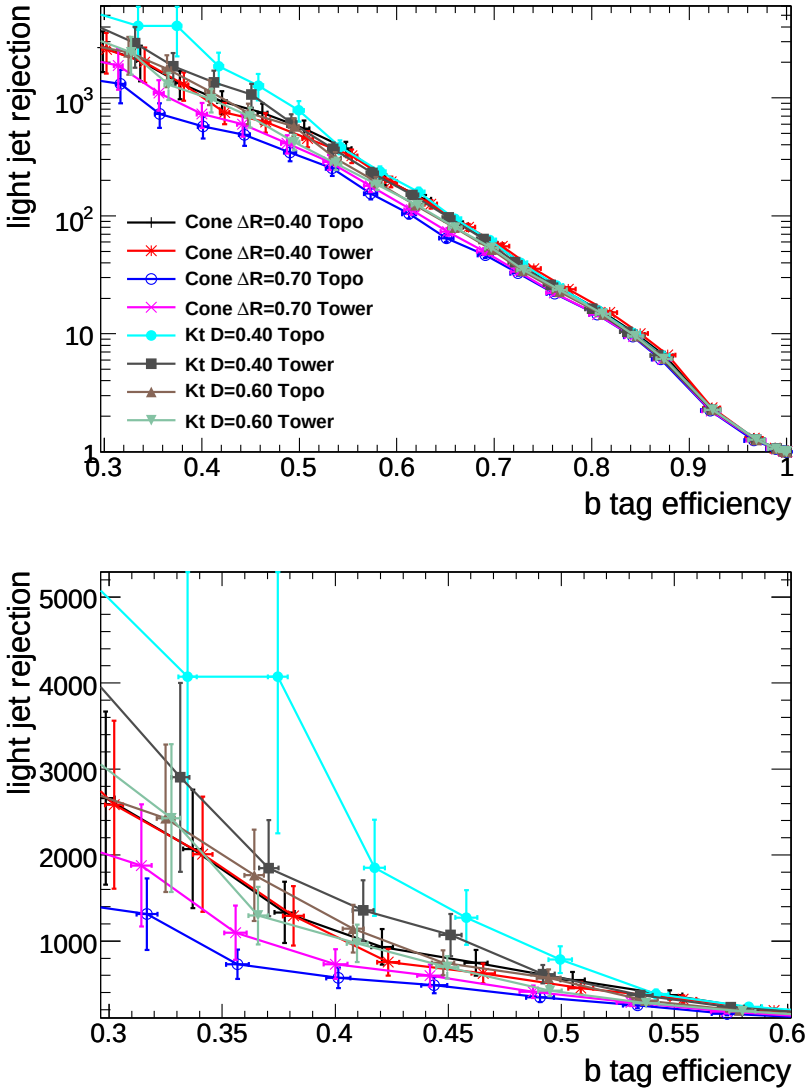

Figure 4.8: The b-tag efficiency versus the light jet rejection for the ATLAS standard b-tagging algorithm "SV1+IP3D" comparing different jet algorithms. The upper plot shows the entire efficiency spectrum from 30% to 100%, the lower plot shows the efficiency region between 30% and 60% more precisely.

4.7.2 The standard ATLAS IP3D+SV1 algorithm: Special reference histograms

The reference distributions, which are used to calculate the b-tagging weights, are typically produced using a variety of physics processes, light jet purification[3], as well as different versions of the detector geometry, simulation and reconstruction. The idea is to check, if the b-tagging performance in $t\bar{t}$ events improves by using reference histograms, which are created only using the b jets and light jets in top events. Hence, special $t\bar{t}$ reference histograms were produced using in total 250 thousand $t\bar{t}$ events. Then the b-tag performance using these reference histograms to calculate the b-tagging weights is compared to the performance using the default reference histograms. Again the standard b-tagging algorithm "IP3D+SV1" is used for this study and the standard jet algorithm Cone $\Delta R = 0.4$ (calorimeter tower). The results are presented in figure 4.9. The weights for both b jets and light jets calculated with the special top sample reference histograms are on average smaller than those from the default reference histograms. Because the weights are smaller for both b jets and light jets, the performance should not change significantly. This is confirmed by the right plot in figure 4.9. Here the b-tag efficiency versus the light jet rejection is shown. Within the statistical uncertainty there is no difference in the performance. Hence, there appears no significant advantage in using dedicated $t\bar{t}$ reference histograms when applying b-tagging to $t\bar{t}$ events.

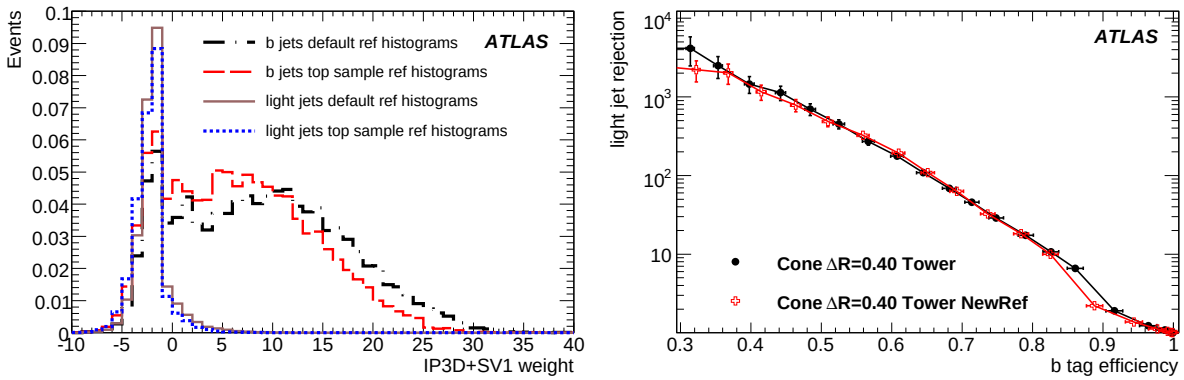

Figure 4.9: The b-tag weights for b jets and light jets calculated using the default reference histograms and reference histograms produced only with $t\bar{t}$ events (left plot). The efficiency versus light jet rejection based on the b-tag weights comparing standard and special reference histograms.

[3] light jets, which are near to b jets, are discarded, because their properties can be influenced by the near b jets

4.8 Summary

Top quarks decay before hadronization takes place, all properties of the top quark can be deduced from its decay products. Because the final states of $t\bar{t}$ events always include quarks and hence jets, the performance of jet clustering algorithms plays an important role for $t\bar{t}$ analyses. In this chapter the performance of various jet algorithms in $t\bar{t}$ events was compared. The emphasis was put on the reconstruction of the energy and the position of initial quark by the jet algorithms. In general jet algorithms with small sizes are favourable for $t\bar{t}$ reconstruction. The ATLAS standard jet algorithm, the Cone $\Delta R = 0.4$ built of calorimeter towers, showed a reasonable behaviour. In the presence of pile-up, topological cell clusters as input for jet clustering are preferable. Comparing the b-tagging performance for the different jet algorithms, jet algorithms with small jet sizes show the highest performance. Also here Cone $\Delta R = 0.4$, built of calorimeter towers, is a reasonable choice. It was tested, if the usage of dedicated $t\bar{t}$ event reference histograms as basis for b-tagging implicates advantages. This was not confirmed, inside the uncertainties no differences in the performance were attested. In the context of these studies additional Cone and k_T jet collections with a larger variety of ΔR and R parameters were produced and investigated. The results are published in [44].

Chapter 5

Motivation of measuring W+jets/Z+jets

With a centre-of-mass energy of up to 14 TeV the LHC will provide the possibility to investigate Standard Model processes and beyond-Standard Model searches in kinematic regions so far unreached. In the proton-proton collisions a large variety of physics processes will take place. Figure 2.7 shows the cross sections of important processes to be investigated at the LHC. From the graphic the most prominent difficulty becomes transparent. The total cross section of the LHC is magnitudes higher than the cross sections of processes of interest, for example the top quark cross section. The rare processes of interest have to be filtered from the multitude of interactions. Because it is completely unknown, which processes are actually taking place inside the ATLAS detector, the only possibility to select the processes of interest is to consider their expected event signature and investigate only events which satisfy the defined criteria. However, there a typically many other processes, which show a similar event signature and are selected, too. These are called background events. Hence, discoveries of new physics and precision measurements are not possible without well understood Standard Model physics. Physics analyses of particular processes, for example top quark production, are always also analyses of all processes, which have to be cut away.

5.1 Top quark analysis

Precision measurements of the top quark are one of the goals of LHC physics. As mentioned in section 1.2, the top quark decays with a probability of almost 100% to a W boson and a b quark. The top quark decay is classified by the decay channels of the W bosons. The semi-leptonic channel - with one W boson decaying into a charged lepton-neutrino pair and one W boson decaying into a quark-antiquark pair - is easiest to select. The decay rate is sufficiently high in order to provide enough event statistics and the event signature including one high energy isolated lepton is best suited to achieve a proper signal to background ratio after event selection.
The signature of a semi-leptonic $t\bar{t}$ event includes:

- one isolated lepton with high transverse momentum from the leptonic W decay
- a large amount of $\not{E}_T$ caused by the neutrino from the leptonic W decay

- at least four jets; two light flavour (up, down, charm, strange) jets from the hadronically decaying W boson and two jets from the bottom quarks

Except for the requirement of at least four jets, the event selection for semi-leptonic $t\bar{t}$ events does not differ from the event selection of a $W \rightarrow l\nu$ event. At hadron-hadron colliders W bosons can be produced accompanied by jets, so called W+jets events. W bosons with four additional jets, W + 4 jets events, then have the same signature as $t\bar{t}$ events and form a very important and irreducible background to top quark analysis.
Because of the magnitude of Feynman diagrams, which have to be considered, the cross section of W+jets production has only been calculated in NLO with up to two additional final state partons [63]. Hence, the W + 4 jet cross section is calculated only at tree level or using parton shower models, i.e. it is only known with limited precision. Top quark pair analysis at DØ suffers from these uncertainties. The method to estimate the W+jets background at DØ is to normalize the number of W+jets events to data. This means, the number of W+jets events is the difference between all the other background contributions and data (for example as described in [64]). This additional degree of freedom worsens the precision of the results. With regard to the LHC these uncertainties will not vanish.
Because predictions for the W + 4jets background are not calculable precisely, a solution is to measure the cross section of this background. However, W+jets events are difficult to measure. The neutrino is only detectable by the transverse momentum imbalance it produces and W+jets and top quark pair events are not to keep apart. Hence, it is better to measure a different process with similar properties, which is easier to detect.
A candidate are Z+jets events. Here, the event signature of two oppositely charged leptons with an invariant mass near the Z mass presents hard kinematic constraints. The cross section of the Z boson is a factor of ten smaller than the cross section of the W boson, but the smaller statistics is compensated by an almost background free Z boson candidate sample.
Already in [65] the properties of W and Z events have been compared in leading order (LO) calculations. The conclusion of this investigation was that there are only very small differences between W and Z events. Most of these differences are caused by the different event selection cuts (one charged lepton and missing transverse energy for the W boson and two charged leptons for the Z boson).
Of special interest were the cross sections of W/Z + n jets events with n=0,1,2 and 3 jets, more precisely the fractions

$$f_n(W\ /\ Z) = \frac{\sigma(W\ /\ Z\ +\ n\,\text{jets})}{\sum_m \sigma(W\ /\ Z\ +\ m\,\text{jets})} \tag{5.1}$$

Comparing the function f_n for W and Z in simulated events led to the conclusion that there are only very small differences between $f_n(W)$ and $f_n(Z)$. Hence, Z+jets events should be well adopted to investigate W+jets events. This is discussed in more detail in the following section.

5.2 W and Z events

At pp-colliders W and Z events are produced via the Drell-Yan process, the production of a lepton pair of large invariant mass in hadron-hadron collisions via $q\bar{q}$ annihilation. In the following only on-shell W and Z production is considered. The Drell-Yan LO cross sections for on-shell W and Z production are calculated to be [63]:

$$\hat{\sigma}^{q\bar{q}'\to W} = \frac{\pi}{3}\sqrt{2}G_F M_W^2 |V_{qq'}|^2 \delta(\hat{s} - M_W^2) \tag{5.2}$$

$$\hat{\sigma}^{q\bar{q}\to Z} = \frac{\pi}{3}\sqrt{2}G_F M_Z^2 (c_V^2 + c_A^2)\delta(\hat{s} - M_Z^2) \tag{5.3}$$

where

$$c_V^f = I_{3L}^f + I_{3R}^f - 2e_f \sin^2\Theta_W \tag{5.4}$$

$$c_A^f = I_{3L}^f - I_{3R}^f \tag{5.5}$$

c_V is the vector and c_A is the axial vector part of the coupling of the Z to fermion f, I_3 denotes the third component of the weak isospin.
These formulae are only valid for narrow width production. The cross sections for $W \to e\nu$ and $Z \to ee$ are obtained by $\sigma_W \cdot BR(W \to e\nu)$ and $\sigma_Z \cdot BR(Z \to ee)$. The branching ratios are [4]:

$$BR(W^\pm \to e^\pm \nu_e) = (10.75 \pm 0.13)\% \tag{5.6}$$

$$BR(Z^0 \to e^+e^-) = (3.363 \pm 0.004)\% \tag{5.7}$$

and in general:

$$BR(W^\pm \to l\bar{\nu}\ (\text{or}\ \bar{l}\nu)) = (10.80 \pm 0.09)\% \tag{5.8}$$

$$BR(W^\pm \to q\bar{q}') = (67.60 \pm 0.27)\% \tag{5.9}$$

$$BR(Z^0 \to l^+l^-) = (3.3658 \pm 0.0023)\% \tag{5.10}$$

$$BR(Z^0 \to q\bar{q}) = (69.91 \pm 0.06)\% \tag{5.11}$$

$$BR(Z^0 \to q\nu\bar{\nu}) = (20.00 \pm 0.06)\% \tag{5.12}$$

The cross section formulae are obviously very similar. Only the couplings are different, resulting in about ten times less Z events. A small additional difference comes from the mass difference between W and Z of roughly ten percent. Similar cross section formulae imply that W and Z boson events contain the same production and decay mechanisms. These mechanisms are investigated more precisely.
A selection of Feynman diagrams for W and Z production is shown in figure 5.1. Here Feynman diagrams for W/Z + 0 partons, W/Z + 1 parton and W/Z + 2 partons are presented. W and Z bosons with more than two additional partons are produced by additional gluon radiations and gluon splittings. If W and Z bosons are accompanied by at least one parton in the final state, initial states containing a quark and a gluon or

two gluons (at least two final state partons) are possible. Formula 5.2 already showed that there are almost no differences between W and Z events, which are accompanied by no jets. Also in the other Feynman diagrams there are no differences between W and Z bosons. Hence, W and Z events are expected to show very similar properties with comparable event shapes.
Similar production mechanisms imply a similar behaviour of the processes and especially a similar dependence of the centre-of-mass energy. Figure 2.7 shows the cross section development with increasing centre-of-mass energy. σ_W and σ_Z show a proportional behaviour. The values for the cross sections for W and Z production with up to four additional partons for the LHC centre-of-mass energies of 7 TeV, 10 TeV and 14 TeV are presented in table 5.1. The cross section ratios as a function of the parton multiplicity can be seen in figure 5.2. The cross section ratio changes only slightly with different centre-of-mass energies. W and Z events scale equally with different centre-of-mass energies. This was already expected due to the similar production and decay mechanisms and attests that there are almost no differences between W and Z events, especially in the mechanisms to produce associated jets.

Process	**xsec/pb (14 TeV)**	**xsec/pb (10 TeV)**	**xsec/pb (7 TeV)**
$\mathbf{W^+ \to e^+ \nu_e}$			
+ 0p	4435.0 ± 3.9	3388.2 ± 3.2	2544.1 ± 2.5
+ 1p	704.6 ± 0.8	490.5 ± 0.6	327.7 ± 0.5
+ 2p	235.0 ± 0.9	152.2 ± 0.5	94.5 ± 0.3
+ 3p	71.2 ± 0.4	43.5 ± 0.3	24.6 ± 0.2
+ 4p	20.7 ± 0.2	11.5 ± 0.2	5.9 ± 0.08
$\mathbf{W^- \to e^- \nu_e}$			
+ 0p	3335.0 ± 2.2	2364.0 ± 1.7	1625.3 ± 1.3
+ 1p	566.0 ± 0.5	368.0 ± 0.4	227.4 ± 0.2
+ 2p	178.4 ± 0.4	108.1 ± 0.3	60.9 ± 0.1
+ 3p	51.4 ± 0.3	28.5 ± 0.1	14.7 ± 0.06
+ 4p	13.7 ± 0.1	7.1 ± 0.07	3.2 ± 0.03
$\mathbf{Z^0 \to e^+ e^-}$			
+ 0p	603.0 ± 0.3	442.4 ± 0.2	318.9 ± 0.2
+ 1p	135.0 ± 0.09	90.5 ± 0.07	58.3 ± 0.04
+ 2p	42.4 ± 0.07	26.6 ± 0.04	15.8 ± 0.03
+ 3p	12.5 ± 0.05	7.3 ± 0.03	4.0 ± 0.02
+ 4p	3.5 ± 0.046	1.9 ± 0.01	0.9 ± 0.008

Table 5.1: Cross sections for $W^{\pm}/Z$ + n parton production as calculated with the HELAC-PHEGAS Monte Carlo generator [66–69] for LHC centre-of-mass energies of 7 TeV, 10 TeV and 14 TeV ($p_T^{\text{parton}} > 20\,\text{GeV}$, $p_T^{\text{lepton}} > 25\,\text{GeV}$, $|\eta_{\text{parton}}| < 2.5$, $|\eta_{\text{electron}}| < 2.4$, $|\eta_{\text{neutrino}}| < 5$).

However, differences between W and Z events exist, these are investigated in the following.

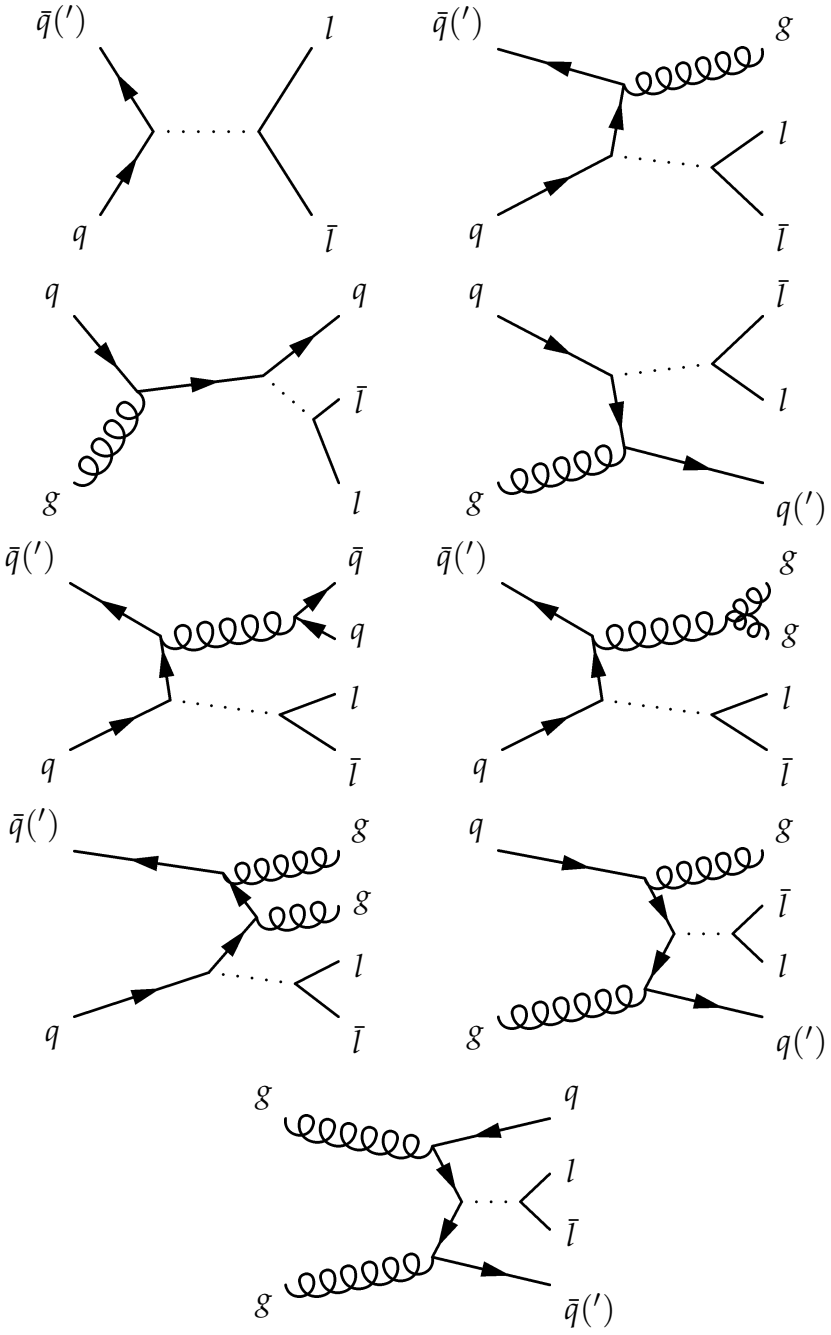

Figure 5.1: A selection of Feynman diagrams for vector boson production with 0, 1 and 2 associated partons. These Feynman diagrams are valid for both W and Z production.

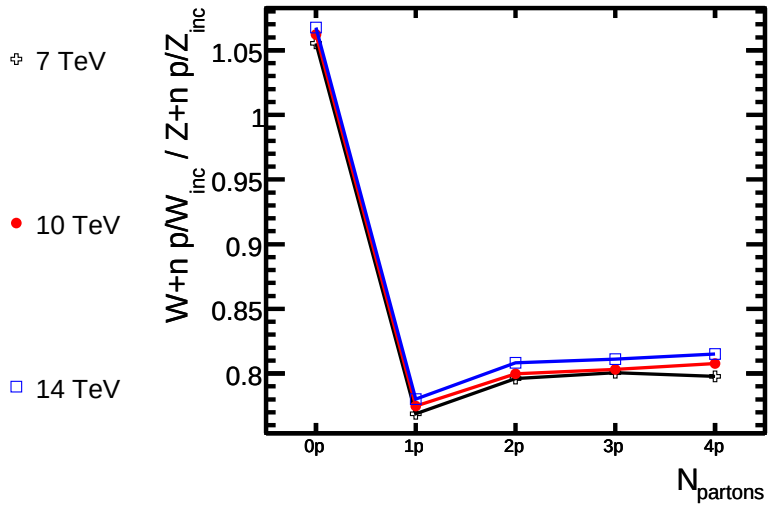

Figure 5.2: The cross section ratio of W and Z as a function of the parton multiplicity ($\frac{\sigma(W+n\,\text{partons})}{\sum_m \sigma(W+m\,\text{partons})} / \frac{\sigma(Z+n\,\text{partons})}{\sum_m \sigma(Z+m\,\text{partons})}$) for LHC centre-of-mass energies of 7 TeV, 10 TeV and 14 TeV as generated with the HELAC-PHEGAS Monte Carlo generator [66–69] ($p_T^{\text{parton}} > 20\,\text{GeV}$, $p_T^{\text{lepton}} > 25\,\text{GeV}$, $|\eta_{\text{parton}}| < 2.5$, $|\eta_{\text{lepton}}| < 2.4$).

5.2.1 Final State

The selected Z boson decays into two charged leptons and the W boson into a charged lepton and a neutrino. This implies experimental differences: the Z is easy to select and reconstruct. The neutrino from the W boson has to be reconstructed from the p_T imbalance in the detector, resulting in far higher uncertainties than for Z reconstruction.
The bottom Feynman diagram of figure 5.1 shows a process with two quarks in the final state. This process with two b quarks in the final state only exists for Z production and not for W production. This is a difficulty with regard to top quark pair analyses. $t\bar{t}$ events are mainly selected by the presence of two b jets in the final state. If measuring Z+jets to estimate the W+jets background in $t\bar{t}$ analysis, the presence of additional Z+bb+X events compared to W+bb+X events has to be considered (if including b-tagging).

5.2.2 Initial State

The Z boson is produced via $q\bar{q}$ annihilation, which means in case of a proton-proton collision mainly $u\bar{u}$ and less $d\bar{d}$, $s\bar{s}$ and $c\bar{c}$. The W^+ is mostly produced from $u\bar{d}$ and the W^- from $d\bar{u}$. Figure 5.3 shows the Parton Distribution Functions (PDFs) of the proton. The PDFs for the valence quarks up and down differ, whereas the PDFs for the sea quarks are comparable. The different momentum fractions of the up and down quarks affect the rapidity distributions of the bosons.

In figure 5.4 the rapidity distributions of the W^+, W^- and Z are presented itemized by the initial flavours. The complete rapidity distributions of W^+, W^- and Z reveal the expected differences. The W^- is most central, the W^+ most boosted and the Z in between. Additionally, the rapidity of the Z boson is much more limited than the rapidity of the W boson. For the Z two electrons within $|\eta| < 2.4$ are required, for the W boson one electron within $|\eta| < 2.4$ and the neutrino inside the detector. This is mainly an experimental difference. If only looking at W^+, W^- and Z bosons produced from sea quarks, which show comparable PDFs, the differences in rapidity almost vanish (of course also no differences occur for gluon initial states). This is also proved by figure 5.5. Here the rapidity distributions of W^+, W^- and Z are shown only for sea quark initial states. For this plot the rapidity requirements were relaxed to $|y| < 5$ for both electrons and neutrinos.
Hence, differences between W and Z occur for initial states containing valence quarks. The PDFs for valence quarks are well understood from Deep Inelastic Scattering (DIS) experiments (for example ZEUS [70] and H1 [71]). The sea quark PDFs are not as well measured, but here the differences between W and Z vanish. This means, the occurring differences between W and Z bosons occur for well understood processes and can be modelled.

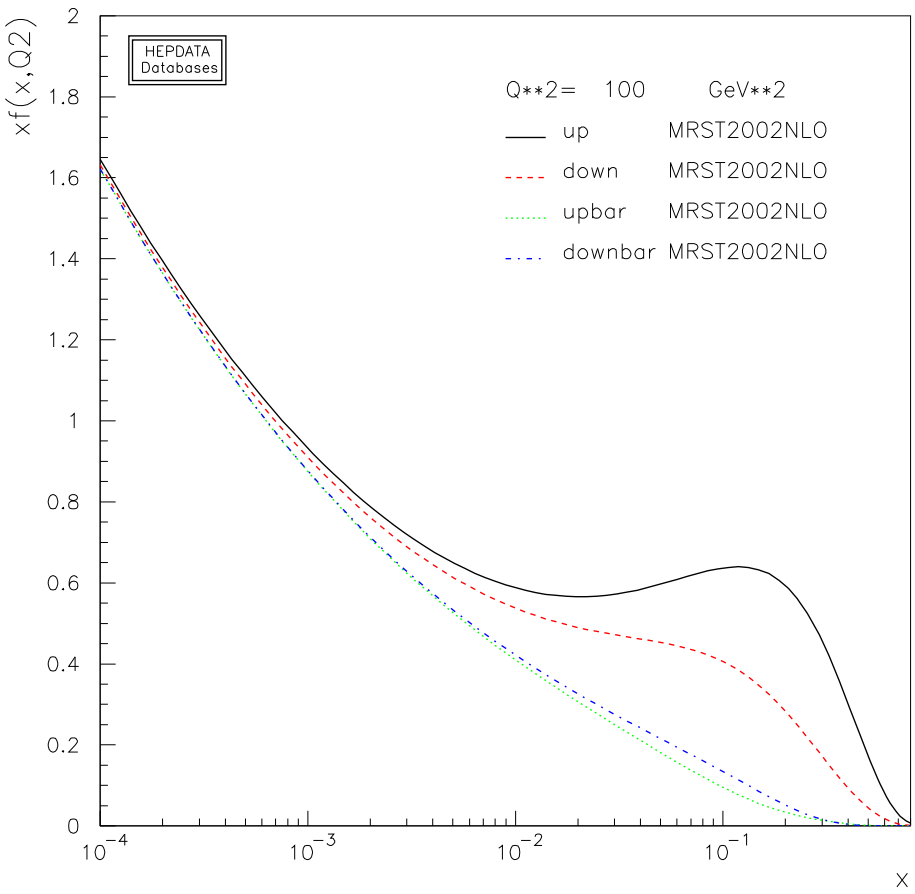

Figure 5.3: The Parton Distribution Functions (PDFs) for the proton [72].

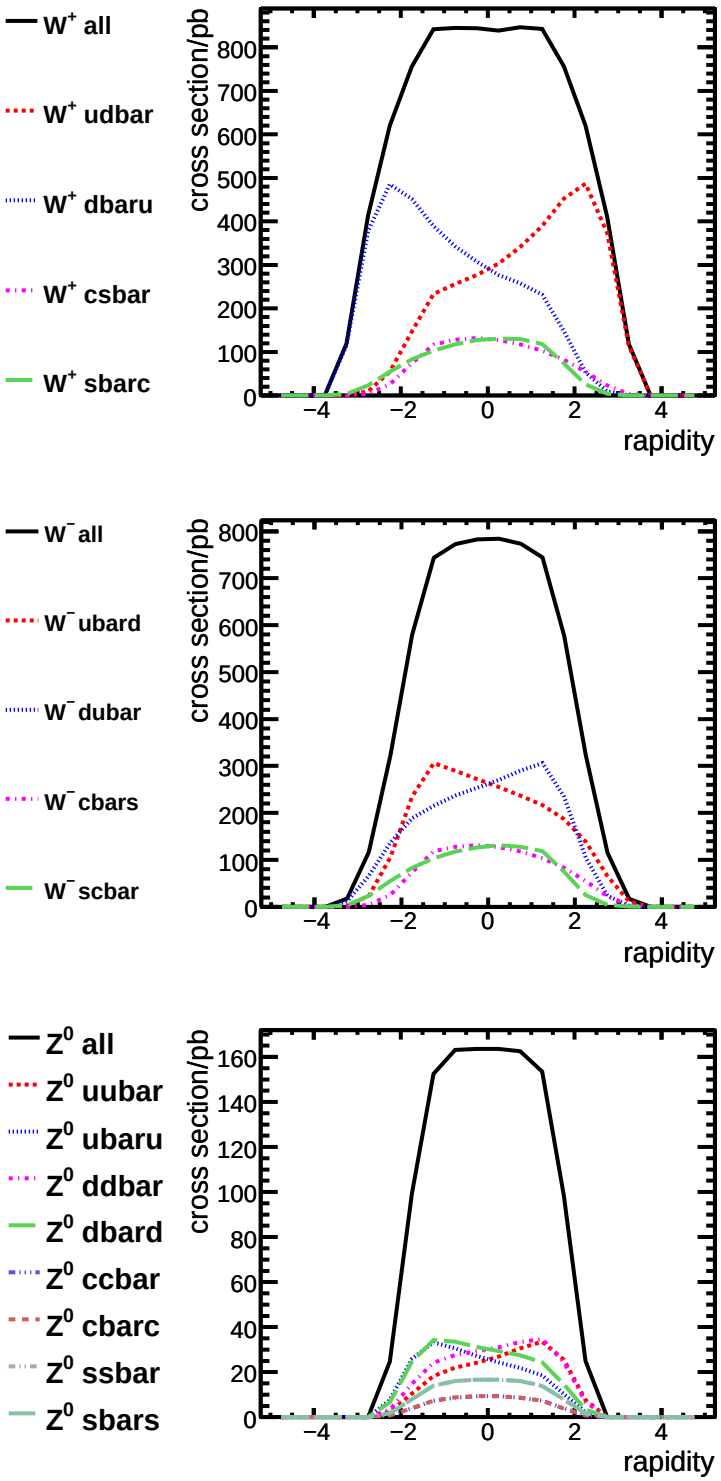

Figure 5.4: The rapidity distributions for W^+, W^- and Z^0 itemized by the initial flavours. The distributions are generated with the HELAC-PHEGAS Monte Carlo generator [66–69] (p_T^{parton} >20 GeV, p_T^{lepton} >25 GeV, $|\eta_{\text{parton}}| < 2.5$, $|\eta_{\text{electron}}| < 2.4$, $|\eta_{\text{neutrino}}| < 5$).

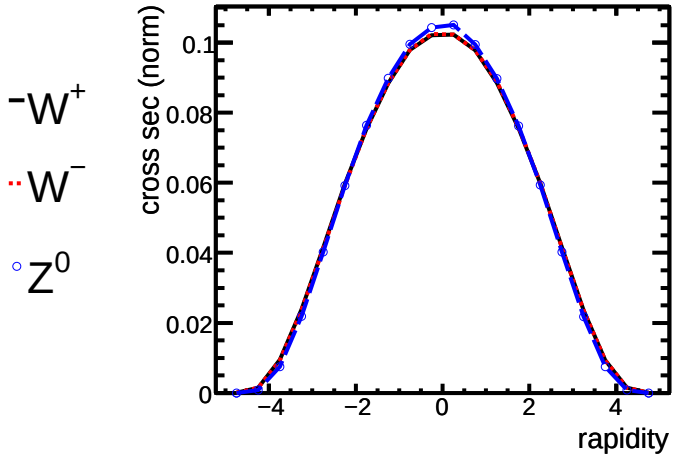

Figure 5.5: The rapidity distributions for W^+, W^- and Z^0. Shown are only the distributions for bosons produced from sea quark initial states. The distributions are generated with the HELAC-PHEGAS Monte Carlo generator [66–69] (p_T^{parton} >20 GeV, p_T^{lepton} >25 GeV, $|\eta_{\text{parton}}| < 2.5$, $|\eta_{\text{electron}}| < 5$, $|\eta_{\text{neutrino}}| < 5$).

5.2.3 Masses

The 10% higher mass of the Z requires a higher momentum transfer (higher Q^2) resulting in a larger phase space. To balance this higher mass the average jet multiplicity and the average jet p_T is higher.

The cross section ratio of W and Z, which is shown in figure 5.2, demonstrates the differences in the number of jets in W and Z events. The probability for the less heavy W to be accompanied by no hard partons ($p_T^{parton} > 20$ GeV) is higher than for the Z. For one and more additional partons the cross section ratio is consistently smaller than one, because in Z events more jets are produced. The interesting point is that the ratio W+njets/Z+njets is approximately constant for one and more jets. Hence, the mass difference results in more jets in Z events, but as soon as at least one additional hard parton exists, the QCD effects, which produce one and more jets, show almost no differences between W and Z. Different Monte Carlo generators are discordant in predicting the extent of these differences between W and Z. This is discussed in [73].

If m_W is set equal to m_Z, the differences in the jet multiplicity and p_T between W and Z mostly vanish as shown in [73]. Because jets with a higher p_T are reconstructed more efficiently and more accurately, small (< 10%) differences in the migrations behaviour of the jets between W and Z events are expected (see chapter 8 for discussion).

5.2.4 Couplings

The W boson couples to all quarks and leptons with the universal V-A coupling, described by the $W^{\pm}$ vertex factor [74]:

$$\frac{-ig_W}{2 \cdot \sqrt{2}} \gamma^{\mu}(1-\gamma^5) \tag{5.13}$$

The Z vertex factor depends on the flavours of the particles and is a composition of V-A and V+A interaction, described by the Z vertex factor [74]:

$$\frac{-ig_Z}{2} \gamma^{\mu}(c_V^f - c_A^f \gamma^5), \tag{5.14}$$

where $g_W = g_e / \sin\Theta_W$ and $g_Z = g_e/(\sin\Theta_W \cdot \cos\Theta_W)$; $g_e = e\sqrt{8\pi^2/hc}$, e is the charge of the electron; γ^{μ} are the Dirac-matrices.
The different couplings influence the number of events and the angular distributions of the particles during production and decay, detectable in the angular distributions of the final state particles. In $p\bar{p}$ collisions the differential cross section $\frac{d\hat{\sigma}}{d\cos\hat{\Theta}}$ for the electron from the $W \rightarrow e\nu$ decay was measured. $\hat{\Theta}$ is the emission angle of the electron (positron) with respect to the proton (antiproton) direction in the W rest frame. It was predicted to be and measured as [75]

$$\frac{d\hat{\sigma}}{d\cos\hat{\Theta}} \sim (1+\cos\hat{\Theta})^2, \tag{5.15}$$

For the electrons from the $Z \rightarrow ee$ decay a similar dependency was found [75]

$$\frac{d\hat{\sigma}}{d\cos\hat{\Theta}} \sim c_1 \cdot (1+\cos^2\hat{\Theta}) + c_2 \cdot \cos\hat{\Theta}, \tag{5.16}$$

where c_1 and c_2 are constants given by c_V and c_A. The different couplings of W and Z bosons are the reason that differences between W and Z in the rapidity distributions not completely vanish if only looking at sea quark initial states (see figure 5.5).

5.2.5 Summary

In [65] a similar behaviour of $f_n(W)$ and $f_n(Z)$ was found. Looking closer at W and Z events, only small differences were seen. These differences are well understood and can be modeled, they do not apply to the jet structure of the events. Therefore Z+jets events are well adopted to investigate W+jets events.
The ratio R_n is defined as

$$R_n = \frac{f_n(W)}{f_n(Z)} = \frac{\sigma(W + n\,\text{jets})}{\sigma(Z + n\,\text{jets})} \cdot \frac{\sigma(Z_{inc})}{\sigma(W_{inc})} \tag{5.17}$$

The ratio $\frac{\sigma(Z_{inc})}{\sigma(W_{inc})}$ is dominated by $\sigma_{\mathrm{W/Z + 0 \text{ or } 1 \text{ jets}}}$ events and can be calculated or measured with high precision. So a measurement of the ratio R_n leads to

$$\frac{\sigma(W + n\,\mathrm{jets})}{\sigma(Z + n\,\mathrm{jets})} = R_n \cdot \frac{\sigma(W_{inc})}{\sigma(Z_{inc})} \tag{5.18}$$

From the measured ratio R_n the cross section ratio $\frac{\sigma(W+n\,\mathrm{jets})}{\sigma(Z+n\,\mathrm{jets})}$ can be obtained. Differences in selection efficiency and acceptance are included in this ratio. This allows one to measure the number of Z events with n additional jets as tool in order to estimate the number of W events with n additional jets. The similar behaviour of f_n(W) and f_n(Z) and figure 5.2 implies:

$$R_1 \approx R_2 \approx ... \approx R_n \approx \text{constant}. \tag{5.19}$$

The constant behaviour of R_n implies that it is possible to measure the ratio R_n for the 1,2,3 additional jets and extrapolate to the ratio of the fourth jet, which is of interest for top quark analyses. R_4 cannot be measured directly. The event shapes of W + 4 jets and $t\bar{t}$ events are very similar. For this reason W + 4 jets events are background to $t\bar{t}$, but $t\bar{t}$ events are background to W + 4 jets events, too. Hence, in order to measure R_4 the $t\bar{t}$ cross section is be needed, making a $t\bar{t}$ cross section measurement impossible.

The ratio R_n is expected to be quite robust against expected uncertainties, because W and Z events are expected to behave similarily and keep the ratio R_n unchanged. This was already proposed by [76]. The same jet production mechanisms apply for W and Z events, hence very similar jets are expected. Effects due to jet clustering and jet calibration cancel out by calculating the ratio.

A measurement of the cross section ratio R_n is not only interesting for W+jets background determination. The cross section calculations for W/Z+jets production include parton cross sections, PDFs, higher order QCD effects, and factors for the couplings of the different quarks and antiquarks to the W and Z bosons. A precise measurement of R_n helps to test these QCD predictions. W and Z events are well adopted for this purpose, because the production of a W or a Z boson is a well understood and manageable Standard Model process. Such a process can be used to learn more about processes like for example QCD mechanisms to produce associated jets. The production of associated jets is as well understood as the production of a W or Z boson, but the huge number of Feynman diagrams to consider renders the calculation of more than two additional partons in the final state impossible in NLO todate. Because the ratio R_n is expected to be robust against uncertainties, especially in the early days of the LHC this ratio will provide a possibility to test Standard Model predictions soon. In order to compare QCD predictions to the measured values of R_n directly, detector effects, which change the number of measured jets with respect to hadron jets, have to be considered. The measured values have to be corrected for these effects. This will be discussed in chapter 8.

Chapter 6

Event shapes in W and Z events

The method to use Z+jets events as tool to investigate W+jets events is based on the assumption that the event structures of W+jets and Z+jets events are very similar, almost identical. Before describing the measurement of the ratio of jet multiplicities, the behaviour of W and Z events in different variables is compared. The focus is put on variables, where differences or similarities between W and Z events are predicted.

6.1 Event selection

For these comparisons only W $\rightarrow$ eν and Z $\rightarrow$ ee signal events generated with ALPGEN and including full detector simulation with GEANT4 are used (the properties of these samples are given table 7.1). Only simulated signal events are used, in principal no event selection is necessary. However, these studies are performed to prepare the W and Z cross section ratio measurements. Therefore the behaviour of accepted and selected W and Z events is of interest. A W and a Z event selection, as described and discussed in detail in section 7.3, is applied to the Monte Carlo signal events, too. Briefly summarized these cuts are:

- W event selection
  - exactly one isolated electron with $p_T > 25\,\text{GeV}$ and $|\eta| < 2.4$
  - $\not{E}_T > 25\,\text{GeV}$
  - $\text{m}_T(\text{e},\not{E}_T) > 40\,\text{GeV}$
- Z event selection
  - exactly two isolated electrons with $p_T > 25\,\text{GeV}$ and $|\eta| < 2.4$ and oppositely charged
  - $80\,\text{GeV} < \text{m}_{\text{inv}}(\text{e,e}) < 102\,\text{GeV}$

- jets selection (as described in more detail in section 7.3.4)
  - ATLAS Cone ΔR = 0.4, built of calorimeter towers
  - $p_T > 20\,\text{GeV}$ and $|\eta| < 2.5$

In case of some distributions it is interesting to compare the W and Z distributions unaltered by the effects resulting from the detector and the reconstruction. In these cases the properties of W and Z events are compared at generator level without detector simulation. In these cases different event selection cuts are applied. This will be explicitly mentioned at the particular point.

6.2 Expected differences in W and Z events

As mentioned in section 5.2, no perfect agreement of event shapes is expected. There are several issues, which induce differences between W+jets and Z+jets events:

- $m_Z > m_W$ ($\approx 10\%$ difference)
- a different flavour content in the initial state and hence different PDFs
- the different couplings of W bosons and Z bosons to quarks, resulting in an absolute cross section difference of the order of roughly 10

Differences are predicted for the pseudorapidity and p_T distributions of the bosons, of their decay products (the electrons) and for the multiplicity and the p_T of the jets. These distributions are compared to test the predictions and to get a quantitative impression, in which extent differences between W+jets and Z+jets occur.
On the left of figure 6.1 the normalized jet multiplicity distribution is presented for W and Z events. For Z events a slightly higher jet multiplicity is expected. The average jet multiplicities are:

$< N_{\text{jets}} >$ for W events: 0.76

$< N_{\text{jets}} >$ for Z events: 0.80

Dividing the jet multiplicity distribution of W events by the distribution of Z events, deviations of up to 20% occur in the tails.
On the right of figure 6.1 the jet p_T in W and Z events is compared. The average jet p_T in Z events is expected to be higher than in W events, the values are:

$< p_T^{\text{jet}} >$ for W events: 40 GeV

$< p_T^{\text{jet}} >$ for Z events: 42 GeV

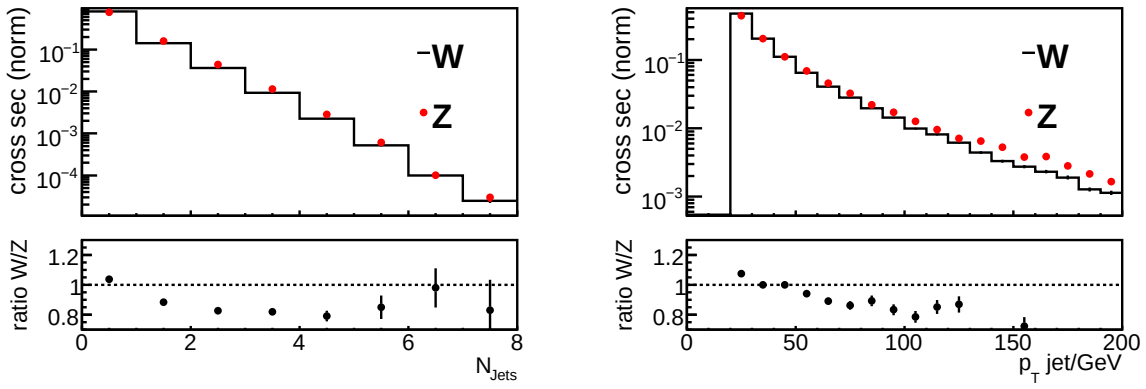

Figure 6.1: The jet multiplicity (left) and p_T (right) of W and Z events as normalized distribution (upper plot) and as ratio W/Z (lower plot). The W/Z+jets events are generated with ALPGEN including detector simulation. All event selection cuts are applied.

Comparing the jet p_T distributions, for jets with a transverse momentum of < 120 GeV the deviations are not bigger than 20% in the tails. Figure 6.2 compares the same distributions separately for each number of jets. Here the differences are always smaller than 20%, too. The biggest difference is found for the leading jet. Hence, the p_T differences are small enough that a measurement of the cross section ratio as a function of the jet multiplicity is possible. The behaviour of jets of different p_T in the detector and during reconstruction differs. The efficiency and accuracy increases with increasing jet p_T. However, as figures 6.1 and 6.2 show, the deviations are small, no big differences are expected. In chapter 8 a closer look on the migration of jets in Z+jets and W+jets events is taken.
Figure 6.3 presents the pseudorapidity distributions and transverse momentum distributions of the true electrons from the boson decays. These plots do not include detector simulation and no event selection cuts are applied. As expected - because of $m_Z > m_W$ - the electron p_T in Z events is higher than in W events. Looking at the pseudorapidity distributions, the e^+ from the W^+ is a bit more boosted than the e^- from the W^- and the electrons from the Z are located in between. A similar behaviour could be already seen in figure 5.4.
Figure 6.4 shows the corresponding distributions of the electron p_T and η after detector simulation and including event selection cuts. The distributions agree with the distributions at generator level. The average electron p_T for W and Z events are:

$$< p_T^{\text{electron}} > \text{for W events: } 38\,\text{GeV}$$

$$< p_T^{\text{electron}} > \text{for Z events: } 42\,\text{GeV}$$

A difference of about 10% in the electron p_T is obtained. This difference is small enough to be neglected in W and Z event selection and it is possible to apply the same electron p_T cut without implying large biases.

The expected differences between W and Z events could be verified. However, the observed differences are small and qualitatively understood.

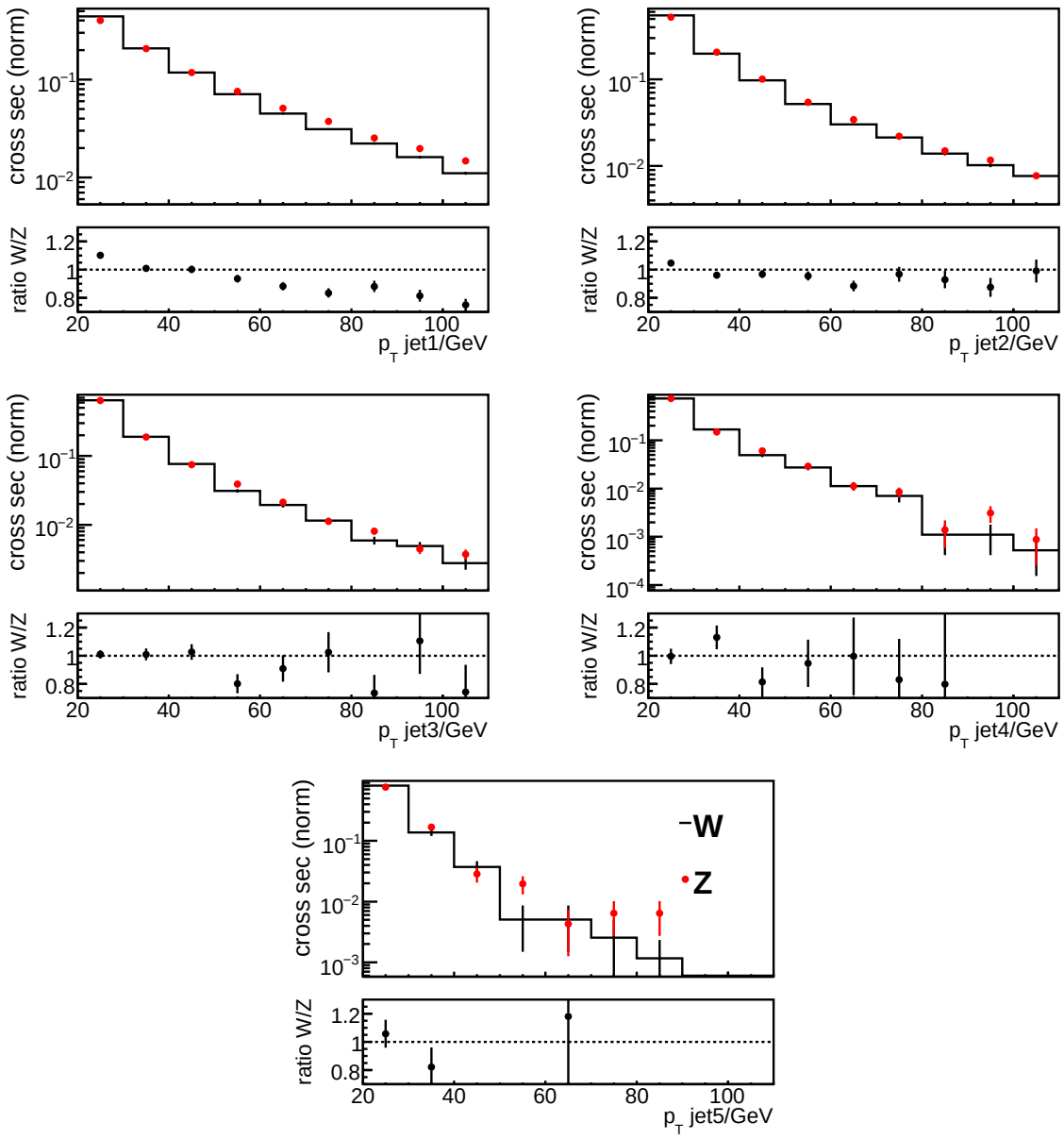

Figure 6.2: The normalized jet transverse momenta distributions and ratios of the distributions for W and Z events after W and Z event selection, generated with ALPGEN and including detector simulation. Presented are the distribution for the leading jet (upper left), the second leading jet (upper right) up to the 5^{th} jet (bottom plot).

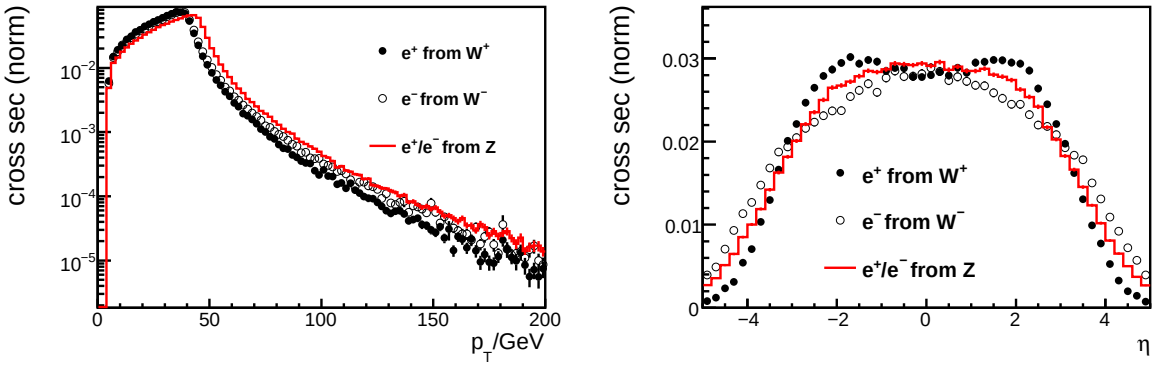

Figure 6.3: The p_T and pseudorapidity distributions of the electrons, classified if originating from the Z, the W^+ and W^-. The samples are generated with ALPGEN without detector simulation and without applying W and Z event selection cuts.

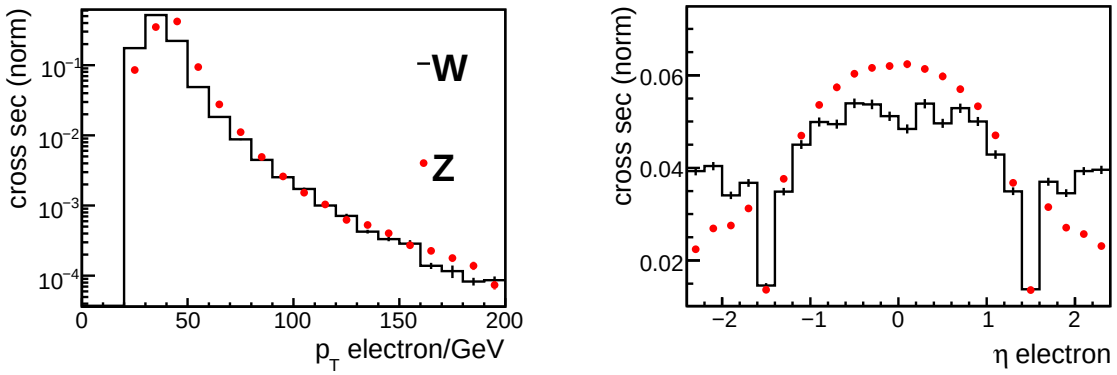

Figure 6.4: The p_T and η distributions of the electrons originating from the W and Z bosons. Plots are generated with ALPGEN, including detector simulation and event selection cuts.

6.3 Similarities of W and Z events

The purpose of this analysis is to investigate W+jets events using the clear event structure of Z+jets events as tool. Here besides the cross section of W+jets production also event properties are of interest.
The behaviour of W+jets and Z+jets events in several event shape variables is compared. Variables are chosen which are insensitive to the masses of the bosons and depend on the distributions of the jets in space, the form of the event and angles between jets. Some of the event shape variables are chosen, which are used in top quark analyses mainly to discriminate $t\bar{t}$ events from the W+jets background. These variables are of special interest, because one aim of the analysis is to improve the estimation of the W+jets background using Z+jets in $t\bar{t}$ analysis. Especially for top quark mass measurements variables are used, which are not explicitly sensitive on the mass of the objects. Hence, these variables are mostly sensitive to the shape of the events and here no differences between W and Z events are expected.
The jets in a $t\bar{t}$ event are part of the hard process as they are the decay products of the top quarks. The jets in W+jets events arise from initial or final state radiation. So differences of the distribution of the jets in space compared to $t\bar{t}$ events are expected. There should be only small differences between W and Z events, because the jet production mechanisms in W and Z do not differ.
The chosen variables are:

- $\Delta\eta_{max}$(jet,jet): The maximum $\Delta\eta$ between two jets in the event. All jets of the event are taken into account.
- centrality: defined as C = $\frac{H_T}{H_E} = \sum_{jets} \frac{E_T\,(jet)}{E\,(jet)}$.
  All jets of the event are taken into account. Of course on the first glance this observable depends on the mass. However, this sensitivity cancels out to some extent by dividing E_T by E.
- circularity and sphericity: based on the normalized quadratic momentum tensor $\mathcal{M}_{ij=jets} = \frac{\sum_k p_i^k p_j^k}{\sum_k |\vec{p^k}|^2}$. All jets of the event are taken into account.
  - circularity = $2\frac{min(\lambda_1,\lambda_2)}{\lambda_1+\lambda_2}$
  - sphericity = $\frac{3}{2}(\lambda_2+\lambda_3)$
    λ_i are the eigenvalues of the tensor, sorted in descending order
- the pseudorapidity distribution of all jets of the event
- the second Fox-Wolfram-Moment, H_2:
  $H_l = \sum_{i,j=jets} \frac{|\vec{p}_i||\vec{p}_j|}{|\vec{p}|^2} P_l(cos\Theta_{ij})$
  with $P_l(cos\Theta_{ij})$ = the l^{th} Legendre polynomial

The variables are presented in figure 6.5. For each variable the upper plot shows the normalized distribution and the lower plot shows the distribution of W events divided

by the distribution of Z events. A very good agreement with most differences being $\leq 10\%$ is revealed. The η distribution reflects the slightly higher jet p_T of Z events, but the difference is smaller than 10%, too. W and Z events look very similar in variables which are sensitive to the jet production mechanisms. Hence, it is possible to estimate W+jets events using Z+jets.
Figure 6.6 shows the same distributions using SHERPA as generator and figure 6.7 using PYTHIA . The prediction for the ratio of jet multiplicities in W and Z events differs for these generators (see figure 7.1; more detailed studies on the model dependence of the simulation of W and Z events and similarities and differences between them are described in [73]), but figure 6.6 and figure 6.7 attest that compatible event structures for W and Z events are predicted by all generators.

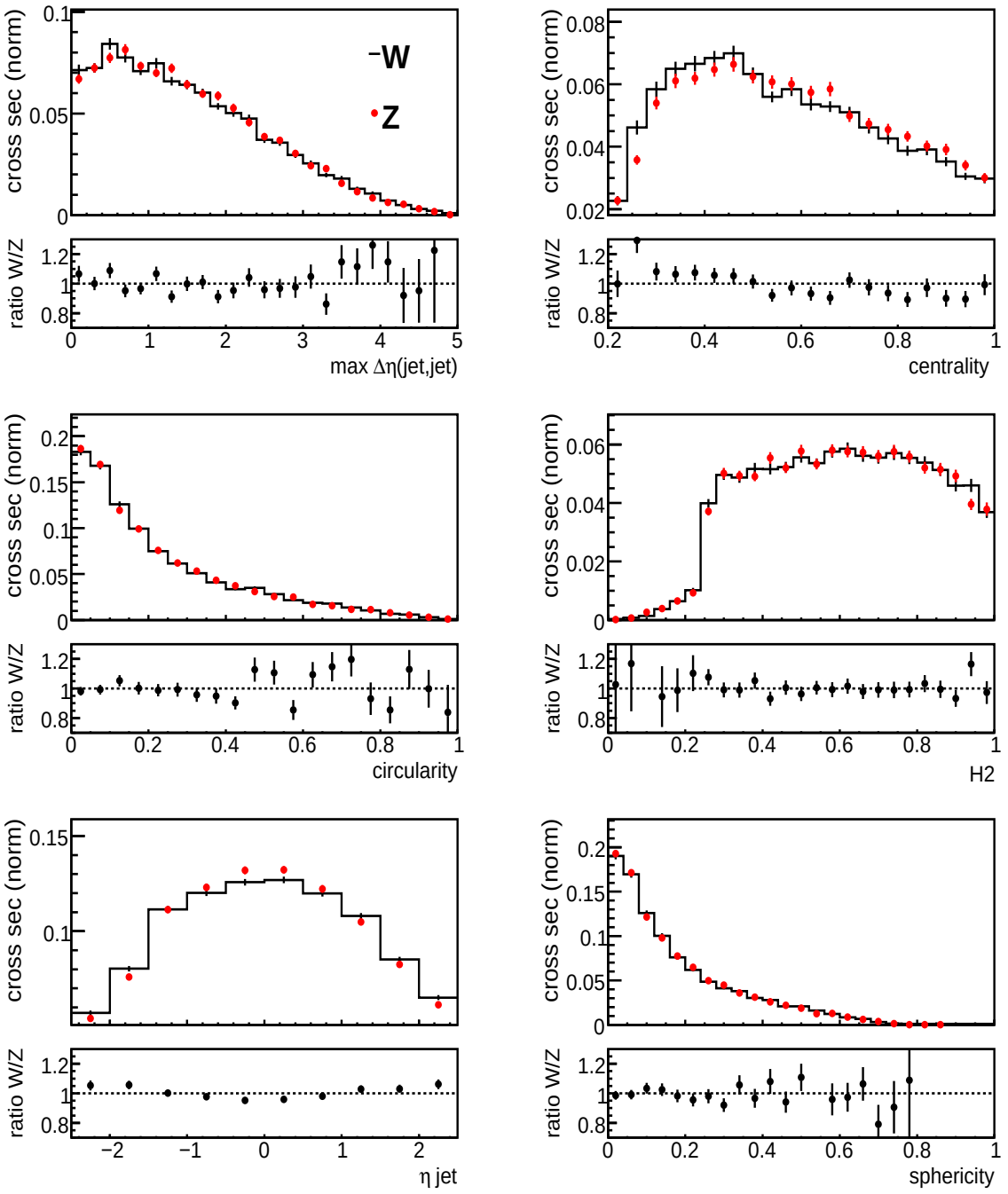

Figure 6.5: Comparison of W and Z events in several variables. As generator ALPGEN is used. Plots include detector simulation and event selection cuts. The deviations between W and Z are within 10%.

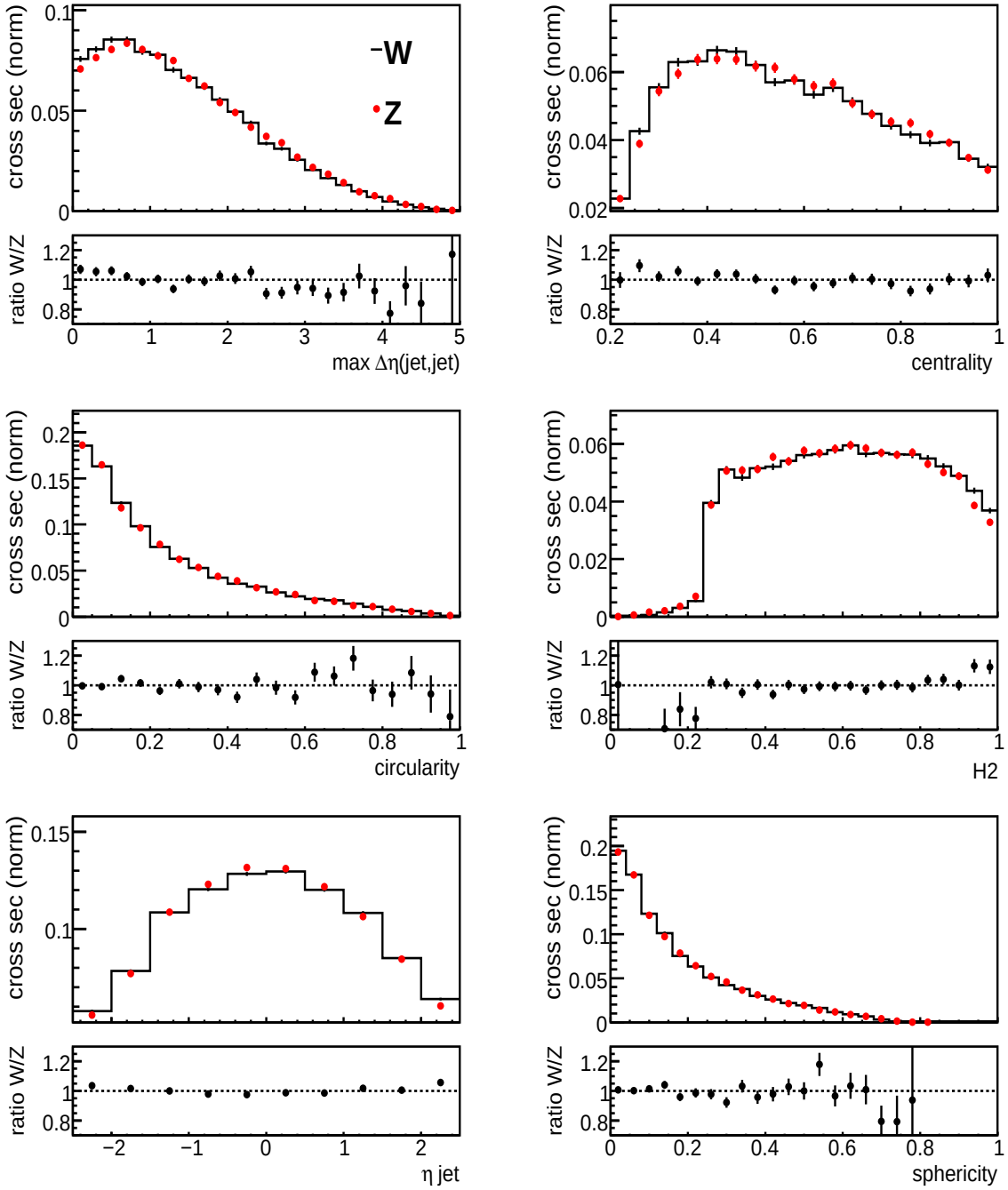

Figure 6.6: Comparison of W and Z events in several variables. As generator SHERPA is used. Plots include detector simulation and event selection cuts. The deviations between W and Z are within 10%.

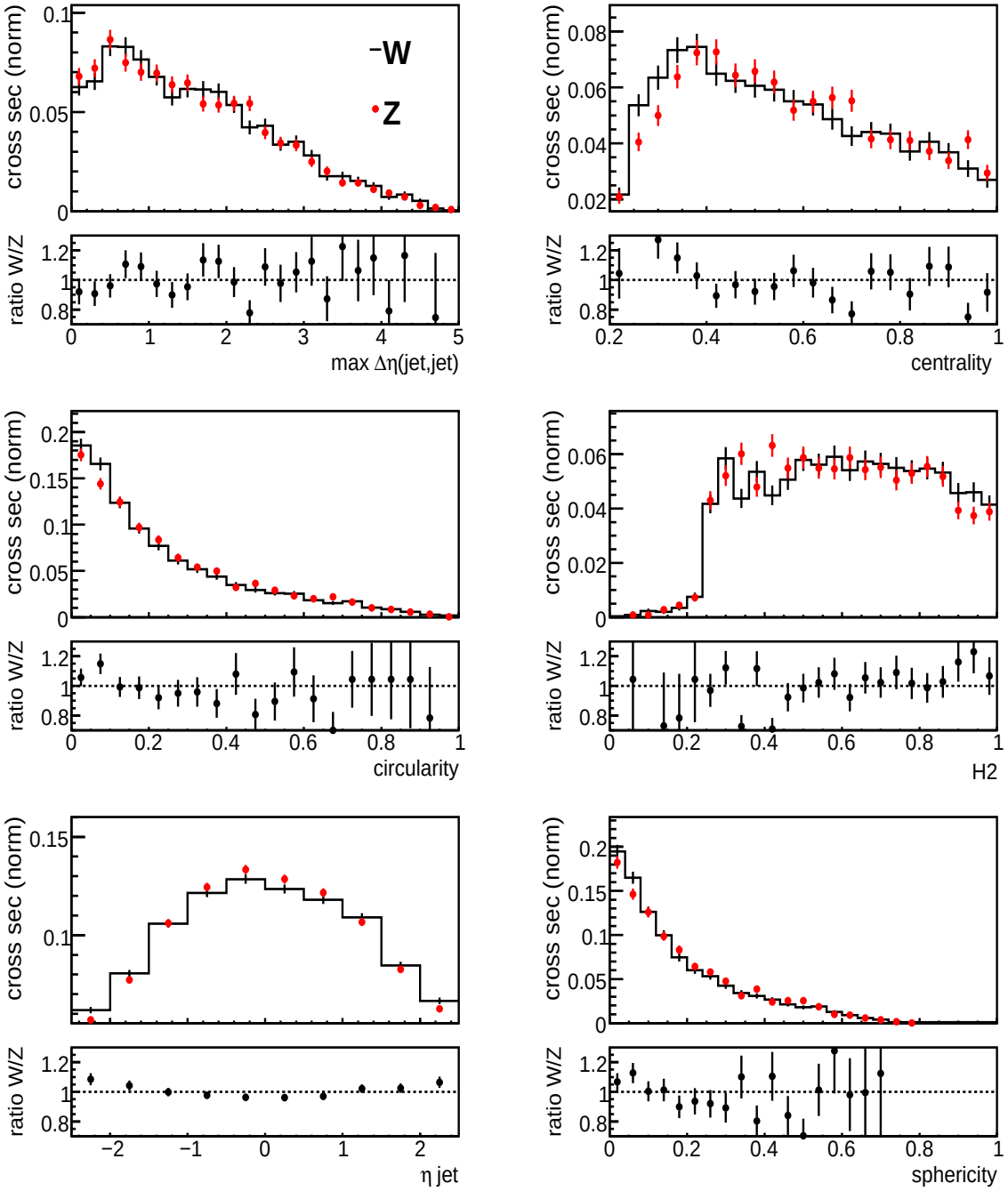

Figure 6.7: Comparison of W and Z events in several variables. As generator PYTHIA is used. Plots include detector simulation and event selection cuts. The deviations between W and Z are within 10%.

6.4 Using Z+jets to estimate W+jets as background for top quark analysis

W+jets events after W event selection and Z+jets events after Z event selection are very similar. The top quark event selection is identical to the W event selection except for a cut on the number of jets. Hence, the W+jets background to $t\bar{t}$ analyses can be estimated using Z+jets events.
Usually the top quark event selection is extended by cuts on several event shape variables in order to improve the $t\bar{t}$ and W+jets separation. Some of these variables are already discussed in the previous section, here no differences between W and Z events are detected. However, often variables are additionally chosen, which use the $\not\!\!E_T$ of the event as input. Here a strategy has to be developed to estimate the corresponding W+jets distribution using Z+jets events.
The chosen procedure is to convert Z+jets events into W+jets events by dropping one of the two electrons and adding its transverse energy (E_x and E_y) to the $\not\!\!E_T = \sqrt{E_x^2 + E_y^2}$ of the event. The electron to be converted is chosen by chance, with equal probability for each electron. Then the W event selection is applied. The expected event numbers for $100\,\mathrm{pb}^{-1}$ are:

- Z events passing Z event selection cuts: 27399.6
- exactly one "tight" electron (after dropping one electron): 24638.4
- $\not\!\!E_T > 25\,\mathrm{GeV}$ (after dropping one electron): 23829.0
- m_T (after dropping one electron): 23695.3

About 86% of the selected Z events pass the W event selection cuts after conversion.

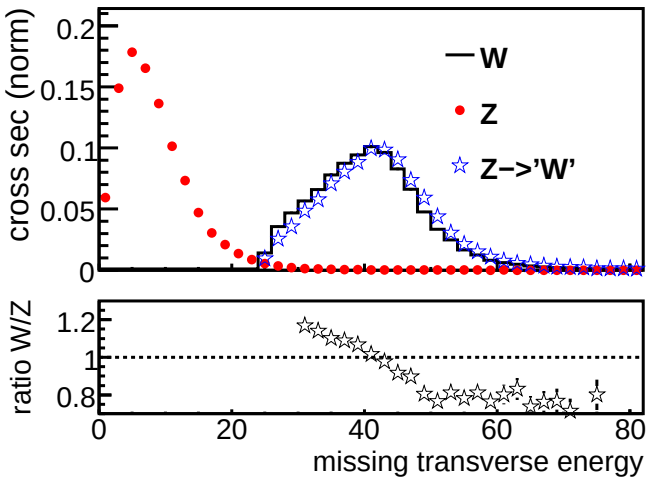

Figure 6.8: $\not\!\!E_T$ for W, Z and converted Z events.

Figure 6.8 presents the $\not\!\!E_T$ distribution for W events, Z events and converted Z events. After conversion the $\not\!\!E_T$ distribution of the Z events is very similar to the $\not\!\!E_T$ distribution of the W events, it is only shifted by a few GeV due to the mass difference between W and Z bosons. If Z+jets events are used to estimate W+jets events and variables depending on $\not\!\!E_T$ are used, this difference has to be taken into account and has to be modeled.
It has to be checked if the event shapes of Z events change by applying the conversion procedure. The jet structure is not changed, but differences can appear because the Z events now have to pass cuts on the $\not\!\!E_T$. Despite the fact that the electron, which is converted to $\not\!\!E_T$, already passed the event selection cuts, the fake $\not\!\!E_T$ of the event can reduce the $\not\!\!E_T$ vector of the event that it does not pass the $\not\!\!E_T$ cuts. This can have an influence also on the event structure.
Figure 6.9 shows the same distributions like figure 6.5, but here also the shapes of the converted Z events are presented. The event structure of Z events is not changed by converting one electron to $\not\!\!E_T$ and applying the W event selection.
Figure 6.10 shows the number of jets distributions for W, Z and converted Z events. The figure reveals that the N_{jets} distributions of W and converted Z events are more similar than the distributions of W and Z events. This can be explained by looking at the Z events lost by applying the conversion procedure. About two thirds of the lost events are lost by requiring "tight" quality for electrons. The remaining lost events do not pass the $\not\!\!E_T > 25$ GeV and $m_T > 40$ GeV cuts even though the electron passed the $p_T > 25$ GeV cut in the Z selection.
The reason is that fake $\not\!\!E_T$ always exists in the events. Figure 6.8 shows the $\not\!\!E_T$ distributions for Z events. The mean $\not\!\!E_T$ for Z events is about 7 GeV although there are no neutrinos in the event. This fake $\not\!\!E_T$ vector can point in the opposite direction of the E_T vector of the electron. So the resulting $\not\!\!E_T$ is reduced and sometimes does not exceed the required amount. This happens for W events, too. If the neutrino and fake $\not\!\!E_T$ point into different directions, the W event can happen not to pass the selection cuts. So by converting a Z event into a W event, the selected W and Z events become more similar.
That this behaviour affects the N_{jets} distribution is proved by figure 6.11. Here the $\not\!\!E_T$ in W events is shown as a function of the number of jets. The fraction of events with small amount of $\not\!\!E_T$ is higher for events with a small number of jets (small p_T of the W boson $\rightarrow$ small p_T of the electron and the neutrino; small p_T of the W boson $\rightarrow$ small p_T of the associated jets). So due to the missing transverse energy cut proportionately more events with a small number of jets are lost than events with a larger number of jets.

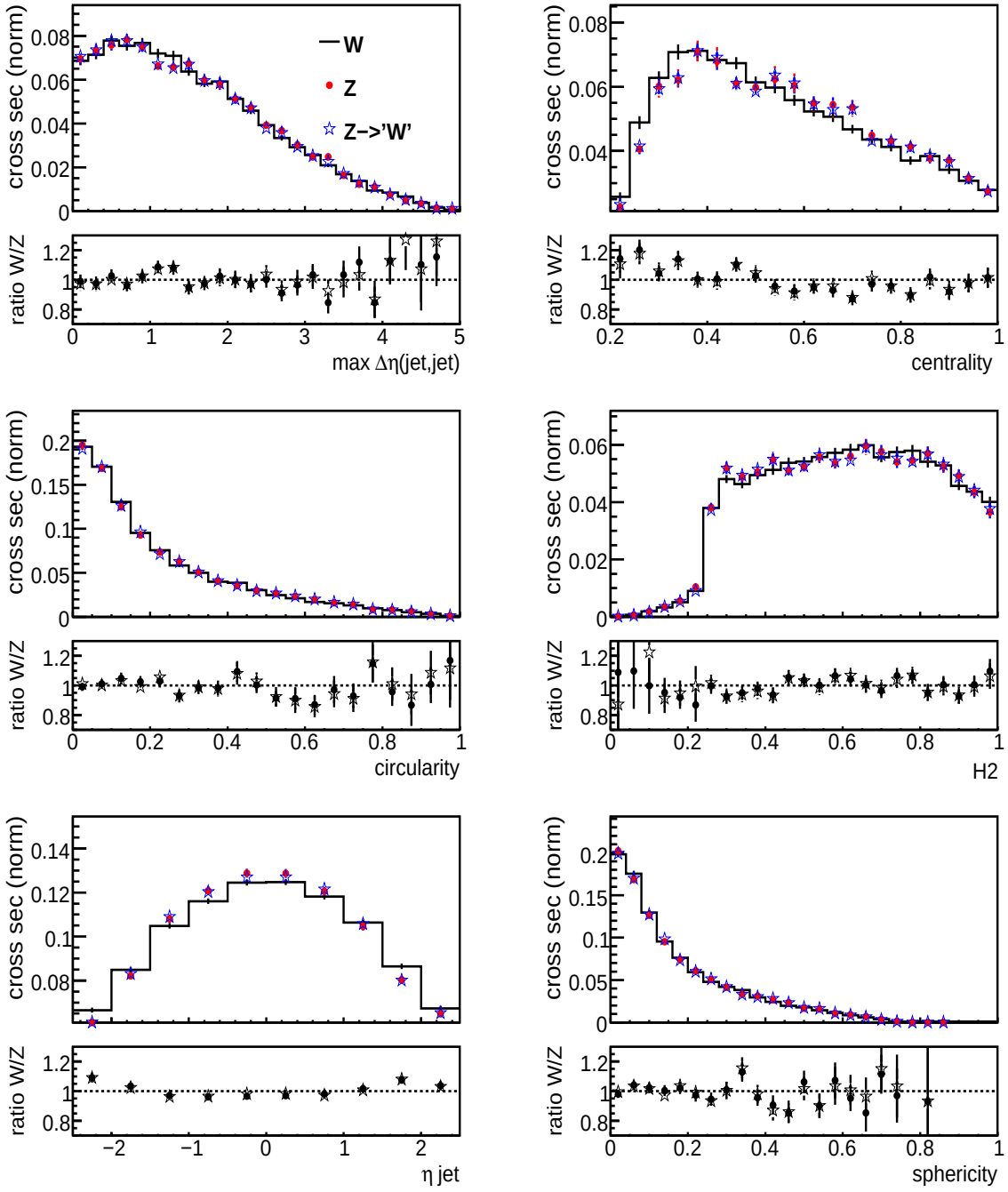

Figure 6.9: Comparison of W and Z events in several variables after dropping one electron. As generator ALPGEN is used. Plots include detector simulation. The deviations between W and Z are within 10%.

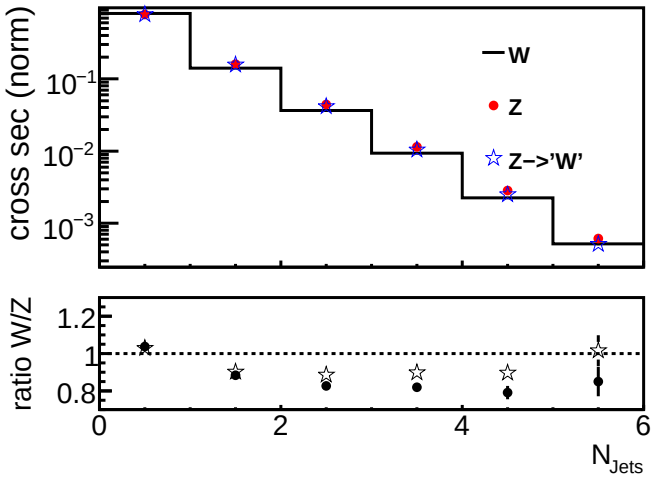

Figure 6.10: The number of jets for W, Z and converted Z events.

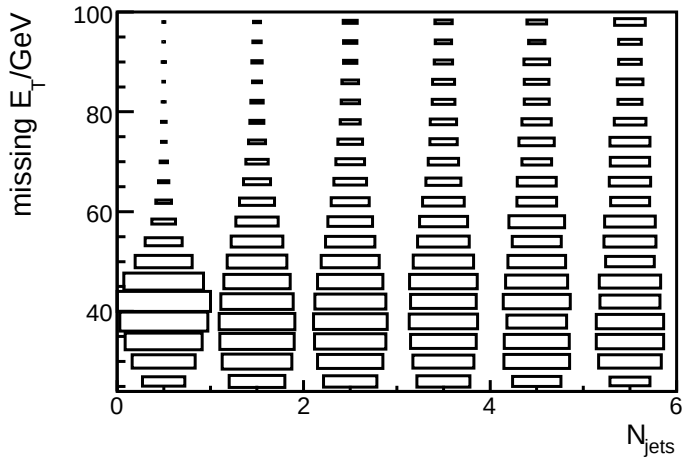

Figure 6.11: The $\not\!\!E_T$ as a function of the number of jets for W events.

6.5 Summary

In this chapter the event shapes of W and Z events are compared. These comparisons refer to the theoretical discussion of W and Z events in section 5.2.
The mass of the Z boson is about 10% higher than the mass of the W boson and the flavour content in the initial state is different for W and Z events. Hence, different PDFs have to considered. These are the main causes for differences between W and Z events. No differences are expected for the QCD effects to produce jets, which take place in association of the vector boson production. The idea to use Z+jets events to estimate jet structure of W+jets events is based on this assumption.
W and Z events look very similar. Even in the distributions, where differences are predicted, these differences are small. These differences are well understood and can be modelled. Hence, Z+jets are well adopted to be used as tool to investigate W+jets events. In addition a method has been tested to convert Z events into W events by converting one of the electron of the Z decay into $\not{E}_T$. After this conversion the $\not{E}_T$ distributions of W+jets events and Z+jets events almost agree. Hence, even the $\not{E}_T$ distribution of W+jets events can be estimated using Z+jets events.

Chapter 7

The ratio W+*n*jets/Z+*n*jets

The production of W and Z bosons in association with jets is an important Standard Model process. Most Standard Model processes like the top quark pair production and also New Physics processes include jets and (the decay products of) a W boson in their final states. So W+jets events are a serious background. The more accurate their cross sections and properties are known, the more precisely Standard Model and possible New Physics processes can be investigated.
Measurements of W+jets and Z+jets production are dominated by systematic uncertainties. They suffer especially from uncertainties in the measurement and definition of jets. The productions of W and Z bosons in association with jets are very similar processes [65], hence by measuring the cross section ratio as a function of the jet multiplicity, many systematic uncertainties cancel out. The measurement of the cross section ratio was already suggested in [76].
Because many uncertainties cancel out, the measurement of the cross section ratio as a function of the jet multiplicity is a fast way to test generator predictions. These are different as presented in figure 7.1. A comparison of the generator predictions to measurements provides an early test of the generators with LHC data.
In this chapter the prospects of a measurement of $R_n = \frac{\sigma(W + n\,\text{jets})}{\sigma(Z + n\,\text{jets})} \cdot \frac{\sigma(Z_{inc})}{\sigma(W_{inc})}$ for n = 0,1,2,3,4,5 are presented assuming an integrated luminosity of $100\,\text{pb}^{-1}$ at a centre-of-mass energy of 10 TeV.

7.1 Strategy of the measurement

The aim of this analysis is to measure the cross section ratio

$$R_n = \frac{\sigma(W + n\,\text{jets})}{\sigma(Z + n\,\text{jets})} \cdot \frac{\sigma(Z_{inc})}{\sigma(W_{inc})} \quad \text{for n = 0, 1, 2, 3, 4, 5.} \tag{7.1}$$

Higher jet multiplicities are neglected. This section briefly summarizes the strategy of the measurement:
As presented in figure 2.7 the total cross section at the LHC is several orders of magnitudes higher than the cross sections for W and Z production. So the first step of the

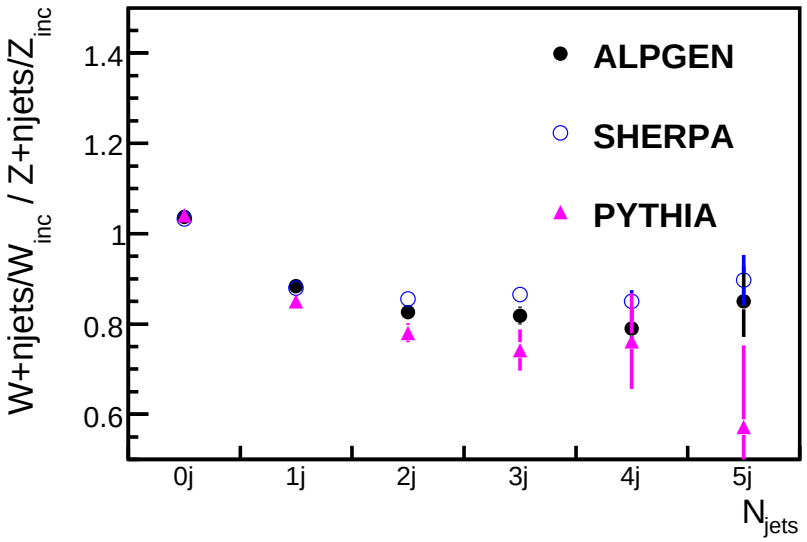

Figure 7.1: Cross section ratio of W and Z production as a function of the jet multiplicity for SHERPA , PYTHIA and ALPGEN after all event selection cuts.

analysis is to filter W+jets and Z+jets events from the multitude of processes taking place.
W and Z events are filtered by selecting only events, which show an event signature compatible with the expected signature of W or Z events. However, these events do not exclusively contain W or Z events. There are many processes, which show a similar event structure and are selected as background events. The W and Z candidate events are split into sub-samples with 0, 1, 2, 3, 4, 5 additional jets. Before calculating the cross section ratio, the signal events have to be separated from the background events. Handling the background contribution for each jet multiplicity separately is advantageous. The dominant backgrounds differ for each jet multiplicity and have to be treated differently.
Then the cross section ratio is calculated as a function of the jet multiplicity. The influence of systematic uncertainties on the results is investigated.
Until now no data are available. The analysis will test the prospects of a measurement using simulated events.

7.2 Data samples

The Monte Carlo data samples, which were used for signal and background events, are summarized in table 7.1 for signal and table 7.2 for background. All samples include detector simulation with GEANT4 and are official ATLAS Monte Carlo data sets (except the fast simulated SHERPA samples).
For the simulated production of the signal events, W+jets and Z+jets, three common event generators are available: PYTHIA , ALPGEN and SHERPA . From these ALP-

GEN is the most common generator for simulating W+jets and Z+jets events. Table 7.1 shows that ALPGEN offers separate samples providing weighted events with parton multiplicities from 0 to 5, resulting in a higher event statistics for high jet multiplicities. Hence, ALPGEN is used as generator to simulate the signal events in this analysis. The SHERPA $W \to e\nu$ and $Z \to ee$ samples in table 7.1, containing 5 million events each, include fast detector simulation with ATLFAST II and are unofficial samples. They will be needed in chapter 8 to calculate a migration matrix with high event statistics.

Process	Matrix element	parton shower	sample Xsec [pb]	k factor	events
$W \to e\nu$	Pythia	Pythia	10343.9	1.5411	401096
$Z \to ee$	Pythia	Pythia	980.5	1.5009	500941
$W \to e\nu$ f	Sherpa	Sherpa	13238.4	1.22	5000000
$Z \to ee$ f	Sherpa	Sherpa	1274.62	1.22	5000000
$W \to e\nu$	Sherpa	Sherpa	13238.4	1.22	800000
$Z \to ee$	Sherpa	Sherpa	1274.62	1.22	800000
$W \to e\nu$ 0p	Alpgen	HerwigJimmy	10184.7	1.22	139842
$W \to e\nu$ 1p	Alpgen	HerwigJimmy	2112.4	1.22	201977
$W \to e\nu$ 2p	Alpgen	HerwigJimmy	676.0	1.22	118309
$W \to e\nu$ 3p	Alpgen	HerwigJimmy	203.3	1.22	171739
$W \to e\nu$ 4p	Alpgen	HerwigJimmy	56.1	1.22	25000
$W \to e\nu$ 5p	Alpgen	HerwigJimmy	16.6	1.22	17492
$Z \to ee$ 0p	Alpgen	HerwigJimmy	898.18	1.22	112475
$Z \to ee$ 1p	Alpgen	HerwigJimmy	206.57	1.22	61767
$Z \to ee$ 2p	Alpgen	HerwigJimmy	72.5	1.22	216945
$Z \to ee$ 3p	Alpgen	HerwigJimmy	21.08	1.22	63412
$Z \to ee$ 4p	Alpgen	HerwigJimmy	6.00	1.22	18314
$Z \to ee$ 5p	Alpgen	HerwigJimmy	1.73	1.22	5500

Table 7.1: Signal Monte Carlo samples used for this study. Shown is the process, the generator used for the matrix element, or the parton shower and the hadronization, the cross section, the k-factor and the number of events generated for the process. The k-factor corrects the expected cross section, the resulting sample cross section then is $\sigma \cdot$ k. f behind the process means that the data set does not include full detector simulation, but fast detector simulation.

Process	Matrix element	parton shower	sample Xsec [pb]	k factor	events
$W \to \tau\nu$ 0p	Alpgen	HerwigJimmy	10178.3	1.22	129644
$W \to \tau\nu$ 1p	Alpgen	HerwigJimmy	2106.9	1.22	60950
$W \to \tau\nu$ 2p	Alpgen	HerwigJimmy	672.8	1.22	12216
$W \to \tau\nu$ 3p	Alpgen	HerwigJimmy	202.7	1.22	22903
$W \to \tau\nu$ 4p	Alpgen	HerwigJimmy	55.3	1.22	12000
$W \to \tau\nu$ 5p	Alpgen	HerwigJimmy	17.0	1.22	3500
$Z \to \tau\tau$ 0p	Alpgen	HerwigJimmy	902.71	1.22	268348
$Z \to \tau\tau$ 1p	Alpgen	HerwigJimmy	209.26	1.22	16178
$Z \to \tau\tau$ 2p	Alpgen	HerwigJimmy	70.16	1.22	209967
$Z \to \tau\tau$ 3p	Alpgen	HerwigJimmy	21.07	1.22	63391
$Z \to \tau\tau$ 4p	Alpgen	HerwigJimmy	6.04	1.22	18300
$Z \to \tau\tau$ 5p	Alpgen	HerwigJimmy	1.71	1.22	5279
$W \to \mu\nu$	Pythia	Pythia	10488.3	1.5411	227009
$Z \to \mu\mu$	Pythia	Pythia	980.3	1.5009	160220
$W \to \tau\nu$	Pythia	Pythia	10246.2	1.	252398
$Z \to \tau\tau$	Pythia	Pythia	1125.05	1.	88682
$t\bar{t}$	MC@NLO	HerwigJimmy	202.86	1.07	231090.0
single top	AcerMC	Pythia	14.41	0.99	9999
$W^+W^- \to e\nu e\nu$	MC@NLO	HerwigJimmy	0.828	1.	3428
$W^+W^- \to e\nu\mu\nu$	MC@NLO	HerwigJimmy	0.828	1.	3462
$W^+W^- \to e\nu\tau\nu$	MC@NLO	HerwigJimmy	0.828	1.	3438
$W^+W^- \to \mu\nu\mu\nu$	MC@NLO	HerwigJimmy	0.828	1.	3271
$W^+W^- \to \mu\nu e\nu$	MC@NLO	HerwigJimmy	0.828	1.	3510
$W^+W^- \to \mu\nu\tau\nu$	MC@NLO	HerwigJimmy	0.828	1.	3532
$W^+W^- \to \tau\nu\tau\nu$	MC@NLO	HerwigJimmy	0.828	1.	3390
$W^+W^- \to \tau\nu e\nu$	MC@NLO	HerwigJimmy	0.828	1.	3269
$W^+W^- \to \tau\nu\mu\nu$	MC@NLO	HerwigJimmy	0.828	1.	3476
$ZZ \to llll$	MC@NLO	HerwigJimmy	0.0406	1.	6726
$ZZ \to ll\nu\nu$	MC@NLO	HerwigJimmy	0.247	1.	6730
$W^+Z \to l\nu ll$	MC@NLO	HerwigJimmy	0.265	1.	3650
$W^-Z \to l\nu ll$	MC@NLO	HerwigJimmy	0.156	1.	3666
Dijet (QCD)	Pythia	Pythia	112584660	1.	10000000

Table 7.2: Background Monte Carlo samples used for this study. Shown is the process, the generator used for the matrix element, or the parton shower and the hadronization, the cross section, the k-factor and the number of events generated for the process. The k-factor corrects the expected cross section, the resulting sample cross section then is $\sigma \cdot k$.

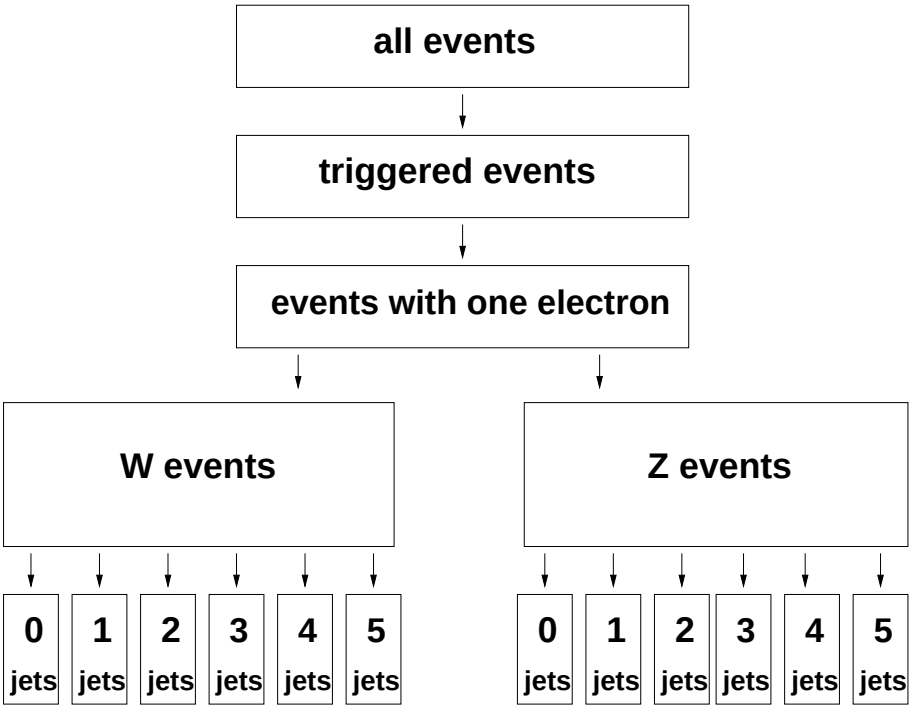

Figure 7.2: Event selection strategy.

7.3 Event selection

The event selection strategy for W + 0,1,2,3,4,5 jet and Z + 0,1,2,3,4,5 jet events is illustrated in figure 7.2. Each step will be described and explained in more detail in the following sections.

7.3.1 Trigger

The ATLAS Trigger System centrally reduces the event rate by picking up and storing only events with signatures defined as interesting for the analyses. Events passing one of these requirements are classified by the relevant property.
$W \rightarrow e\nu$ and $Z \rightarrow ee$ events contain isolated electrons with a transverse momentum of roughly $m_{boson}/2$. Hence, the main triggers to select these events are based on high p_T isolated electrons. For this analysis the "EF_e20_loose" trigger item - triggering events containing at least one isolated electron of "loose"[1] quality, $|\eta| < 2.4$ and $p_T > 20\,\text{GeV}$ - is used. Because both $W \rightarrow e\nu$ and $Z \rightarrow ee$ events are triggered, the trigger uncertainties cancel out in the cross section ratio.
Figure 7.3 shows the trigger efficiencies for W (upper plots) and Z (lower plots) events

[1]The electron quality is explained in section 3.2 and specifies the probability for a reconstructed electron that the detector signature was initiated by a true electron. The electrons are classified by "loose", "medium" and "tight". The quality of an electron increases from "loose" to "tight".

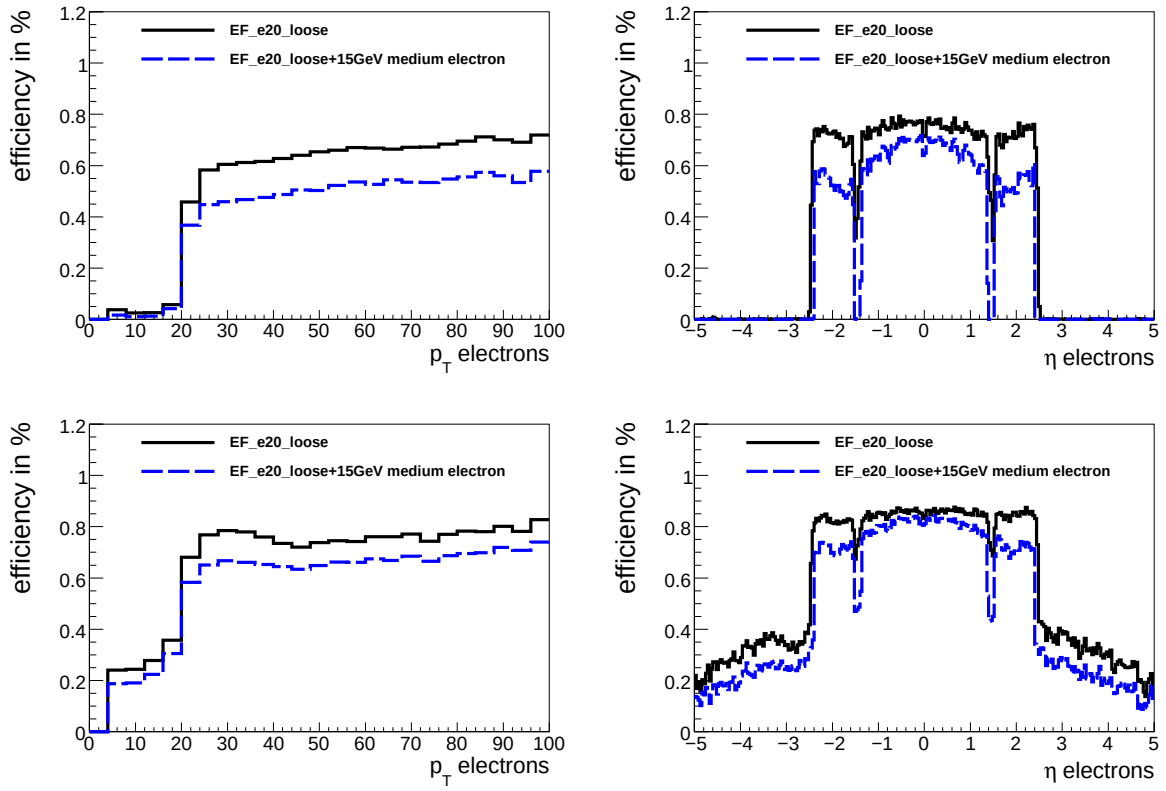

Figure 7.3: Trigger efficiency vs the Monte Carlo truth p_T and η for electrons using the EF_e20_loose trigger for W bosons (upper plots) and Z bosons (lower plots).

as a function of the electron p_T and η. The efficiencies are defined as (x = η, p_T):

$$\epsilon^{\mathrm{x}}_{\mathrm{trigger}} = \frac{\text{x of truth electron if event has been triggered}}{\text{x of truth electron of all events}} \tag{7.2}$$

The total trigger efficiency for Z events is higher than for W events, because in Z events two electrons exist, which increase the probability for an event to be triggered. If one of these two electrons initiates the trigger, the whole event is triggered, which explains the electron efficiency bigger zero in the pseudorapidity region $|\eta| > 2.4$. Here one of the electrons lies inside $|\eta| < 2.4$ and triggered the event. W events only contain one electron. Therefore, the trigger efficiency for electrons with $|\eta| > 2.4$ is zero. Apart from the trigger, which only searches for electrons inside $|\eta| < 2.4$, electrons with $|\eta| > 2.4$ have to be discarded. Only for $|\eta| < 2.4$ the first layer of the electromagnetic calorimeter provides high granularity (see table 2.3) improving the reconstruction.
For $|\eta| < 2.4$ the trigger efficiency is roughly constant for W and Z events. The trigger only uses calorimeter information, however, the electron reconstruction efficiency decreases for higher $|\eta|$, caused by a decreasing tracking efficiency. In regions of higher pseudorapidity more material has to be passed, increasing the probability for bremsstrahlung.
The trigger efficiency and the electron reconstruction efficiency is low for electrons of

$|\eta| \approx 1.7$. This region marks the transition between barrel and end-cap electromagnetic calorimeter and is called calorimeter crack region. In this region of $1.37 < |\eta| < 1.52$ electrons are completely lost or deposit only a fraction of their energy. Electrons near the crack region have to be avoided.
The trigger efficiency increases with increasing electron p_T. The calorimeter signals of electrons with a higher p_T are easier to select than the signals of low p_T electrons. Hence, they are more efficiently recognized and triggered. This behaviour is clearly visible for W events. For Z events the slope of the efficiency distribution as a function of p_T is less evident. A Z event is triggered if at least one of the two electrons initiated the trigger. Clearly the trigger efficiency of about 20% for electrons with $p_T < 20\,\text{GeV}$ is caused by events, where the other electron has triggered. For p_T regions above 40 GeV the efficiency increases with increasing electron p_T and the same behaviour as in W events can be seen.
For both W and Z events the trigger efficiency for electrons with $p_T < 20\,\text{GeV}$ is very low and increases between 20 and 25 GeV. For $p_T > 25\,\text{GeV}$ the trigger efficiency is about 60% for W events and about 80% for Z events. For the W and Z event selection, a p_T cut for electrons of at least 25 GeV has to be chosen.

7.3.2 Selection of W and Z events

After concentrating on events triggered by the "EF_e20_loose" trigger item, the data set only consists of events, which contain at least one electron of "loose" quality and $p_T > 20\,\text{GeV}$ inside $|\eta| < 2.4$. These are events of a large variety of processes, which include at least one electron in their final state or an object, for example a jet, which accidentally triggered the event as electron.
From these events the W and Z events have to be filtered by applying an event selection adopted to the expected W and Z event signature. The chosen event selections are based on [44]. These are modified to be as similar as possible for W and Z events. The measured W to Z ratio should reflect properties of the jet production mechanisms and should not be biased by different event selection requirements. Some differences cannot be avoided:

- The obvious difference between W and Z events is the W decay into an electron-neutrino pair and the Z decay into two electrons. Because electrons and neutrinos are leptons, there is little difference, except for the neutrino, which escapes the detector undetected and can only be measured indirectly by the caused $\not{E}_T$. Electron reconstruction and $\not{E}_T$ reconstruction differ in the efficiencies and uncertainties (see chapter 3). Here differences between W and Z selection cannot be avoided.

- The mass of the Z is about 10% higher than the mass of the W, resulting in a higher average p_T of electrons from the Z decay. This was already shown in chapter 6. However, the electron p_T differences are small and effects from different electron p_T cuts for W and Z events are to be avoided. Hence, the same electron p_T cut is chosen for W and Z event selection.

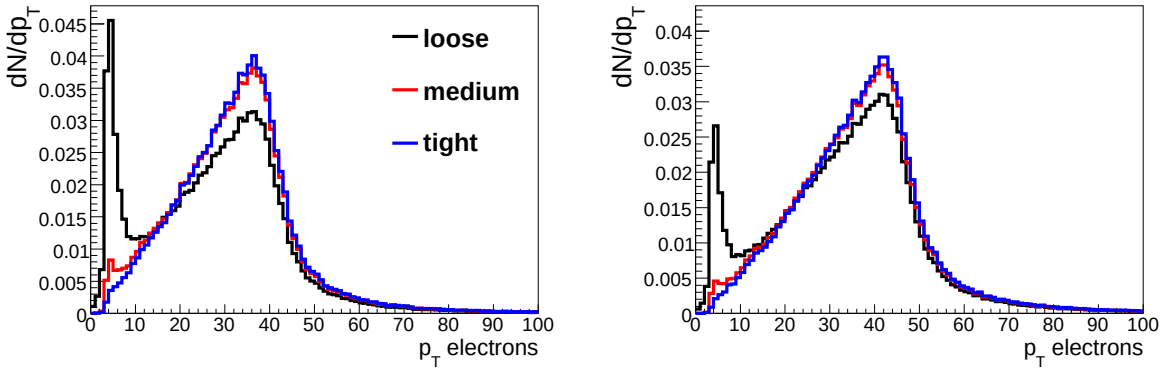

Figure 7.4: p_T distribution for "loose", "medium" and "tight" quality electrons before p_T cuts for W events (left plot) and Z events (right plot).

There are some processes, which show an event signature, which is similar to W or Z events. These processes can pass the event selection cuts and yield background events. The following processes are considered:

- $t\bar{t}$ and single top events
  Top quarks always decay into a W boson, which can decay leptonically. These events then can contain a real $W \rightarrow e\nu$ decay and form an irreducible background.

- diboson events (WW, WZ, ZZ)
  All these events contain isolated electrons and WW and WZ events also contain true $\not{E}_T$.

- W and Z events, decaying into muons and taus
  A τ decay into an electron and two neutrinos is very difficult to distinguish from a direct $W \rightarrow e\nu$ decay. A hadronic τ decay can be misidentified as an electron, because τ leptons initiate narrow jets of low particle multiplicity.

- QCD dijet events
  QCD events do not include high p_T isolated electrons or neutrinos, but each event contains an amount of fake $\not{E}_T$ and b and c quark decays produce neutrinos. Hence, the $\not{E}_T$ can sum up until it exceeds 25 GeV. Jets can be misidentified as electrons. The jet rejection for electron reconstruction is high, but due to the very large cross section of QCD dijet events it is a serious background especially to W events.

In the following the W and Z event signatures are discussed and appropriate event selection cuts are chosen:

- Both W and Z events contain at least one isolated electron with a high p_T of very roughly $m_{\text{boson}}/2$ if fulfilling $|\eta| < 2.4$ (confirmed by figure 7.4 and chapter 6) in the final state. The presence of true electrons provides potential to separate W and Z events from the background events. Hence, the definition of an electron is refined with respect to the object identification described in section 3.2:

  - Figure 7.4 shows the p_T of electrons of "loose", "medium" and "tight" quality, on the left for electrons in W events, on the right for electrons in Z events. It becomes transparent that for "loose" electrons there is a number of electrons with small p_T, which are probably not part of the vector boson decays. For "medium" quality there are only a few low p_T electrons. This suggests that the definition of "loose" electrons is not sufficient. Therefore only electrons with "medium" quality are considered in this analysis. "Medium" electrons also provide a jet rejection, which is about a factor four higher than for "loose" electrons (see table 3.2). A high jet rejection is needed especially to reduce the selection efficiency of QCD dijet background
  - To further increase the rejection against jets, single hadrons reconstructed as electrons and electrons inside jets, the transverse energy inside a cone of $\Delta R = 0.2$ around the electron is required to be smaller than 6 GeV. The electrons from the $W \rightarrow e\nu$ and $Z \rightarrow ee$ decay are isolated. Because electrons produce narrow showers (see section 3.2), they scatter less energy into calorimeter cells around the electromagnetic shower than hadrons or jets.

- A minimal p_T of 25 GeV for electrons is required.
  - The p_T cut has to be well below the average electron p_T, because the selection efficiency for W and Z has to be high.
  - The trigger efficiencies show a good behaviour for electrons with $p_T > 25$ GeV.
  - The p_T cut has to be high enough to reduce the probability for jets, which are misidentified as electrons, to pass the cut.
  - τ leptons, which decay into electrons, always include additional $\not{E}_T$ from the τ neutrino and the electron neutrino, hence the p_T of the electron is lower than the p_T of electrons directly from the W decay. The p_T cut should reject some of these electrons.

- The neutrino in the W decay is treated similar to the electrons, therefore a $\not{E}_T$ cut of $\not{E}_T > 25$ GeV is chosen. A cut on the pseudorapidity of the neutrino is impossible, because the pseudorapidity of the neutrino cannot be determined. The neutrino is expected to carry roughly the same p_T as the electron. Hence, if the neutrino causes $\not{E}_T$ of at least 25 GeV, it is expected to show similar properties like an electron of $p_T > 25$ GeV inside $|\eta| < 2.4$.

- To improve the purity of the selected events, especially with respect to QCD dijet events, the two electrons from the Z decay are required to be oppositely charged and to have an invariant mass comparable to the Z mass.

  The invariant mass of two electrons is defined as:

$$m_{inv} = \sqrt{(E^{e^+} + E^{e^-})^2 - (\vec{p}^{e^+} + \vec{p}^{e^-})^2} \tag{7.3}$$

The invariant mass of the two electrons is required to fulfill $80\,\text{GeV} < m_{inv}(e,e) < 102\,\text{GeV}$. The invariant mass cut on the two electrons rejects most of the background events as it is a tight constraint on the event kinematics (see table 7.4).

- For the W boson similar constraints are defined. Here only the transverse mass defined as:

$$m_T = \sqrt{(E_T^e + E_T^\nu)^2 - (\vec{p}_T^{\,e} + \vec{p}_T^{\,\nu})^2} \tag{7.4}$$

can be determined.

The transverse mass is always smaller than the invariant mass. To not loose too many W events, but to reject as many QCD dijet events as possible, a transverse mass of $m_T > 40\,\text{GeV}$ is required.

- A serious background for $W \rightarrow e\nu$ events are QCD dijet events, with one jet misidentified as electron and fake $\not{E}_T > 25\,\text{GeV}$. The probability that the fake $\not{E}_T$ and the fake electron cause $m_T > 40\,\text{GeV}$ is small. However, due to the high cross section of QCD dijet events still too many QCD dijet events are selected as W events. Hence, the electron is required to fulfill "tight" quality criteria. The jet rejection for "tight" electrons is about a factor ten higher than for "medium" electrons (see table 3.2), reducing the QCD dijet background by about two thirds (see table 7.3). Due to the tight requirements on the event kinematics, the electron quality does not have to be raised to "tight" for Z events.

- By applying these event selection cuts $Z \rightarrow ee$ events with one electron not passing the "medium" quality criteria and fake $\not{E}_T > 25\,\text{GeV}$ are selected as $W \rightarrow e\nu$ events. Hence, all events which include electrons with "loose" or "medium" quality in addition to the "tight" electron are rejected in the W event selection.

- Both W and Z events in the electron decay channel do not include muons. Hence, events containing an isolated muon of $p_T > 20$ GeV inside $|\eta| < 2.4$ are rejected.

7.3.3 W and Z event selection results

Both event selections include the same trigger item and at least one isolated electron of "medium" quality and $p_T > 25\,\text{GeV}$. After these common selection requirements, the data set is split in two selection channels, which are then enriched by W or Z events. The criteria for the leptons (electrons and neutrinos) in both selections are kept as similar as possible. Both selections include a mass requirement. Differences between W and Z events caused by differences in the event selection are kept as small as possible.

Summarized the chosen event selection cuts for $W \rightarrow e\nu$ and $Z \rightarrow ee$ events are:

- $W \rightarrow e\nu$
  - Exactly one isolated electron, "tight" quality, from the $W \rightarrow e\nu$ decay with $p_T > 25\,\text{GeV}$.
  - One neutrino - hence $\not{E}_T$ - from the $W \rightarrow e\nu$ decay with $\not{E}_T > 25\,\text{GeV}$.
  - The transverse mass of the electron-neutrino system has to be $> 40\,\text{GeV}$.
  - The electrons are required to fulfill "tight" quality criteria.
  - Events containing an isolated muon of $p_T > 20$ GeV inside $|\eta| < 2.4$ are rejected.
  - No additional electrons with "loose" or "medium" quality.
- $Z \rightarrow ee$
  - Exactly two isolated electrons, "medium" quality, with opposite charge and $p_T > 25\,\text{GeV}$ from the $Z \rightarrow ee$ decay.
  - The invariant mass of the two electrons is compatible with m_Z: $80\,\text{GeV} < m_{inv} < 102\,\text{GeV}$.
  - Events containing an isolated muon of $p_T > 20$ GeV inside $|\eta| < 2.4$ are rejected.

The event selection results are presented in table 7.3 for W events and in table 7.4 for Z events. The tables also summarize the expected background contributions. The expected event numbers correspond to an integrated luminosity of 100 pb^{-1} and a centre-of-mass energy of 10 TeV. Comparing the selected W and Z events with the expected number of W and Z events following the cross sections in table 5.1, an efficiency of very roughly 50% can be attested.
As expected a clean signal sample with few background events is achieved for the Z boson. Requiring two oppositely charged electrons with an invariant mass compatible to m_Z is a tight constraint reducing the background. However, more than 50% of the Z signal events, which are triggered, are lost by requiring two "medium" electrons of opposite charge, i.e. the statistics of Z events is limited by the electron reconstruction efficiency.
For W events more background events are kept. The dominant background contributions are as expected $t\bar{t}$, $W \rightarrow \tau\nu$ and QCD dijet events. The overall background contribution is small: ~ 2200 $t\bar{t}$,$\sim$ 6600 $W \rightarrow \tau\nu$ and ~ 12000 QCD dijet events compared to ~ 430000 W signal events. The efficiency of the almost irreducible $t\bar{t}$ background is about 10%, of $W \rightarrow \tau\nu$ about 0.4% and of QCD about 10^{-4}%. The chosen event selection cleary suppresses the background, especially the cut flow of QCD events shows that the cuts are well chosen to reject QCD dijet events.

Process	all	trigger +medium e	no muons	one electron tight	E_T^{miss}	m_T > 40 GeV
$W \to e\nu$	1616390.2	533409.6	533402.6	475208.2	432783.3	429540.6
$Z \to ee$	147139.3	80087.6	80086.9	38464.2	812.3	763.8
$t\bar{t}$	21706.0	4233.0	3838.8	3129.5	2694.4	2265.2
$W \to \mu\nu$	1616348.9	242.1	192.2	35.6	35.6	35.6
$Z \to \mu\mu$	147136.6	53.3	17.4	2.8	0.9	0.9
$W \to \tau\nu$	1614426.0	12279.7	12278.0	10380.8	7555.7	6638.2
$Z \to \tau\tau$	147735.9	3059.7	2989.8	2411.5	656.9	401.8
singletop	1426.6	286.1	260.8	214.2	181.8	151.8
WW	745.2	194.1	152.8	113.8	96.9	91.6
WZ	42.1	19.7	12.4	4.8	4.1	3.8
ZZ	28.8	11.2	10.0	4.5	3.8	3.5
QCD	11201441792.0	1443808.0	1442605.9	527753.3	32458.6	12021.7

Table 7.3: Expected number of W candidate events after the different selection steps assuming an integrated luminosity of $100 pb^{-1}$ at a center of mass energy of 10 TeV. For all event numbers N a statistical error of $\sqrt{N}$ is expected.

Process	all	trigger + medium e	no muons	two electrons	m_{inv} $\sim m_Z$
$Z \to ee$	147139.3	80087.6	80086.9	35602.4	27399.6
$W \to e\nu$	1616390.2	533409.6	533402.6	968.0	5.5
$t\bar{t}$	21706.0	4233.0	3838.8	288.1	27.0
$W \to \mu\nu$	1616348.9	242.1	192.2	0.0	0.0
$Z \to \mu\mu$	147136.6	53.3	17.4	0.0	0.0
$W \to \tau\nu$	1614426.0	12279.7	12278.0	44.9	0.0
$Z \to \tau\tau$	147735.9	3059.7	2989.8	92.3	1.4
singletop	1426.6	286.1	260.8	18.4	2.0
WW	745.2	194.1	152.8	24.6	3.5
WZ	42.1	19.7	12.4	4.1	2.7
ZZ	28.8	11.2	10.0	4.2	3.4
QCD	11201441792.0	1443808.0	1442605.9	4808.7	0.0

Table 7.4: Expected number of Z candidate events after the different selection steps assuming an integrated luminosity of $100 pb^{-1}$ at a center of mass energy of 10 TeV. For all event numbers N a statistical error of $\sqrt{N}$ is expected.

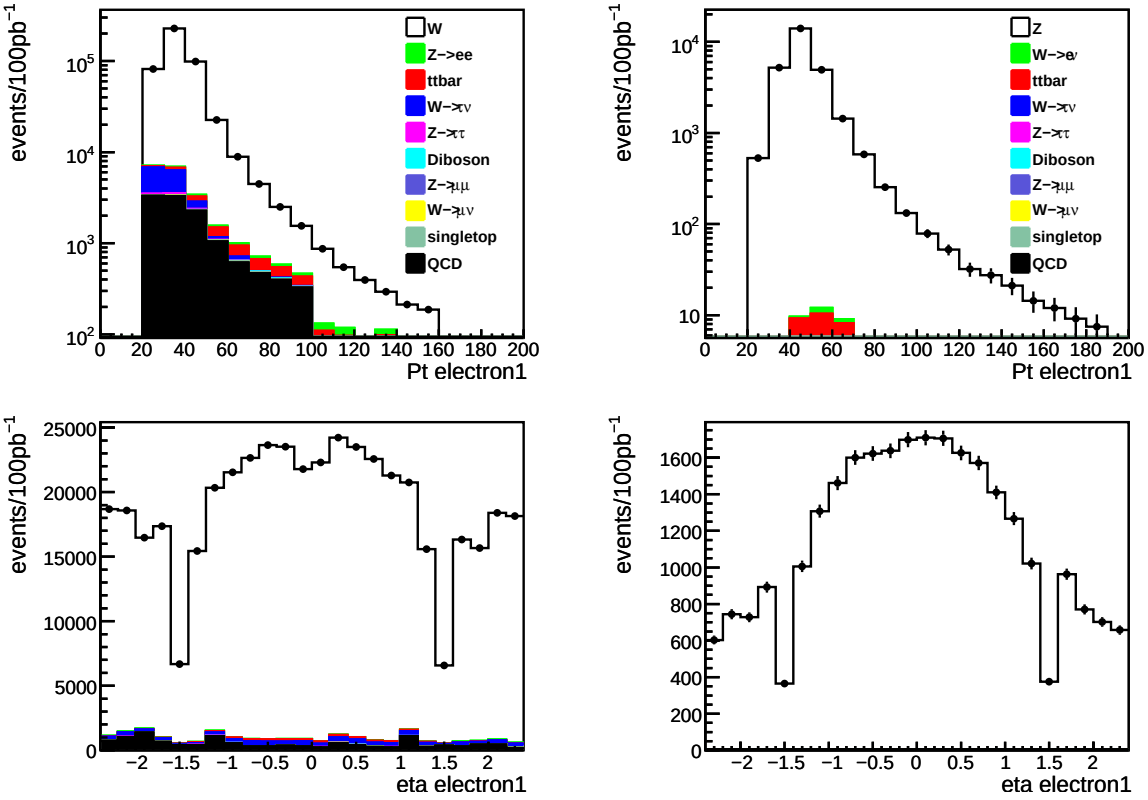

Figure 7.5: p_T (top) and η (bottom) of the leading electron for W (left) and Z (right) candidate events after selection cuts. The statistical errors are calculated by $\sqrt{N}$ and are normalized to the expected number of events assuming an integrated luminosity of $100\,\mathrm{pb}^{-1}$.

Also some $Z \rightarrow ee$ events are selected as $W \rightarrow e\nu$ events. Z events are no serious background to W events, because the cross section for Z production is a factor of ten smaller than for W production. However, these Z events have to be handled more carefully than other background events with a comparable frequency, because the cross section ratio of W and Z events as a function of the jet multiplicity is to be calculated.

At this stage no statement can be made on the influence of the background contribution on the measurement. First the W+jets and Z+jets candidate samples have to be split according to the number of associated jets. Then for each jet multiplicity the background contribution and its influence on the measurement has to be discussed. A high statistics of W+jets events is expected for the low jet multiplicities, a smaller statistic for the high jet multiplicities.

Before performing further analysis steps the simulated data distributions have to be compared to data (as soon as available). Important for these studies are the η and p_T distributions of the electrons, as presented in figures 7.5 and 7.6. Differences in the numbers of expected events or in the shape of the distributions imply mismeasurements of the luminosity or the trigger and reconstruction efficiencies. Also misinterpretations of the detector response or possible background contributions can be traced.

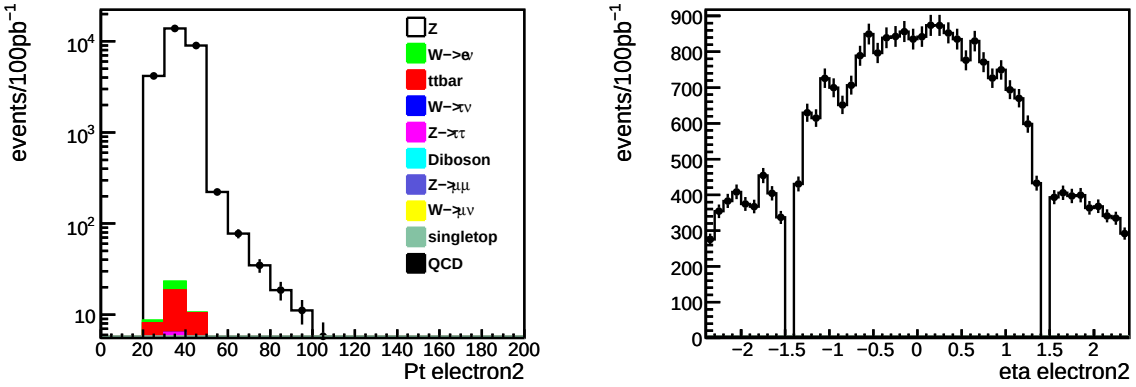

Figure 7.6: p_T (left) and η (right) of second leading electron for Z candidate events after selection cuts. The statistical errors are calculated by $\sqrt{N}$ and are normalized to the expected number of events assuming an integrated luminosity of 100 pb^{-1}.

7.3.4 Jet definition and selection

After applying the W and Z event selection two sets of candidate events are obtained. To determine the cross section ratio of W and Z events as a function of the jet multiplicity both candidate samples have to be split into sub-samples with 0, 1, 2, 3, 4, 5 jets.
To split the event candidates according to the number of jets, first the jets have to be reconstructed and selected. Jets are reconstructed by the ATLAS default jet algorithm, the Cone jet clustering algorithm with $\Delta R = 0.4$, built of calorimeter towers (see section 3.3). All jets are required to be within a pseudorapidity region of $|\eta| < 2.5$. Here a full coverage of the electromagnetic and the hadronic calorimeter is assured.
In ATLAS a minimal p_T of 7 GeV of the clustered jet objects is required. In this analysis jets arising from initial or final state radiation are investigated. The average p_T of these jets is smaller than of the jets from the $t\bar{t}$ decay for example. Hence, the p_T cut has to be lower than the p_T cut in $t\bar{t}$ analyses. In order to avoid too soft processes to be selected a cut on $p_T > 20$ GeV for the jets is chosen. In chapter 6 the average jet p_T of W and Z events (after the $p_T > 20$ GeV cut on the jets) is compared. For W an average p_T of 40 GeV is obtained and for Z of 42 GeV. Due to the mass difference the average p_T of jets in Z events is slightly higher than in W events, but the p_T difference is small and the average p_T value is well above 20 GeV.
Todate jet reconstruction and electron/photon reconstruction are done independently in ATLAS. This leads to a double counting of electrons/photons, because all calorimeter clusters initiated by electrons/photons are reconstructed both as an electron/photon object and as a jet object. To avoid this double counting, the electrons/photons are removed from the jet objects:

- Electron/photon removal: all jet objects within a cone of ΔR=0.4 around reconstructed electrons/photons are removed.

Problems arise if a jet is by chance located closer than ΔR=0.4 to an electromagnetic object. This jet is removed by the overlap removal procedure by mistake. Also electrons

can be completely lost, if they are located inside a jet. The probability for electrons to be closer to a jet increases with jet multiplicity. Figure 7.7 shows the minimal ΔR between an electron and the nearest jet for the different jet multiplicities after overlap removal. The ΔR clearly decreases with increasing jet multiplicity. Hence, the probability to remove true jets in the overlap removal procedure or to loose electrons inside jets is higher for higher jet multiplicities. Therefore the measurement of the cross section ratio as a function of the jet multiplicity is affected. The electron reconstruction efficiency is expected to decrease with increasing jet multiplicity. In [77] first studies concerning the electron reconstruction efficiency as a function of the jet multiplicity are presented. Only small dependencies are observed todate.

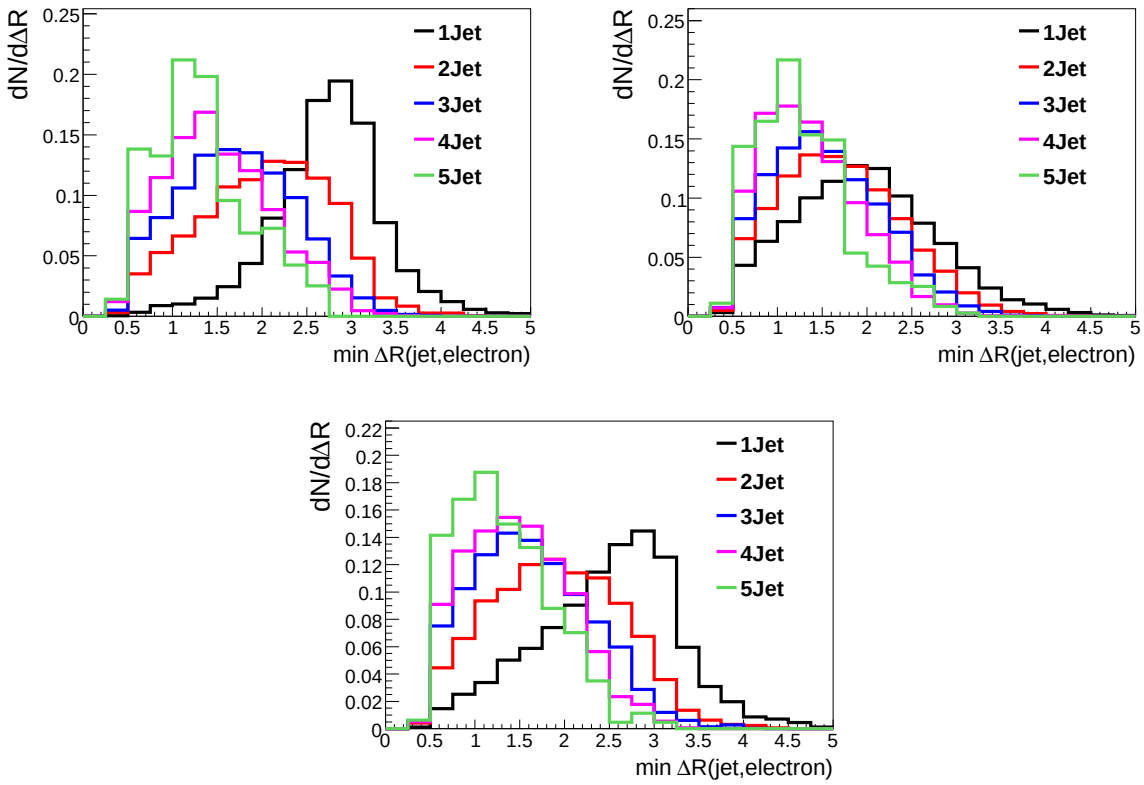

Figure 7.7: Minimum ΔR(jet, leading electron) on the top left and ΔR(jet, second leading electron) on the top right for Z signal events. The bottom plot shows the according distribution for W events. It can be seen that with increasing jet multiplicity the ΔR decreases. This leads to a lower electron reconstruction efficiency if an electrons is lost inside a jet. Or during the overlap removal procedure too many jets are removed.

All jet objects remaining after p_T and η cuts and overlap removal are treated as jets. The expected numbers of W+jets and Z+jets candidate events classified by the number of jets are presented in tables 7.5 (W) and 7.6 (Z). In the next section the selection results are discussed.

Process	0 jets	1 jet	2 jets	3 jets	4 jets	5 jets
$W \rightarrow e\nu$	347648.0	60888.7	15743.5	4017.2	965.7	222.7
$Z \rightarrow ee$	240.4	190.0	176.2	99.6	40.1	12.8
$t\bar{t}$	6.2	81.7	340.8	637.0	647.9	377.8
$W\rightarrow \mu\nu$	21.4	14.2	0.0	0.0	0.0	0.0
$Z\rightarrow \mu\mu$	0.0	0.9	0.0	0.0	0.0	0.0
$W\rightarrow \tau\nu$	5362.8	939.5	254.5	55.1	20.0	5.1
$Z\rightarrow \tau\tau$	281.1	77.1	27.2	11.0	4.0	1.0
singletop	1.3	14.1	45.1	50.2	28.4	9.7
WW	44.9	30.8	11.7	3.3	0.8	0.2
WZ	1.2	1.4	0.8	0.3	0.0	0.0
ZZ	1.3	1.4	0.6	0.1	0.0	0.0
QCD	1799.7	5327.0	2555.5	1295.8	755.9	252.0

Table 7.5: Expected number of W candidates per jet bin for 100pb^{-1} after the selection. For all event numbers N a statistical error of $\sqrt{N}$ is expected.

Process	0 jets	1 jet	2 jets	3 jets	4 jets	5 jets
$Z \rightarrow ee$	21376.5	4396.3	1215.2	313.0	78.0	16.7
$W \rightarrow e\nu$	3.0	2.1	0.1	0.1	0.1	0.0
$t\bar{t}$	0.4	3.4	10.9	7.8	3.2	0.7
$W\rightarrow \mu\nu$	0.0	0.0	0.0	0.0	0.0	0.0
$Z\rightarrow \mu\mu$	0.0	0.0	0.0	0.0	0.0	0.0
$W\rightarrow \tau\nu$	0.0	0.0	0.0	0.0	0.0	0.0
$Z\rightarrow \tau\tau$	1.2	0.0	0.1	0.0	0.0	0.0
singletop	0.1	1.0	0.7	0.1	0.0	0.0
WW	2.2	1.2	0.1	0.0	0.0	0.0
WZ	1.1	1.0	0.4	0.1	0.0	0.0
ZZ	2.3	0.8	0.3	0.1	0.0	0.0
QCD	0.0	0.0	0.0	0.0	0.0	0.0

Table 7.6: Expected number of Z candidates per jet bin for 100pb^{-1} after the selection. For all event numbers N a statistical error of $\sqrt{N}$ is expected.

7.3.5 W+jets and Z+jets event selection results

As expected a very clean Z+jets candidate sample is obtained. The largest background contribution are $t\bar{t}$ events. These are full leptonic $t\bar{t}$ decays, where the charged leptons from the two W bosons mimic the Z mass. Most of the events can be found in the two jet bin. The worst signal to background ratio is found in the five jet bin with roughly 16:1.
For W+jets most background is caused by W bosons decaying to $\tau\nu$, QCD dijet events and semileptonic $t\bar{t}$ events. QCD dijet events are evenly spread over the different jet multiplicities.
$W \rightarrow \tau\nu$ events are mostly found in the low jet multiplicity bins. The cross sections for jet production are the same for $W \rightarrow e\nu$ and $W \rightarrow \tau\nu$ events, hence most $W \rightarrow \tau\nu$ events are accompanied by no or few additional jets. The $W \rightarrow \tau\nu$ background is mostly caused by τ leptons decaying into electrons and partly by τ jets misidentified as electrons. τ´s decaying into electrons are very difficult to separate from direct electrons from the $W \rightarrow e\nu$ decay. The signal to background ratio for the 0 jet bin is approximately 70:1 and for the 1 jet bin 60:1. The $W \rightarrow \tau\nu$ background does not have to be further reduced by applying additional cuts.
The dominant background to W+jets events in the high jet multiplicity bins are semileptonic $t\bar{t}$ events. The signal to background ratio is much lower: in the four jet bin there are ~ 960 W events and ~ 650 $t\bar{t}$ events, in the five jet bin there are more $t\bar{t}$ events (380) than W events (220). An additional reduction of the $t\bar{t}$ background is very difficult, because W and $t\bar{t}$ events show a very similar event structure. The jets in $t\bar{t}$ events have a larger p_T than the jets in W+jets, because these jets are partly decay products of the top quarks. Also the $t\bar{t}$ events are more spherical, because of the high mass of the $t\bar{t}$ system. Additional cuts on the jet p_T and other event shape variables were tested. A performance far better than $\epsilon_W \sim 65\%$ compared to $\epsilon_{t\bar{t}} \sim 30\%$ could not be achieved, because of the similarity of W and $t\bar{t}$ events. These cuts have to be applied to both W and Z events in order not to bias the measurement. Too many W and especially Z events were lost, hence no additional cuts were applied.
The event selection is chosen as similar as possible for W and Z events. However, Z events are selected with almost no background, while the W candidate sample includes a high fraction of background events, especially in the high jet multiplicity bins. Therefore uncertainties in the background normalization affect W events much stronger than Z events and are not expected to cancel out in the cross section ratio measurement. This is investigated in section 7.6.
The simulated data have to be compared to data. Mis-identifications and wrong estimates of efficiencies can be traced using control plots. Of special interest are the p_T and η distributions of the jets. These are shown in figures 7.8 and 7.10 for W events and in figures 7.9 and 7.11 for Z events. The p_T and η distributions of data and simulated events also have to be compared for each jet separately to check, if the simulations reflect the data. Until now no 10 TeV data are available, hence they only give an overview on the expected shape and the signal and background contributions. Only the inclusive distributions are shown.

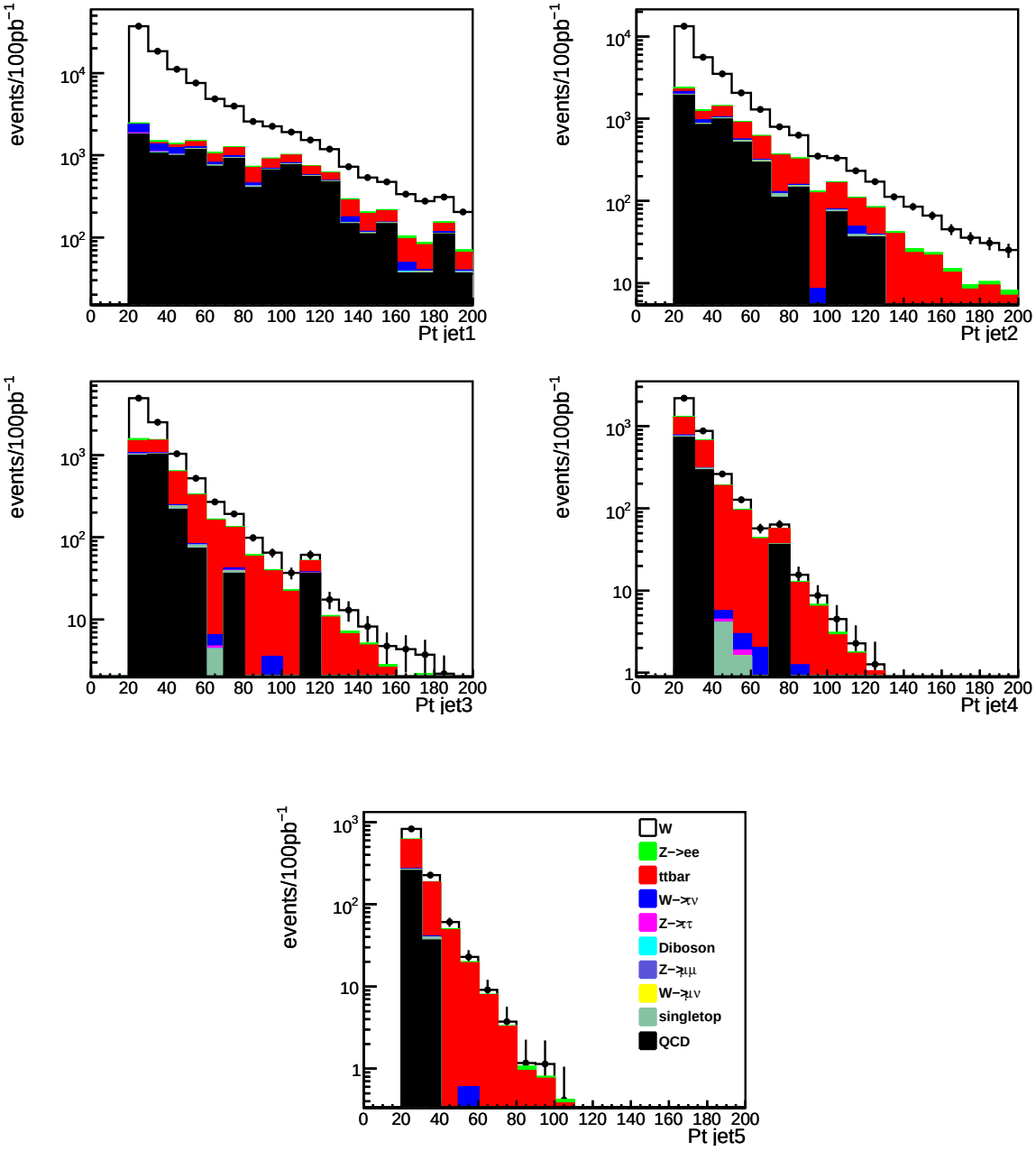

Figure 7.8: Jet p_T for W candidates after all selection cuts. Shown is the highest energetic jet at the top (left), followed by the second highest energetic jet up to the 5th jet. The statistical errors are calculated by $\sqrt{N}$ and are normalized to the expected number of events assuming an integrated luminosity of $100\,\mathrm{pb}^{-1}$.

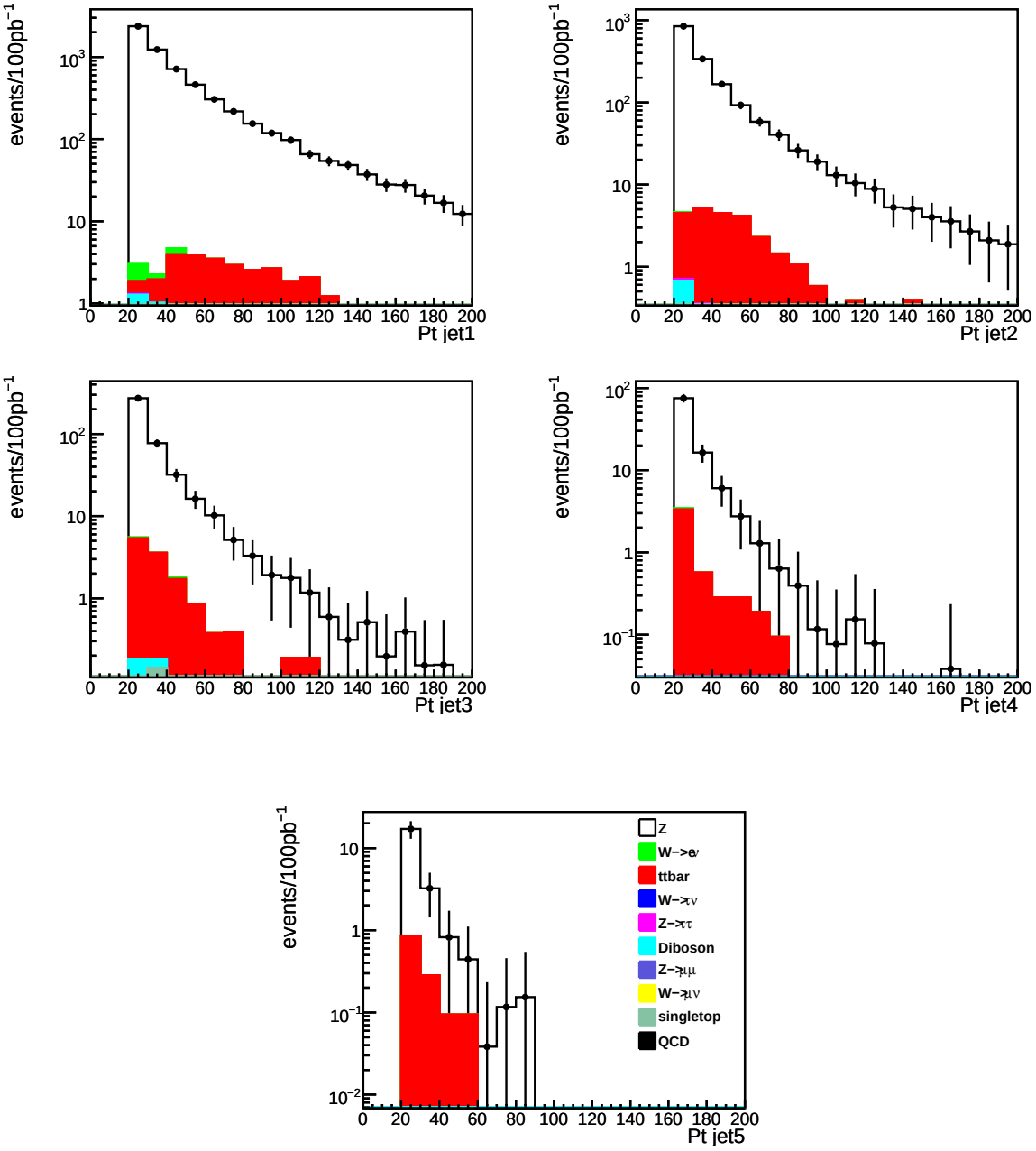

Figure 7.9: Jet p_T for Z candidates after all selection cuts. Shown is the highest energetic jet at the top (left), followed by the second highest energetic jet up to the 5th jet. The statistical errors are calculated by $\sqrt{N}$ and are normalized to the expected number of events assuming an integrated luminosity of $100\,\mathrm{pb}^{-1}$.

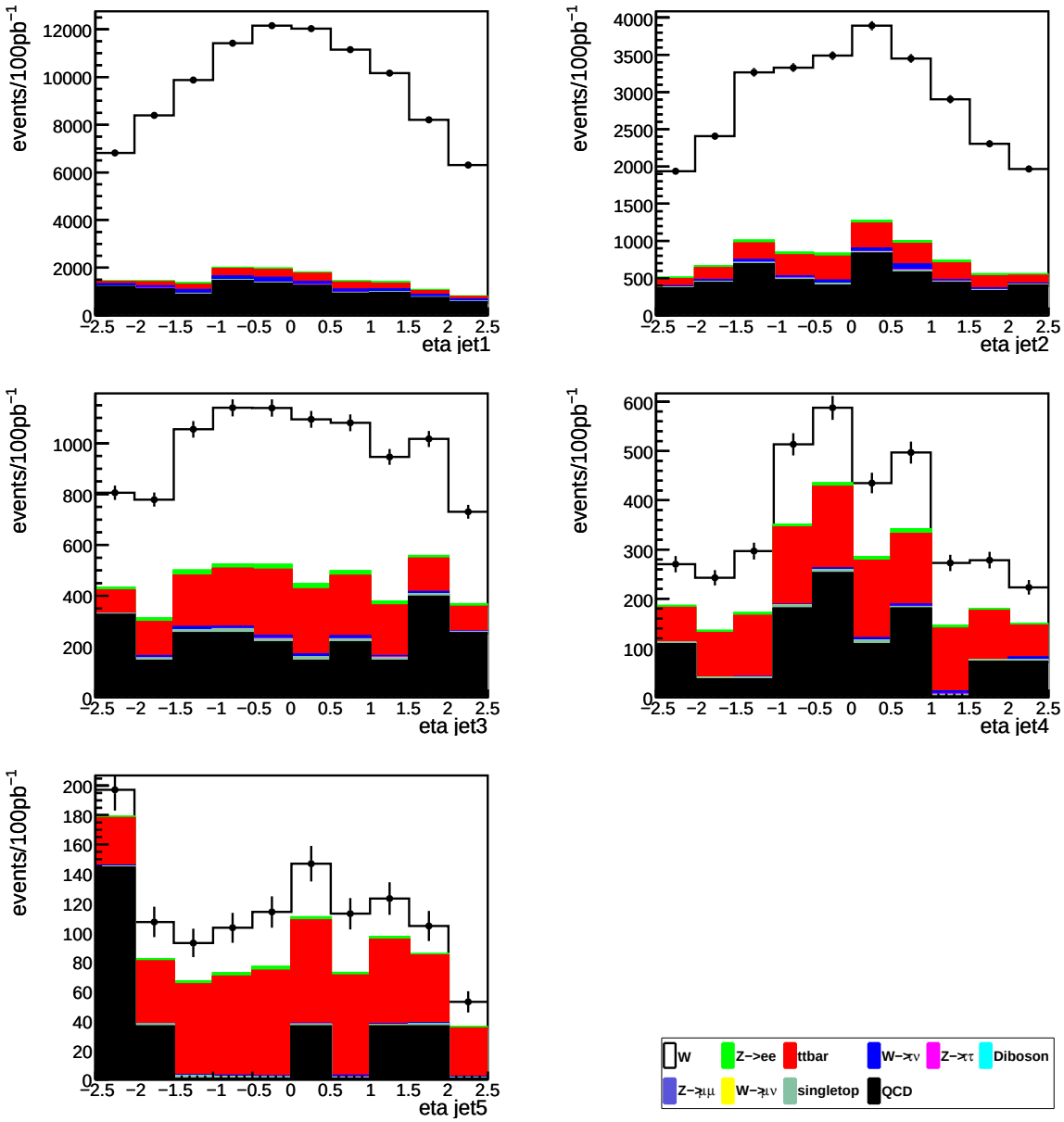

Figure 7.10: Jet η for W candidates after all selection cuts. Shown is the highest energetic jet at the top (left), followed by the second highest energetic jet up to the 5th jet. The statistical errors are calculated by $\sqrt{N}$ and are normalized to the expected number of events assuming an integrated luminosity of $100\,\mathrm{pb}^{-1}$.

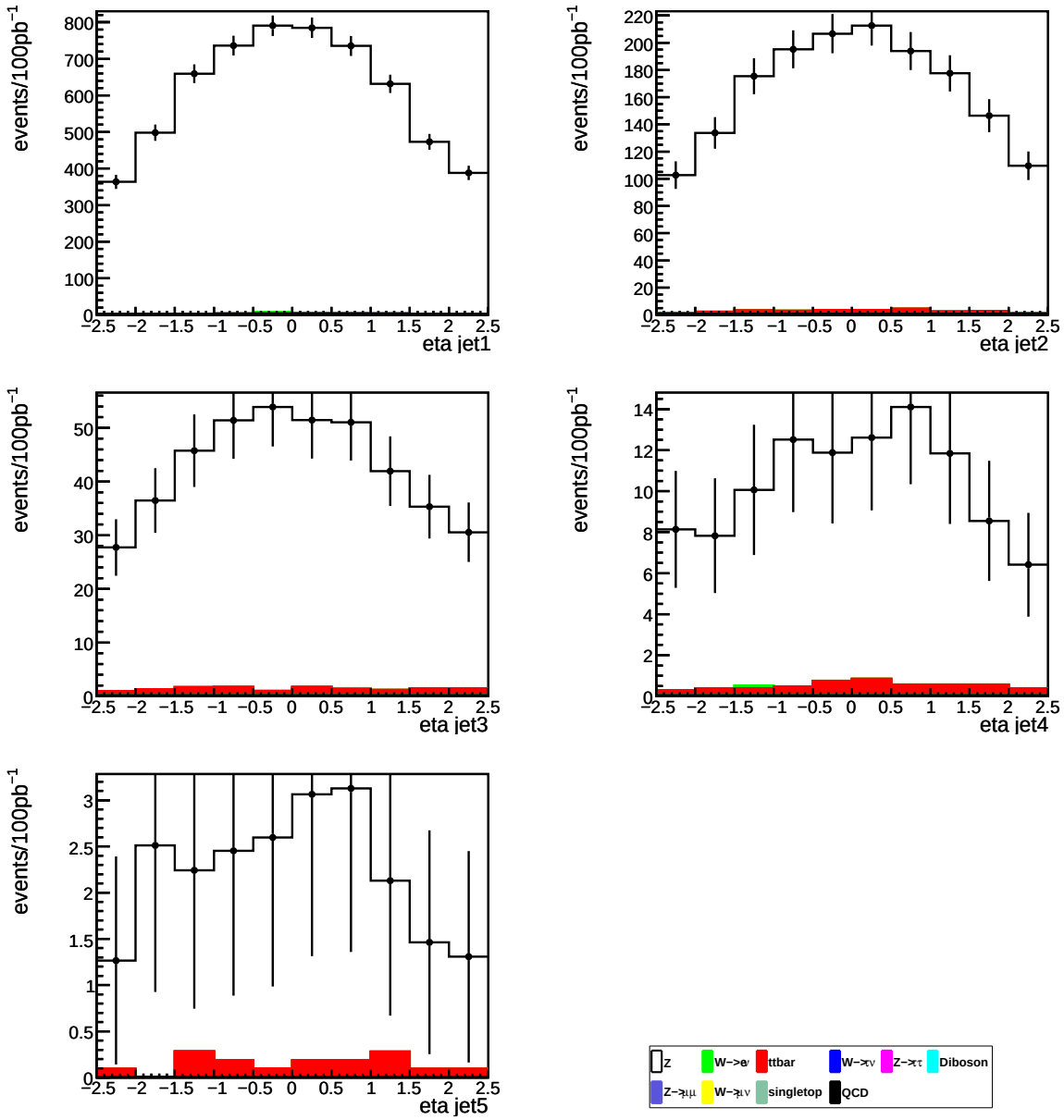

Figure 7.11: Jet η for Z candidates after all selection cuts. Shown is the highest energetic jet at the top (left), followed by the second highest energetic jet up to the 5th jet. The statistical errors are calculated by $\sqrt{N}$ and are normalized to the expected number of events assuming an integrated luminosity of $100\,\mathrm{pb}^{-1}$.

7.3.6 Nomenclature

After splitting the W and Z candidate samples into sub-samples depending on the number of associated jets, numbers of events for each jet multiplicity are obtained. These are referred to as:

$$\vec{N}_{\text{events}}^{\text{W + n jet}} = \begin{pmatrix} N_{\text{events}}(\text{W + 0 jet}) \\ N_{\text{events}}(\text{W + 1 jet}) \\ N_{\text{events}}(\text{W + 2 jet}) \\ N_{\text{events}}(\text{W + 3 jet}) \\ N_{\text{events}}(\text{W + 4 jet}) \\ N_{\text{events}}(\text{W + 5 jet}) \end{pmatrix} \tag{7.5}$$

$$\vec{N}_{\text{events}}^{\text{Z + n jet}} = \begin{pmatrix} N_{\text{events}}(\text{Z + 0 jet}) \\ N_{\text{events}}(\text{Z + 1 jet}) \\ N_{\text{events}}(\text{Z + 2 jet}) \\ N_{\text{events}}(\text{Z + 3 jet}) \\ N_{\text{events}}(\text{Z + 4 jet}) \\ N_{\text{events}}(\text{Z + 5 jet}) \end{pmatrix} \tag{7.6}$$

7.4 Background subtraction

After applying the W and Z event selection, the data sample is reduced to a W candidate and a Z candidate sample. These samples contain both W and Z signal and background events.
The composition of signal and background events for each jet bin is shown in table 7.5 for W events and in table 7.6 for Z events and illustrated in figure 7.12.
The background events (especially for W+jets events) have to be subtracted before calculating the cross section ratio as a function of the jet multiplicity.
The different background contributions can be divided into two classes, whether their behaviour with regard to systematic uncertainties is similar to the signal events or not. In the first the events scale and change similar to the signal events. Hence, the subtraction of these background events is associated with less uncertainties than other background contributions. A similar behaviour is caused by comparable production and decay mechanisms. $W \to e\nu$, $W \to \mu\nu$ and $W \to \tau\nu$ (similarly for $Z \to ee$, $Z \to \mu\mu$ and $Z \to \tau\tau$ events) events only differ by the decay channel of the W boson. The jets in all these events are initiated by the same mechanisms. These events scale in the same way if, for example, the jet energy measurement is biased. If the jet structure of the events is investigated, it is expected that the ratios of selected $W \to e\nu$ events to $W \to \mu\nu$ events and to $W \to \tau\nu$ events do not change. This class of background is mostly found in the low jet multiplicity bins (0, 1, 2 additional jets) and conveniently corrected by a constant multiplicative factor. Because of a high signal to background ratio with a well-behaving background the systematic uncertainties in the low jet multiplicity bins are expected to be small.

All other sources of background events - which are mostly $t\bar{t}$ and QCD dijet events - are corrected additive. The production mechanisms of these events are described by Feynman diagrams, which are different to the diagrams included in the W+jets production.
$t\bar{t}$ and W+jets events have in common the leptonic decay of the W boson, complicating the separation of W+jets and $t\bar{t}$ events. The production mechanisms of the W bosons are very different, in $t\bar{t}$ events the W boson is a decay product of the top quark. The jet production differs, too. Some of the jets in $t\bar{t}$ events are decay products of the $t\bar{t}$ pair. QCD dijet events are selected as W+jets or Z+jets events, because jets are misidentified as electrons. These events show a different behaviour compared to the signal events.
The expected numbers of QCD and $t\bar{t}$ events are subtracted from the number of W or Z candidate events. The $t\bar{t}$ background is mostly found in the W candidate samples with 3, 4 and 5 additional jets. Because of a disadvantageous signal to background ratio a large influence of the background contribution on the systematic uncertainties is expected. The effects are investigated in section 7.6.
The following sections describe how the two classes of backgrounds - additive and multiplicative - are treated.

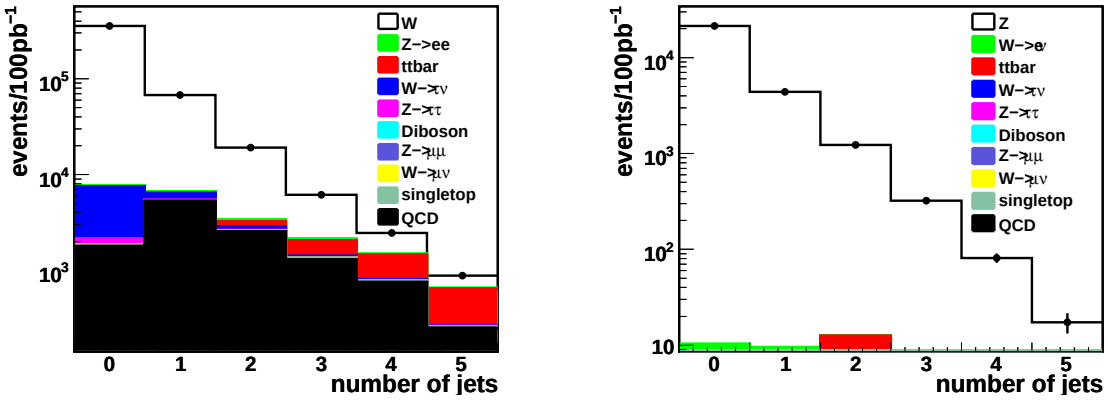

Figure 7.12: Number of jets distribution for W candidates (left) and Z candidates (right) after all event selection cuts.

7.4.1 Additive background (mostly QCD and $t\bar{t}$)

The additive background contribution is calculated by summing up the numbers of expected additive background events for each jet bin. These numbers are subtracted from the W and Z candidate samples.

$$\vec{N}_{\text{events}}^{\text{W/Z + n jet candidates: signal+mult.}} = \vec{N}_{\text{events}}^{\text{W/Z + n jet candidates}} - \vec{N}_{\text{events}}^{\text{W/Z + n jet add background}} \quad (7.7)$$

The number of additive background events for W and Z is presented in table 7.7.

N_{jets}	signal W	background W	signal Z	background Z
0	347648.0	2376.0 ± 18.5	21376.5	9.1 ± 1.9
1	60888.7	5724.5 ± 12.6	4396.3	9.5 ± 1.3
2	15743.5	3158.0 ± 10.1	1215.2	12.6 ± 1.2
3	4017.2	2097.3 ± 10.1	313.0	8.3 ± 1.0
4	965.7	1477.1 ± 9.5	78.0	3.3 ± 0.6
5	222.7	653.4 ± 7.1	16.7	0.6 ± 0.3

Table 7.7: Number of additive (mostly QCD and $t\bar{t}$) background events for W (left) and Z (right) candidate sample after the selection in the 0 to 5 jet sample. The statistical error of the background contributions corresponds to available number of simulated events (see tables 7.1 and 7.2) and is not normalized to a luminosity of $100 pb^{-1}$.

The error ΔN is the statistical error obtained from the number of simulated events. This error is usually smaller than $\sqrt{N}$, because the available statistics of simulated events is higher than the expected data statistics.

7.4.2 Multiplicative background (W/Z $\rightarrow$ el,μl, τl)

The signal fractions of the multiplicative background contributions are defined as

$$f^{\text{n jets}}_{\text{boson signal}} = \frac{N^{\text{boson} \rightarrow \text{el + n jets after event selection}}_{\text{events}}}{N^{\text{boson} \rightarrow \text{el + } \mu\text{l + } \tau\text{l + n jets after event selection}}_{\text{events}}} \tag{7.8}$$

$$l = \begin{cases} \nu & \text{boson = W} \\ e, \mu, \tau & \text{boson = Z} \end{cases}$$

The error of $f^{\text{n jets}}_{\text{W/Z signal}}$ is determined by binomial statistics:

$$\Delta f^{\text{n jets}}_{\text{W/Z signal}} = \frac{1}{\sqrt{N^{\text{W/Z + n jets before selection}}_{\text{events}}}} \sqrt{f^{\text{n jets}}_{\text{W/Z signal}} (1 - f^{\text{n jets}}_{\text{W/Z signal}})} \tag{7.9}$$

After subtracting the additive background contributions the number of events of each jet multiplicity is multiplied by the appropriate signal fraction:

$$N^{\text{n jets}}_{\text{W/Z signal}} = N^{\text{n jets}}_{\text{W/Z candidates:signal+mult.bg}} \cdot f^{\text{n jets}}_{\text{W/Z signal}} \tag{7.10}$$

The signal fractions are listed in table 7.8. The errors of the signal fraction are caused by the statistical errors of the simulated events. The signal fraction is always larger than 97%. So this analysis would not gain from a deeper investigation of this background.

N_{jets}	signal in W candidates in %	signal in Z candidates in %
0	98.47	99.99
1	98.46	100.00
2	98.41	99.99
3	98.65	100.00
4	97.97	100.00
5	97.75	100.00

Table 7.8: Fractions of signal in the $W \to e\nu$ (left) and $Z \to ee$ (right) candidate sample with respect to all simulated $W \to l\nu$ and $Z \to ll$ events (see tables 7.1 and 7.2) after the selection in the 0 to 5 jet sample. The expected statistical errors are smaller than 0.1%.

7.5 Ratio measurement

The ratio $R_n = \frac{\sigma(W + n\,\text{jets})}{\sigma(Z + n\,\text{jets})} \cdot \frac{\sigma(Z_{inc})}{\sigma(W_{inc})}$ is measured performing the following steps:

1. Trigger and select W and Z events. Two candidate samples, $N_{events}^{W\,candidates}$ and $N_{events}^{Z\,candidates}$, are obtained. Both samples are split into sub-samples according to the jet multiplicity (0, 1, 2, 3, 4, 5 jets): $\vec{N}_{events}^{W + n\,jet\,candidates}$ and $\vec{N}_{events}^{Z + n\,jet\,candidates}$.

2. The additive background contribution is subtracted, then the remaining events for each jet multiplicity are multiplied with the expected signal fraction, leading to $\vec{N}_{events}^{W + n\,jet}$ and $\vec{N}_{events}^{Z + n\,jet}$.

   The W+jets and Z+jets candidate samples contain both signal and background events. The statistical error is $\sqrt{N_{events}^{signal+background}}$ for each jet bin. The statistical errors of the expected background contributions in tables 7.7 and 7.8 are caused by the statistics of the simulated events, which is higher than the expected data statistics. To avoid double counting of the statistical errors, the subtracted number of additive background events and the signal fractions are taken without errors. The uncertainty of the background cross sections is considered as systematic uncertainty and treated separately.

3. The cross section ratio as a function of the jet multiplicity is calculated:

$$R_n = \frac{N_{events}^{W + n\,jet}}{\sum_{m=0}^{5} N_{events}^{W + m\,jet}} \Big/ \frac{N_{events}^{Z + n\,jet}}{\sum_{m=0}^{5} N_{events}^{Z + m\,jet}} \tag{7.11}$$

   The error of R_n is determined by error propagation.

N_{Jets}	W	rel. stat. error	Z	rel. stat. error	R_n	rel. stat. error
0	347648.0 ± 596.2	0.00	21376.5 ± 146.2	0.01	1.04 ± 0.01	0.01
1	60888.7 ± 259.9	0.00	4396.3 ± 66.4	0.02	0.88 ± 0.01	0.02
2	15743.5 ± 138.4	0.01	1215.2 ± 35.0	0.03	0.83 ± 0.02	0.03
3	4017.2 ± 78.6	0.02	313.0 ± 17.9	0.05	0.82 ± 0.05	0.06
4	965.7 ± 49.6	0.05	78.0 ± 9.0	0.12	0.79 ± 0.10	0.13
5	222.7 ± 29.7	0.13	16.7 ± 4.2	0.25	0.85 ± 0.24	0.28

Table 7.9: Shown are the total numbers of events for W and Z, the ratio R_n and the relative statistical errors after event selection and background subtraction for jet multiplicities from 0 to 5 jets.

7.5.1 Statistical results

The results with the statistical errors of the measurement are presented in table 7.9. The ratio for zero jets can be measured with a relative precision of 1%, for 4 jets with a relative precision of 13% and for 5 jets of 28%. The precision is limited by the number of Z events. The statistical error of the measurement decreases when assuming a higher integrated luminosity L by a factor of $\sqrt{\frac{100\text{pb}^{-1}}{\text{L}}}$. However, the measurement is also affected by systematic uncertainties, which do not, at first instance, scale with the statistics of data. The effect of these uncertainties on the precision of the measurement is investigated in the next section.

7.6 Systematic uncertainties

The results of a measurement are affected also by systematic uncertainties caused by imperfectly controlled estimates impacting the whole measurement. These estimates are for example mismeasurements of jet energies or wrong cross section estimates of the background. The influence of these uncertainties on the results is tested in this section.
If the used models of event generator and detector simulation do not exactly represent the data, problems occur when cuts are applied on event variables. In this analysis cuts are applied on the jet energy, the electron energy, the $\not{E}_T$ and the selected background events. Uncertainties in these variables are expected to influence the analysis and will be discussed.
In [76] it is already suggested to replace the measurements of the W + n jets and Z + n jets cross sections by measurements of the cross section ratio W + n jets/Z + n jets. Measurements of W/Z + n jets separately are dominated by uncertainties in the identification of jets and the jet energy scale. These uncertainties mostly cancel out when calculating the cross section ratio. This also applies for systematics associated with the luminosity, the detector acceptance and efficiency, jet finding (as shown in [73]) and to a large extent parton distribution functions (PDFs).

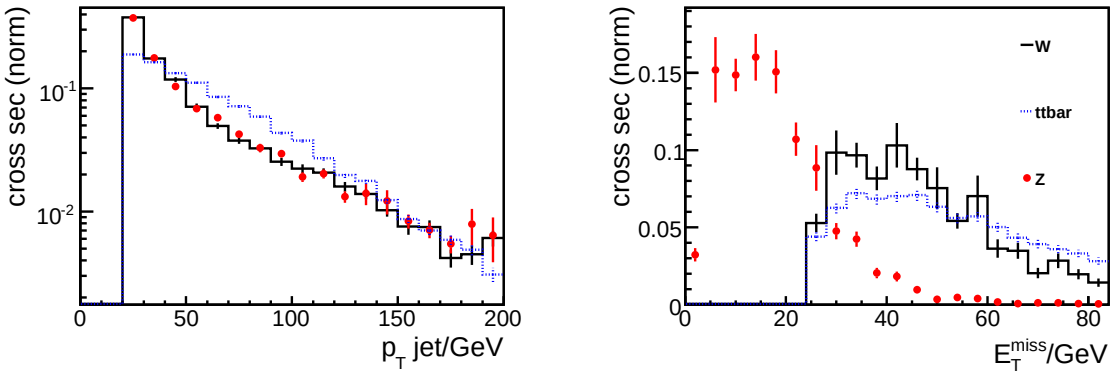

Figure 7.13: Jet p_T and $\not{E}_T$ distribution of W, Z and $t\bar{t}$ events only for events with four jets after all event selection cuts. The average values for the jet p_T are: $<p_T^W>$ = 50 GeV, $<p_T^Z>$ = 51 GeV, $<p_T^{top}>$ = 60 GeV. The average values for the $\not{E}_T$ are: $<\not{E}_T{}^W>$ = 46 GeV, $<\not{E}_T{}^{top}>$ = 50 GeV.

In [76] the systematic uncertainty of R_n due to changes in the PDFs is found to be only about 1.5%.
However, small differences between W+jets events and Z+jets events are predicted. The jet and electron p_T in Z+jets is higher than in W+jets events (see section 6.2); W+jets events need the $\not{E}_T$ for event selection. Uncertainties in the background estimate predominantly affect W+jets events. Hence, uncertainties due to the jet energy, the electron energy, the $\not{E}_T$ determination and the background estimate are not expected to completely cancel out and influence the measurement of R_n.
The background events also influence other uncertainties, like the jet energy and the $\not{E}_T$ scale. For W+jets events with more than 3 jets, $t\bar{t}$ is the dominant background. As already discussed, $t\bar{t}$ events behave differently compared to W+jets events. Despite W+jets and Z+jets events scale similarily, the different scaling of the background contribution influences R_n. Figure 7.13 shows the jet p_T and the $\not{E}_T$ of W, Z and $t\bar{t}$ events for events with 4 additional jets (a similar behaviour can be seen for events with 3 and 5 jets). While W and Z show a very similar jet p_T, the p_T of the jets in the $t\bar{t}$ events is clearly larger. Also the $\not{E}_T$ of $t\bar{t}$ events is larger than the $\not{E}_T$ of W+jets events. Hence, the fraction of $t\bar{t}$ events, which suddenly fails at or passes the jet p_T or $\not{E}_T$ event selection cut is smaller than for W+jets events.

In the following sections, the influence of uncertainties in the jet energy determination, the electron energy determination, the $\not{E}_T$ determination, the background normalization and the QCD dijet background normalization are investigated and discussed.

7.6.1 Jet energy scale and resolution

The jet energy calibration relies on simulations of hadronic showers in the detector. If the simulations are imperfectly modeled, the true jet energy and the measured jet energy differ. In this case typically all jet energies deviate by a factor from the true jet energy. The slightly larger jet p_T of the Z+jets events prevents the jet energy scale effects from cancelling out completely.

A larger influence is expected from the background contribution in the W+jets candidate sample. For W+jets events with 3, 4 and 5 jets $t\bar{t}$ is the dominant background contribution. The jets in $t\bar{t}$ events have a larger p_T than the jets in W+jets events and are produced by different mechanisms. Hence the $t\bar{t}$ events are expected to scale differently compared to W+jets events. Therefore the cross section ratio as a function of the jet multiplicity is influenced.

In [78] values of $\pm$ 5% and of $\pm$ 10% for the jet energy scale uncertainty were investigated. In this analysis the same values and additionally an uncertainty of $\pm$ 20% are examined. The uncertainty for the first 100 pb^{-1} is expected to be 5%. The variations of the values allow one to interpolate to the uncertainty of the results for actually differing systematic effects.

The performance goal for the resolution of the hadronic calorimeter is $50\%/\sqrt{E/GeV}$. For jets with $p_T \approx 25\,\mathrm{GeV}$ a resolution of 10% is obtained. The influence of this resolution is considered as expected uncertainty, but also the effects of a reduced resolution of 20% ($100\%/\sqrt{E/GeV}$) and 50% ($250\%/\sqrt{E/GeV}$) are tested.

To consider the jet energy scale, all jet energies are scaled by the expected factor. Miscalibrations of the jet energy also affect the $\not\!\!E_T$ reconstruction. The difference between unscaled ("real") and scaled jet energy is vectorially added to (if E_{jet}^{real}-$E_{jet}^{scale} > 0$) or subtracted vectorially from (if E_{jet}^{real}-$E_{jet}^{scale} < 0$) the $\not\!\!E_T$. To test the influence of resolution effects for each jet a Gaussian random number with a width of the uncertainty/100 and mean value one is used to calculate the smeared jet energy.

The results are presented in figure 7.15. For the expected uncertainties in scale and resolution deviations of up to 10% can be seen. Only for the 5 jet bin the deviations are almost 30%. It is interesting to assess, which deviations are caused by W+jets and Z+jets events or by the $t\bar{t}$ background. This can be checked using simulated events. The number of jets distribution of $t\bar{t}$ is not varied by the different jet energies, but always the distribution for the unscaled jet energies is chosen. The obtained deviations for the jet energy scale are compared to the deviation obtained when varying also the $t\bar{t}$ background. Figure 7.14 shows the result. The deviations are much smaller than if varying $t\bar{t}$. For a jet energy scale of 5% a deviation of approximately 5% in the 5 jet bin is observed. Hence, by calculating the cross section ratio most uncertainties due to the jet energy determination cancel out for W+jets and Z+jets events (as expected), but not for the $t\bar{t}$ background. Uncertainties caused by the jet energy scale are dominated by the uncertainty of the $t\bar{t}$ background estimate.

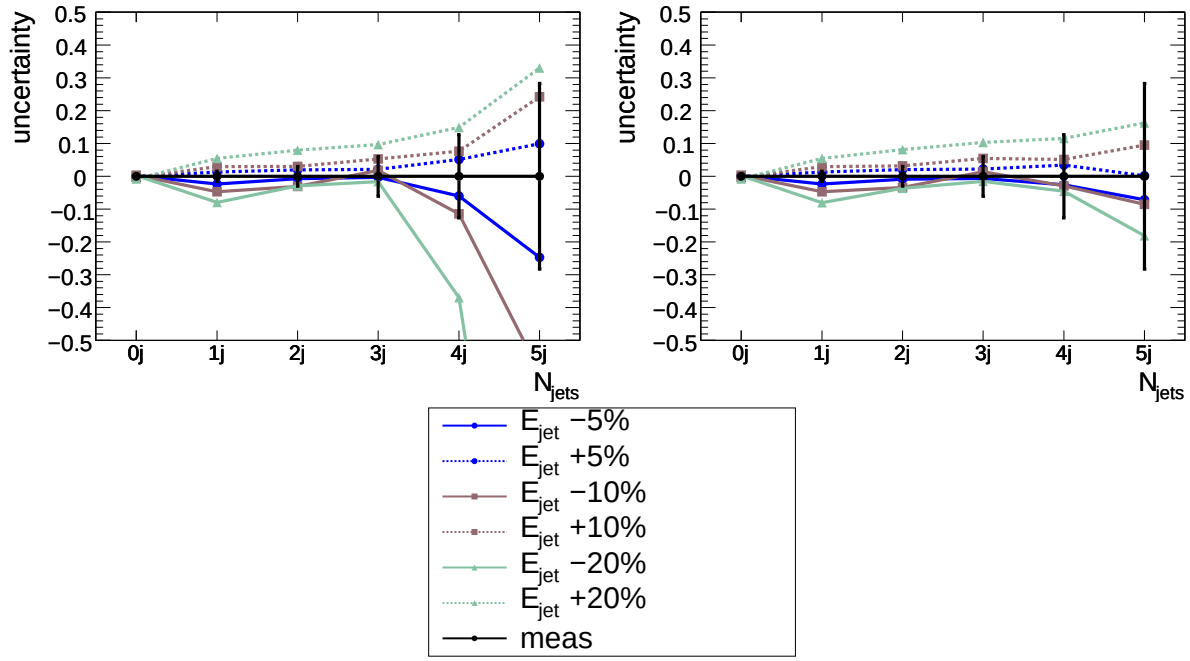

Figure 7.14: Relative difference for the measurement while changing the jet energy scale by -20,-10,-5, 5, 10 and 20 percent. On the left signal and all background are varied, on the right the $t\bar{t}$ background is set to constant (not changed by the jet energy scale).

7.6.2 Electron energy scale and resolution

The average p_T of the electrons from the Z decay is higher than the average p_T of the electrons from the W decay. With regard to the electron energy scale the probability to suddenly pass or fail at the electron p_T cut is higher for the electrons from the W. The p_T of the electrons from the W and Z decay is related to the p_T of the vector bosons themselves, which is proportional to the number of produced associated jets. Hence, W+jets events with a small number of jets are more affected by the electron energy scale and resolution.
Using the Z mass peak for calibration and the better energy resolution of electromagnetic showers provides the possibility to determine the electron energy five times better than the jet energy. An electron p_T independent deviation of 2% is considered to be the uncertainty of the first $100\,\mathrm{pb}^{-1}$; $\pm$ 5% and $\pm$ 10% deviations are used as more pessimistic scenarios. The performance goal of the ATLAS detector is a resolution of $10\%/\sqrt{E/GeV}$ for the electromagnetic calorimeter. For electrons with $p_T = 30\,\mathrm{GeV}$ this implies a resolution of $\approx$ 2%. To test the precision the first $100\,\mathrm{pb}^{-1}$ the resolution is changed by 5% ($30\%/\sqrt{E/GeV}$). The values 10% and 20% are tested to see the tendency of the deviations.

The deviations of the ratio are also presented in figure 7.15. Except for the maximum tested values, the deviations are very small (below 5%).

7.6.3 $\not{E}_T$ energy scale and resolution

The $\not{E}_T$ precision is correlated with the precision of the energy determination of all other reconstructed objects, especially of jets. Similar systematic effects in the $\not{E}_T$ and jet determination are expected. Numerically the $\not{E}_T$ uncertainties are a bit larger, because all uncertainties of the reconstructed objects form the $\not{E}_T$ uncertainty. These are enlarged by additional sources of uncertainty only affecting the $\not{E}_T$ reconstruction, like noise and defect calorimeter cells. Hence, a $\not{E}_T$ error scale of $\pm$ 10%, $\pm$ 20% and $\pm$ 50% is chosen, for the resolution the same uncertainties as for jets are chosen. Like for the jet energy scale, the smallest values for the scale (10%) and the resolution (10%) are considered as uncertainty and used to calculate the combined systematic uncertainty. The larger values show the deviations for more pessimistic scenarios.
Uncertainties in the $\not{E}_T$ determination only affect W+jets events. Like the electron p_T, the $\not{E}_T$ is proportional to the p_T of the W boson and hence proportional to the number of produced jets. A mis-measurement of $\not{E}_T$ results in proportionately more W+jets events not passing the $\not{E}_T$ and transverse mass cut, which have a small number of jets. Hence, the cross section ratio as a function of the jet multiplicity is changed.
The deviations are presented in figure 7.16. Except for a mis-calibration of -50% the deviations are maximaly 25% and inside the statistical uncertainty.

7.6.4 Background estimate

All considered background processes are normalized using the calculated cross sections for the simulated events. These cross section calculations are affected by uncertainties. It is not expected that this uncertainty cancels out by calculating the cross section ratio, because W+jets events are selected with a much higher background fraction than Z+jets events.
The estimate of the magnitude of the uncertainty on the Monte Carlo cross sections is difficult. The influence of the background contribution for events with 0, 1 and 2 jets can be neglected. Here a high signal to background ratio is obtained. Much more affected are events with 3, 4 and 5 jets. Here the signal to background ratio is much lower, for events with 4 jets it is roughly 1:1, for events with 5 jets more background events than signal events are obtained. Hence, particulary in these bins an influence of the background estimate is expected. Here the $t\bar{t}$ background is the dominant background (apart from QCD dijet events, which are considered separately) and the estimate of the background cross section uncertainty is mainly an estimate of the $t\bar{t}$ cross section uncertainty. In section 1.2.1 the $t\bar{t}$ cross section is specified with an uncertainty of $\pm$ 7% for a centre-of-mass energy of 10 TeV. This uncertainty is chosen and tested as default value for all background events. In addition the deviations of the cross section ratio for an uncertainties $\pm$ 5% and $\pm$ 10% are investigated. The number of $t\bar{t}$ background events directly changes the number of W+jets candidate events. Hence, a proportional variation of the cross section ratio with respect to the $t\bar{t}$ cross section is expected.

The results are presented in figure 7.16. The influence of the $t\bar{t}$ cross section uncertainty for the cross section ratio of 0, 1, and 2 jets can be neglected. For the ratio in the 3 jet bin the deviations are still small, but in the 4 jet bin a deviation of 5% can be seen for the default value of 7% uncertainty, in the 5 jet bin of about 10%. Hence, the $t\bar{t}$ cross section uncertainty limits the precision of the cross section ratio measurement.

7.6.5 QCD background estimate

A correct simulated estimate of the QCD multijet background contribution is very difficult due to the high cross section and limited statistics available to date. The selection efficiency for QCD multijet events using the W/Z event selection cuts is very low. Only 10 out of 10 000 000 simulated QCD events (including a cut that each QCD event includes at least one jet fulfilling $p_T > 17\,\text{GeV}$) pass the W event selection cuts. No events pass the Z event selection cuts. However, with 10 events it is not possible to estimate the shape of the QCD multijet background. So the W event selection cuts, especially the electron selection, are loosend. The electron quality is reduced to "loose". With this about 300 QCD events survive the W selection cuts. These events provide the shape of the QCD background, but the number of QCD events is obtained by scaling these 300 QCD events by $\frac{\epsilon_{\text{tight electron}}}{\epsilon_{\text{loose electron}}}$.
For the measurement of the ratio R_n it is planned to estimate the QCD multijet background using data. The advantage of this method is that enough statistics will be available. This background already includes all systematic uncertainties, which are investigated for this measurement.
In this analysis only a guess can be made on how the QCD background affects the measurement, as no data are available. The statistical results include the QCD multijet background contribution.
To estimate the effect of mismeasurements of the QCD multijet background on the ratio R_n, the consequences of a wrong estimate of $\pm$ 10%, $\pm$ 20% and $\pm$ 50% are investiged. The results are presented in figure 7.16. As at the moment no QCD events pass the Z event selection cuts, the impact on the ratio is the same size as the uncertainty of QCD, because only W+jets events are concerned. So the impact is maximal. As default for the combined systematic uncertainty an error of the estimate of $\pm$ 10% is assumed.

7.6.6 W $\Longleftrightarrow$ Z migrations

Tables 7.5 and 7.6 show that the $W \to e\nu$ candidate sample contains $Z \to ee$ events and the $Z \to ee$ candidate sample contains $W \to e\nu$ events. This background has to be subtracted like the other background contributions. Hence, the cross section of the process is needed, which actually is to be measured. Because of the smallness of these background contributions, the corresponding uncertainty can be neglected. Even if the W or Z cross section deviates 50% from the estimate, the influence on the cross section ratio due to the background subtraction will be smaller than 2% for all jet bins.

	uncertainties in %					
N_{jets}	0	1	2	3	4	5
$E_{jet}^{scale} \mp 5\%$	+0.2 -0.1	-2.3 +1.3	-0.7 +1.9	-0.3 +2.2	-6.0 +5.1	-24.7 +10.0
E_{jet}^{res} 10%	-0.0	-0.9	+3.0	+4.8	+8.8	+11.8
$E_{electron}^{scale} \mp 2\%$	-0.1 +0.0	+0.5 -0.1	+0.4 0.0	+0.1 -0.0	-0.9 +1.4	-4.6 -1.1
$E_{electron}^{res}$ 5%	-0.0	+0.1	+0.6	-0.4	+1.5	-1.0
$E_T^{miss,scale} \mp 10\%$	+0.6 -0.5	-2.5 +2.1	-2.8 +2.4	-3.8 +4.3	-6.8 +6.2	-11.8 +11.6
$E_T^{miss,res}$ 10%	0.0	-0.2	-0.2	+0.6	-0.4	+0.2
background$^{scale} \pm 1\,\sigma$	-0.0 0.0	-0.0 0.0	+0.1 -0.2	+1.1 -1.1	+4.8 -4.8	+12.0 -12.1
QCD $\pm$ 10%	+0.2 -0.2	-0.6 +0.6	-1.3 +1.3	-2.9 +2.9	-7.4 +7.4	-10.8 10.8
combined	$\pm$ 0.5	$\pm$2.4	$\pm$3.9	$\pm$6.1	$\pm$12.5	$\pm$ 22.9
statistic	$\pm$ 1%	$\pm$ 2%	$\pm$ 3%	$\pm$6%	$\pm$ 13%	$\pm$ 28%

Table 7.10: Systematic uncertainties (in %) for the measurement of the ratio R_n for events with 0 to 5 additional jets.

7.6.7 Combined systematic uncertainty

For all systematic uncertainties studied it is seen that higher jet bins are more affected. The systematic uncertainties are dominated by the jet energy scale, the $\not\!\!E_T$ scale, the $t\bar{t}$ and QCD dijet background estimate. There is an uncertainty of about 25% resulting from the jet energy scale for the five jet bin. The deviation is mainly caused by the background contribution, which only affects W+jets events and reacts differently to uncertainties in the jet energy determination.
Many observed systematic uncertainties turn out to be asymmetric. The biggest asymmetry appears for 5 jet events and the jet energy scale (-25%,+10%). As, however, the statistical uncertainties are always dominating the systematic uncertainties it is legitimate to symmetrize the systematic uncertainties. This is done by calculating the errors by $\sqrt{\sigma_+^2 + \sigma_-^2}/2$, where σ_+ and σ_- are the positive and negative relative systematic uncertainties, respectively.
The errors are added quadratically for the combined systematic uncertainty. The results are presented in table 7.10.

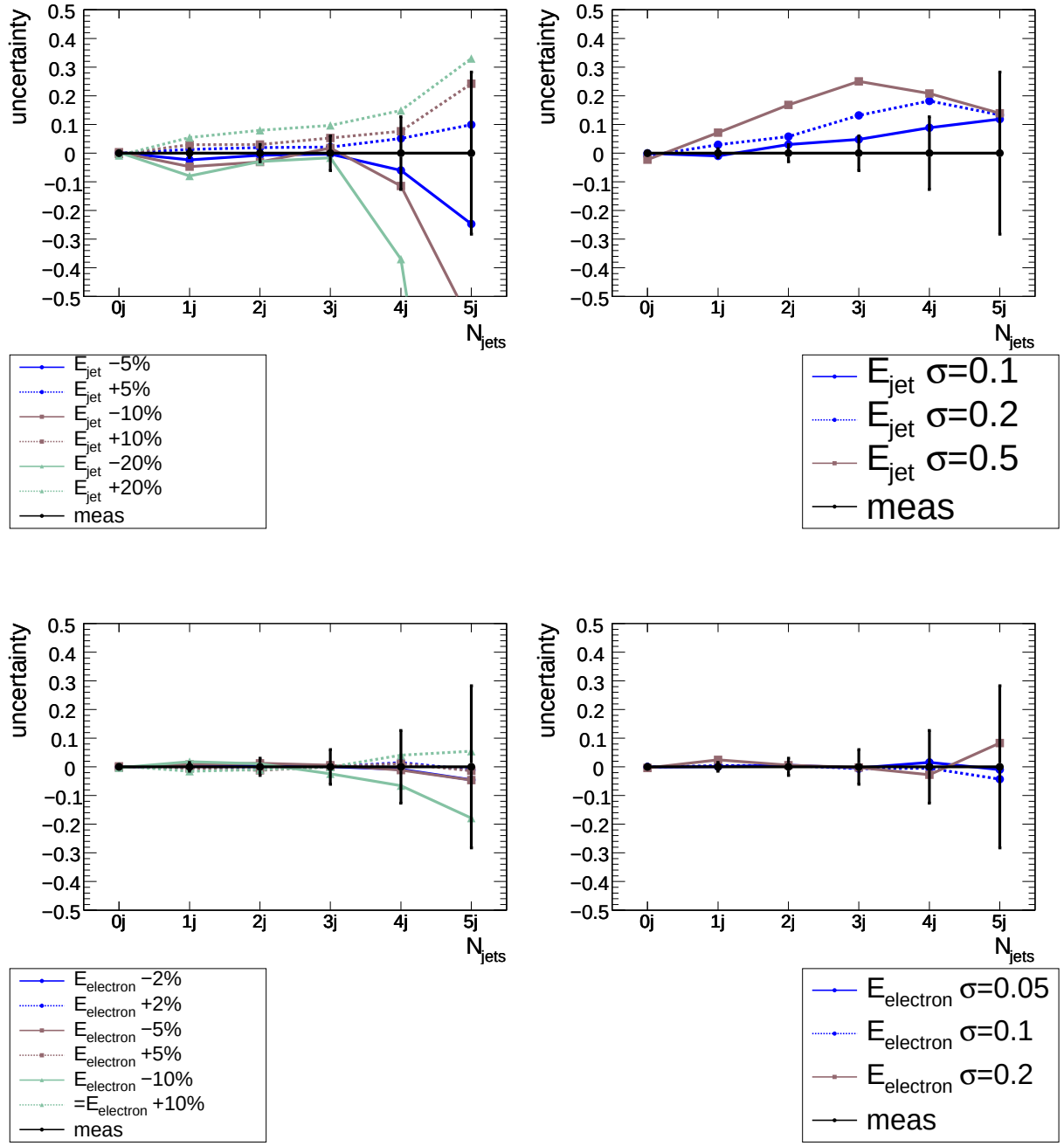

Figure 7.15: Upper plots: Relative difference for the measurement while changing the jet energy scale by -20, -10, -5, 5, 10 and 20 percent (left) and the jet energy resolution by 10 (smeared by a Gaussian with mean=1 and σ=0.1), 20(σ=0.2) and 50(σ=0.5) percent (right) with statistical errors. Lower plots: Relative difference for the measurement while changing the electron energy scale by -10, -5, -2, 2, 5 and 10 percent (left) and the electron energy resolution by 5(smeared by a Gaussian with mean=1 and σ=0.05), 10(σ=0.1) and 20(σ=0.2) percent (right) with statistical errors.

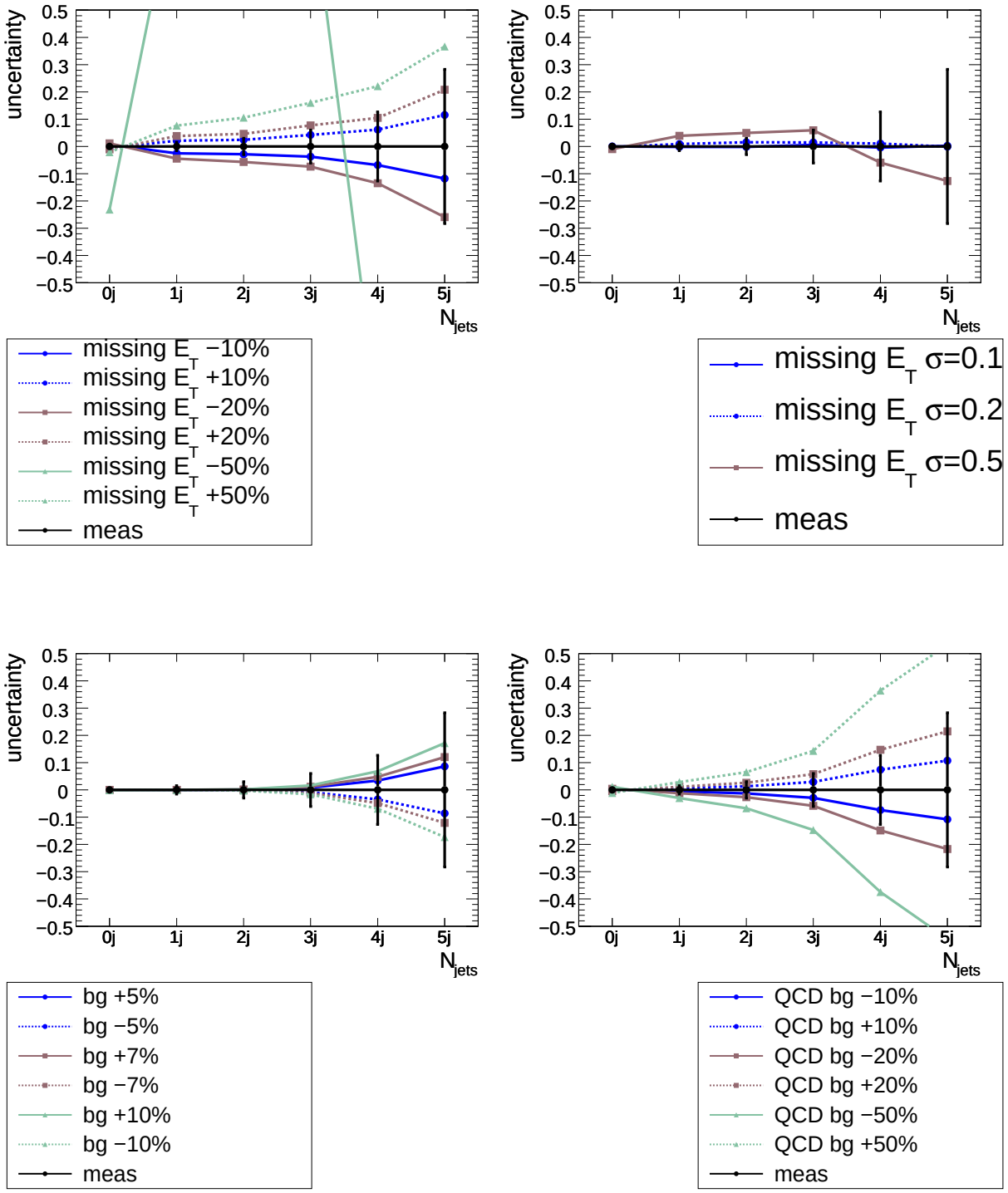

Figure 7.16: Upper plots: Relative difference for the measurement while changing the missing energy scale by -50, -20, -10, 10, 20 and 50 percent (left) and the missing energy resolution by 10 (smeared by a Gaussian with mean=1 and σ=0.1), 20 (σ=0.2) and 50(σ=0.5) percent (right) with statistical errors. Lower plots: Relative difference for the measurement while changing the cross section of the MC samples by -10,-7,-5,5, 7 and 10 percent (left). Relative difference for the measurement while changing the QCD background normalisation by 10, 20 and 50 percent with statistical errors (right).

7.7 Results

In this chapter the prospects of the measurement of the cross section ratio of W and Z events as a function of the jet multiplicity are presented. The results are supposed to reflect the jet production mechanisms of the events. Therefore, W and Z events are handled as similar as possible in order to avoid biases caused by the measurement itself.
First an event selection adopted to the W and Z event signature was developed to filter W and Z candidate events. Then the jets are reconstructed and defined. The contribution of background events for W and Z is discussed and subtracted. Then the cross section ratio is calculated and systematic uncertainties are discussed.
The expected statistical and systematic uncertainties of a measurement of $\frac{\sigma(\mathrm{W + n\,jets})}{\sigma(\mathrm{Z + n\,jets})} \cdot \frac{\sigma(\mathrm{Z_{inc}})}{\sigma(\mathrm{W_{inc}})}$ assuming a luminosity of $100\,\mathrm{pb}^{-1}$ at a centre-of-mass energy of 10 TeV are summarized in table 7.11 and figure 7.17. A measurement for up to 5 additional jets is possible and yields reasonable results. It is interesting that statistical and systematic uncertainties are of similar size. Hence, to improve the precision of the measurement the systematic uncertainties will have to be reduced. They are dominated by the background uncertainties. The precision of the measurement scales with the precision of the estimate of the QCD dijet background and the $t\bar{t}$ background. $t\bar{t}$ events are the dominant background for W+jets events with three and more jets. Also the jet energy scale uncertainty is dominated by the uncertainty of the subtraction of the $t\bar{t}$ background contribution. A more precise estimate of the $t\bar{t}$ background would definitely improve the results. A meaningful option is to measure the cross sections of W, Z and $t\bar{t}$ simultaneously. Here already first studies with promising preliminary results have been performed using a Neural Network. However, a final result is outside the scope of this analysis.

N_{Jets}	$\frac{\frac{W+njets}{\sum_{n=0}^{4} W+njets}}{\frac{Z+njets}{\sum_{n=0}^{4} Z+njets}}$			
0	1.04	$\pm$	1% (stat.)	$\pm$ 1% (syst.)
1	0.88	$\pm$	2% (stat.)	$\pm$ 2% (syst.)
2	0.83	$\pm$	3% (stat.)	$\pm$ 4% (syst.)
3	0.82	$\pm$	6% (stat.)	$\pm$ 6% (syst.)
4	0.79	$\pm$	13% (stat.)	$\pm$ 13% (syst.)
5	0.85	$\pm$	28% (stat.)	$\pm$ 23% (syst.)

Table 7.11: Measured ratio R_n after all event selection cuts and background subtraction including statistic and systematic errors for 0 to 5 jets.

In figure 7.1 is shown that the predictions for R_n of different generators deviate. Comparing the generator predictions with the measured ratio using the first $100\,\mathrm{pb}^{-1}$ will be an important cross check. The results can be used to test the generators. It is possi-

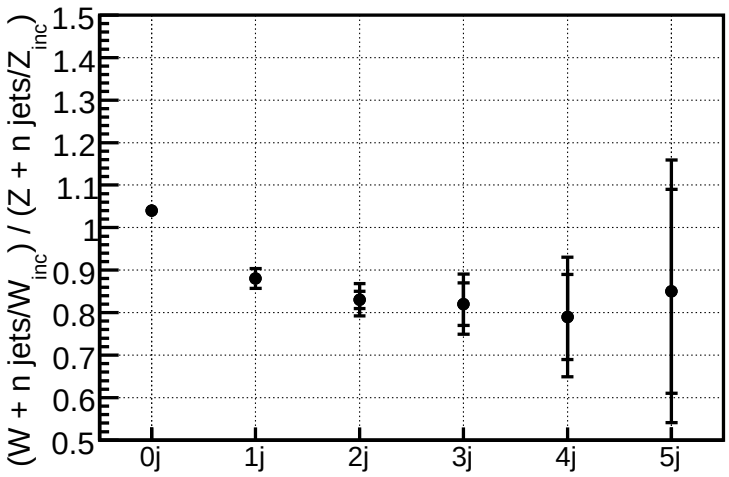

Figure 7.17: Measured ratio R_n after all event selection cuts and background subtraction including statistic (inner error bars) and systematic (outer error bars) errors for 0 to 5 jets.

ble to verify if W+jets and Z+jets events are really similar events and if a detector reacts similar to both types of events.
In [76] CDF Run I results on the cross section ratio W/Z as a function of the jet multiplicity are published. There the ratio for 4 jets is measured with a precision of $\sim$ 60%. Here a precision of $\sim$ 18% can be achieved for R_4, which is a clear improvement with respect to the CDF results.
The $t\bar{t}$ analysis suffers from uncertainties in the W+jets - especially W + 4 jets - normalization. Until now uncertainties in the W+jets estimate of 20%-50% are considered (see [78] for example). The cross section ratio R_n for n = 0,1,2,3 can be measured with good precision. In these jet bins the $t\bar{t}$ contribution is still small. R_0 reflects the effects of the mass difference between W and Z on the probability to produce hard partons. As soon as one parton is produced, the QCD effects dominate and the ratio R_n shows a linear trend. Hence, leaving R_0 out, the results for n = 1,2,3 can be used to extrapolate to R_4.
Figure 7.18 shows the result. A linear function y(R) = p0 + p1 (4-R) is fitted between R_1 and R_3. p0 = 0.76 $\pm$ 0.08 is the extrapolated value for R_4. A relative error of about 11% can be achieved. The number of W + 4 jet events is then obtained by N_{events}(W + 4 jet) = N_{events}(Z + 4 jet) $\cdot$ p0 $\cdot$ $\frac{\sigma(W_{inc})}{\sigma(Z_{inc})}$, with N_{events}(Z + 4 jet) = 78 $\pm$ 9. The error of $\frac{\sigma(W_{inc})}{\sigma(Z_{inc})}$ is expected to be $<$ 1%. Hence, the resulting relative error is $\sqrt{0.11^2 + \frac{9}{78}^2}$ = 0.16. This is clearly smaller than 20%-50% and also smaller than 23.9%, which is obtained as uncertainty in [78] for the data driven W+jets estimate. This measurement will improve the W+jets background estimate to $t\bar{t}$ analyses.

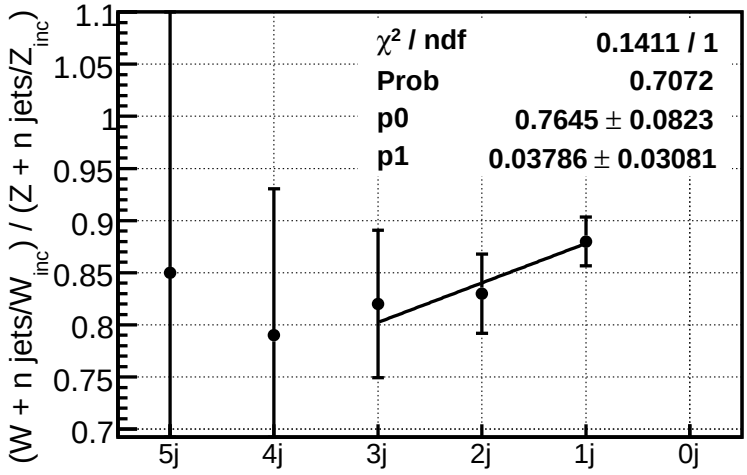

Figure 7.18: Measured ratio R_n after all event selection cuts and background subtraction for 0 to 5 jets. The results for R_1, R_2 and R_3 can be used to extrapolate to R_4 in order to estimate the W + 4 jets background in $t\bar{t}$ analysis. A linear function y(R) = p0 + p1 (4-R) is fitted between R_1 and R_3, hence p0 is the extrapolated value for R_4.

Chapter 8

The unfolded ratio W+$n$jets/Z+$n$jets

Generator predictions cannot be directly compared to measured distributions, because these include detector and reconstruction effects. The measured distribution $\vec{N}_{\text{measured}}$ can be seen as

$$\vec{N}_{\text{measured}} = M_{\text{detector}} \cdot \vec{N}_{\text{generated}},$$

where $\vec{N}_{\text{generated}}$ is the generated distribution and M_{detector} describes the convolution matrix representing the detector and resolution effects. To compare generator predictions with data, one method would be to simulate the detector effects for different generators (models and parameters) and then judge, which generator agrees best with the data. However, the detector simulation is extremely time consuming and the results of different detectors cannot be compared. Also new models cannot be compared to existing measurements as a detector simulation including the new model is, in general, no more available. The superior choice is to remove the detector effects from the measured distributions by unfolding. Then the theory and generator predictions can be directly compared to the results of measurements.
The first section of this chapter addresses the unfolding method itself. Then the prospects of a measurement of $R_n = \frac{\sigma(W + n \text{ jets})}{\sigma(Z + n \text{ jets})} \cdot \frac{\sigma(Z_{\text{inc}})}{\sigma(W_{\text{inc}})}$, which is calculated after the unfolding procedure is applied to the W+jets and Z+jets distributions, are presented. Up to four additional jets are considered.

8.1 Correcting detector effects

QCD calculations predict cross sections for the production of a W or a Z boson accompanied by a certain number of additional partons. However, partons are quantum mechanical states which cannot be observed. Instead, only (jets of) hadrons can be measured. The measurement addresses W and Z bosons accompanied by a certain number of calorimeter jets. These W/Z + n jet events include all effects of the detector and the measurement. The aim of this analysis is to unfold the measured W/Z + n jets distributions. Then the Monte Carlo generator predictions can be compared to measurements.

8.1.1 Migrations of events

Due to the detector and the reconstruction process, in general, the number of reconstructed jets does not match the number of hadron ("truth") jets. In section 3.3 the difficulties in reconstructing the hadron jets from the calorimeter signals were described. These are amongst others:

- Particles belonging to the hadron jets possibly do not reach the calorimeter and/or deposit their energy in dead detector material.
- The hadronic and electromagnetic fractions of each hadronic shower differ, each hadronic shower consists partly of invisible energy deposits.
- There is noise in the calorimeter.
- The energy of particles not originating from the initial parton can accidentally be added to the reconstructed jet. Or energy depositions of particles belonging to the hadron jet lie outside the reconstructed jet.

$\rightarrow$ If energy is lost (added), the energy of the reconstructed jet can be smaller (bigger) than the p_T cut of 20 GeV, even if the truth jet p_T was bigger (smaller) than 20 GeV, i.e. a jet is lost (added).

- There are inefficiencies of the jet reconstruction algorithms.
- The signals of two hadron jets cannot be dissolved by the detector and are reconstructed as one calorimeter jet, or one hadron jet is reconstructed as two calorimeter jets.

These effects can result in the reconstruction of a W/Z + m jet truth event (conveniently called W/Z + m truth jet event) as a W/Z + n jet event with in general m $\neq$ n. The transitions from a W/Z + m truth jet event to a W/Z + n jet event are called migrations. W $\longleftrightarrow$ Z migrations are due to:

- a Z + m truth jet event is reconstructed as W + m jet event, because one electron does not pass the p_T or η cut.
- The mis-identification of a jet as an electron or vice versa results in (see also section 3.2):
  - a Z + m truth jet event is reconstructed as W + (m+1) jet event, because one electron is not passing the identification criteria during the reconstruction process and by mistake identified as a jet.
  - a W + m truth jet event is reconstructed as Z + (m-1) jet event, because one jet by chance is identified as an electron.

In principle the W $\longleftrightarrow$ Z migrations could be corrected like migrations of W (Z) + m truth jets events inside the W (Z) candidate samples. In order to be consistent with the previous chapter and to avoid large uncertainties due to the W $\leftrightarrow$ Z cross talk during the correction process, W events selected as Z candidates and vice versa are treated as background events like before. The W+jets and Z+jets distributions are corrected separately for the detector effects.
Migrations from m truth jets ("N_{jets}^{truth}") to n measured jets ("N_{jets}^{reco}", "reco jets") can be described and visualized by a migration matrix (sometimes referred to as "response matrix" or "smearing matrix"). A migration matrix specifies the probability for a particular W/Z + m truth jet event to be measured as W/Z + n jet event. Each W/Z + m truth jet event is measured, no events are lost. Therefore, the sum of probabilities for all possible final states of a W/Z + m truth jet event is equal to one (or 100%)[1].
Using a migration matrix $\mathbf{M}_{\text{truth-reco}}$, the relation between $\vec{\mathbf{N}}_{jets}^{truth}$ and $\vec{\mathbf{N}}_{jets}^{reco}$ with

$$\vec{N}_{jets}^{truth,reco} = \begin{pmatrix} N_{events}(W/Z^0 + 0\,jet) \\ N_{events}(W/Z^0 + 1\,jet) \\ N_{events}(W/Z^0 + 2\,jet) \\ N_{events}(W/Z^0 + 3\,jet) \\ N_{events}(W/Z^0 + 4\,jet) \end{pmatrix} \tag{8.1}$$

can be expressed by the following linear equation:

$$\vec{\mathbf{N}}_{jets}^{reco} = \mathbf{M}_{\text{truth-reco}} \cdot \vec{\mathbf{N}}_{jets}^{truth}. \tag{8.2}$$

The migration matrix only describes the effects of the detector and the reconstruction process on the measured number of jets. Only migrations of events from one to another jet multiplicity are described. The migration matrix is calculated only with W events passing the W event selection and Z events passing the Z event selection. For the calculation of the migration matrix, the same W and Z event selection criteria are applied as already described in the previous chapter (see section 7.3). Consistently, the jets are defined as described in section 7.3.4.
To calculate the migration matrix also truth jets are needed. The only meaningful possibility is to define the truth jets in analogy to the reconstructed jets. Different p_T or η criteria would imply biases. Truth jets are defined as:

- ATLAS Cone ΔR = 0.4, built of stable generator particles
- $p_T > 20\,\text{GeV}$, $|\eta| < 2.5$
- Electron removal: all jet objects within a cone of ΔR=0.4 around true electrons are removed (Like on detector level, the jet algorithms on truth level reconstruct the two electrons from the Z decay and the electron from the W decay as jets.

[1] Events with five or more jets are neglected. Hence, the total probability for each truth event is slightly smaller than 100%. However, the migration probabilities for 0-4 truth jets to 5 and more jets are very small and are neglected.

These jets have to be removed. Here a small difference in the event selection criteria occurs. To be sure that all true electrons are removed from the jet object list, these electrons have to be found in the event record. In very few cases the event record is corrupt and does not contain the truth electrons, but the electrons are contained as jets in the jet list. Hence, an event is only used to calculate the migration matrix, if the event record contains all expected true electrons. In this case it is guaranteed that all truth jets initiated by electrons are removed. The fraction of events with corrupt event record is very small. They mainly appear for PYTHIA and cause biases in the PYTHIA migration matrix. Effects due to this additional event selection criterion are expected to be very small for ALPGEN and SHERPA ($< 1\%$) and are neglected.)

Figure 8.1 shows the migration matrix for W (Z) + truth jets $\rightarrow$ W (Z) + measured jets. Each entry of the matrix specifies the probability (in integer percent) for a W (Z) + m truth jets event to pass into a particular W (Z) + n jets final state after reconstruction. As no events disappear, the sum of all entries of each line of the migration matrix is 100% (final states with five and more jets are discarded).
The migration probabilities are determined based on simulated events. These matrices are calculated with ALPGEN W $\rightarrow e\nu$ and Z $\rightarrow$ ee signal events including full detector simulation performed with GEANT4 .
W and Z events are very similar events and show comparable migrations. Due to the slightly higher average jet p_T, Z events show slightly less migrations.
For both W and Z events the migrations to smaller numbers of reconstructed jets increase with increasing number of truth jets. For example W/Z + 4 truth jet events are reconstructed as W (Z) + 4 jets with a probability of less than 50%. In contrast, for W (Z) + 1 truth jets events the corresponding probability is larger than 70%. The reason is that with increasing jet multiplicity the events are more complex and more difficult to reconstruct. And the probability for jets to overlap with other jets or electrons increases with increasing jet multiplicity. This results in the loss of jets. Moreover the probability to pass the jet p_T cut decreases with increasing order (i.e. falling p_T) of a jet.

8.1.2 Reversing the migrations: Unfolding

As already mentioned, the correlation between the numbers of truth and measured jets can be described as

$$\vec{\mathbf{N}}_{\text{jets}}^{\text{reco}} = \mathbf{M}_{\text{truth-reco}} \cdot \vec{\mathbf{N}}_{\text{jets}}^{\text{truth}} .$$

Therefore, the truth jets distribution can, in principle, be obtained by

$$\vec{\mathbf{N}}_{\text{jets}}^{\text{truth}} = \mathbf{M}_{\text{truth-reco}}^{-1} \cdot \vec{\mathbf{N}}_{\text{jets}}^{\text{reco}} . \tag{8.3}$$

This implies that the migration matrix can be inverted in order to obtain the jet multiplicity distributions on truth level. A matrix inversion only works for matrices, which

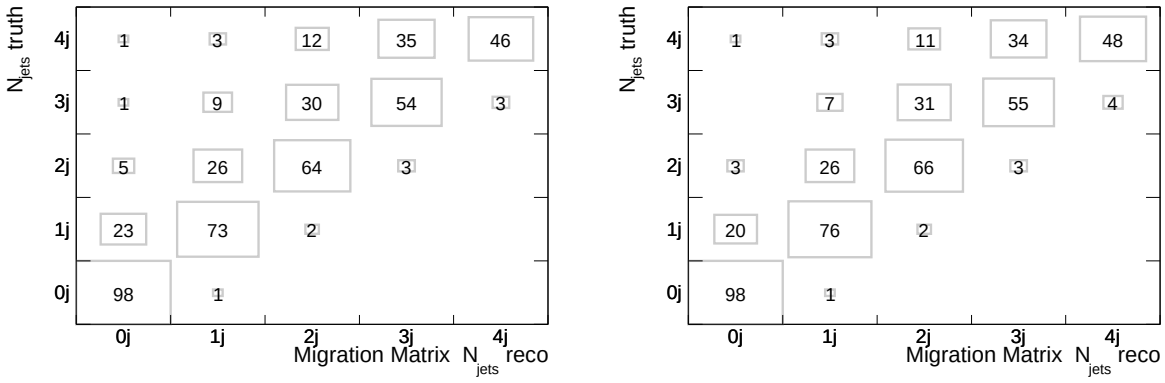

(a) ALPGEN W events (b) ALPGEN Z events

Figure 8.1: The migration matrices for W and Z events generated with ALPGEN including full detector simulation using GEANT4. All event selection cuts are applied (W event selection for W events, Z event selection for Z events). Shown is the relative size of the matrix elements in percent. The normalization of the migration matrix is done in that way that the sum of probabilities for all final states for an event on truth level is equal to one.

are "regular". A realistic migration matrix is in general only invertible if the migrations are small.
Large off-diagonal elements - indicating an insufficient resolution - in the migration matrix are a general problem for unfolding, because these cause strong correlations between the unfolded bins and their errors. Also statistical fluctuations cause problems. Statistical fluctuations are amplified by the unfolding procedure. This general problem of each unfolding procedure is discussed in detail in [79].
Here the inverse of the matrix is obtained by applying the method presented by G. D´Agostini in [80], based on Bayes' Theorem [81]. G. D´Agostini disclaims an explicit inversion of the migration matrix. The method is described in the next section.

8.1.3 Unfolding based on Bayes' Theorem

Bayes' Theorem is well adopted to be applied to the problem of unfolding a jet multiplicity distribution. Assuming a certain number of W/Z + n jet events is measured. A set of true states m_i (W/Z + m truth jet events, with m=0,1,..,4) exists, which can cause a W/Z + n jet event. The question is, how many W/Z + 0 truth jet, W/Z + 1 truth jet, .. and W/Z + 4 truth jet events caused this certain number of W/Z + n jet events. Hence, the probability $P(m_i \mid n)$ of m_i is of interest, after n was measured. However, this probability cannot be determined directly, only the probability $P(n \mid m_i)$ for m_i to cause n can be calculated. The Bayes´ formula addresses this problem and states

$$P(m_i|n) = \frac{P(n|m_i) \cdot P(m_i)}{P(n)} = \frac{P(n|m_i) \cdot P(m_i)}{\sum_{k=1}^{N} P(n|m_k) \cdot P(n_k)}. \tag{8.4}$$

In this case there is not only one final state W/Z + n jets possible, but there are several final states n_j (W/Z + n jet events, with n=0,1,..4). Then Bayes´ formula modifies to:

$$P(m_i|n_j) = \frac{P(n_j|m_i) \cdot P(m_i)}{\sum_{k=1}^{N}(P(n_j|m_k) \cdot P(m_k))} \tag{8.5}$$

In this case $P(m_i \mid n_j)$ is exactly the matrix searched for, the unfolding matrix **U** with:

$$N_{\text{jets}}^{\text{truth}} = U \cdot N_{\text{jets}}^{\text{measured}} \tag{8.6}$$

$P(n_j \mid m_i)$ is the migration matrix **M**.

The method

A measured distribution $\vec{N}_{\text{jets}}^{\text{meas}}$ and the migration matrix **M** are at hand. The aim is to achieve a distribution $\vec{\mu}$ as estimator for the truth jet distribution $N_{\text{jets}}^{\text{truth}}$. Iteratively the most probable values for the μ_i are searched for. First the start values have to be defined.
$\vec{p}$ describes a set of initial probabilities $\vec{p}=(p_1, p_2, ..., p_{N_{bins}})$, describing the probability for an event to be found in each bin. $\vec{p}$ is set to the start value $p_i=1/N_{bins}$. N_{bins} is the dimension of $\vec{N}$. The initial estimator for the truth jet distribution is set to $\vec{\mu} = \vec{p} \cdot N_{\text{observed}}$, where N_{observed} is the sum of all measured events in all bins.
The estimators $\vec{\mu}$ and $\vec{p}$ are calculated iteratively

$$\mu_i = \sum_{j=1}^{N_{bins}} P(m_i|n_j) \cdot N_{\text{jets}}^{\text{meas,j}} \tag{8.7}$$

$$= \underbrace{\sum_{j=1}^{N_{bins}} \left(\frac{M_{ji} p_i}{\sum_k M_{jk} p_k} \right)}_{U} \cdot N_{\text{jets}}^{\text{meas,j}} \tag{8.8}$$

$$\vec{p} = \vec{\mu}/\mu_{tot} \tag{8.9}$$

- $\mu_{tot} = N_{\text{observed}}$, because the events are only re-sorted by the unfolding process

In each iteration step the values for $\vec{\mu}$ and $\vec{p}$ are compared to the values of the previous iteration. If $\vec{N}_{\text{jets}}^{\text{meas}}$ is compatible with the migrations described by **M**, $\chi_{\mu}^{\text{i,i-1}} = |\mu_{\text{ith step}} - \mu_{\text{(i-1)th step}}|$ and $\chi_{p}^{\text{i,i-1}} = |\vec{p}_{\text{ith step}} - \vec{p}_{\text{(i-1)th step}}|$ decrease with increasing number of iterations. If $\chi_{\mu}^{\text{i,i-1}}$ and $\chi_{p}^{\text{i,i-1}}$ are smaller than a certain cut value or a previously defined maximum number of iterations is reached, the iteration procedure is stopped. Then $\vec{\mu}$ is the unfolded distributions, an estimate of the true distribution.
By applying this method an explicit matrix inversion is avoided. The method is quite simple and robust.

Error estimation

To estimate the errors of the unfolded distribution $\vec{\mu}$, it has to be considered, which uncertainties affect each μ_i. Formula 8.8 shows that $\vec{\mu}$ depends on the migration matrix M and on $\vec{N}_{\text{jets}}^{\text{meas}}$. Hence, the statistical error of $\vec{\mu}$ is composed of the statistical errors of these two objects. The covariance matrix **V** of the unfolded distribution consists of two parts

$$\mathbf{V} = \mathbf{V}(\mathrm{N}_{\text{jets}}^{\text{meas}}) + \mathbf{V}(\mathrm{M}). \tag{8.10}$$

The method of D´Agostini provides this error matrix **V** as error estimate of the unfolded bins. After stopping the iteration process an iteratively determined unfolding matrix **U** is obtained, which is an approximation of the inverse of the migration matrix:

$$\text{Unfolding Matrix } U_{ij} = \frac{M_{ji}P_0(i)}{\sum_l M_{jl}P_0(l)} \tag{8.11}$$

with **M** being the migration matrix and $\mathrm{P}_0(\mathrm{i})=\mathrm{p}_i$ the set of probabilities obtained in the last but one iteration step.
The statistical uncertainty of the measured distribution to be unfolded is in [80] estimated by the square root of the number of events in each jet bin. The difficult aspect is that during the unfolding process a repeated cross talk between the different bins appears, which leads to a correlation of the individual bin results. In order to account for the interactions of the entries in the different jet bins in the unfolding procedure and hence the interactions of the errors, D´Agostini writes $\mathbf{V}(\mathrm{N}_{\text{jets}}^{\text{meas}})$ as:

$$\begin{aligned} V_{kl}(N_{\text{jets}}^{\text{meas}}) = &\sum_j U_{kj}U_{lj}N_{\text{jets}}^{\text{meas,j}}(1-\frac{N_{\text{jets}}^{\text{meas,j}}}{N_{\text{true}}})- \\ &\sum_{i,j;i\neq j} U_{ki}U_{lj}\frac{N_{\text{jets}}^{\text{meas,i}}N_{\text{jets}}^{\text{meas,j}}}{N_{\text{true}}} \end{aligned} \tag{8.12}$$

i.e. as the error of a multi-nominal process. $\mathrm{N}_{\text{true}} = \mathrm{N}_{\text{observed}}$, because the events are only re-sorted. The first part of $V_{kl}(\mathrm{N}_{\text{jets}}^{\text{meas}})$ describes the errors of the main diagonal elements, the second part of the off-diagonal elements.
Especially for unfolding a N_{jets} distribution represented by W + jets and Z + jets events, several difficulties arise. The number of events for each jet multiplicity bin decreases by a factor of about four from events with i jets to events with i+1 jets (see tables 7.5 and 7.6). Hence, small relative errors in the i^{th} jet bin cause proportionally larger relative errors in the $(\mathrm{i+1})^{\text{th}}$ jet bin.
The migration matrix is calculated using simulated events and affected by statistical uncertainties. The migration probabilities are determined from the relative frequency of how often a W/Z + n truth jet event in the Monte Carlo data set is reconstructed as

W/Z + m jet event. So a high statistics of Monte Carlo events in each W/Z + n truth jet bin is needed to reduce the statistical error on the fraction of events in each bin of the migration matrix. Especially for high jet multiplicity events with large migration tendency enough Monte Carlo statistics is needed to minimize the consequences of statistical fluctuations and keep the error of the matrix small. The statistical error of a cell of a migration matrix affects all possible final states of a certain truth jet event. During the unfolding process errors from the reconstructed jet bins distribute repeatedly (due to the iterations) over the appropriate unfolded jet bins and cause strongly correlated errors.
The statistical error of **V**(M) is obtained by applying error propagation. The entries of **U** are differentiated with respect to the entries of **M** they are depending on. D´Agostini defines **V**(M) by:

$$V_{kl}(M) = \sum_{i,j} N_{\text{jets}}^{\text{meas,i}} N_{\text{jets}}^{\text{meas,j}} Cov(U_{ki}U_{lj}) \tag{8.13}$$

where

$$Cov(U_{ki}U_{lj}) = \sum_{\{ru\},\{su\}} \frac{\partial U_{ki}}{\partial M_{ru}} \frac{\partial U_{lj}}{\partial M_{su}} \cdot Cov(M_{ru}, M_{su}) \tag{8.14}$$

with

$$\frac{\partial U_{ki}}{\partial M_{ru}} = U_{ki}\left(\frac{\delta_{ku}\delta_{ri}}{M_{ru}} - \delta_{ku} - \frac{\delta_{ri}U_{ui}}{M_{iu}}\right) \tag{8.15}$$

and

$$Cov(M_{ru}, M_{su}) = \begin{cases} \frac{1}{n_u} M_{ru}(1 - M_{ru}) & \text{for r=s} \\ \frac{-1}{n_u} M_{ru} M_{su} & \text{for r}\neq\text{s} \end{cases} \tag{8.16}$$

- n_u is the number of simulated events in the u^{th} truth jet bin used to calculate the migration matrix. The larger n_u for a particular truth jet bin is, the smaller are the statistical errors resulting from the migration matrix. Here a difficulty arises if using weighted events like for example provided by ALPGEN. The formula has to be corrected in that way that the statistical errors of the weighted events are considered correctly. The term containing n_u describes a binominal distribution. Hence, $\frac{1}{n_u}$ is replaced by

$$\begin{aligned} \frac{1}{n_u} &= \left(\frac{1}{\sqrt{n_u}}\right)^2 = \left(\frac{\sqrt{n_u}}{n_u}\right)^2 = \left(\frac{\Delta n_u}{n_u}\right)^2 \\ &= \left(\frac{\sqrt{\sum_i^{\text{events with u jets}} (\text{event weight}_i)^2}}{\sum_i^{\text{events with u jets}} \text{event weight}_i}\right)^2 . \end{aligned} \tag{8.17}$$

  This method to introduce weighted events is also suggested by [82].

The elements of **V** correspond to events. The variances of the unfolded numbers are obtained by $\sqrt{V(i,i)}$ (as described in [79]) and can be referred to as the errors of the

i^{th} unfolded bin. However, it has to be kept in mind that the different unfolded bins - and hence their errors - are strongly correlated. Therefore, it has been tested if the so calculated errors of the unfolded bins reflect the statistical fluctuations of the measured distribution (see section 8.4).
With the formula for **V** only the errors of the measured distribution itself are handled. However, in the measurement the selected W and Z candidate events also contain background events. The expected background contribution has to be subtracted before unfolding the distribution. After background subtraction the measured distribution is still affected by the statistical errors of the signal and the background events. The error formulae are modified to include this error. All $N_{jets}^{meas,i}$ in the error formulae for **V**(M) and **V**(N_{jets}^{meas}) can be seen as $(\Delta N_{jets}^{meas,i})^2 = (\sqrt{N_{jets}^{meas\ signal,i}})^2$ and are replaced by $(\sqrt{N_{jets}^{meas\ signal+background,i}})^2$. It will have to be tested if this estimation describes the uncertainties resulting from the statistical signal and background uncertainties.

8.1.4 Testing the unfolding method

The unfolding method described has been tested. In a first step the unfolding procedure is only applied to the number of jets distributions of the W and Z signal events. The N_{jets}^{meas} distribution, the N_{jets}^{truth} distribution and the migration matrix are all calculated with the same Monte Carlo generator. N_{jets}^{reco} is normalized to a luminosity of $100\,pb^{-1}$. After applying the unfolding procedure the unfolded distribution is compared to the truth distribution to get a handle on the accuracy of the unfolding method. As already mentioned, the W+jets and the Z+jets distributions are unfolded separately. Only events passing the W/Z event selection cuts are used for the distributions of truth jets, reco jets and the migration matrix. The unfolding procedure only re-sorts the migrated events. Hence, by unfolding the $\vec{N}_{jets}^{meas}$ distributions, the total number of events remains unchanged.
The results are presented in figure 8.2 for SHERPA , ALPGEN and PYTHIA including full detector simulation. For each jet bin the plots show the deviation of the unfolded distribution from the truth distribution. Deviations of at most 2% from the truth distribution for all jet bins except for Z + 4 jets and W + 4 jets are observed. For these boundary bins the deviations are about 10% to 20%. The method clearly works for W/Z + 0 - 3 jets.
Differences can be distinguished from the errors of the unfolded distributions. The statistical error of N_{jets}^{meas} is of the same size for all three generators, because N_{jets}^{meas} is normalized to $100\,pb^{-1}$. The differences in the error size have to be caused by the different sample sizes available to calculate the migration matrices. SHERPA and ALPGEN both provide weighted events in order to achieve an effectively higher event statistics for the higher jet multiplicities. Hence, the errors resulting from the migration matrices are smaller for ALPGEN and SHERPA . For PYTHIA no weighted events are available. This results in a much smaller number of high jet multiplicity events available to generate the migration matrix. Hence, the errors are larger.

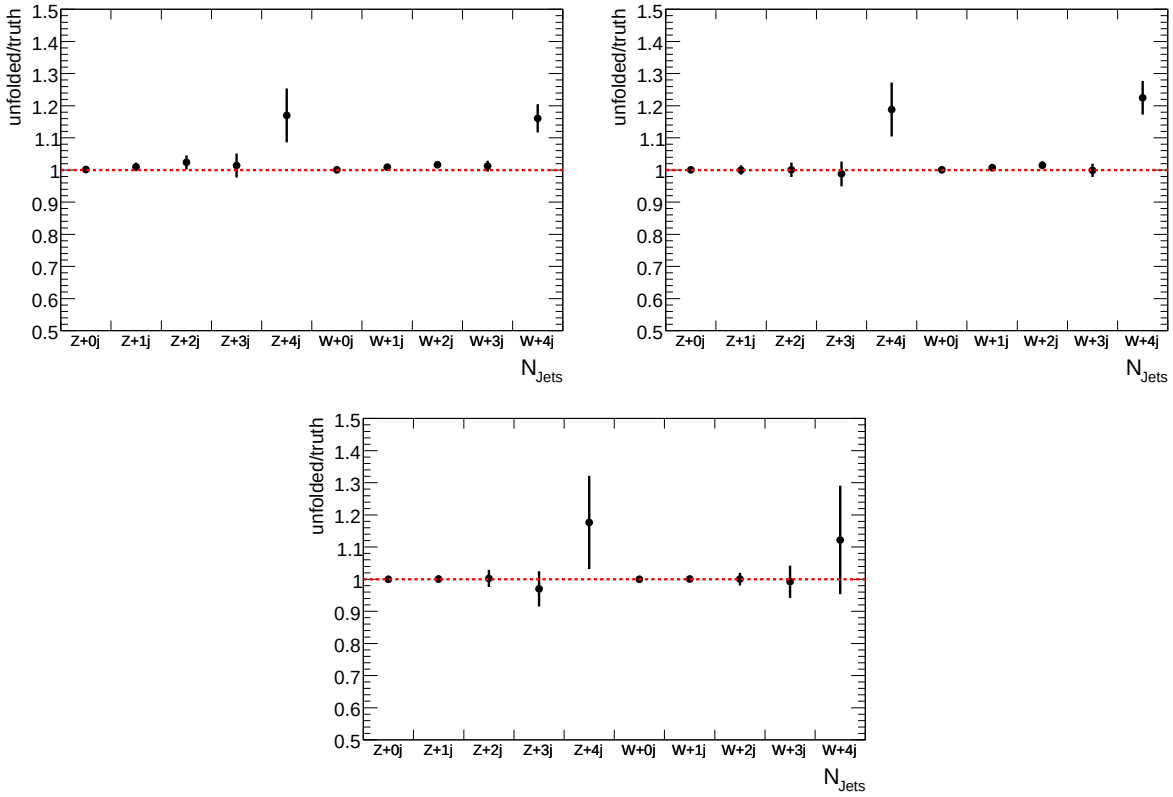

Figure 8.2: The deviation of the unfolded distribution from the truth distribution for SHERPA (upper left plot), ALPGEN (upper right plot) and PYTHIA (bottom plot) for W and Z events with 0-4 jets.

The deviations visible in the boundary bins are explained by the migration behaviour. Only W and Z events with up to 4 jets are considered. From the migration matrix in figure 8.1 it becomes transparent that for 4 jet events the tendency to migrate to a smaller jet multiplicity is high. So the W/Z + 3 jet bins contain many W/Z + 4 truth jet events. During unfolding these events are sorted back to the 4 jet bin. This principle also affects the W/Z + 4 jet bin. It contains many original W/Z + 5 truth jets events. The unfolding is only performed for up to = 4 additional jets. Hence, these events remain in the 4 jet bin and cause the deviation. As cross check figure 8.3 shows the same distribution (here only for SHERPA) as the plot above, but here for the unfolding for up to 5 jets. Here for events with up to 4 additional jets a very good agreement with the true distribution can be seen. The boundary bin effects now apply to the 5 jet bins. It was tried to remove the boundary bin effects by splitting the candidate events into = 0 jets, = 1 jets, = 2 jets, = 3 jets, = 4 jets and $\geq$ 5 jets and unfold this distribution. However, for five and more jets the differences between the models (ALPGEN full simulation and SHERPA fast simulation, which will be used for the measurement, see section 8.2) are too large and hence this was not feasible.

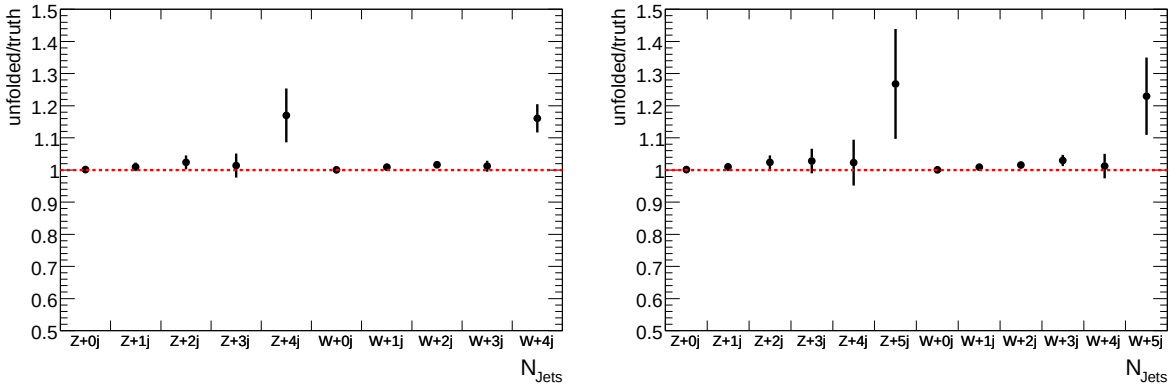

Figure 8.3: The deviation of the unfolded distribution from the truth distribution for SHERPA for W and Z events with 0-4 jets (left plot) and for 0-5 jets (right plot).

8.1.5 Model dependence of the migration matrix

The errors quoted by the unfolding procedure only consider the statistical uncertainties of measured distribution and migration matrix. However, a larger uncertainty is caused by the models, which form the basis of the migration matrix. The calculation of a migration matrix relies on Monte Carlo simulations of the events and the detector. In this section migration matrices and unfolding results of different Monte Carlo generators and different detector simulations are compared. Still only the signal W and Z jet multiplicity distributions are considered.

Choice of the Monte Carlo generator

Figure 8.4 shows the migration matrices calculated with SHERPA, ALPGEN and PYTHIA. Surveying the migration matrices already indicates that there are differences in the characteristic of the migrations. SHERPA shows the smallest migrations, PYTHIA the largest (for example W+3 truth jet → W+3 jet: SHERPA 60%, ALPGEN 54%, PYTHIA 48%; Z+3 truth jet → Z+3 jet: SHERPA 59%, ALPGEN 55%, PYTHIA 48%).
A reason for the differences can be the transverse momenta distributions of the truth jets, which are presented in figure 8.5. SHERPA produces the hardest jets and PYTHIA the softest jets. The generators show differences of up to 20%-30% in the tails. The same behaviour can be attested for the reconstructed jets shown in figure 8.6. The jet reconstruction efficiency and accuracy increases with increasing jet p_T. This is shown in chapter 4 and in [39] and [44]. So the different migration behaviour can be explained by the differences of the p_T spectra. The differences between SHERPA and ALPGEN are smaller for Z events than for W events. This is reflected by the migration matrices.

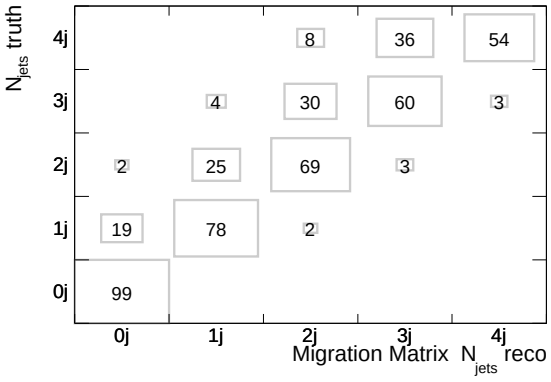

(a) SHERPA W events

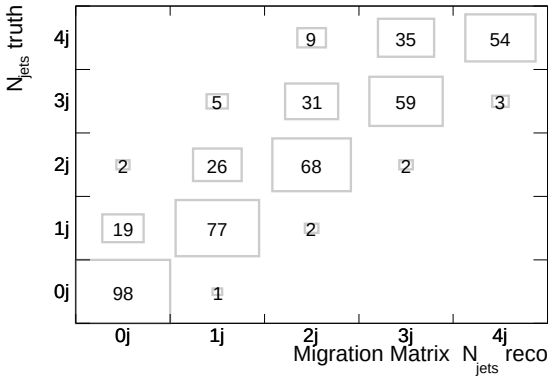

(b) SHERPA Z events

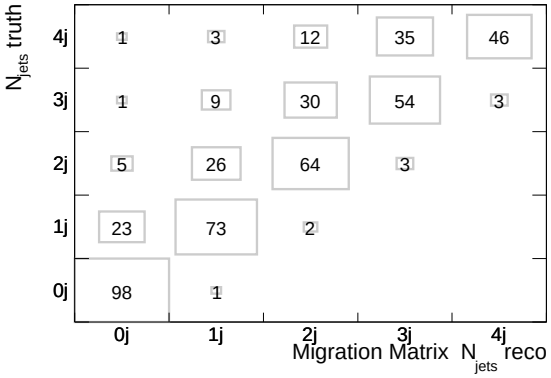

(c) ALPGEN W events

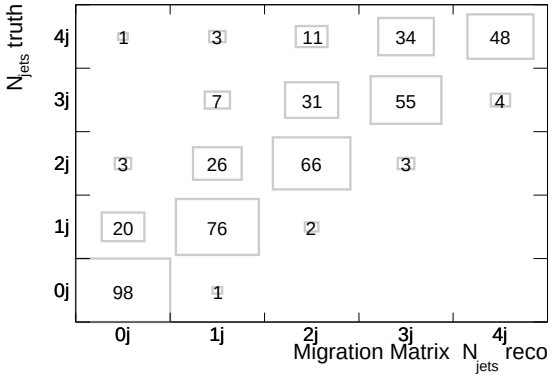

(d) ALPGEN Z events

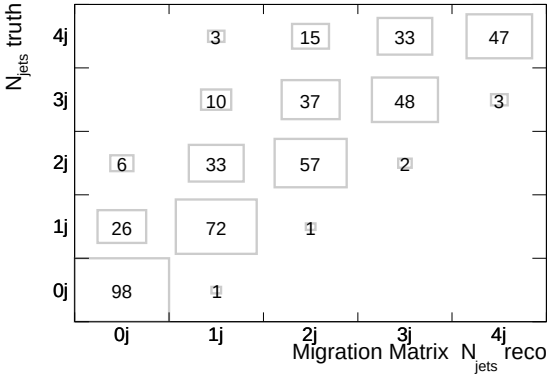

(e) PYTHIA W events

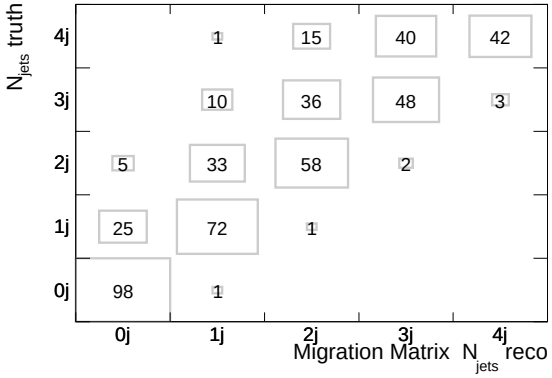

(f) PYTHIA Z events

Figure 8.4: The migration matrices generated with SHERPA, ALPGEN and PYTHIA. GEANT4 detector simulation is applied to all generators. Shown is the relative size of the matrix elements in percent. The normalization of the migration matrix is done in that way that the sum of probabilities of what happens to an event on truth level when it goes through the detector is equal to one. All event selection cuts are applied.

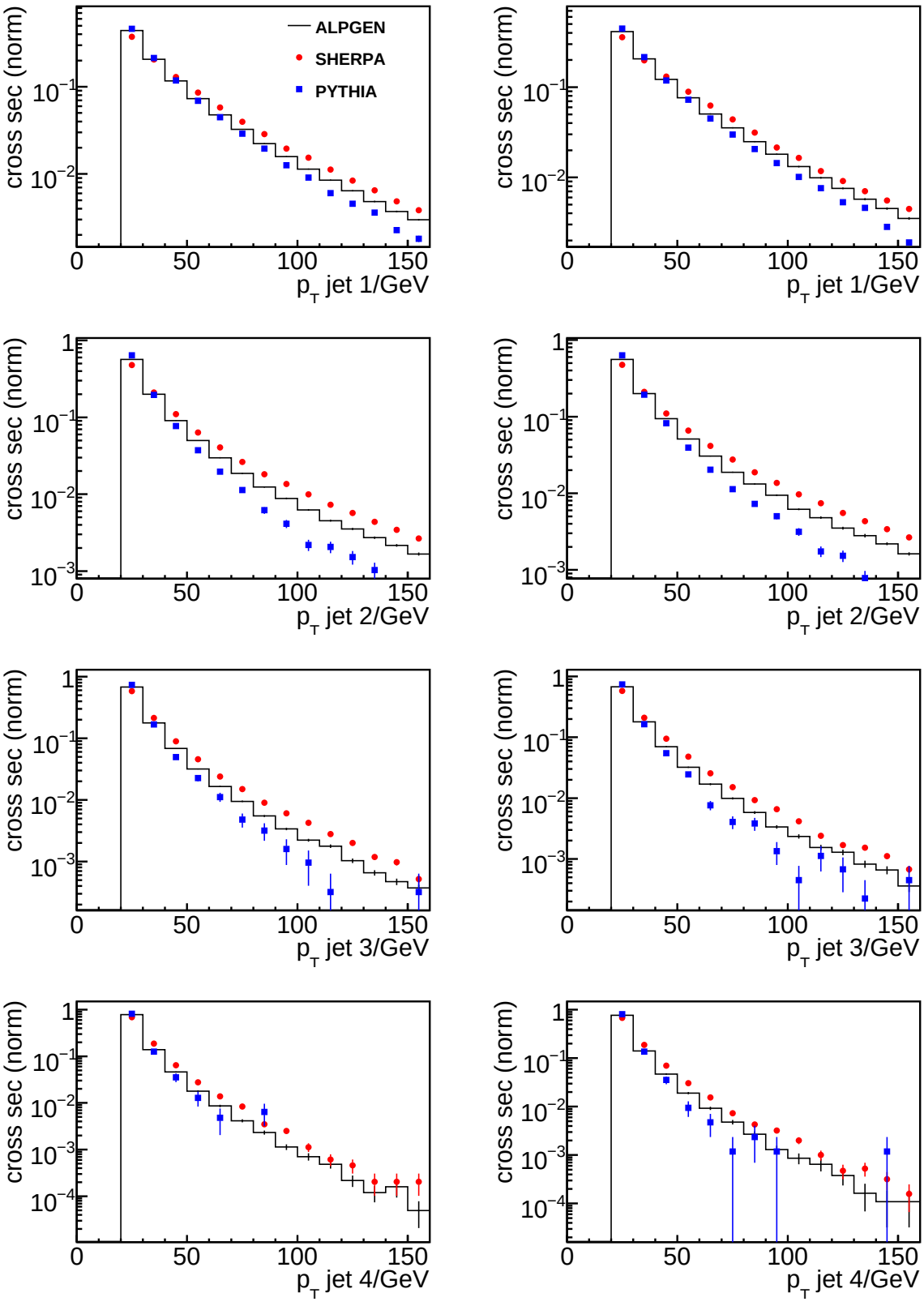

Figure 8.5: Transverse momentum p_T of hadron jet 1,2,3,4 for W (left) and Z (right) events for hadron jets passing $p_T > 20\,\text{GeV}$ and $|\eta| < 2.5$ cuts. No additional event selection cuts are applied. Compared are the generators ALPGEN , SHERPA and PYTHIA . For PYTHIA the statistics for three and four jets is very small.

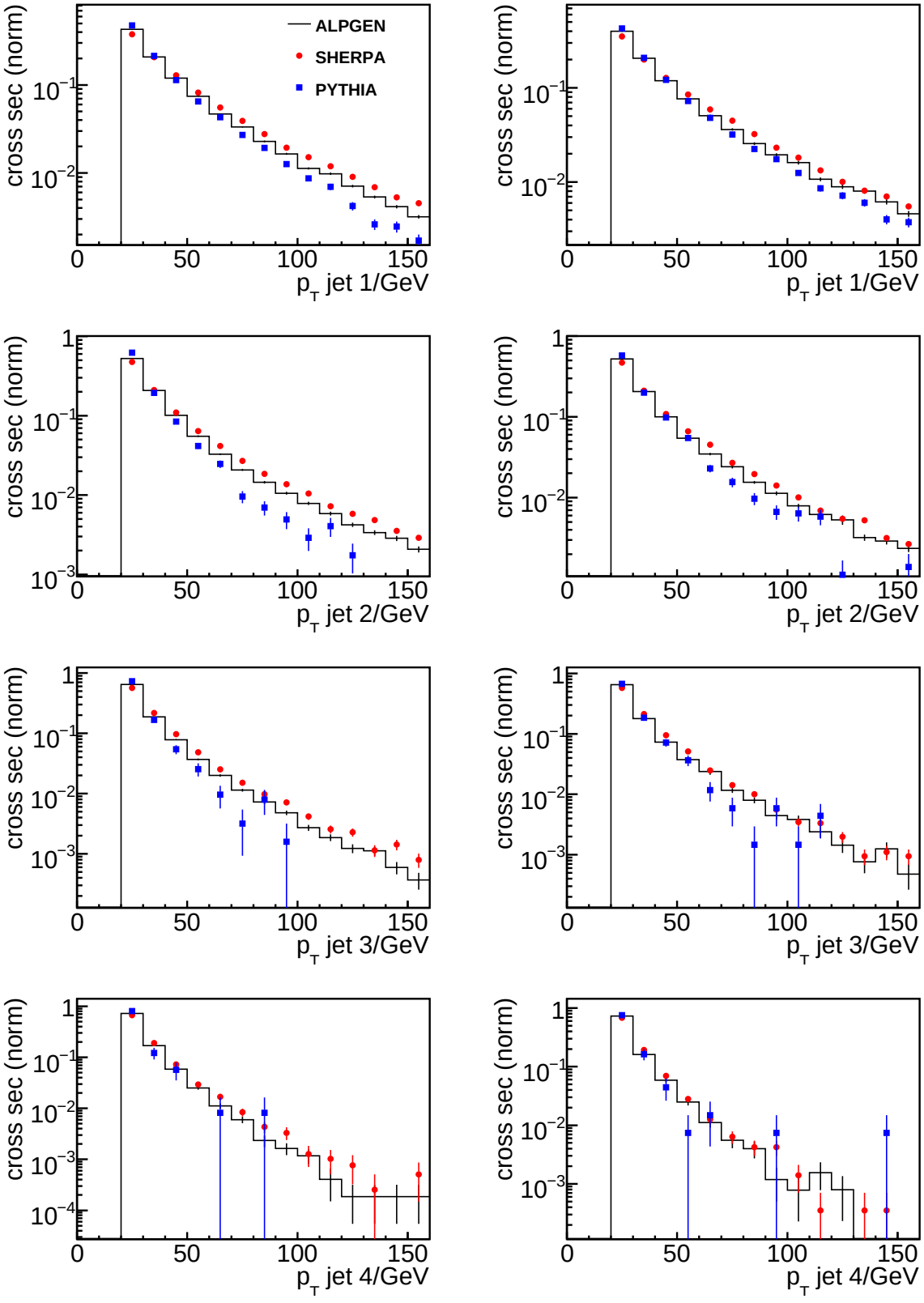

Figure 8.6: Transverse momentum p_T of reconstructed jet 1,2,3,4 for W (left) and Z (right) events for reconstructed jets passing $p_T > 20\,\text{GeV}$ and $|\eta| < 2.5$ cuts after all W and Z event selection cuts. Compared are the generators ALPGEN, SHERPA and PYTHIA. For PYTHIA the statistics for three and four jets is very small.

To check if the different jet p_T are the only cause for the observed migration differences, the jet p_T resolution of ALPGEN and SHERPA are compared. Events with exactly one truth jet and one reconstructed jet are investigated. Apart from some exceptions, in these events the truth jet and the reconstructed jet are identical. Figure 8.7 shows the p_T of the reconstructed jet for truth jets of different transverse momenta. A comparable resolution of SHERPA and ALPGEN can be attested. The migration behaviour differences can be explained by differences in the jet p_T distributions. With regard to analysing data it is important to compare the jet p_T of data and simulation and choose the Monte Carlo generator for calculating the migration matrix, whose jet p_T distributions describe the jet p_T distributions of the data best.
From figures 8.5 and 8.6 it becomes transparent that the statistics of high jet multiplicity events for PYTHIA is very small and the p_T tails are partly empty. Hence, in the following PYTHIA is not considered.

The Monte Carlo generators ALPGEN and SHERPA are compared in order to test the influence of the different migration behaviour. Both samples include full detector simulation and the same event selection cuts have been applied. By comparing the N_{jets}^{meas} with the N_{jets}^{truth} distribution (from the same Monte Carlo generator) the impact of using migration matrices calculated with different Monte Carlo generators is tested. Figure 8.8 shows both migration matrices and the results obtained by unfolding ALPGEN with SHERPA and SHERPA with ALPGEN .
The migration matrix of SHERPA shows a smaller migration tendency than ALPGEN . This is reflected in the unfolding results. Unfolding the ALPGEN jet multiplicity distribution with SHERPA , too few events are re-sorted into the higher jet bins. For SHERPA unfolded with ALPGEN , too many events are re-sorted into the high jet multiplicity bins. The W+jets distributions clearly reveal this behaviour. The largest deviations are seen for W + 2 and 3 jets with about 8%. These differences are caused by jet p_T differences of 20%-30% in the tails. For Z+jets the migration differences are slightly smaller than for W+jets, mostly the deviations are inside the statistical errors. The consequences of resorting too few or too many events are not as pronounced as for W+jets, but nevertheless they are existent. Boundary effects can be seen both when unfolding ALPGEN with SHERPA (about 10%) and vice versa (about 20%-30%). For ALPGEN unfolded with SHERPA , the boundary effects are partly compensated (in figure 8.2 boundary effects of 10-20% are observed) by re-sorting too few events back into the higher jet bins. For SHERPA unfolded with ALPGEN the boundary effects are amplified, because too many events are re-sorted. The boundary bin effects are roughly of the same size for W and Z events and cancel out by calculating the cross section ratio. Also the effects from re-sorting too few or too many events into the higher jet bins veer toward the same direction for W and Z events. The resulting deviation for the W to Z ratio is smaller than than the deviations separately for W and Z.

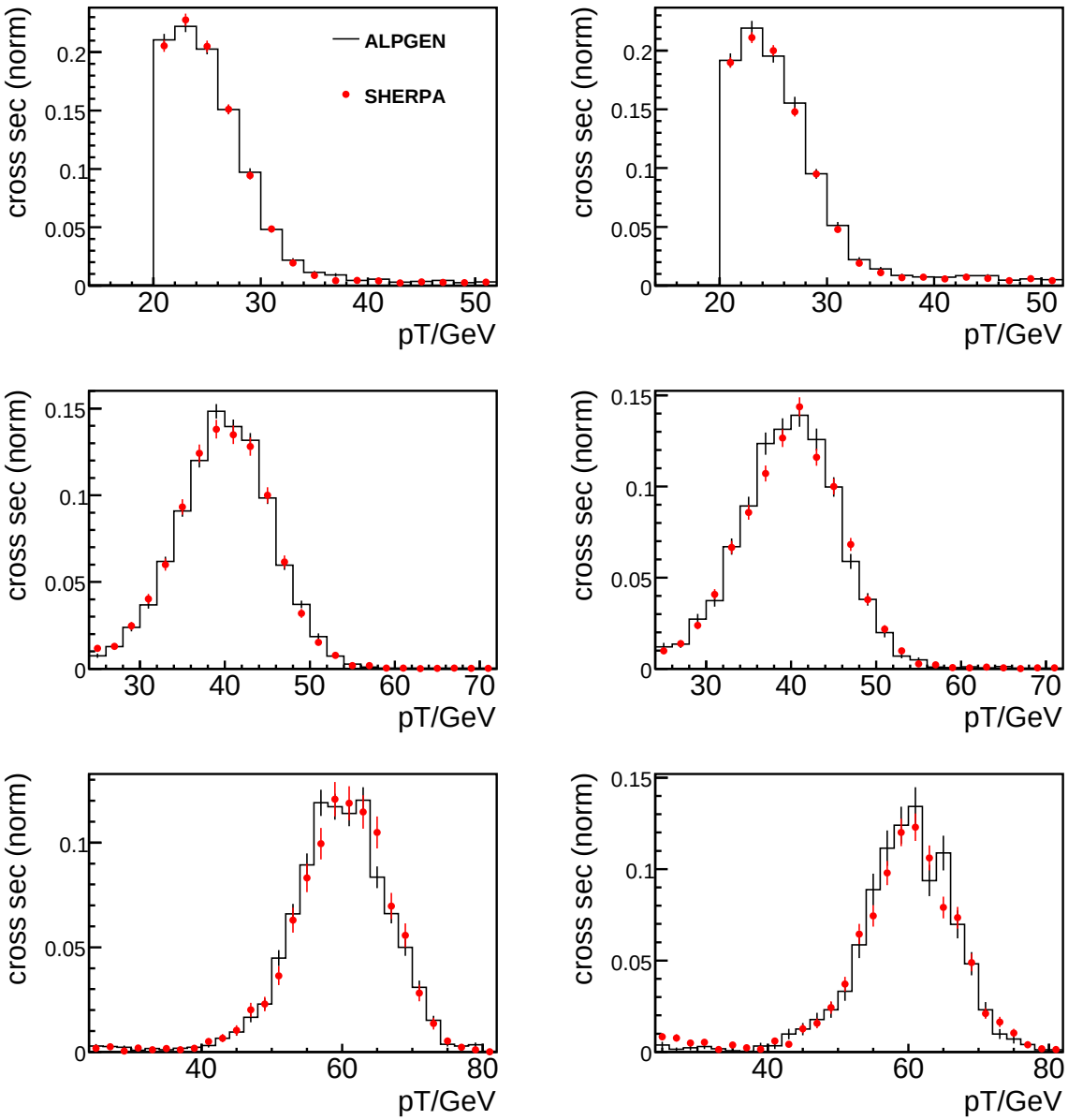

Figure 8.7: The reconstructed jet p_T in one jet events for truth jets with $24\,\text{GeV} < p_T < 28\,\text{GeV}$ (top plot), $40\,\text{GeV} < p_T < 46\,\text{GeV}$ (middle plot) and $60\,\text{GeV} < p_T < 66\,\text{GeV}$ (bottom plot) comparing ALPGEN full simulation and SHERPA full simulation. The left plots show the resolution for W events, the plots on the right for Z events.

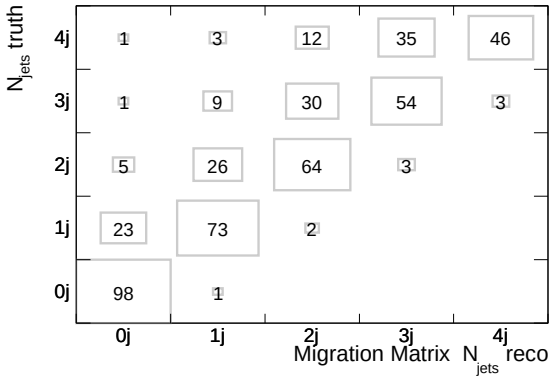

(a) ALPGEN W events

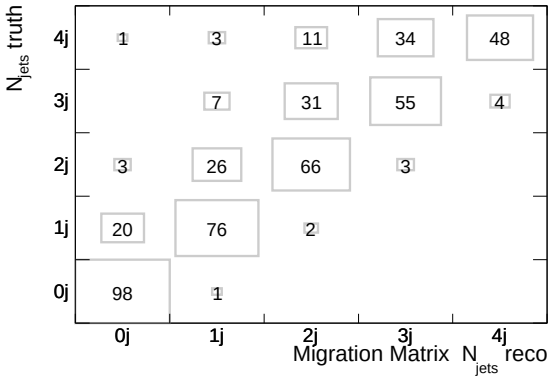

(b) ALPGEN Z events

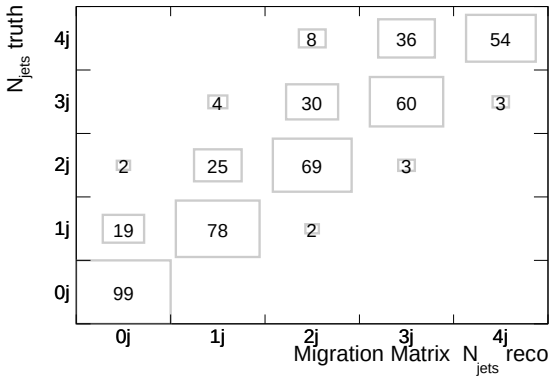

(c) SHERPA W events

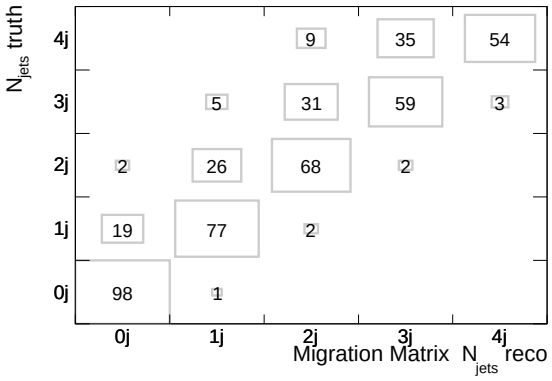

(d) SHERPA Z events

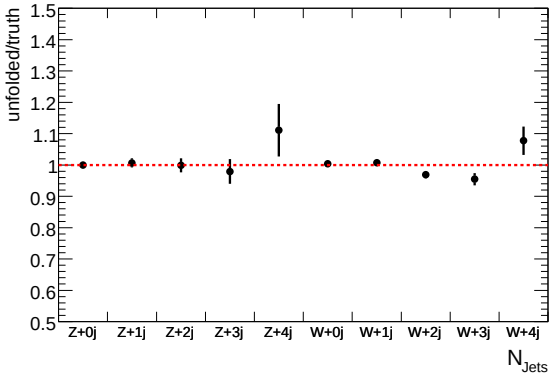

(e) ALPGEN unfolded with SHERPA

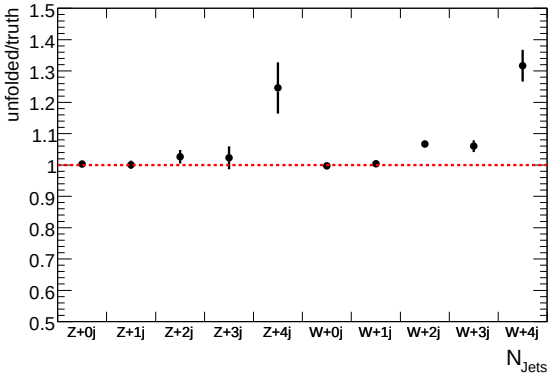

(f) SHERPA unfolded with ALPGEN

Figure 8.8: Comparison of the unfolding results obtained by unfolding ALPGEN full simulated events with a SHERPA full simulated migration matrix and vice versa.

Choice of the detector simulation

The next step is to test the sensitivity of the migration matrix to the detector simulation. The migration matrix calculated with full simulated events (using GEANT4) is compared to the migration matrix calculated with the fast detector simulation ATLFAST-II. In both cases the same generator, SHERPA , was used. The matrices are presented in figure 8.9. The fast simulated events show a smaller migration tendency than the full simulated events. Again the differences for W events are slightly larger than for Z events (for example W+4 truth jets → W+4 jets; full: 54%, fast: 58%; Z+4 truth jets → Z+4 jets; full: 54%, fast: 55%).
In analogy to the previous section, the fully simulated $N_{jets}{}^{meas}$ distribution is unfolded with the fast simulation migration matrix and vice versa. The results are presented in figure 8.9. The fast simulation shows a smaller tendency to migrations than the full simulation. Therefore when unfolding fast simulation with full simulation, too many low jet multiplicity events are re-sorted to the higher jet multiplicities. When unfolding full simulation with fast simulation, the opposite effect is observed. This behaviour is clearly visible for the W+jets distributions, for Z+jets the same behaviour is attested, but the deviations are smaller and are partly inside the statistical errors. The boundary effects still are visible. For full simulation unfolded with fast simulation they are partly compensated (5-10%), for fast unfolded with full they are amplified (20-30%). The boundary effects are roughly of the same size for W and Z and cancel out when calculating the cross section ratio. Again the differences in the migration matrices are smaller for Z than for W events. For all jet bins the deviations are smaller than 5% (except for the boundary bins) and veer towards the same direction for W and Z events.

8.1.6 Summary

In the previous sections the migration of W and Z events of one jet multiplicity to another jet multiplicity caused by the measurement of the detector and the reconstruction have been discussed. An unfolding method is presented to correct the measured jet multiplicity distributions from these migrations. The described method is based on [80] and works reliably.
The unfolding method needs a migration matrix, which describes the effects of detector and reconstruction on the jet multiplicity distributions. The migration matrix specifies the probability for a W/Z + m truth jet to be measured as a W/Z + n jet event and can only be calculated using simulated events. This model dependence of the Monte Carlo generator to produce the events and the detector simulation has been discussed. Different generator models were found to cause deviations of up to 8% in the unfolded results (mostly due to differences in the jet p_T spectra of 20%-30% in the tails), different detector simulations caused deviations of up to 5%. For both W+jets and Z+jets events the deviations veer towards the same direction. Until now only W and Z signal events were considered.

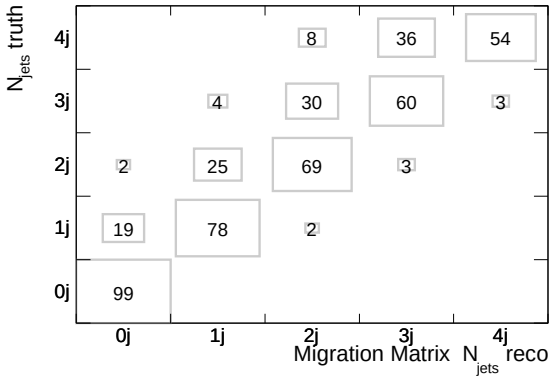

(a) SHERPA W events full simulation

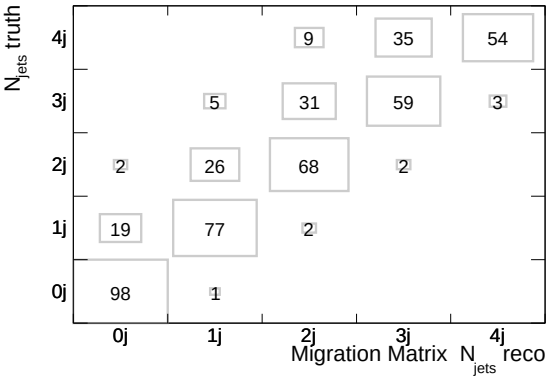

(b) SHERPA Z events full simulation

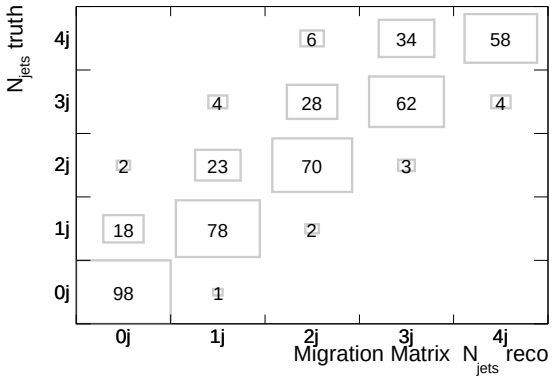

(c) SHERPA W events fast simulation

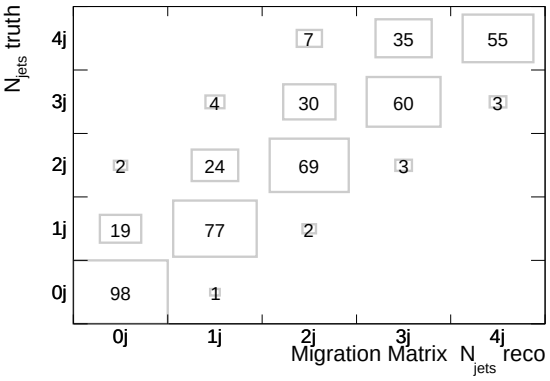

(d) SHERPA Z events fast simulation

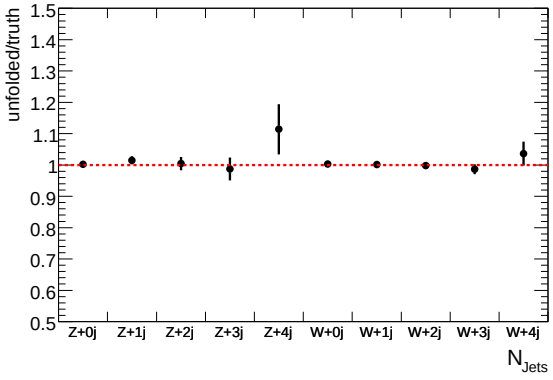

(e) SHERPA full unfolded with SHERPA fast

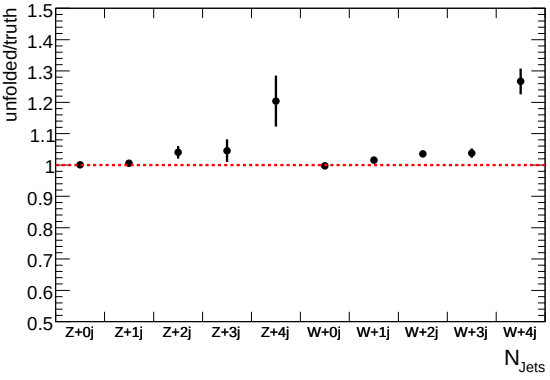

(f) SHERPA fast unfolded with SHERPA full

Figure 8.9: Comparison of the unfolding results obtained by unfolding SHERPA full simulated events with a SHERPA fast simulated migration matrix and vice versa.

8.2 Strategy of the measurement

In order to be able to compare generator predictions to the measured ratio R_n, the unfolding procedure is applied to the number of jets distributions of W and Z events before calculating the cross section ratio. Practically, the same analysis is performed as described in the previous chapter. The difference is that the unfolding procedure is integrated into the analysis after event selection and background correction and before calculating the cross section ratio. Then a result for the ratio R_n is obtained, which is calculated from unfolded W+jets and Z+jets distributions.
The previous section clarifies that the migration matrix and the unfolding procedure are sensitive to the exact description of the data by simulated events. Especially the jet transverse momenta distributions influence the migration behaviour of jets. Hence, at this point data have to be compared to the simulated events in different distributions. If there is imperfect agreement the unfolding procedure will not work, then the "real" migration behaviour most likely is not reflected by the simulation.
Because no data are available the jet multiplicity distributions for W and Z events generated with the ALPGEN Monte Carlo generator (including full detector simulation) are again considered as data. The jet multiplicity distributions are unfolded using migration matrices, which are generated using SHERPA fast simulated events. In the previous section is shown that the jets in SHERPA events reveal less migrations than jets in ALPGEN events, because of a higher average jet p_T in SHERPA events. However, the SHERPA fast simulation data set provides the highest statistics resulting in the smallest errors caused by the migration matrix. Another advantage when unfolding ALPGEN full simulation based on SHERPA fast simulation is, that deviations both due to the differences of the generators as well as due to the differing detector simulation are expected. The observed differences are however small for the 0,1 jet bin and increase to 5% and 8% respectively for the 2 and 3 (4) jet bins (see figure 8.10).

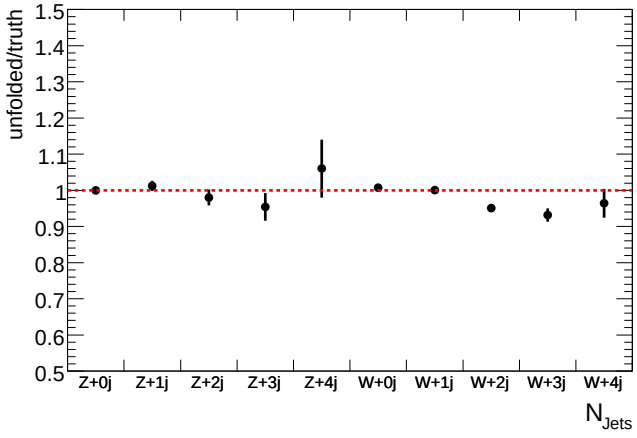

Figure 8.10: Expected deviations of the unfolded distribution from the truth distributions if unfolding ALPGEN full simulated events using a SHERPA fast simulated migration matrix. Deviations of about 10% are expected.

N_{jets}	W	rel. stat. error	Z	rel. stat. error	R_n	rel. stat. error
0	338355.0 ± 239.5	0.00	20634.3 ± 62.8	0.00	1.05 ± 0.00	0.00
1	67177.8 ± 213.3	0.00	4858.5 ± 49.9	0.01	0.88 ± 0.01	0.01
2	17781.4 ± 112.5	0.01	1402.2 ± 27.4	0.02	0.81 ± 0.02	0.02
3	4674.3 ± 60.2	0.01	373.0 ± 13.3	0.04	0.80 ± 0.03	0.04
4	1274.7 ± 39.8	0.03	111.1 ± 7.5	0.07	0.73 ± 0.05	0.07

Table 8.1: Results for the unfolded W+jets and Z+jets distributions and the cross section ratio including statistical errors calculated by using the formulae provided by [80].

8.3 Statistical unfolded results

After W and Z event selection, subtraction of the additive background and correcting for the multiplicative background, the unfolding procedure is applied to the W+jets and the Z+jets distributions. The migration matrices and the final unfolding matrices for W and Z are shown in figure 8.11. The unfolded event numbers for each jet multiplicity and the cross section ratios assuming $100\,\mathrm{pb}^{-1}$ at a centre-of-mass energy of 10 TeV are presented in table 8.1.
The statistical errors associated with each jet multiplicity after unfolding are obtained by calculating the square root of the appropriate diagonal element of the covariance matrix $\mathbf{V}$. $\mathbf{V}$ is obtained by using the formulae 8.10 as described in [80]. The covariance matrices for W and Z are presented in figure 8.12.
The statistical errors of the unfolded distributions are very small. Except for W + 4 jets all statistical errors are smaller than $\Delta N = \sqrt{N^{signal}}$. This is remarkable, because before applying the unfolding procedure all jet bins are associated with a statistical error of $\Delta N = \sqrt{N^{signal}_{events} + N^{background}_{events}}$. It is to be expected that after applying the unfolding procedure the relative errors are larger than before. Looking at the correlation matrices, which are shown in figure 8.13, it is obvious that there are strong correlations between the different jet bins, i.e. also the errors of the individual jet bins must be correlated. Especially the W/Z + 0 jet bins, which have the highest statistics of events, have a large influence on the other jet bins. This complicates the interpretation of the quoted errors. It has to be checked if the errors obtained after unfolding describe the statistical fluctuations, which are expected for an integrated luminosity of $100\,\mathrm{pb}^{-1}$. Therefore pseudo experiments were performed and are described in the next section.

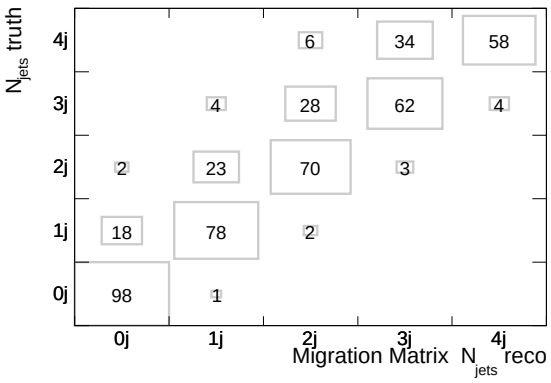

(a) Migration matrix for W

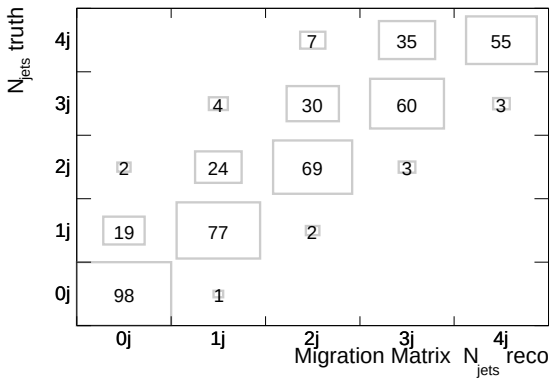

(b) Migration matrix for Z

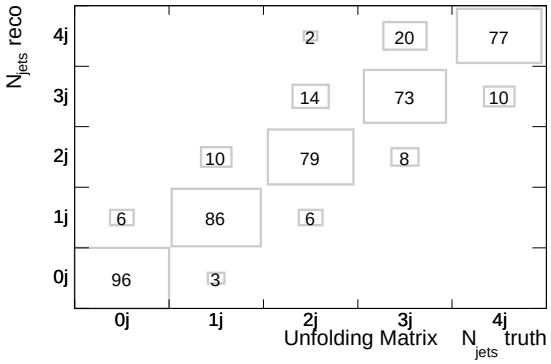

(c) Unfolding matrix for W

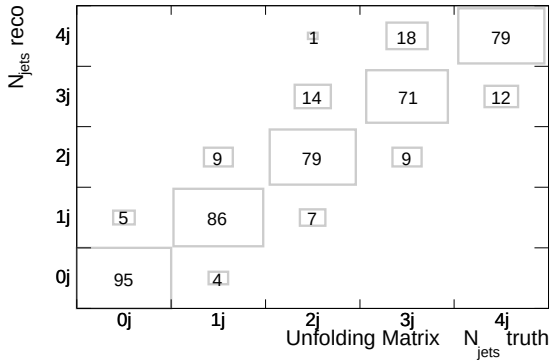

(d) Unfolding matrix for Z

Figure 8.11: The migration matrices (upper plots) and iteratively determined unfolding matrices (lower plots) for W (left) and Z (right) events. The migration matrices are generated with SHERPA fast simulated events. Entries are rounded to integer percent.

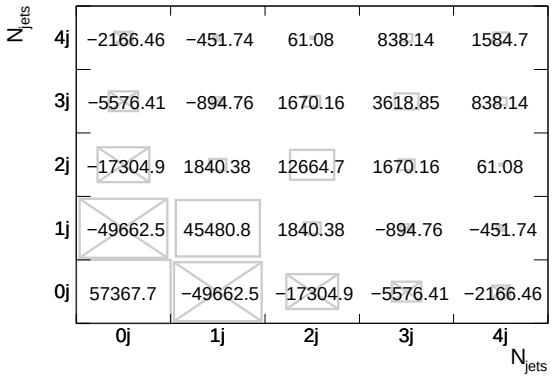

(a) Covariance matrix V for W

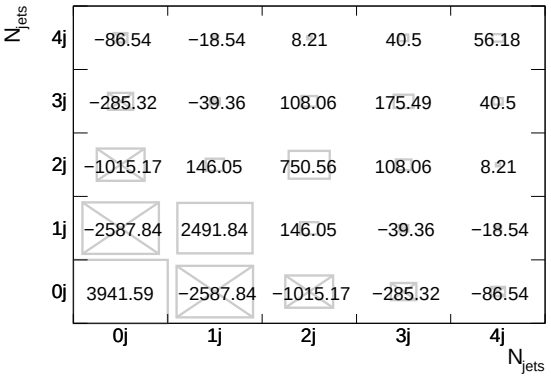

(b) Covariance matrix V for Z

(c) Covariance matrix V(M) for W

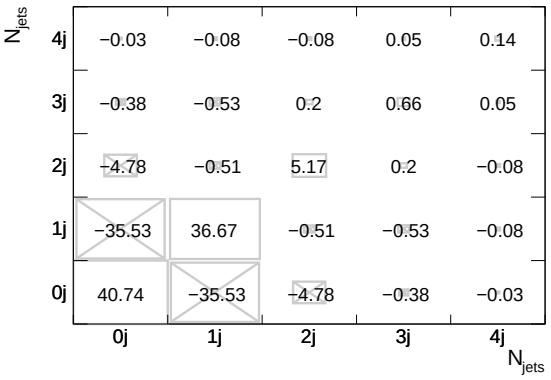

(d) Covariance matrix V(M) for Z

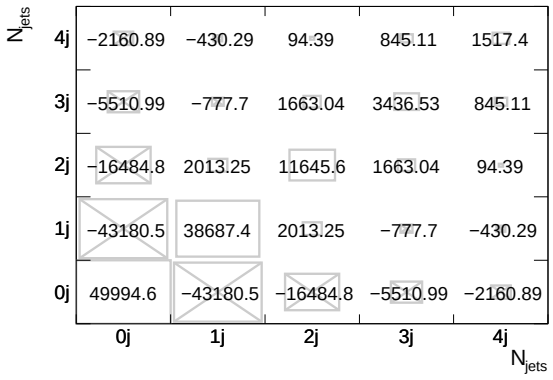

(e) Covariance matrix V(N_{meas}) for W

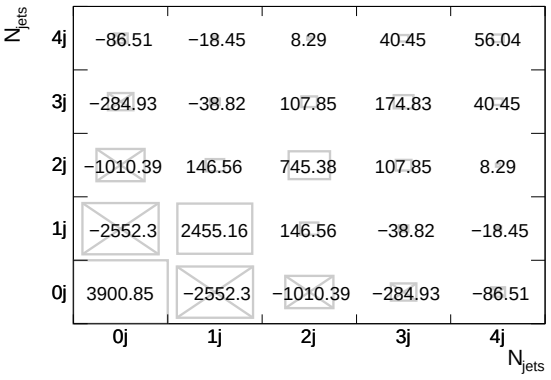

(f) Covariance matrix V(N_{meas}) for Z

Figure 8.12: The covariance matrices V of the unfolded distributions for W (left) and Z (right) events as obtained using the formulae provided by [80]. On the top the complete covariance matrices (V) are presented, in the middle the contribution resulting from the statistical uncertainty of the migration matrix (V(M)) itself, on the bottom the uncertainties resulting from the statistical uncertainty of the measured events (V(N_{meas})).

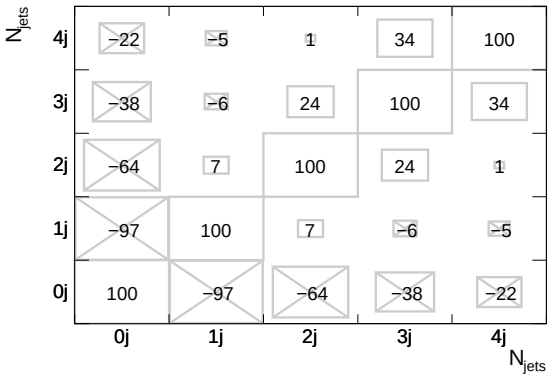

(a) Correlation matrix V for W

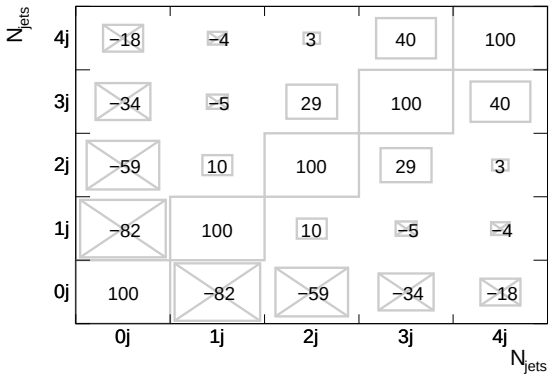

(b) Correlation matrix V for Z

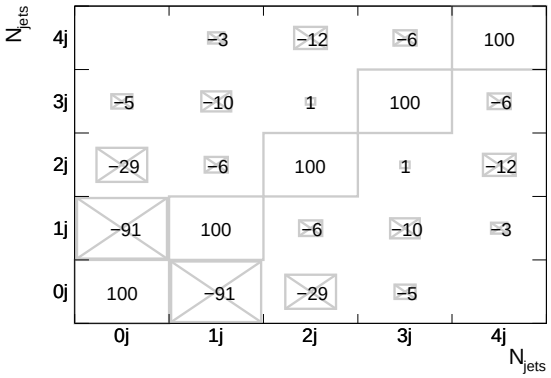

(c) Correlation matrix V(M) for W

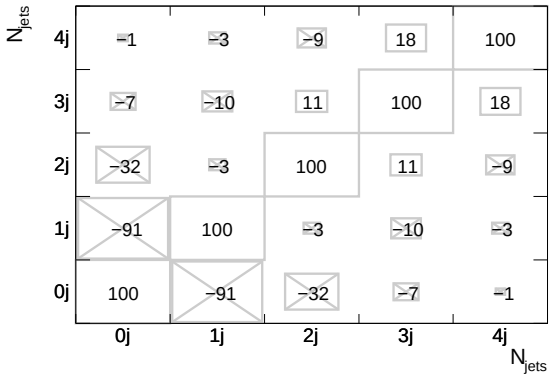

(d) Correlation matrix V(M) for Z

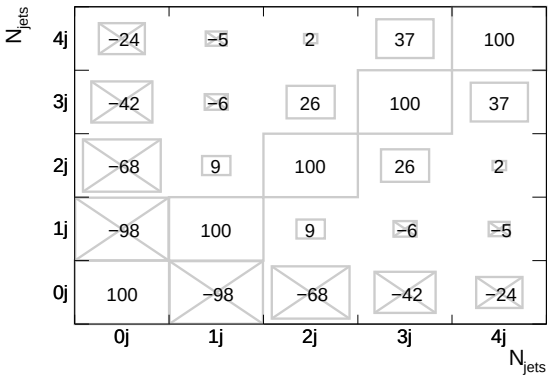

(e) Correlation matrix V(N_{meas}) for W

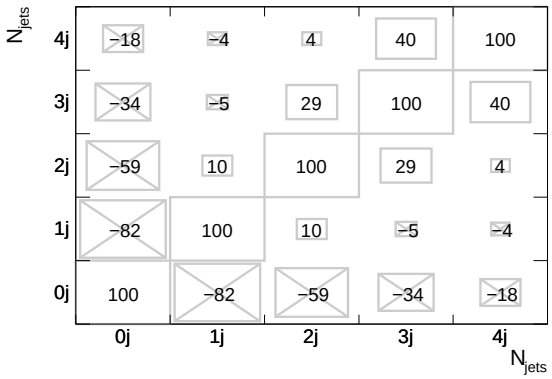

(f) Correlation matrix V(N_{meas}) for Z

Figure 8.13: The correlation matrices ($V(i,j)/\sqrt{V(i,i)\cdot V(j,j)} = \rho_{i,j}$) of the unfolded distributions for W (left) and Z (right) events as obtained using the formulae provided by [80]. On the top the complete correlation matrices are presented, in the middle the contribution resulting from the statistical uncertainty of the migration matrix itself, on the bottom the uncertainties resulting from the statistical uncertainty of the measured events. Entries are rounded to integer percent.

8.4 Pseudo experiments

The effects of statistical fluctuations of the measured values on the unfolding procedure are tested by performing pseudo experiments. Each jet bin of the W+jets candidate sample and of the Z+jets candidate sample is independently varied according to a Poisson distribution (before correcting the background). After each jet bin is varied, the background is subtracted and the unfolding procedure is applied. From the results of the pseudo experiments for each jet bin the pull is calculated, defined by:

$$\text{pull}^{\text{W/Z + n jets}} = \frac{N_{\text{measured}}^{\text{W/Z + n jets}} - N_{\text{measured, pseudo experiment}}^{\text{W/Z + n jets}}}{\Delta N_{\text{measured, pseudo experiment}}^{\text{W/Z + n jets}}} \tag{8.18}$$

where $\text{N}_{\text{measured}}^{\text{W/Z + n jets}}$ is the original number of W/Z + n jet events. $\text{N}_{\text{measured, pseudo experiment}}^{\text{W/Z + n jets}}$ is the number of W/Z + n jet events obtained from unfolding the pseudo experiments, $\Delta N_{\text{measured, pseudo experiment}}^{\text{W/Z + n jets}}$ is the error calculated as described in [80].
If the errors are estimated correctly, the pull distribution is expected to be a Gaussian with $\mu = 0$ and $\sigma = 1$. The resulting pull distributions for W are presented in figure 8.14 and for Z in figure 8.15 for 10000 pseudo experiments. The widths of all distributions are clearly larger than 1. Hence, the errors quoted by the unfolding procedure are too small and do not reflect the expected statistical fluctuations. Similar statements have been made before for other analyses [82].
In order to quote correct statistical errors, the results of the pseudo experiments are used to estimate appropriate errors. New covariance matrices C are calculated by:

$$C_{kl} = \frac{1}{n_{\text{pseudo experiments}}} \cdot \sum_{j=1}^{n_{\text{pseudo experiments}}} (N_{\text{pseudo experiment}}^{\text{W/Z + k jets}} - N_{\text{measured}}^{\text{W/Z + k jets}})^j \cdot (N_{\text{pseudo experiment}}^{\text{W/Z + l jets}} - N_{\text{measured}}^{\text{W/Z + l jets}})^j \tag{8.19}$$

The obtained covariance and correlation matrices for W and Z are presented in figure 8.16. The diagonal entries of the new covariance matrices are clearly larger than the diagonal entries of the covariance matrices, which are obtained from the unfolding. The correlation coefficients for the off-diagonal elements are smaller than before. The correlations of neighbouring bins are higher for higher jet multiplicities, because in these jet bins a higher tendency to migrations occurs (see migration matrices in figure 8.11). The correlation coefficients for $\text{N}_{\text{jets}} \leq 3$ are smaller than $\sim \frac{1}{3}$. This allows here to approximately neglect the correlation terms and to interpret $\sqrt{C_{ii}}$ as statistical errors. **C** does not describe the statistical uncertainties caused by the migration matrices. However, comparing **C** and **V(M)** (see figure 8.12), **C** is much bigger than **V(M)** and hence here the contribution of **V(M)** is neglected.

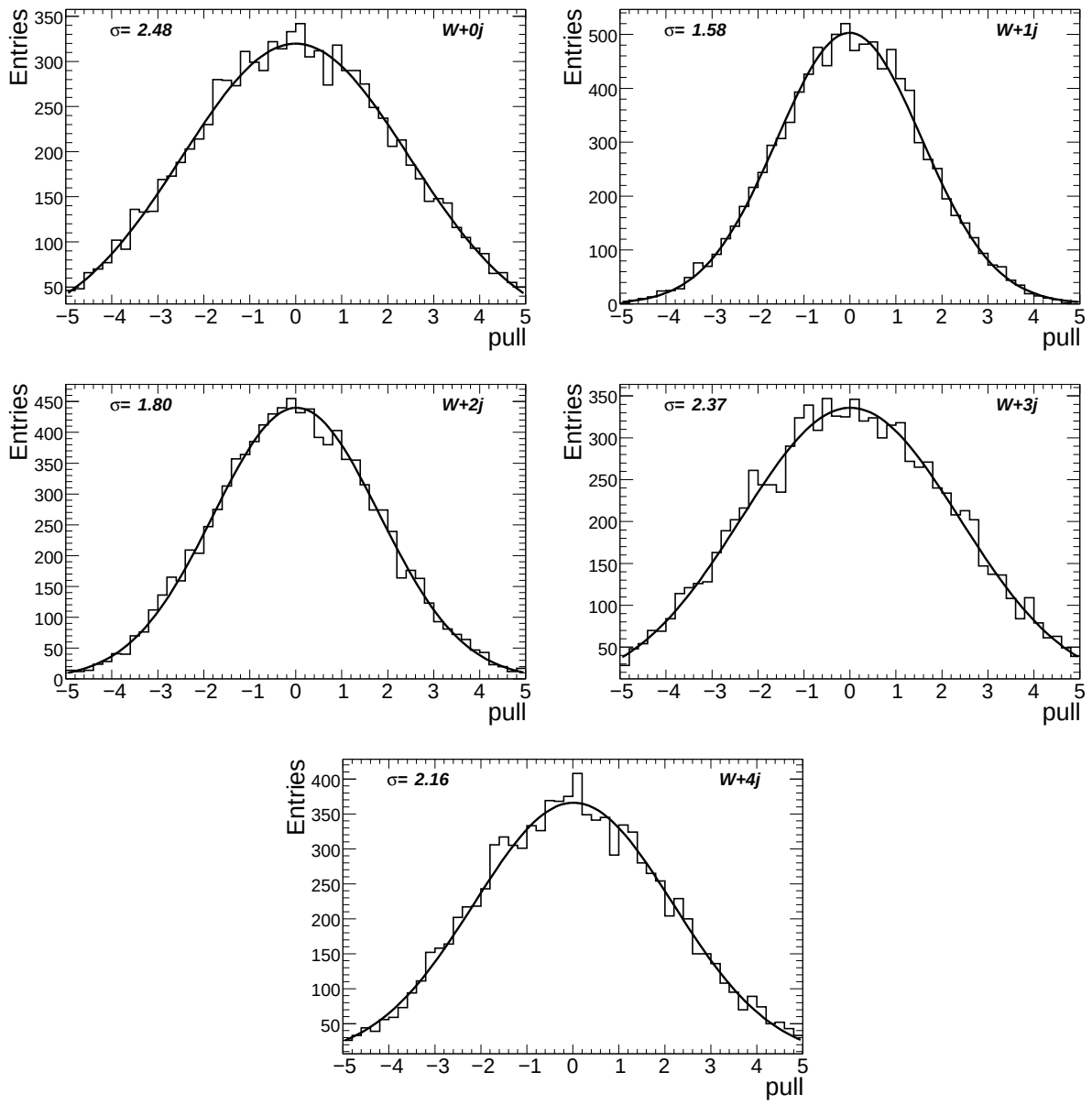

Figure 8.14: Pull distributions obtained by performing 10000 pseudo experiments for the unfolded W+jets events using the errors obtained by the formulae provided by [80]. Shown are the Gaussian fit functions and the σ of the fits.

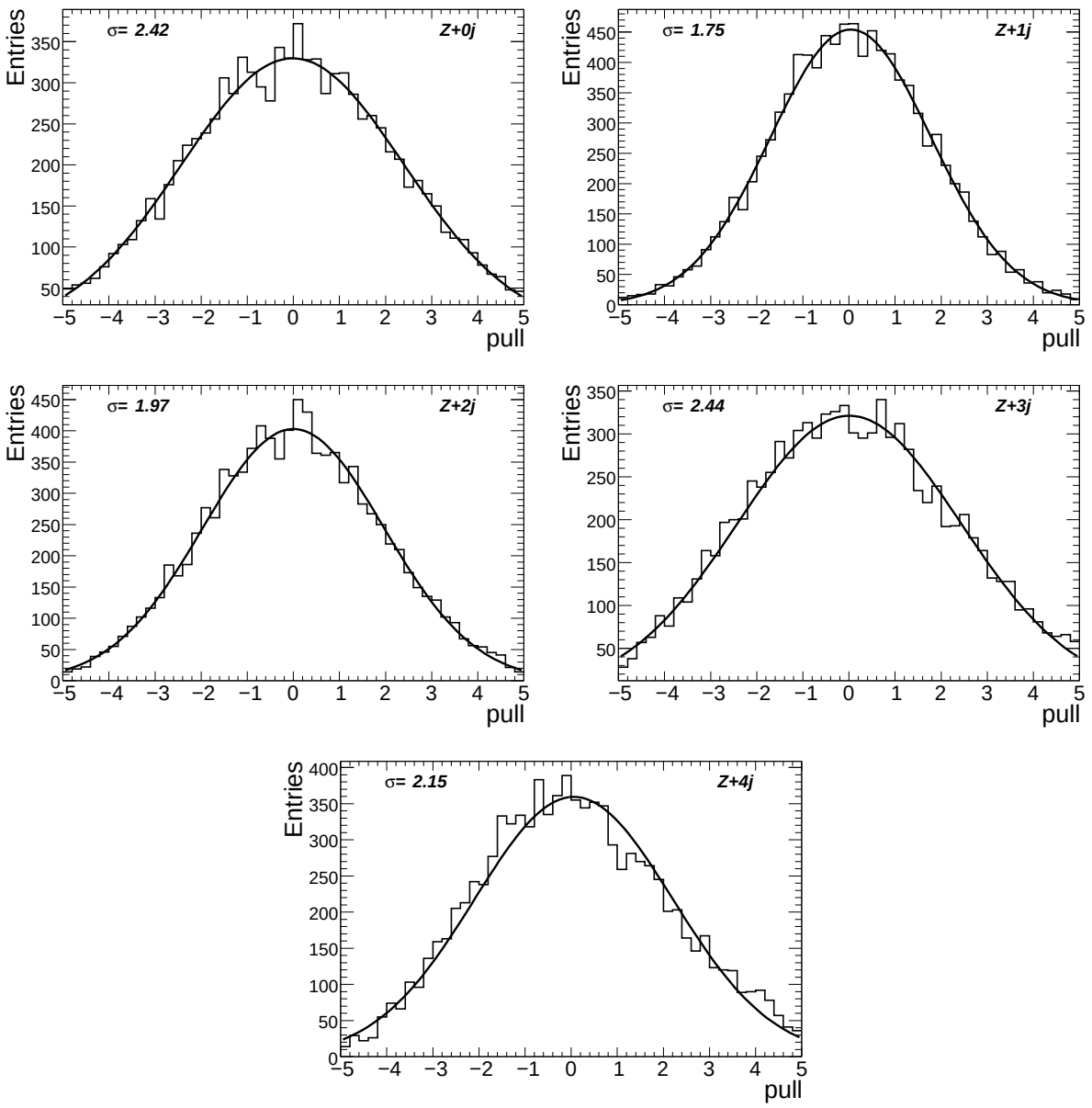

Figure 8.15: Pull distributions obtained by performing 10000 pseudo experiments for Z+jets events using the errors obtained by the formulae provided by [80]. Shown are the Gaussian fit functions and the σ of the fits.

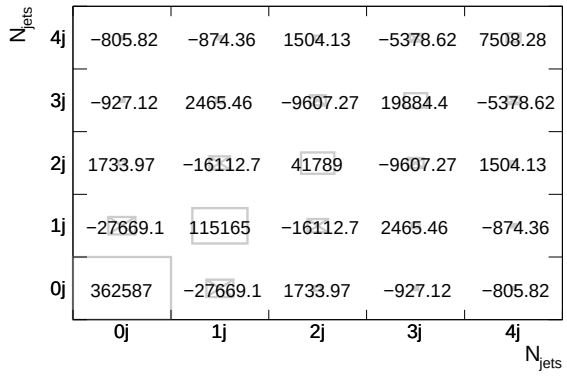

(a) Covariance matrix for W

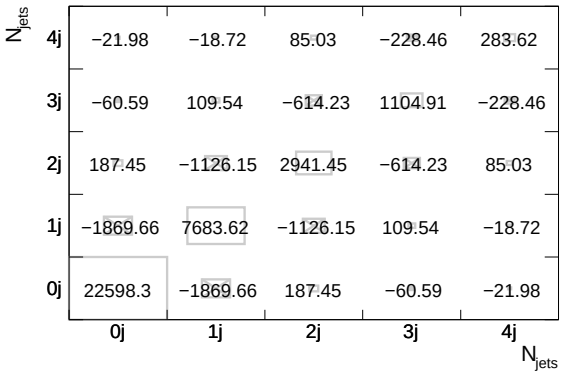

(b) Covariance matrix for Z

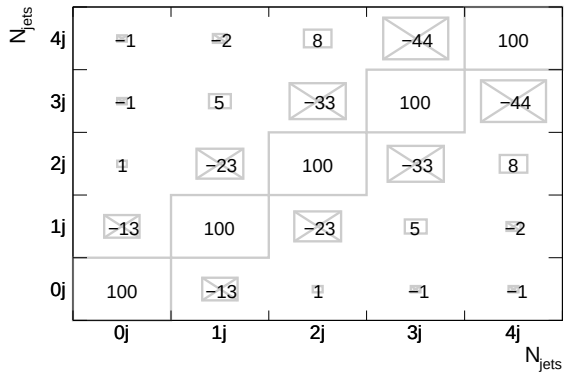

(c) Correlation matrix for W

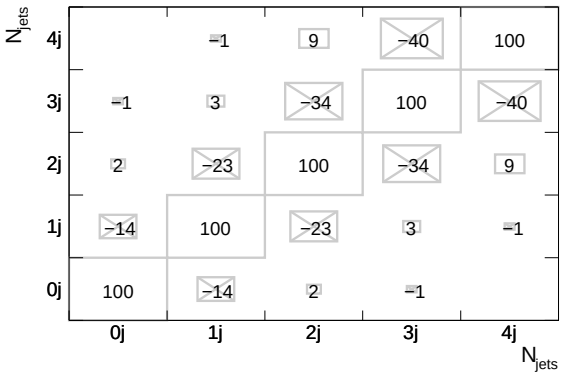

(d) Correlation matrix for Z

Figure 8.16: Covariance matrices (upper plots) and correlation matrices (lower plots, entries are rounded to integer percent) for W (left) and Z (right) events. These matrices are calculated based on the pseudo experiments. The statistical error of the correlation coefficients ρ of the correlation matrix is $\Delta\rho = \frac{1-\rho^2}{\sqrt{1-N}}$ with N = 10000. Hence, for all ρ the statistical error is smaller than 1%.

N_{jets}	W	rel. stat. error	Z	rel. stat. error	R_n	rel. stat. error
0	338355.0 ± 602.2	0.00	20634.3 ± 150.3	0.01	1.05 ± 0.01	0.01
1	67177.8 ± 339.4	0.01	4858.5 ± 87.7	0.02	0.88 ± 0.02	0.02
2	17781.4 ± 204.4	0.01	1402.2 ± 54.2	0.04	0.81 ± 0.03	0.04
3	4674.3 ± 141.0	0.03	373.0 ± 33.2	0.09	0.80 ± 0.08	0.09
4	1274.7 ± 86.7	0.07	111.1 ± 16.8	0.14	0.73 ± 0.12	0.17

Table 8.2: Results for the unfolded W+jets and Z+jets distributions and the cross section ratio including the adjusted statistical errors calculated using the covariance matrices obtained by performing pseudo experiments.

8.5 Final statistical results

The statistical results with adjusted errors are presented in table 8.2. For each jet multiplicity the adjusted statistical error is larger than $\sqrt{N}$. Comparing the precision of the results of the unfolded cross section ratio and the cross section ratio of the previous chapter, the statistical uncertainty is higher for the unfolded results. This is expected, because the statistical uncertainty must be increased by the unfolding procedure. The statistical errors of the unfolded results are determined by pseudo experiments, they should be a realistic estimate of the actual fluctuations. Hence, the cross section ratio for the four jet bin can be measured with a reasonable statistical precision of about 20% for $\mathcal{L} = 100\,\mathrm{pb}^{-1}$.

8.6 Systematic uncertainties

In this chapter the same analysis is performed like in the previous chapter. Hence, the same considerations as described in section 7.6 concerning systematic effects apply. Uncertainties due jet energy, electron energy and $\not\!\!E_T$ determination and (QCD) background normalization are investigated. The results are presented in table 8.3 and in figures 8.17 and 8.18. Comparing figures 8.17 and 8.18 with figures 7.15 and 7.16 a similar behaviour can be attested. As expected, on average the systematic uncertainties are amplified by the unfolding procedure.
The only difference to the previous chapter is that in this chapter systematic effects arising from the unfolding procedure have to be additionally considered. This especially applies to the migration matrix itself. The migration matrix has to be calculated by using simulated events and completely relies on the chosen Monte Carlo generator and the detector simulation. The influence of imperfect models is tested.

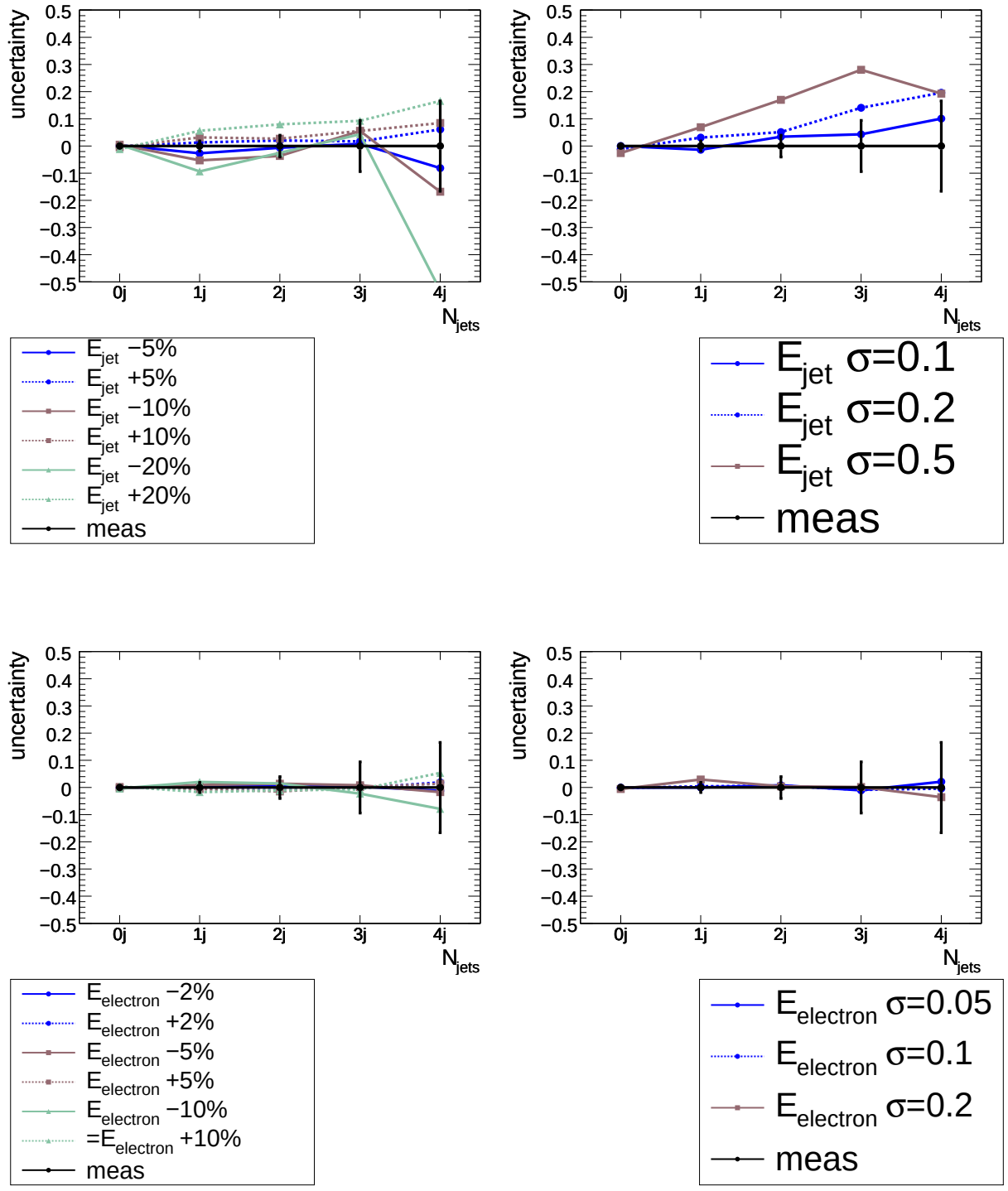

Figure 8.17: Upper plots: Relative difference for the measurement while changing the jet energy scale by -20, -10, -5, 5, 10 and 20 percent (left) and the jet energy resolution by 10 (smeared by a Gaussian with mean=1 and σ=0.1), 20(σ=0.2) and 50(σ=0.5) percent (right) with statistical errors. Lower plots: Relative difference for the measurement while changing the electron energy scale by -10, -5, -2, 2, 5 and 10 percent (left) and the electron energy resolution by 5(smeared by a Gaussian with mean=1 and σ=0.05), 10(σ=0.1) and 20(σ=0.2) percent (right) with statistical errors.

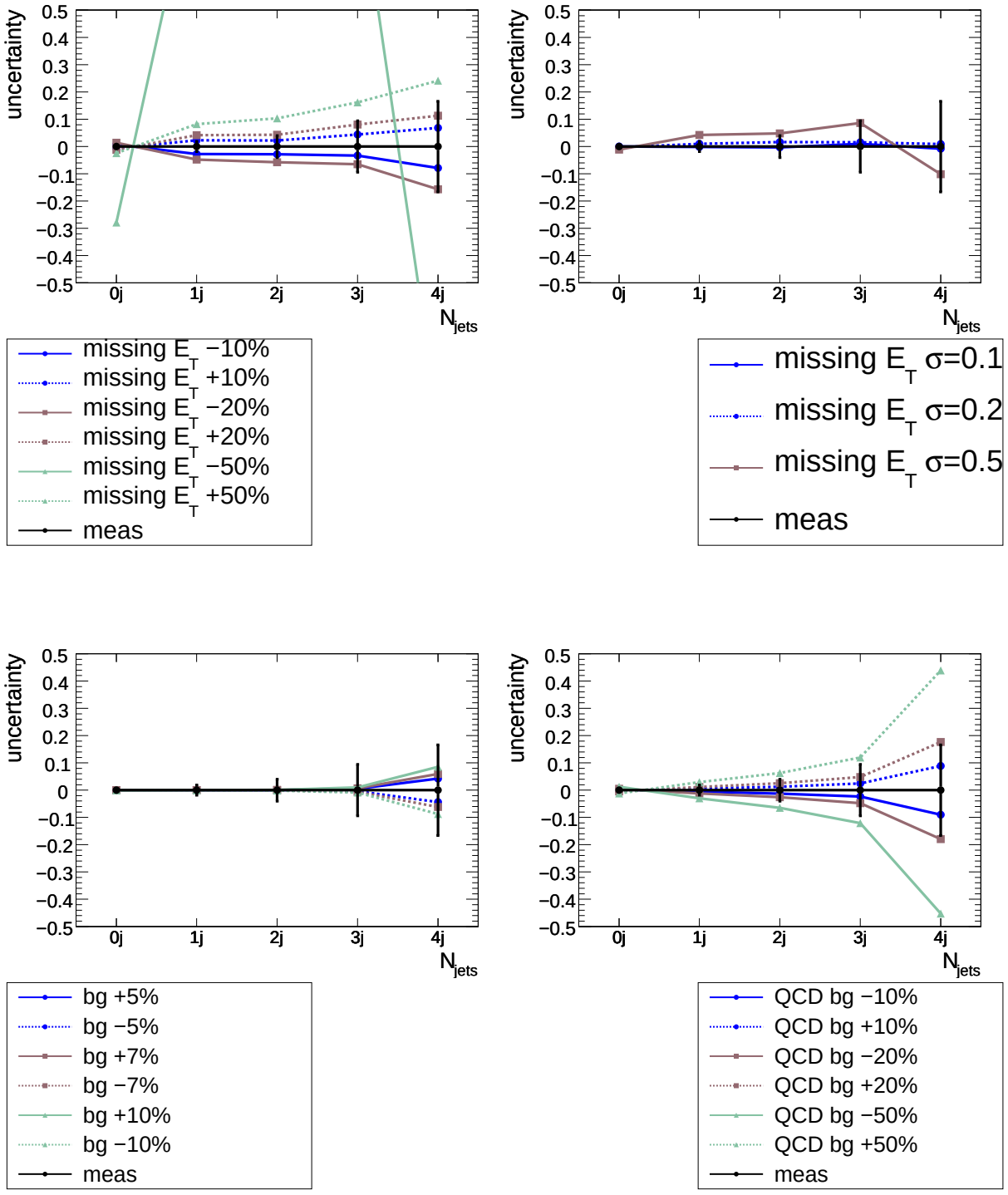

Figure 8.18: Upper plots: Relative difference for the measurement while changing the missing energy scale by -50, -20, -10, 10, 20 and 50 percent (left) and the missing energy resolution by 10 (smeared by a Gaussian with mean=1 and σ=0.1), 20 (σ=0.2) and 50(σ=0.5) percent (right) with statistical errors. Lower plots: Relative difference for the measurement while changing the cross section of the MC samples by -10,-7,-5,5, 7 and 10 percent (left). Relative difference for the measurement while changing the QCD background normalisation by 10, 20 and 50 percent with statistical errors (right).

8.6.1 Model - calculation of the migration matrix

A migration matrix is needed for unfolding, which must be calculated from Monte Carlo. There are always uncertainties due to representation of the data by the event generators or by imperfect simulation of the detector by the simulation program.
Both uncertainties have been tested separately in section 8.1.5 and deviations of up to 10% percent were found. For this analysis W and Z number of jets distributions generated with ALPGEN full simulation are unfolded with a migration matrix generated with SHERPA fast simulation. Hence, both uncertainties - a different Monte Carlo generator with deviating jet p_T spectra and a different detector simulation - are contained in the results. To get a handle on the uncertainty, the resulting ratio R_n is compared to the ratio R_n as obtained, if unfolding the ALPGEN number of jets distributions with an ALPGEN migration matrix. The deviations for each jet bin are assumed to represent the systematic uncertainties. Both the ALPGEN and the SHERPA Monte Carlo data set contain enough events that deviations because of statistical fluctuations are small compared to the deviations caused by the different models. The obtained deviations are listed in table 8.3.
In general, with increasing jet multiplicity the deviations increase. This behaviour is expected, because the migration matrices for ALPGEN and SHERPA show larger differences for the high jet multiplicity bins. A possibility to determine the systematic uncertainty more precisely is to cross check the results of more than two Monte Carlo generators. However, at the moment there are no data sets of other generators with appropriate statistics in the high jet multiplicity bins available. The deviations due to different p_T spectra can be reduced by re-weighting the Monte Carlo, as soon as data are available.

8.6.2 Combined systematic uncertainties

The same systematic effects are considered like in the previous chapter and the combined systematic uncertainty is determined identically. For all asymmetric uncertainties the statistical uncertainties are larger than the asymmetry. The errors are symmetrized and added quadratically. The results are presented in table 8.3. The systematic uncertainties and the statistical uncertainties are again of similar size for $\mathcal{L} = 100\,\mathrm{pb}^{-1}$. Here again the major problem is the normalization of the QCD and $t\bar{t}$ backgrounds.
The uncertainties are amplified by 7-20% by the unfolding procedure (except for R_3, but this is most likely a statistical effect).
The systematic uncertainty due to the model dependence of the migration matrix is not included in the combined systematic uncertainties. This uncertainty is considered completely independent of the other uncertainties and will be handled separately. The uncertainty caused by the calculation of the migration matrix is of similar size as the combined systematic uncertainty of all other systematic effects. Presumably this uncertainty can be reduced by re-weighting.

	uncertainties in %				
N_{jets}	0	1	2	3	4
$E_{jet}^{scale} \mp 5\%$	+0.2 -0.1	-2.8 +1.4	-0.7 +2.1	+0.8 1.8	-8.2 +6.2
E_{jet}^{res} 10%	0.0	-1.4	3.4	4.4	10.1
$E_{electron}^{scale} \mp 2\%$	-0.1 +0.0	+0.5 -0.2	+0.4 0.0	+0.3 -0.3	-1.2 +1.9
$E_{electron}^{res}$ 5%	-0.0	0.0	0.9	-1.0	2.1
$E_T^{miss,scale} \mp 10\%$	+0.8 -0.7	-2.7 +2.3	-2.8 +2.2	-3.3 +4.4	-7.9 +6.8
$E_T^{miss,res}$ 10%	0.0	-0.2	-0.3	+1.0	-0.8
background$^{scale} \pm 1\,\sigma$	-0.0 0.0	-0.0 0.0	0.1 -0.1	+0.7 -0.6	+6.0 -6.1
QCD $\pm$ 10%	+0.3 -0.3	-0.6 +0.6	-1.3 +1.2	-2.4 +2.4	-9.0 +8.8
model	0.0	2.2	4.8	3.5	13.6
combined	$\pm$ 0.6	$\pm$ 2.8	$\pm$4.2	$\pm$5.7	$\pm$14.8
statistic	$\pm$ 1%	$\pm$ 2%	$\pm$ 4%	$\pm$9%	$\pm$ 17%

Table 8.3: Systematic uncertainties (in %) for the measurement of the ratio R_n for events with 0 to 4 additional jets with migration corrections. The systematic uncertainties are about the same size as the statistical uncertainties.

8.7 Signal efficiency

The unfolded number of jets distribution is an estimate of the truth jet multiplicities for W+jets and Z+jets events. In this analysis the unfolding procedure only corrects the effects of the detector. This is done for W and Z events passing all event selection cuts. Hence, the unfolded number of jets distribution corresponds to the truth jets distribution after all event selection cuts. By applying event selection cuts on the events, the truth jets distributions and the ratio R_n are modified, because the selection efficiencies differ for different jet multiplicities. Figure 8.19 shows the ratio R_n for truth jets for events without cuts and events passing all event selection cuts. The ratios clearly differ. The unfolded number of jets distributions are corrected for these selection efficiencies. The advantage is that these efficiency corrections can be described by a simple factor, because between "all events" and "selected events" no migrations between jet bins occur. The only difficulty is to define which stage is referred to as "all events". All Monte Carlo generators include cut-offs and normally are adopted to simulate only events, which are located inside the acceptance region of the detector.
In this analysis "all events" are defined as all events contained in the ALPGEN data set. The definition criteria for truth jets are not changed between "all events" and "selected events". Hence, the signal efficiencies are defined as

$$\epsilon^n_{\text{signal W/Z}} = \frac{N_{events}(\text{W/Z + n truth jets}^{\text{selected as W/Z}})}{N_{events}(\text{W/Z + n truth jets before all selection cuts})} \tag{8.20}$$

$N_{\text{events}}^{\text{W/Z + n jet}}$ after unfolding is then corrected by $N_{\text{events}}^{\text{W/Z + n jet}} / \epsilon^n_{\text{signal W/Z}}$.
The signal efficiencies are summarized in table 8.4. Comparing the signal efficiencies for the different jet bins it is obvious that there are cuts inside the ALPGEN data set.

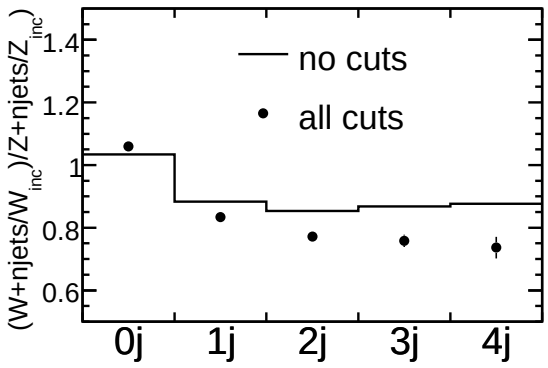

Figure 8.19: The ratio R_n for truth jets after applying W and Z event selection cuts and before.

N_{jets}	signal eff. in % for selected W candidates $\epsilon^n_{\text{W signal}}$	signal eff. in % for selected Z candidates $\epsilon^n_{\text{Z signal}}$
0	27.1 ± 0.1	18.8 ± 0.1
1	28.1 ± 0.1	20.2 ± 0.1
2	27.6 ± 0.1	20.0 ± 0.1
3	27.0 ± 0.2	20.4 ± 0.2
4	26.0 ± 0.3	20.1 ± 0.4

Table 8.4: Signal selection efficiencies for W (left) and Z (right) for the 0 to 4 jet sample.

The signal efficiency is expected to decrease with increasing jet multiplicity, but here the efficiencies are roughly constant. The results for W+jets and Z+jets and the cross section ratio including the signal efficiency correction are presented in figure 8.5.

8.8 Results

In this chapter a method is presented to correct the W and Z jet multiplicity distributions for detector effects before calculating the cross section ratio as a function of the jet multiplicity. This measurement is performed in analogy to the measurement described in chapter 7. The unfolding procedure is applied to the W+jets and Z+jets distribution after event selection and background subtraction and before calculation of the ratio. For the detector effect correction the unfolding method presented in [80] is used. This method works reliable, but by performing pseudo experiments it has been shown that the statistical errors of the unfolded distribution are underestimated. Hence, the statistical errors were recalculated using pseudo experiments.
Like in the previous chapter the uncertainties due to some systematic effects are tested. The same uncertainties are considered, but these are completed by uncertainties arising from the unfolding procedure. Already at a luminosity of $100\,\text{pb}^{-1}$ at a centre-of-mass

N_{jets}	W	rel. stat. error	Z	rel. stat. error	R_n	rel. stat. error
0	1247442.3 ± 2220.0	0.00	110008.1 ± 801.5	0.01	1.03 ± 0.01	0.01
1	239374.7 ± 1209.2	0.01	24029.5 ± 433.6	0.02	0.91 ± 0.02	0.02
2	64447.5 ± 740.9	0.01	6998.9 ± 270.7	0.04	0.84 ± 0.03	0.04
3	17296.2 ± 521.8	0.03	1826.0 ± 162.7	0.09	0.86 ± 0.08	0.09
4	4910.5 ± 333.8	0.07	551.7 ± 83.7	0.14	0.81 ± 0.13	0.17

Table 8.5: Results for the unfolded and corrected W+jets and Z+jets distributions and the cross section ratio including the adjusted statistical errors calculated using the covariance matrices obtained by performing pseudo experiments.

N_{Jets}	$\frac{\frac{W+njets}{\sum_{n=0}^{4} W+njets}}{\frac{Z+njets}{\sum_{n=0}^{4} Z+njets}}$						
0	1.03	±	1% (stat.)	±	1% (syst.)	±	0% (model)
1	0.91	±	2%(stat.)	±	3% (syst.)	±	2% (model)
2	0.84	±	3%(stat.)	±	4% (syst.)	±	5%(model)
3	0.86	±	9%(stat.)	±	6% (syst.)	±	4% (model)
4	0.81	±	17%(stat.)	±	15% (syst.)	±	14%(model)

Table 8.6: Unfolded and corrected ratio R_n after all event selection cuts and background subtraction including statistic and systematic errors for 0 to 4 jets.

energy of 10 TeV the statistical and systematic uncertainties are of similar size (like in the previous chapter). The dominant uncertainties mostly arise from the background normalization and the unfolding procedure. The results will not improve only by increasing the size of the data set. Only a more precise normalization of the background contributions - especially $t\bar{t}$ and QCD dijet events - will improve the precision of the results. The uncertainty due to the model dependence of the unfolding procedure can be reduced by comparing the jet p_T spectra of Monte Carlo and data and in case of discrepancies produce a reweighed migration matrix.
Nevertheless, the unfolded cross section ratio of W and Z for events with four jets can be determined with a reasonable precision of roughly 25%. In [76] CDF Run I results on the cross section ratio W/Z as a function of the jet multiplicity are published. There the ratio for 4 jets is measured with a precision of $\sim$ 60% (without unfolding). About 25% uncertainty after unfolding is a clear improvement.

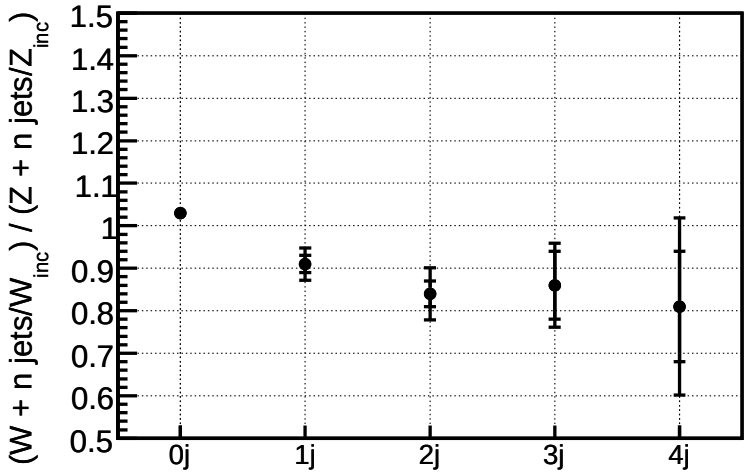

Figure 8.20: Measured ratio R_n after all event selection cuts and background subtraction including statistic and systematic errors for 0 to 4 jets.

Summary and Outlook

The LHC has recently been put into operation. The acquisition of collision data has started. This thesis addresses the preparation of a physics analysis of W and Z events with early data.

A precise knowledge of W+jets and Z+jets events is crucial at the LHC. W bosons, Z bosons and jets are expected in the decay products of for example top events and almost all New Physics processes. It is difficult to observe New Physics or perform measurements of top quarks without well predicted W+jets and Z+jets cross sections and properties. In contrast to W+jets events, investigations of Z+jets events are easier, because of the clear event structure of the Z. Because W+jets and Z+jets events are very similar, the idea of this analysis is to use Z+jets events as tool to learn more about and to predict W+jets events. This strategy allows one to gain important information about the jet production mechanisms in Z+jets and W+jets events, which, because of their complexity, cannot be calculated precisely.

The event shapes of W and Z events were compared. Some small differences are expected from theory, but these were found to be small and well predictable. However, in observables, which are sensitive to the production mechanisms of associated jets, W and Z events are very similar. Hence, Z+jets events are well adopted to be used as template to estimate W+jets events.

Then the prospects of a measurement of the cross section ratio of W and Z events as a function of the jet multiplicity are presented. The analysis was performed in two steps. First, the cross section ratio $R_n = \frac{\sigma(\mathrm{W + n\ jets})}{\sigma(\mathrm{Z + n\ jets})} \cdot \frac{\sigma(\mathrm{Z_{inc}})}{\sigma(\mathrm{W_{inc}})}$ was measured. The values of R_1, R_2 and R_3 can be fitted and extrapolated to R_4, in order to estimate the number of W+4 jets events by measuring Z+4 jets events. An uncertainty on the W+4 jet estimate of about 16% could be achieved, which is smaller than the actual uncertainty of 20%-50% on the W+4 jets normalization. This result will contribute to improve the precision of $t\bar{t}$ analysis.

Additionally the measured values of R_0 to R_5 can be used to test theory and generator predictions. Until now collision data at these high energies are not available. The presented cross section ratio measurement is a very fast analysis, where most systematic uncertainties cancel. R_5 for example can be measured with a precision of about 35% with the first $100\,\mathrm{pb}^{-1}$ at a centre-of-mass energy of 10 TeV. Generator predictions then can be compared to the results in order to test and tune the models.

Although this analysis is held easy in order to be performed with first data, statistical and systematic errors are already of similar size. This analysis is perfectly adopted for the early data, but later a different strategy has to be developed. It was found that the

systematic uncertainties are dominated by the $t\bar{t}$ cross section uncertainty. Therefore, a promising possibility is to simultaneously measure the $t\bar{t}$, W and Z cross sections. Here already first studies using a Neural Network were performed. The results look promising, however, details are outside the scope of this analysis.
In the second step a measurement analogously to the former was performed, but here the number of jets distributions of W and Z events were corrected for detector effects before calculating the cross section ratio. This allows to compare theoretical predictions directly to the corrected values and to compare the results of different detectors. For the unfolding of the distributions the approach of G. D'Agostini was used and tested to work reliable. The quoted errors are, however, not reflecting the expected statistical fluctuations. They were recalculated based on pseudo experiments. The statistical and systematic uncertainties are, as expected, amplified by unfolding. With regard to systematic uncertainties the same effects as observed in the previous measurement contribute. The $t\bar{t}$ background dominates the systematic uncertainties, complemented by the model dependence of the unfolding procedure. However, for up to 4 jets reasonable results are obtained with an uncertainty of about 25% for R_4. The precicision of the results can again be improved by simultaneously determining the W, Z and $t\bar{t}$ cross sections
In the first period the LHC will reach a centre-of-mass energy of 7 TeV. Until summer 2010 an integrated luminosity of about $20\,\mathrm{pb}^{-1}$ is expected. The number of W and Z events will reduce by a factor of $\frac{2}{3} \cdot \frac{1}{5}$ ($\frac{2}{3}$: the W and Z cross sections are decrease by roughly one third when reducing the centre-of-mass energy from 10 TeV to 7 TeV; $\frac{1}{5}$: $20\,\mathrm{pb}^{-1}/100\,\mathrm{pb}^{-1}$) compared to the quoted numbers for $100\,\mathrm{pb}^{-1}$, allowing R_n to be measured for up to two jets with reasonable results. For these jet multiplicities the $t\bar{t}$ background can be neglected, only the QCD dijet background has to be controlled. However, for the low jet multiplicities a high signal to background ratio is expected. Therefore, this analysis is also well adopted for these first $20\,\mathrm{pb}^{-1}$ at a centre-of-mass energy of 7 TeV.

Bibliography

[1] Johann Wolfgang von Goethe. *Urfaust*. 1772-1775.

[2] Michael Edward Peskin, Daniel V. Schroeder. An Introduction to quantum field theory. Reading, USA: Addison-Wesley (1995) 842 p.

[3] Francis Halzen, Alan D. Martin. *Quarks and Leptons: An Introductory Course in Modern Particle Physics*. John Wiley and Sons Inc., 1984.

[4] Particle Data Group. *Particle Physics Booklet*. The European Physical Journal B 667,1 (2008), July 2008.

[5] Torsten Harenberg. *AMANDA und DØ als Testumgebung fuer das LHC Computing Grid*. WUB-DIS 2005-09, 2005.

[6] G. Zweig. An SU(3) model for strong interaction symmetry and its breaking. CERN-TH-401.

[7] S. L. Glashow. Partial Symmetries of Weak Interactions. *Nucl. Phys.*, 22:579–588, 1961.

[8] Jeffrey Goldstone, Abdus Salam, Steven Weinberg. Broken Symmetries. *Phys. Rev.*, 127:965–970, 1962.

[9] Steven Weinberg. A Model of Leptons. *Phys. Rev. Lett.*, 19:1264–1266, 1967.

[10] Abdus Salam. Weak and Electromagnetic Interactions. Originally printed in *Svartholm: Elementary Particle Theory, Proceedings Of The Nobel Symposium Held 1968 At Lerum, Sweden*, Stockholm 1968, 367-377.

[11] Vernon D. Barger, R. J. N. Phillips. COLLIDER PHYSICS. REDWOOD CITY, USA: ADDISON-WESLEY (1987) 592 P. (FRONTIERS IN PHYSICS, 71).

[12] A. Lagarrigue. Neutral Currents in Gargamelle. (Talk). In *Erice 1974, International School Of Subnuclear Physics*, New York 1975, 543-559.

[13] D. Denegri. The discovery of the W and Z. *Phys. Rept.*, 403-404:107–145, 2004.

[14] Peter W. Higgs. Broken symmetries, massless particles and gauge fields. *Phys. Lett.*, 12:132–133, 1964.

[15] F. Abe et al. Observation of top quark production in $\bar{p}p$ collisions, hep-ex/9503002. *Phys. Rev. Lett.*, 74:2626–2631, 1995.

[16] S. Abachi et al. Observation of the top quark, hep-ex/9503003. *Phys. Rev. Lett.*, 74:2632–2637, 1995.

[17] Kenneth D. Lane. Technicolor 2000, hep-ph/0007304. 2000.

[18] Rikkert Frederix, Fabio Maltoni. Top pair invariant mass distribution: a window on new physics, 0712.2355. *JHEP*, 01:047, 2009.

[19] Daniel Wicke. *Properties of the Top Quark*. Habilitationsschrift, Aug. 2009.

[20] S. Moch, P. Uwer. Heavy-quark pair production at two loops in QCD, hep-ph/0807.2794. *Nucl. Phys. Proc. Suppl.*, 183:75–80, 2008.

[21] Johann H. Kuhn. Theory of top quark production and decay, hep-ph/9707321. 1996.

[22] M. Jezabek, Johann H. Kuhn. QCD Corrections to Semileptonic Decays of Heavy Quarks. *Nucl. Phys.*, B314:1, 1989.

[23] M. Jezabek, Johann H. Kuhn. SEMILEPTONIC DECAYS OF TOP QUARKS. *Phys. Lett.*, B207:91, 1988.

[24] Combination of CDF and D0 Results on the Mass of the Top Quark, hep-ex/0903.2503. 2009.

[25] LEP Electroweak Working Group. `http://lepewwg.web.cern.ch/LEPEWWG/`.

[26] Tevatron Electroweak Working Group. Combination of CDF and D0 Measurements of the Single Top Production Cross Section, hep-ex/0908.2171. 2009.

[27] CERN Communication Group. *CERN faq: LHC the guide*. CERN-Brochure-2009-003-Eng, February 2009.

[28] Lyndon Evans, (ed.), Philip Bryant, (ed.). LHC Machine. *JINST*, 3:S08001, 2008.

[29] `http://cms.web.cern.ch/cms/index.html/`.

[30] `http://aliceinfo.cern.ch/Public/Welcome.html/`.

[31] `http://lhcb.web.cern.ch/lhcb/`.

[32] `http://www.stelab.nagoya-u.ac.jp/LHCf/`.

[33] `http://totem.web.cern.ch/Totem/`.

[34] `http://www.atlas.ch/`.

[35] C. Amsler et al. (Particle Data Group). *Review of Particle Physics*. Physics Letters B667, 1 (2008) and 2009 partial update for the 2010 edition, 2008.

[36] J. Alcaraz et al. A Combination of preliminary electroweak measurements and constraints on the standard model, hep-ex/0612034. 2006.

[37] Precision electroweak measurements on the Z resonance, hep-ex/0509008. *Phys. Rept.*, 427:257, 2006.

[38] G. D. Coughlan, J. E. Dodd. The Ideas of particle physics: An Introduction for scientists. Cambridge, UK: Univ. Pr. (1993) 244 p.

[39] G. Aad et al. The ATLAS Experiment at the CERN Large Hadron Collider. *JINST*, 3:S08003, 2008.

[40] Jorg Wotschack. *MDT Parameter Book (Draft 03)*. November 28 2007.

[41] (ed.) Duckeck, G. et al. ATLAS computing: Technical design report. CERN-LHCC-2005-022.

[42] ATLAS HLT/DAQ/DCS Group. *ATLAS High-Level Trigger, Data Acqusition and Controls, Technical Design Report*. October 2003.

[43] T Cornelissen, M Elsing, S Fleischmann, W Liebig, E Moyse, A Salzburger. Concepts, Design and Implementation of the ATLAS New Tracking (NEWT). ATL-SOFT-PUB-2007-007.

[44] G. Aad et al. Expected Performance of the ATLAS Experiment - Detector, Trigger and Physics, hep-ex/0901.0512. 2009.

[45] The ATLAS Collaboration. *Reconstruction and Identification of Electrons*. ATL-PHYS-PUB-2009-004, April 2009.

[46] `http://www.fnal.gov/`.

[47] The ATLAS Collaboration. *Reconstruction and Identification of Photons*. ATL-PHYS-PUB-2009-005, April 2009.

[48] M. Lefebvre, P. Loch. *Jet Reconstruction and Calibration*. `https://twiki.cern.ch/twiki/bin/view/AtlasProtected/IntroductionToHadronicCalibration/view/AtlasProtected/IntroductionToHadronicCalibration`.

[49] J. M. Butterworth, J. P. Couchman, B. E. Cox, B. M. Waugh. KtJet: A C++ implementation of the K(T) clustering algorithm, hep-ph/0210022. *Comput. Phys. Commun.*, 153:85–96, 2003.

[50] Gerald C. Blazey et al. Run II jet physics, hep-ex/0005012. 2000.

[51] P. A. Delsart. *k(t) Algorithms in Athena: timing performances and new implementation*. ATL-COM-SOFT-2006-007, 2006.

[52] Matteo Cacciari, Gavin P. Salam. Dispelling the N^3 myth for the k_t jet-finder, hep-ph/0512210. *Phys. Lett.*, B641:57–61, 2006.

[53] Frank E. Paige, Sanjay Padhi. Rome Jet Calibration Based on Athena 9.0.4. 2004.

[54] S Corréard, V Kostyukhin, J Lévêque, A Rozanov, J B De Vivie de Régie. b-tagging with DC1 data. Technical Report ATL-PHYS-2004-006, Aix-Marseille 2. Cent. Phys. Part., Marseille, Nov 2003.

[55] T. Gleisberg et al. Event generation with SHERPA 1.1, hep-ph/0811.4622. *JHEP*, 02:007, 2009.

[56] M. A. Dobbs et al. Les Houches guidebook to Monte Carlo generators for hadron collider physics, hep-ph/0403045. 2004.

[57] Torbjorn Sjostrand, Stephen Mrenna, Peter Z. Skands. PYTHIA 6.4 Physics and Manual, hep-ph/0603175. *JHEP*, 05:026, 2006.

[58] Michelangelo L. Mangano, Mauro Moretti, Fulvio Piccinini, Roberto Pittau, Antonio D. Polosa. ALPGEN, a generator for hard multiparton processes in hadronic collisions, hep-ph/0206293. *JHEP*, 07:001, 2003.

[59] S. Agostinelli et al. GEANT4: A simulation toolkit. *Nucl. Instrum. Meth.*, A506:250–303, 2003.

[60] D. Adams et. al. The ATLFAST-II performance in release 14 - particle signatures and selected benchmark processes -. ATL-PHYS-INT-2009-110.

[61] Stefano Frixione, Bryan R. Webber. Matching NLO QCD computations and parton shower simulations. *JHEP*, 06:029, 2002.

[62] G. Corcella et al. HERWIG 6.5: an event generator for Hadron Emission Reactions With Interfering Gluons (including supersymmetric processes), hep-ph/0011363. *JHEP*, 01:010, 2001.

[63] John M. Campbell, J. W. Huston, W. J. Stirling. Hard Interactions of Quarks and Gluons: A Primer for LHC Physics, hep-ph/0611148. *Rept. Prog. Phys.*, 70:89, 2007.

[64] V. M. Abazov et al. DØ Collaboration. *Simultanous Measurement of the Ratio R=B(t $\rightarrow$ Wb)/B(t $\rightarrow$ Wq) and the Top-Quark Pair Production Cross Section with the DØ Detector at $\sqrt{s}$= 1.96 TeV*. Phys. Rev. Letters PRL 100, 192003 (2008), 2008.

[65] Frits A. Berends, W. T. Giele, H. Kuijf, R. Kleiss, W. James Stirling. MULTI - JET PRODUCTION IN W, Z EVENTS AT p anti-p COLLIDERS. *Phys. Lett.*, B224:237, 1989.

[66] private communication with Malgorzata Worek.

[67] Alessandro Cafarella, Costas G. Papadopoulos, Malgorzata Worek. Helac-Phegas: a generator for all parton level processes, hep-ph/0710.2427. *Comput. Phys. Commun.*, 180:1941–1955, 2009.

[68] Costas G. Papadopoulos. PHEGAS: A phase space generator for automatic cross-section computation, hep-ph/0007335. *Comput. Phys. Commun.*, 137:247–254, 2001.

[69] Aggeliki Kanaki, Costas G. Papadopoulos. HELAC: A package to compute electroweak helicity amplitudes, hep-ph/0002082. *Comput. Phys. Commun.*, 132:306–315, 2000.

[70] `http://www-zeus.desy.de/`.

[71] `http://www-h1.desy.de/`.

[72] `http://durpdg.dur.ac.uk/hepdata/pdf3.html/`.

[73] Eva-Lotte Quatuor. Studies on W/Z+jet production at LHC with the SHERPA generator, diploma thesis, 2009.

[74] David Griffiths. *Introduction to Elementary Particles*. Wiley-VCH, 2008.

[75] C. Albajar et al. Studies of Intermediate Vector Boson Production and Decay in UA1 at the CERN Proton - Antiproton Collider. *Z. Phys.*, C44:15–61, 1989.

[76] Erin Abouzaid, Henry J. Frisch. The Ratio of $W + N$ jets to $Z^0/\gamma^* + N$ jets versus N as a precision test of the standard model, hep-ph/0303088. *Phys. Rev.*, D68:033014, 2003.

[77] Peter Steinbach. W/Z + Jets COM note: lepton reconstruction and trigger efficiencies - status report. *SM W/Z + jets meeting*, December 15th, 2009.

[78] *Prospects for the Top Pair Production Cross-section at $\sqrt{s}$ = 10 TeV in the Single Lepton Channel in ATLAS*. ATL-PHYS-PUB-2009-087.

[79] V. Blobel, E. Lohrmann. *Statistische und numerische Methoden der Datenanalyse*. Teubner Verlag, 1998.

[80] G. D'Agostini. A Multidimensional unfolding method based on Bayes' theorem. *Nucl. Instrum. Meth.*, A362:487–498, 1995.

[81] Rev. Thomas Bayes. An essay toward solving a problem in the doctrine of chances. *Phil. Trans. Roy. Soc. Lond.*, 53:370–418, 1764.

[82] `http://www.roma1.infn.it/~dagos/bayes_distr.txt/`.

Acknowledgements

This PhD thesis would not have been possible without the help and backing of many people. I cannot mention them all explicitely, but I would like to express my gratitude to everyone who contributed to this thesis in one way or another.

Explicitely I would like to thank Prof. Dr. Peter Mättig for giving me the opportunity to do my PhD in particle physics and supporting me all the time.

My special thanks go to Dr. Klaus Hamacher for many fruitful discussions, giving me food for thoughts and advising me for all intents and purposes.

Also I would like to thank Prof. Dr. Wolfgang Wagner, Prof. Dr. Christian Zeitnitz and Dr. Thorsten Kuhl for letting me profit from their knowledge and bringing forward my work with their ideas.

And I would like to thank all members of the Wuppertal high energy physics group. Thank you for the pleasant work atmosphere, the collective coffee breaks and discussions of all kinds amongst us. Especially I would like to say thank you to Dr. Torsten Harenberg for his support, especially in computing affairs, and for being a nice and solid companion in good times and in stressy and very hard times.

I would also like to say thank you to all my fellow students, especially Dr. Yvonne Peters and Dr. Henning Hörstermann. Without them the hard times of studying physics would have been much harder and beyond all bearing.

I am especially indebted to my family.